ThermoFisher SCIENTIFIC

Chemical, Elemental and Structural Analysis of Batteries

Application Compendium

thermo scientific

Contents

Imaging techniques for 2D/3D morphology

Raman
- *Ex situ* Raman Analysis of Lithium Ion Batteries 4
- *In situ* Raman Analysis of Lithium Ion Batteries 8
- Raman Analysis of Lithium-Ion Battery Components – Part I: Cathodes 12
- Raman Analysis of Lithium-Ion Battery Components – Part II: Anodes 16
- Raman Analysis of Lithium-Ion Battery Components – Part III: Electrolytes 20

FTIR
- Gas-Phase FTIR for smoke toxicity measurements 23

Electron Microscopes
- Investigate batteries with a SEM for better performance 25
- Ion spectroscopy using TOF-SIMS on a Thermo Scientific Helios DualBeam 28
- Large area automated sample preparation for batteries 32
- Strategies for accurate imaging on battery separator structure 36
- Multiscale Image-Based Control and Characterization of Lithium-Ion Batteries 39
- Assessment of contaminants within battery materials via Axia ChemiSEM 41
- Environmental Transmission Electron Microscopy 45

Elemental and surface analysis

XPS
- Analysis of Electrode Materials for Lithium Ion Batteries 57

Ion Chromatography
- Determination of Electrolyte Solution from Lithium Ion Battery 60
- Determination of Dissolved Manganese in Lithium/Manganese Oxide Battery Electrolyte 65

ICP-OES
- Robust and sensitive measurement of trace element impurities in $LiPF_6$ electrolyte solutions 69
- Determination of elemental impurities in lithium iron phosphate using ICP-OES 75
- Determination of elemental impurities in graphite powder for lithium-ion battery anodes 79
- Determination of lithium and other elements in brine solutions using ICP-OES 83
- Sensitive determination of elements in lithium batteries 89

GC-MS
- Orbitrap GC-MS Technology Provides New Insight into Lithium Ion Battery Degradation 93
- Analysis of electrolyte components of lithium-ion batteries 97
- Identification of lithium-ion battery degradation products using GC Orbitrap mass spectrometry 102
- Comprehensive analysis of electrolyte solutions for lithium ion batteries 109

GC
- Battery drum pack gas analysis through a multi-valve, multi-column GC system 116

IOMS technique
- Characterization of battery samples by the Flash*Smart* Elemental Analyzer 124

Twin-screw compounding and rheological characterization

Extrusion
- Continuous twin-screw compounding of battery slurries in a confined space 127
- Cost-efficient and ecological twin-screw compounding of dry lithium-ion battery pastes 129

The global lithium-ion battery market is expected to reach 93.1 billion USD by 2025. This is largely driven by increased usage in electric vehicles, grid storage, and portable consumer electronics where the higher energy density of the lithium-ion battery offers a clear advantage.

Improvements in battery performance require the development of new, more effective battery components. Also needed is a better understanding of the mechanisms that lead to performance degradation after repeated charging and discharging cycles. Evaluation of batteries and battery components requires a variety of analytical methods that permit the study of materials and component surfaces at various scales.

As the world leader in advancing science, Thermo Fisher Scientific provides the widest range of analytical instrumentation for battery analysis and product formulation. Available options include X-ray photoelectron spectroscopy (XPS/ESCA), electron microscopy (SEM, TEM and FIB-SEM), vibrational spectroscopy (FTIR, Raman and NIR), mass spectrometry (GC-MS, HPLC, LC-MS, HREMS-MS, ICP-MS), microCT, nuclear magnetic resonance (NMR), X-ray diffraction, X-ray fluorescence, rheometry, viscometry, extrusion and torque rheometry.

Imaging techniques such as Raman and electron microscopy cover the full scale from the cellular level, through use of Raman and microCT, down to the atomic scale, using TEM. Raman imaging can be used to observe the distribution of components and to monitor how these components change during the charging/discharging cycles. Electron microscopy is mainly used to study the 2D and 3D morphology of battery components at different stages in the life cycle. 3D imaging provides complete geometric evolution of the cathode micro-structure upon cycling. Geometric parameters such as volume fraction, surface area, particle size distribution and tortuosity are typically assessed using FIB–SEM techniques and Avizo software.

Spectroscopy, NMR, X-ray diffraction and mass spectrometry are key to studying the evolution of structural and chemical changes and the formation of defects in battery electrodes. These techniques permit the analysis of electrode materials as they change during the redox reaction, and they can give information on both crystalline and amorphous phases. Local differences in Raman spectral changes can be used to create a state-of-charge (SOC) distribution map showing the composite electrode. The composition of the solid electrolyte interface (SEI) is commonly studied with *ex situ* XPS and *in situ* FTIR, while Raman spectroscopy is utilized to monitor the SEI formation.

Rheometry helps characterizing flow properties of electrode slurries to optimize the coating process and storage conditions. Understanding the quality of dispersions is a predictor for cell performance. Twin-Screw compounding produces much more homogeneous electrode pasts as alternative mixing technologies. Extruders enable significant solvent reduction to produce almost-dry battery pastes – this saves up to 30% of total energy costs.

This compendium of application notes provides in-depth reports on analyses aimed at improving the performance of lithium-ion batteries.

Find out more about Thermo Fisher Scientific capabilities for batteries at **thermofisher.com/battery-solutions**

Ex situ Raman Analysis of Lithium-Ion Batteries

Abstract

The needs of lithium-ion (Li-ion) battery customers can be segmented into *in situ* and *ex situ* modes of analysis. *Ex situ* lets researchers study battery components removed from the operating battery cell.

Introduction

The use of Raman spectroscopy to analyze battery materials has been around for years. During the 1960s, researchers used Raman spectroscopy to elucidate many of the fundamental spectral features of the minerals and inorganic materials widely used in battery research today.[1,2] Raman spectroscopy is a good fit for these materials because many of the characteristic vibrational and rotational modes occur in the low-wavenumber region of the spectrum, typically accessible only by far-infrared measurements. In the past,, both Raman and far-infrared (FIR) measurements were time-consuming and difficult experiments.

Instrumentation advances have made Raman spectroscopy a much more approachable technique, mainly by increasing the ease of use. New application areas ensued, such as the exploding interest in rechargeable Li-ion batteries. Many have published careful studies of materials specifically related to Li-ion batteries as well as next-generation batteries. The review articles published by Julien in 2018 and Baddour-Hadjean in 2010 are excellent resources for learning more about the developments in this field.[3, 5] The focus of this application note is on the *ex situ* application of Raman spectroscopy as it pertains to battery research.

Thermo Scientific DXR3xi Raman Imaging Microscope

Analysis techniques: *in situ* versus *ex situ*

The term *in situ* is used to describe experiments where the battery components are studied in an assembled cell under operating conditions. Think of *in situ* as the window to the chemical reactions that happen inside a battery, such as charging and discharging a battery.

While *in situ* cells provide valuable information, their use is generally targeted at the research and development of new materials for Li-ion batteries. Once a formulation is designed, a candidate battery is scaled up through pilot production to actual product samples. At this stage of development, researchers are most interested in characterizing failure modes and a better understanding of performance differences. For example, what makes one production run work better than another, and why did one battery fail yet its siblings from the same batch work fine?

To answer these questions, researchers carefully disassemble a battery cell to examine the individual components. This type of analysis is called *ex situ* because the battery components are removed from the operating battery cell. The goal is to prepare the samples for analysis in as close to a native state as possible.

Battery disassembly for *ex situ* analysis is carried out in an inert environment such as an argon-filled glove box to protect the battery components from moisture and oxidation. For example, the anode-separator-cathode sandwich must be carefully separated and rinsed to remove excess electrolytes.

Once the samples are prepared, they must be kept in an inert environment to protect against changes during analysis. When space is available, instruments are installed inside the glove box so the samples can be analyzed. In most cases, the sample must be removed from the glove box and transferred to an external instrument for analysis. This is where an *ex situ* transfer cell becomes a key component of the workflow. It preserves the inert environment around the sample so it can be studied.

From single point measurements to Raman imaging

The majority of published research on Li-ion battery Raman work is based on single point measurements acquired over time during charge/discharge cycles. Single point measurements can be misleading because there is no way of knowing if the sampled point is representative of the entire electrode. It is important to make multiple measurements to be sure. Because the Raman signals are weak, it takes many minutes to generate enough signal-to-noise ratio at each measurement point. A complete, multi-point experiment can be quite time-consuming to complete.

Today, Raman imaging is a viable alternative that enables you to quickly make thousands of measurements over an area of the electrode rather than just single point measurements. Each pixel in a Raman image is a complete Raman spectrum, so you can tell if changes are heterogeneous or hot spots.

The following experimental results demonstrate the flexibility of using Raman imaging for the *ex situ* analysis of Li-ion batteries and their components.

Characterization of Li-ion anodes

After safety concerns, a leading area of interest in Li-ion battery research is understanding the cause of performance degradation over time. Research indicates that the solid electrolyte interphase (SEI) layer formed on the surface of the electrode is key to performance. The SEI layer is formed by the deposition of organic and inorganic compounds during the first several charge/discharge cycles.[4] It stabilizes the electrode from further decomposition and promotes reversible capacity. Because of the complexity of the SEI layer, results from any and all analytical techniques contribute to an incremental understanding of this behavior.

As you might expect, it is a messy business to extract electrodes from a used battery so the SEI can be studied. It takes great care to prepare the sample so as to preserve its integrity for *ex situ* analysis. This is usually achieved by working in an argon-filled glove box to prevent sample degradation due to atmospheric exposure. A transfer cell with a window is used to seal the sample in the inert argon environment so it can be removed from the glove box for analysis using a Raman microscope.

Experiment

Anode samples from a disassembled Li-ion battery were cut and mounted in a Thermo Scientific transfer cell so that a cross-section of the anode could be imaged.

The transfer cell (**Figure 1**) maintains an inert environment surrounding the sample so it can be analyzed using instruments outside a glove box. The cell body accepts various industry-standard sample holders (stubs) developed for scanning electron microscope (SEM) analysis. A 90° stub was used to hold the cut edge of the anode facing the window. A cap containing a calcium fluoride (CaF_2) window seals the sample under an argon blanket. The cap is screwed on until the window height is just above the sample. This provides a minimum working distance between a microscope objective and the sample. A short working distance is an advantage because it allows the use of high magnification objectives having a large numerical aperture (N.A.).

Figure 1. Transfer cell maintains sample in an inert environment for *ex situ* analysis of Li-ion battery materials.

Raman spectra were collected over a single 76 µm × 160 µm area at a spatial resolution of 1.0 µm per pixel using a Thermo Scientific™ DXR™xi Raman Imaging Microscope. Laser power at the sample was 2.0 mW at 532 nm with a 0.2 sec exposure time and four image scans. An Olympus 50× long working distance 0.5 N.A. microscope objective was used to focus through the transfer cell window. Higher laser powers and/or longer exposure times were avoided because they can heat the sample, causing changes that mask the native state of the electrode.

Results

A Raman image is a hyperspectral data set with each pixel in the image being a complete Raman spectrum. Using various spectral processing techniques, this hyperspectral Raman data generates image contrast pertaining to the specific chemical features. This capability is used to visualize minute differences within a sampled area.

A variety of chemical images can be created from each data set, showing changes within the sampled area. For this experiment, image contrast is generated by multivariate curve resolution (MCR) analysis. MCR finds the major components within each image and a different color is assigned to each. This is analogous to the use of dyes in biological fluorescence imaging that tag different parts of a cell.

Alternatively, multiple regions of the sample can be imaged, and the Raman spectral data within each region can be averaged to produce a single spectrum. In this mode, the Raman imaging data set is used as a means of homogenizing any differences in the electrode area. This average spectrum represents a single point measurement, yet each point represents a 30 µm square compared with the typical 1 µm sample area from a standard Raman microscope.

Figure 2 is a micrograph of the anode cross-section. The copper current collector is in the center, with anode material coated on both surfaces. Superimposed is the Raman image created from the spectral differences shown by the inset Raman spectra. The Raman image clearly shows that the coating on one side of the copper current collector is dominated by carbon black (red) whereas the other side has a much greater density of the active graphite phase (blue).

This example demonstrates the advantage of Raman imaging over traditional single point measurements. The major differences in the two coatings could easily have been missed by single point measurements depending on where the points were measured.

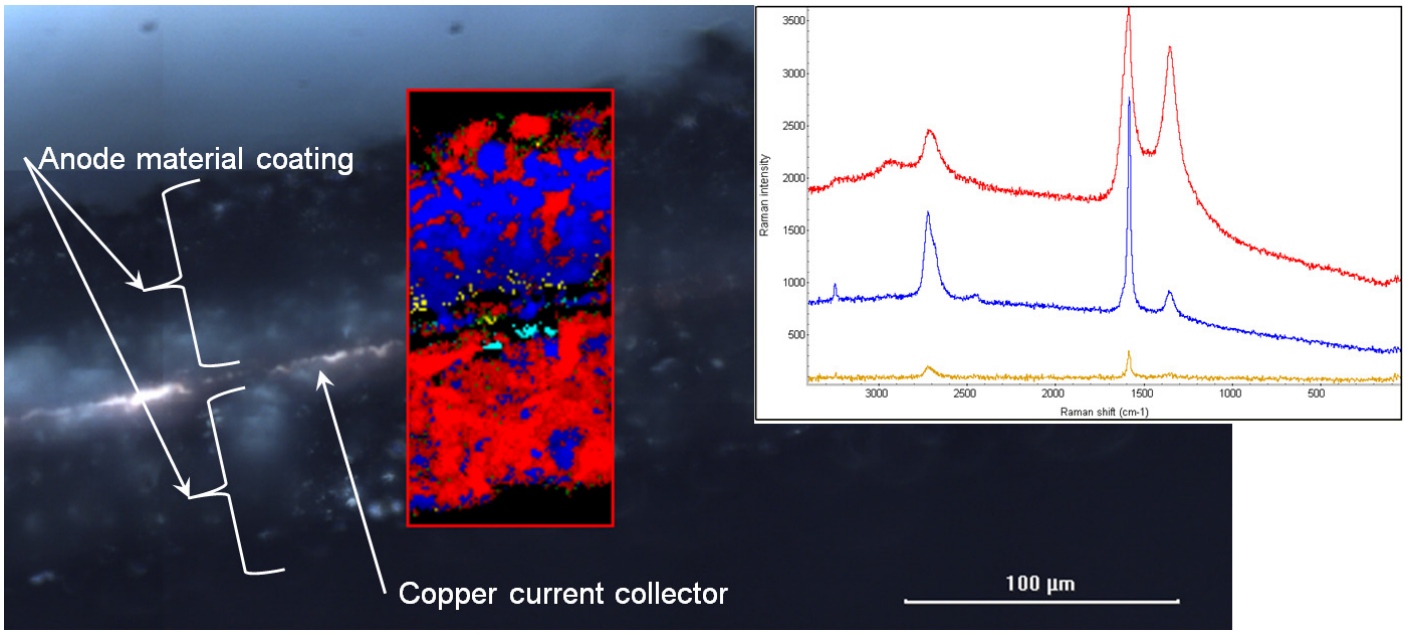

Figure 2. Cross section view of a Li-ion battery anode. Raman image indicates a difference in the anode coating on each side. Inset Raman spectra are color-coded to the areas in the Raman image.

Conclusion

The high sensitivity of Raman imaging is a benefit for Li-ion battery analysis. *Ex situ* Raman imaging measurements give results with a higher degree of confidence compared to single points.

The data were collected using an older model instrument, the Thermo Scientific DXRxi Raman Microscope. Currently, Thermo Fisher Scientific offers an improved model, the Thermo Scientific DXR3xi Raman Microscope, which offers superior speed and performance over its predecessor models

References

1. P. Tarte, *J. Inorg. Nucl. Chem.* 29(4) 915–923 (1967).
2. W.B. White, B.A. De Angelis, *Spectrochimica Acta Part A* 23(4) 985–995 (1967).
3. R. Baddour-Hadjean, J.P. Pereira-Ramos, *Chemical Reviews* 110(3) 1278–1319 (2010).
4. A. Chagnes and J. Swiatowska, *Electrolyte and Solid-Electrolyte Interphase Layer in Lithium-Ion Batteries, Lithium Ion Batteries – New Developments*, Dr. Ilias Belharouak (Ed.), ISBN: 978-953-51-0077-5, InTech, (2012). Available from: http://www.intechopen.com/books/lithium-ion-batteries-newdevelopments/electrolyte-and-solid-electrolyteinterphase-layer-in-lithium-ion-batteries.
5. http://www.aimspress.com/article/10.3934/matersci.2018.4.650/Related.html

Author

Dick Wieboldt, PhD, Thermo Fisher Scientific, Madison, WI, USA

Keywords

Anodes, *Ex Situ* Analysis, Lithium Ion Battery, Raman Microscopy, Raman Imaging, DXR3xi Raman Imaging Microscope

In situ Raman Analysis of Lithium-Ion Batteries

Abstract

The needs of the Li-ion battery customers can be segmented into *in situ* and *ex situ* modes of analysis. *In situ* analysis allows researchers to follow changes in a battery cell during its charge and discharge cycles. Recent improvements in Raman sensitivity enable these changes to be imaged on a dynamic time scale.

Introduction

The use of Raman spectroscopy to analyze battery materials has been around for years. During the 1960s, researchers used Raman spectroscopy to elucidate many of the fundamental spectral features of the minerals and inorganic materials widely used in battery research today.[1,2] Raman spectroscopy is a good fit for these materials because many of the characteristic vibrational and rotational modes occur in the low-wavenumber region of the spectrum, typically accessible only by far-infrared measurements. In the past, both Raman and far-infrared (FIR) measurements were time-consuming and difficult experiments.

Advances in instrumentation have significantly increased the ease of use, making Raman techniques a much more approachable. New areas of application ensued, such as the exploding interest in rechargeable lithium-ion batteries. Many researchers are involved and have published careful studies of materials specifically related to Li-ion batteries and next-generation batteries. The review articles published by Julien in 2018 and Baddour-Hadjean in 2010 are excellent resources for those wishing to learn more about the developments in this field.[3, 12] This application note focuses on the *in situ* application of Raman spectroscopy as it pertains to battery research.

Thermo Scientific DXR3xi Raman Imaging Microscope

Analysis techniques: *in situ* versus *ex situ*

The term *in situ* is used to describe experiments in which the battery components are studied in an assembled cell under operating conditions. Think of *in situ* as the window to the chemical reactions that happen inside a battery, such as charging and discharging a battery. There are very few commercially available cell designs compatible with spectroscopic measurements. Researchers have resorted to building their own cells to meet the needs of their experimental apparatus. Examples of such designs have been published along with experimental results.[4-10, 13]

In situ cells analysis is generally targeted at researching and developing new materials for Li-ion batteries. Once a formulation is designed, a candidate battery is scaled up through pilot production to actual product samples. At this stage of development, researchers are most interested in characterizing failure modes and a better understanding of performance differences. For example, what makes one production run work better than another, and why did one battery fail yet its siblings from the same batch work fine?

To answer these questions, researchers must carefully disassemble a battery cell to examine the individual components. This type of analysis is called *ex situ* because the battery components are removed from the operating battery cell. The goal is to prepare the samples for analysis in as close to a native state as possible. Please see the companion application note for details on *ex situ* analysis.

From single point measurements to Raman imaging

The majority of published research on Li-ion battery *in situ* Raman work is based on single point measurements acquired over time during charge/discharge cycles. An example is the excellent work done by Kostecki's group at Lawrence Berkeley National Lab.[11]

Single point measurements can be misleading because there is no way of knowing if the sampled point is representative of the entire electrode. It is important to make multiple measurements to be sure. Because the Raman signals are weak, it takes many minutes to generate enough signal-to-noise ratio at each measurement point. A complete, multi-point experiment can be quite time-consuming to complete.

Today, Raman imaging is a viable alternative that enables you to quickly make thousands of measurements over an area of the electrode rather than just single point measurements. Each pixel in a Raman image is a complete Raman spectrum, so you can observe if changes are heterogeneous or hot spots.

The following experimental results demonstrate the flexibility of using Raman spectroscopy for *in situ* analysis of Li-ion batteries and their components.

Lithiation of graphite

Graphite is widely used as an anode material for rechargeable Li-ion batteries.

During the Li-ion battery charging cycle, positively charged Li+ ions move from the cathode through the electrolyte, across a separator into the anode to balance the flow of electrons in the external circuit (Figure 1). This process of Li^+ ions entering the graphitic structure of the anode is called intercalation. Intercalation causes changes in the anode structure – primarily a swelling of the graphite structure.

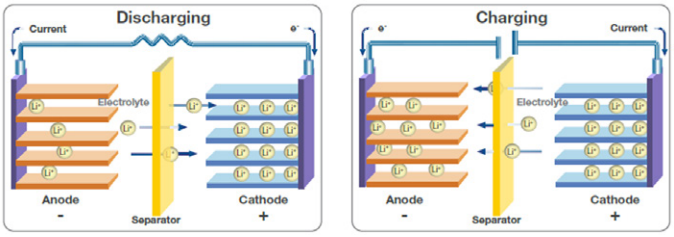

Figure 1. Movement of Li^+ ions balance electrons during the charge and discharge cycles of a Li-ion battery.

Experimental

The experimental setup for this example consists of a Thermo Scientific™ DXR™xi Raman Imaging Microscope and an ELCELL® ECC-Opto-Std Optical Electrochemical Cell. This cell enables the investigation of batteries in a "sandwich" configuration where the working electrode (WE) material is placed under a sapphire (Al_2O_3) window. In this example, the electrode material (graphite powder) is spread onto a copper grid serving as the current collector. This WE is sandwiched from below, with a glass fiber separator soaked with the electrolyte solution and lithium metal as the counter electrode (CE).

The Raman beam from the microscope objective impinges onto the backside of the WE material through the sapphire window (Figure 2). The advantage of investigating the backside of the electrode is that the pathway for the Raman beam is minimized, allowing the use of high magnification objectives to optimize spectra quality. The drawback is the gradient of lithiation concentration along the depth of the electrode. Accordingly, the electrode must be charged very slowly to minimize this unwanted gradient.

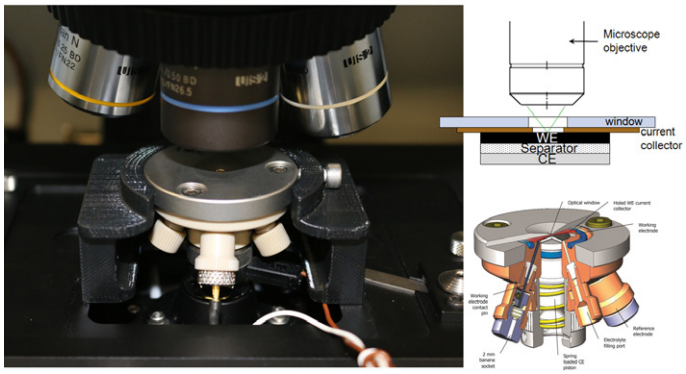

Figure 2. Experimental setup for the *in situ* example showing the electrochemical cell mounted on a Raman imaging microscope stage.

The graphite electrode was cycled at a constant rate of approximately 0.06 C. The C-rate measures how rapidly a battery is charged/discharged. This rate of 0.06 C corresponds to 33 hours for a complete charge/discharge cycle between 1.5 and 0.005 V against Li/Li^+. Raman imaging was carried out during the initial 480 minutes of the charging (lithiation) process only.

Raman spectra were collected over a 30 µm × 30 µm area at 1 µm pixel spacing using two mW of 532 nm laser excitation, a 0.01 sec exposure time for each pixel, and 50 scans per image. Higher laser powers and/or longer exposure times resulted in the burning of the graphite and boiling of the electrolyte.

Results

A Raman image is a hyperspectral dataset, with each pixel in the image being a complete Raman spectrum. This hyperspectral Raman data uses various spectral processing techniques to generate image contrast pertaining to specific chemical features. It is this capability that visualizes minute differences within a sampled area. By collecting a sequence of Raman images, we now can monitor changes in both space and time. As mentioned earlier, various chemical images can be created from each dataset showing changes within the sampled area. Alternatively, the Raman spectral data within each dataset can be averaged to produce a single spectrum for each time slice. In this mode, the Raman imaging dataset is used as a means of homogenizing any differences in the electrode area. This average spectrum represents a single point measurement, yet each point represents a 30 µm square compared with the typical 1 µm sample area from a standard Raman microscope.

In Figure 3, the 3D view (bottom left) shows changes in the Raman spectrum as a function of time over 8.3 hours (1–500 min). During this time, the battery cell is in the charging (lithiation) process only. This portion of the electrochemical cycle is shown in the lower right of Figure 3.

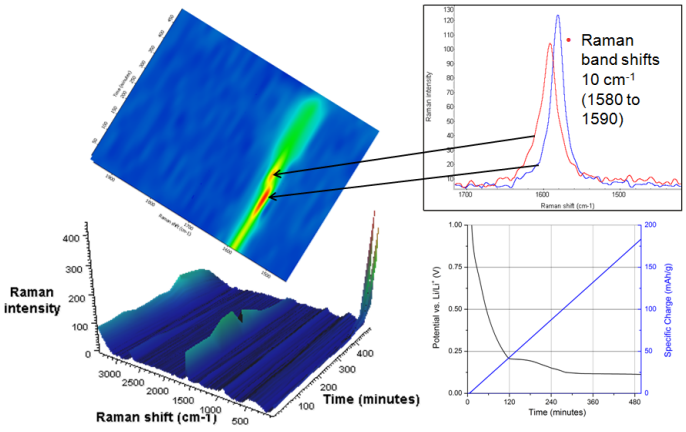

Figure 3. Different views rendered from the time lapse hyperspectral Raman data provide a wealth of experimental information.

The spectrum of graphite exhibits a prominent peak at 1580 cm^{-1} attributed to the E_{2g2} mode (G-band). At potentials between 0.42 and 0.31 V (specific charge 33 and 45 mAh/g), the band gradually disappears along with the simultaneous emergence of a peak centered at 1590 cm^{-1}. This peak shift is attributed to the Li^+ ions intercalated into the graphite structure. This is more easily seen in the center, 2D Raman image. The inset shows Raman spectra before and after the change.

Toward the end of the charge cycle at 8.3 hours (496 min), where the voltage is less than 0.15 V (specific charge greater than 146 mAh/g), a strong Raman band centered at 154 cm^{-1} begins to appear. This Raman band has not been previously reported, so its assignment is not conclusive. Strong Raman bands in this region have been attributed to TiO_2, Sb, and metal chlorides.

The type of views shown in Figure 3 are "spectrum-centric" because they show changes in the Raman spectra captured at different times during a time-based analysis. Figure 4 shows another way of exploring the same Raman imaging dataset from an alternative "image-centric" point-of-view. Here, we are not as interested in the Raman spectrum itself but rather its use as a tool to enhance differences within the image or its image contrast.

In Figure 4, Raman images are presented in which the image contrast is generated by multivariate curve resolution (MCR) analysis. In this case, MCR finds the differences within each image and across the entire time sequence. A different color is assigned to each resolved component. This color use is analogous to using dyes in biological fluorescence imaging which tag different parts of a cell. Each image is from the same 30 µm square portion of the anode. The blue MCR component is indicative of the 1580 cm^{-1} band; green the 1590 cm^{-1} band; yellow the 154 cm^{-1} band; red represents carbon black, a conductivity enhancer.

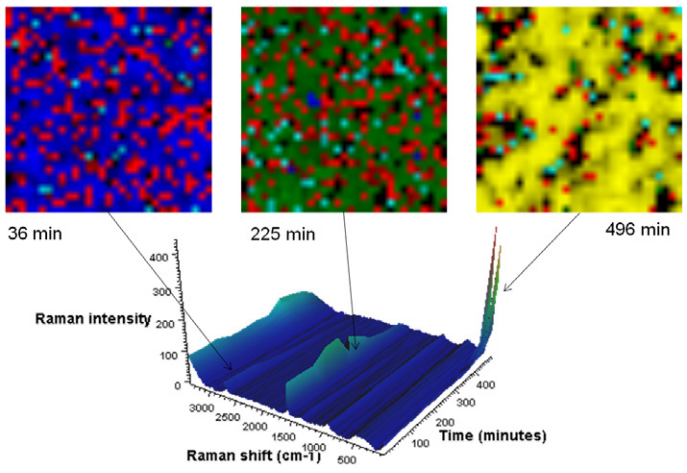

Figure 4. Raman images from different time slices in the graphite lithiation experiment.

It can be challenging to visualize the information content with such a massive wealth of data. Figure 4 shows just three frames to demonstrate this type of analysis. The changes are easy to grasp in the software. Please contact your local Thermo Fisher representative for a demonstration.

Conclusion

The high sensitivity of Raman imaging is a benefit for Li-ion battery analysis. *In situ* Raman imaging techniques show the spatial distribution of phase changes in electrodes over time. This capability was not possible using single point measurements using traditional Raman microscopy.

The data were collected using an older model instrument, the DXRxi Raman Microscope. Currently, Thermo Fisher Scientific offers an improved model, the Thermo Scientific DXR3xi Raman Microscope, which offers superior speed and performance over its predecessor models.

References

1. P. Tarte, *J. Inorg. Nucl. Chem.* 29(4) 915–923 (1967).
2. W.B. White, B.A. De Angelis, *Spectrochimica Acta Part A* 23(4) 985–995 (1967).
3. R. Baddour-Hadjean, J.P. Pereira-Ramos, *Chemical Reviews* 110(3) 1278–1319 (2010).
4. T. Gross, C. Hess, *J Power Sources* 256, 220–225 (2014).
5. P. Novák, D. Goers, L. Hardwick, M. Holzapfel, W. Scheifele, J. Ufheil, A. Wursig, *J Power Sources* 146, 15–20 (2005).
6. C.M. Burba, R. Frech, *Applied Spectroscopy* 60(5), 490–493 (2006).
7. E. Markevich, V. Baranchugov, G. Salitra, D. Aurbach, M. Schmidt, *J Electrochem Soc* 155(2), A132–A137 (2008).
8. Y. Luo, W.B. Cai, X.K. Xing, D.A. Scherson, *Electrochem. Solid-State Lett.* 7(1), E1–E5 (2004).
9. T. Gross, L. Giebeler, C. Hess, *Rev. Sci. Instrum.* 84(7), 073109-1–073109-6 (2013).
10. K. Hongyou, T. Hattori, Y. Nagai, T. Tanaka, H. Nii, K. Shoda, *Power Sources* 243, 72–77 (2013).
11. J. Lei, F. McLarnon, R. Kostecki, *J. Phys. Chem. B,* 109(2), 952–957 (2005).
12. http://www.aimspress.com/article/10.3934/matersci.2018.4.650/Related.html
13. https://www.sciencedirect.com/science/article/abs/pii/S0378775317303531

Authors

Dick Wieboldt, PhD, Thermo Fisher Scientific, Madison, WI, USA

Ines Ruff, PhD, Thermo Fisher Scientific, Dreieich, Germany

Matthias Hahn, PhD, El-Cell GmBH, Homburg, Germany

Keywords

Electrodes, *In Situ* Analysis, Lithium Ion Battery, Raman Microscopy, Raman Imaging, DXR3xi Raman Imaging Microscope

Learn more at **thermofisher.com/energy**

Application note

Raman analysis of lithium-ion battery components Part I: Cathodes

Authors

Robert Heintz, PhD, Thermo Fisher Scientific, Madison, WI, USA

Keywords

DXR3 Microscope, cathodes, lithium-ion battery, Raman

In recent years the increasing demand for powering portable electronic devices from laptops to smart phones has driven the need for improved battery performance, but the emergence of electric and hybrid vehicles is creating additional interest in new battery technologies.

The expanding use of portable energy storage introduces additional factors beyond just improving battery capacity. Cost, safety, and environmental impact are important considerations as the use of battery technology evolves. Lithium-ion batteries offer the highest energy density and output voltage among commercial rechargeable battery systems.[1] Even though lithium-ion batteries are now an established technology there is still considerable interest in improving the current technology and the development of new battery components.

Evaluation of batteries and battery components requires a variety of analytical methods, not only for the development of new materials but also for gaining a greater understanding of the mechanisms involved in charge/discharge cycles. Bulk analysis of components is important but it is also important to understand surface interactions and interfaces. Electrochemical evaluation of cells includes conductivity measurements, electrochemical stability of components, cell capacity, ion mobility, discharge rates, and cycling behavior. Materials characterization of the various cell components can include many different analytical techniques (e.g., XRD, SEM, TEM, TGA, DSC, EDS) but one technique that is rapidly growing in popularity for the analysis of materials is Raman spectroscopy. Raman spectroscopy has many advantages but the most important ones for battery applications are those that involve subtle changes in molecular structure or local chemical environments. The spectral results can usually be correlated with the electrochemical performance.

There have been significant improvements in commercial Raman instrumentation over the last several years. Important advances in both hardware and software have made modern Raman instruments much more user friendly and removed many of the obstacles that in the past made routine use of Raman spectroscopy arduous for users with limited expertise.

Advances in instrumentation also include integration of light microscopes with Raman instrumentation allowing spectroscopic analysis of samples at the microscopic level. Modern Raman instruments, like the Thermo Scientific™ DXR™ 3 Raman Microscope, are fully integrated, high performance research grade instruments that have incorporated extensive automation to simplify the collection of Raman spectra. For example, automated on-demand alignment and calibration present on the DXR3 Raman Microscope are designed to eliminate the need for manual realignment and calibration, resulting in an instrument that is easy to use and maintain at its highest level of performance. This ease of use means it is much quicker to get started and more straightforward to get accurate results. This opens up the use of Raman spectroscopy for all types of users.

Raman spectroscopy has been used for the analysis of many different types of battery components. This includes analysis of cathode materials, anode materials, and electrolytes.[2,3] Part one of this series will focus on some examples of how Raman spectroscopy has been utilized for the analysis of cathode materials. This article is in no way meant as a complete review of the literature, which is beyond the scope of this application note. Included here are some interesting examples from published papers that illustrate how Raman spectroscopy has been used for the analysis of cathode materials.

Developing new cathode materials for lithium-ion batteries has been a very active area of research. Lithium cobalt ($LiCoO_2$) is the classical cathode material, but there are issues with the cost, safety, and toxicity of this material. The manganese spinel, $LiMn_2O_4$, is a low-cost alternative that is safer and is more environmentally friendly. This cathode material is used in some commercial lithium-ion cells. The issue with the use of this material is that the cathodes suffer from capacity fade over time. One main contribution to this capacity fading appears to result from manganese (Mn) dissolution via a disporportionation reaction of MnIII at high potentials. This dissolution can be suppressed by doping the material with other transition metals. An example of this can be seen in some interesting work on mixed metal spinels ($LiNi_{0.5}Mn_{1.5}O_4$ and $LiNi_{0.5}$-x$Mn_{1.5}$-yM_{x+y}O4 M = Cr, Al, Zr).[4] Raman spectroscopy was used to analyze the molecular structures of these spinels. $LiNi_{0.5}Mn_{1.5}O_4$ can be obtained in two different phases depending on the synthesis conditions. The Raman spectra from the two different phases of $LiNi_{0.5}Mn_{1.5}O_4$ are shown in Figure 1.[1] These Raman spectra were collected using a DXR Raman Microscope configured with a 532 nm laser. The peaks in the spectrum of the $P4_332$ material are sharper and stronger and the peak near 580–600 cm^{-1} (the T_{2g} peak of the spinel) is split into two compared to the single peak in the spectra of the Fd3m material.[4] The structures of the two phases have space groups corresponding to Fd3m (normal spinel) and $P4_332$ (ordered spinel). These phases show poor contrast in the XRD but were distinguishable using Raman spectroscopy.[1]

Figure 2 illustrates how different reaction conditions can lead to different phases.[4] Doping the material with aluminum (Al) or zirconium (Zr) favors the formation of the ordered spinel structure whereas doping with chromium (Cr) favors the normal spinel structure (see Figure 3).[4] Utilizing the differences in the Raman spectra, it is also possible to evaluate the spatial distribution of phases in a sample by mapping the sample. Figure 4 shows an example where there are only a couple of small particles of the $P4_332$ phase present in a larger field of the Fd3m material.[1] The mapping data was collected using a DXR Raman Microscope with a motorized stage and a 532 nm laser. Thermo Scientific™ Atlμs™ software allows for easy collection and analysis of Raman maps and is part of the Thermo Scientific™ OMNIC™ software used with the DXR3 Raman Microscope. The material with the ordered spinel structure ($P4_332$) displays lower electrical conductivity compared to the materials with the normal spinel structure (Fd3m), so it is important to have an easy way to distinguish between these phases.[4] This illustrates how the DXR3 Raman Microscope could be used for fast easy evaluation of molecular structure.

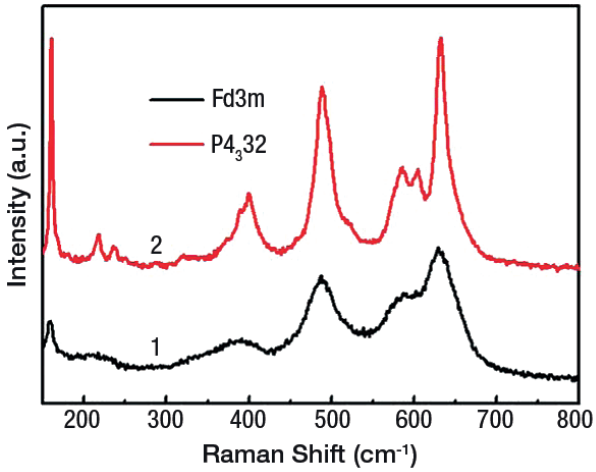

Figure 1. Raman spectra of the two phases of $LiNi_{0.5}Mn_{1.5}O_4$. Spectra were collected using a DXR Raman Microscope and a 532 nm laser. Adapted with permission from Zhang X, Cheng F, Zhang K et al. (2012) *RSC Advances* 2: 5669–5675.

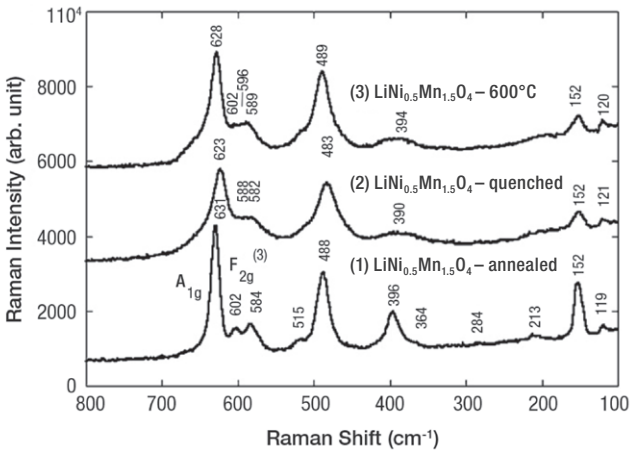

Figure 2. Raman spectra of $LiNi_{0.5}Mn_{1.5}O_4$ synthesized under various conditions. (1) Annealed at high temperature, (2) quenched, and (3) calcined at lower temperature. Spectra were collected using a Thermo Scientific™ Nicolet™ Almega™ XR dispersive Raman spectrometer equipped with a 633 nm laser. Adapted with permission from Oh SH, Chung KY, Jeon SH et al. (2009) *Alloys Compd* 409: 244–250.

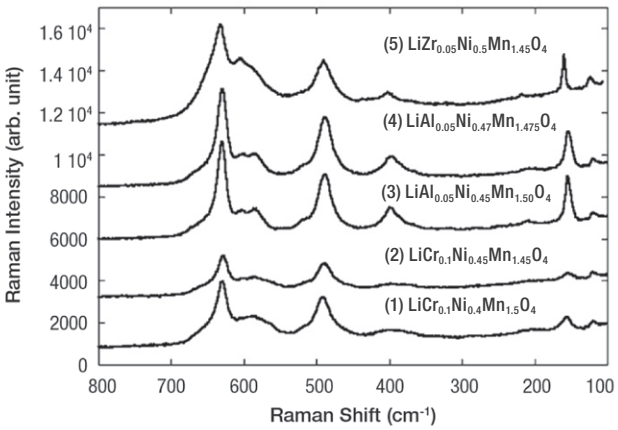

Figure 3. Raman spectra of Zr, Al, and Cr doped $LiNi_{0.5}Mn_{1.5}O_4$. (1) and (2) Cr doped (Fd3m structure); (3) and (4) Al doped ($P4_332$ structure); (5) Zr doped ($P4_332$ structure). Spectra were collected using a Nicolet Almega XR dispersive Raman spectrometer configured with a 633 nm laser. Adapted with permission from Oh SH, Chung KY, Jeon SH et al. (2009) *Alloys Compd* 409: 244–250.

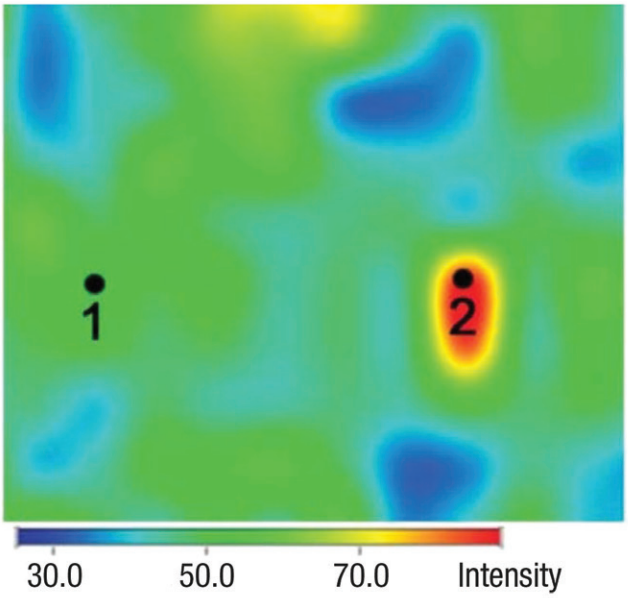

Figure 4. A Raman map showing the distribution of the two different spinel phases in a sample. The red-yellow locations (such as location 2) indicate areas of the $P4_332$ phase whereas the blue-green areas (such as location 1) represent areas of the Fd3m phase. Mapping data collected using a DXR Raman Microscope with a motorized stage and Atlμs software. Adapted with Permission from Zhang X, Cheng F, Zhang K et al. (2012) *RSC Advances* 2: 5669–5675.

An alternative approach to doping with other transition metals is to synthesize materials with different morphologies. The approach is typically to target nanoscale materials because the smaller particles and higher surface areas tend to improve the electrochemical properties of the materials. An example of this is the report that porous nanorods of $LiMn_2O_4$ gave enhanced cyclability and high-rate capacity compared to regular $LiMn_2O_4$ cathodes.[5] The enhanced capacity and cycling behavior was attributed to the morphology providing short ionic diffusion distances and a structure that could more readily accommodate the lattice expansion and contraction associated with repeated lithium-ion intercalation and deintercalation.
A DXR Raman Microscope was used to confirm the spinel structure (Fd3m) of the material and was also used to monitor the stability of the material after multiple charge/discharge cycles.[5]

Doping $LiCoO_2$ with other transition metals has been investigated as a way of improving cathode materials (e.g., cost, safety, performance, and environmental impact). An example of this is the class of materials with the following general formula, $Li[Mn_{1-x-y}Co_xNi_y]O_2$. Raman spectroscopy can also be used to monitor the structure of these types of materials as well. It has been reported in a paper that the Raman spectra of the material changed when the lithium content increased from $Li[Mn_{0.45}Co_{0.40}Ni_{0.15}]O_2$ to $Li_{1.15}[Mn_{0.45}Co_{0.40}Ni_{0.15}]O_2$.[6] Figure 5 shows the Raman spectra of these cathode materials.[6] Increasing the lithium content decreased the electrostatic repulsion between adjacent layers in the structure and resulted in an increase in the Raman intensity and a shift to higher wavenumbers. The change in the Raman spectrum with lithium content illustrates the utility of Raman spectroscopy for monitoring lithium content in these types of materials.

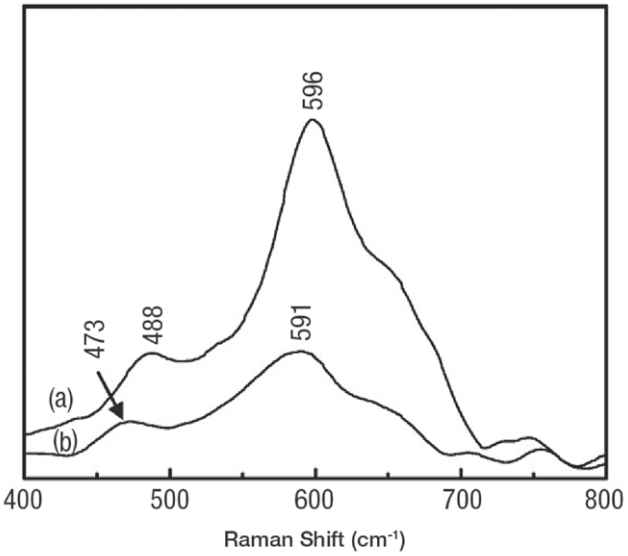

Figure 5. The Raman spectra of (a) $Li_{1.15}[Mn_{0.45}Co_{0.40}Ni_{0.15}]O_2$ and (b) $Li[Mn_{0.45}Co_{0.40}Ni_{0.15}]O_2$. Peak shift and intensity change with change in lithium content. Spectra collected using a Nicolet Almega XR dispersive Raman spectrometer configured with a 532 nm laser. Adapted with premission from Wang T, Liu Z-H, Fan L et al. (2008) *Powder Technol* 187: 124–129.

There are different ways to try improving the properties of cathode materials. In addition to doping and morphology changes an alternative approach is to coat the cathode with a more conductive material to form a hybrid material. This can change the solid electrolyte interface (SEI) and can improve the performance of the cathode. $Li(Li_{0.2}Mn_{0.54}Co_{0.13}\ Mn_{0.13})O_2$ is a member of a class of layered materials with the general form of $Li_2MnO_3 \bullet LiMO_2$ (M = Mn, Ni, Co). These materials have attracted attention because of high theoretical capacities up to 250 mAh/g.[7] Unfortunately, they have poor rate capacities and cycling behavior.

Constructing hybrid composite materials with graphene improves the cycling stability and gives enhanced high rate capacity. A DXR Raman Microscope fitted with a 532 nm laser was used to monitor the structure of the $Li(Li_{0.2}Mn_{0.54}Co_{0.13}Mn_{0.13})O_2$ material and provided evidence for the incorporation of graphene in the hybrid material. Peaks for both the inorganic oxide material and the graphene-derived coating were observed in the Raman spectra. Figure 6 shows the Raman spectra of the cathode material before and after the reaction with graphene.[7] The significant D band indicates substantial defects from the idealized graphene structure. There are many possible contributions to this defect peak including small domains sizes and vacancies in the graphene sheets. The existence of defects is not unexpected and in some applications can be advantageous. For instance, increased disorder in graphene anodes has been correlated with increased lithium-ion capacity.[8]

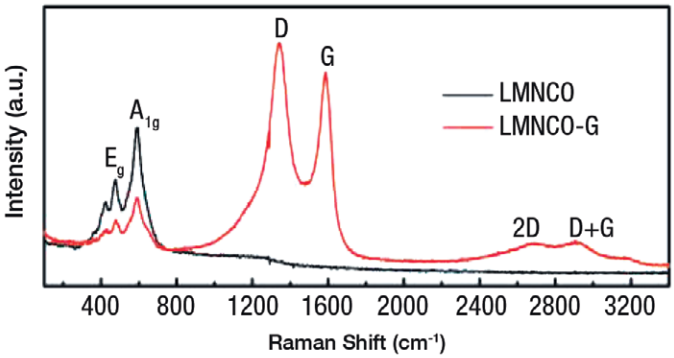

Figure 6. The Raman spectra of $Li(Li_{0.2}Mn_{0.54}Co_{0.13}Mn_{0.13})O_2$ (LMNCO) and the graphene enwrapped hybrid material (LMNCO-G). Spectra were collected using a DXR Raman Microscope and a 532 nm laser. Adapted with premission from Jiang K-C, Wu X-L, Yin Y-X et al. (2012) *ACS Appl Mater Interfaces* 4(9): 4858–4863.

These are just a few examples to illustrate how Raman spectroscopy can be used for the study of cathode materials. This was not meant as a comprehensive review of the literature. There are certainly other applications in the literature beyond those included here. The intent was to encourage and inspire the use of Raman spectroscopy for the analysis of battery components. Raman provides a fast and efficient way to identify materials and confirm molecular structure. It can be used on a wide variety of materials and can be used for both bulk analysis and the study of surfaces and interfaces. It has proven itself as an important analytical method for the analysis of battery components The DXR3 Raman Microscope is a high-performance Raman microscope in an easy-to-use package that puts Raman spectroscopy in the reach of any user.

References

1. Zhang X, Cheng F, Zhang K et al. (2012) *RSC Advances* 2: 5669–5675.
2. Raman Analysis of Lithium Ion Battery Components – Part II: Anodes, Thermo Scientific Application Note.
3. Raman Analysis of Lithium Ion Battery Components –Part III: Electrolytes, Thermo Scientific Application Note.
4. Oh SH, Chung KY, Jeon SH et al. (2009) *J Alloys Compd* 469: 244–250.
5. Cheng F, Wang J, Zhu Z et al. (2011) *Energy Environ Sci* 4: 3668–3675.
6. Wang T, Liu Z-H, Fan L et al. (2008) *Powder Technol,* 187: 124–129.
7. Jiang K-C, Wu X-L, Yin Y-X et al. (2012), *ACS Appl Mater Interfaces* 4(9): 4858–4863.
8. Lambert TN, Luhrs CC, Chavez CA et al. (2010) *Carbon* 48: 4081–4089.

Application note

Raman analysis of lithium-ion battery components Part II: Anodes

Authors

Robert Heintz, PhD, Thermo Fisher Scientific, Madison, WI, USA

Keywords

DXR3 Microscope, anodes, carbon, graphene, lithium-ion battery, Raman

From laptops and mobile phones to power tools and hybrid vehicles, the use of portable energy storage devices is growing rapidly.

As the number and types of applications expand, there is a constant demand for expanding battery functionality. Different applications impose their own requirements on the technology (potential, capacity, discharge rates, charging rates, life time, operating conditions, etc.). With widespread use, there also comes greater concern with factors such as safety and environmental impact.

The analysis of battery components is important not only for the development of new materials but also for the study of charge/discharge mechanisms and even for confirming the quality of materials used in battery production. The complex nature of batteries requires a multifaceted combination of electrochemical analyses and materials characterization techniques. Raman spectroscopy has emerged as an important analytical technique that can be used for the characterization of a variety of battery components. Even though a considerable amount of work has been done on the development and commercialization of lithium-ion batteries, there is still considerable interest in improving the current technology and the development of new battery components.

This application note will focus on examples of the analysis of anode materials for lithium-ion batteries. There are other application notes available that cover examples of the use of Raman spectroscopy for the analysis of cathode and electrolyte materials.[1,2] The examples presented here are not meant to be an exhaustive review of the literature but are intended to illustrate the utility of Raman spectroscopy for the analysis of battery components and, in particular, anodic materials.

Raman spectroscopy probes molecular structure and local chemical environments. It is very useful not only for characterizing new anode materials but also for studying subtle changes in materials. The changes in the Raman spectra can be correlated with changes in the electrochemical performance of the materials. The development of easy-to-use, but still high-quality, Raman instruments such as the Thermo Scientific™ DXR3 Raman Microscope means that Raman spectroscopy can be added as a routine analytical technique to any laboratory. The DXR3 Raman Microscope is a high-performance Raman spectrometer integrated with a research-quality light microscope to produce a powerful molecular spectroscopy instrument for spectroscopic investigations of samples on a microscopic scale. It also includes many automated features that save time and simplify data collection and analysis without sacrificing performance. Features like SMART backgrounds and auto exposure save you time when collecting spectra and assist with setting collection parameters. Automated alignment and calibration routines optimize instrument performance with a minimal amount of effort. These are just some of the time-saving features found on the DXR3 Raman Microscope that make it easy to use and allow anyone to collect high-quality Raman spectra.

One of the classical anode materials for lithium-ion batteries is graphite. The Raman spectrum obtained from a graphite anode using a DXR3 Raman Microscope with a 532 nm laser is shown in Figure 1. Recently, other allotropes of carbon besides graphite have been investigated for anode materials due to their novel physical and chemical properties. Raman spectroscopy is an excellent choice for the analysis of the different allotropes of carbon (see Figure 2).[3] Many of these carbon allotrope materials are strong Raman scatterers and have diagnostic spectral features. Raman spectra can be used not only to distinguish different allotropes of carbon but also to provide additional information on the molecular structure.[4] For example, Raman spectral data can be used to determine the number of sheets of graphene in a stack, provide information on defects and disorder in the structure of graphene, and determine diameters of single-wall carbon nanotubes.[4,5]

Raman spectroscopy can also be used to monitor changes in anode materials during use. In one published example, a DXR Raman Microscope was used to study the insertion of lithium into a hard carbon anode.[6] The G band (graphite type structure) of the anode material displayed a slight shift to lower wavenumbers as the lithium insertion increased with the state of charge (SOC) of the battery. This shift has been attributed to a weakening of carbon bonds in the graphite type structures due to negative charge transfer. This is an example of how Raman spectroscopy can be used to monitor the changes in the anode material with different states of the battery.

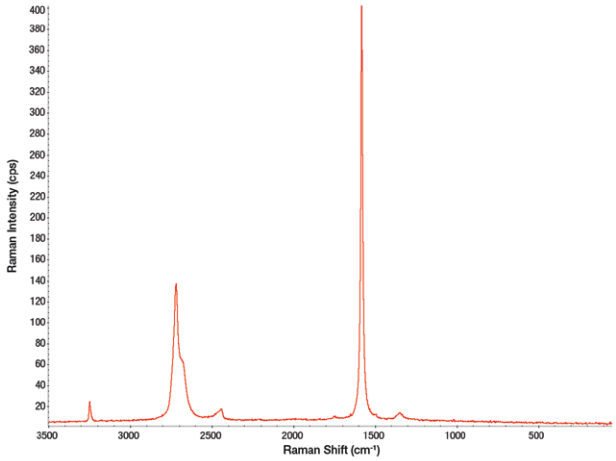

Figure 1. Raman spectrum of a graphite anode collected using a DXR3 Raman Microscope equipped with a 532 nm laser.

An active area of research is the use of carbon coatings to improve the electrochemical properties of other potential anodic materials. These carbon coatings are used to improve properties like low conductivity and cycling stability. Graphene composites have shown improved electrochemical properties. High-surface-area graphene improves lithium-ion intercalation. Also, the presence of graphene at the interfaces decreases the mechanical deterioration of anodes caused by large volume changes during cycling. One of the interesting aspects of this is that when many other applications are trending toward the fabrication of defect-free graphene, the presence of defects appears to be advantageous for anode materials. The presence of defects due to edges and vacancies in the graphene actually improves the capacity and cycling stability because it provides additional reversible storage sites for lithium ions.[7] This means that the evaluation of defects in the graphene structures is important because it is directly related to the electrochemical properties. Raman spectroscopy can provide relative defect concentrations, and this is typically expressed as the ratio of the defect peak (D band) to the graphite peak (G band) (I_D/I_G).

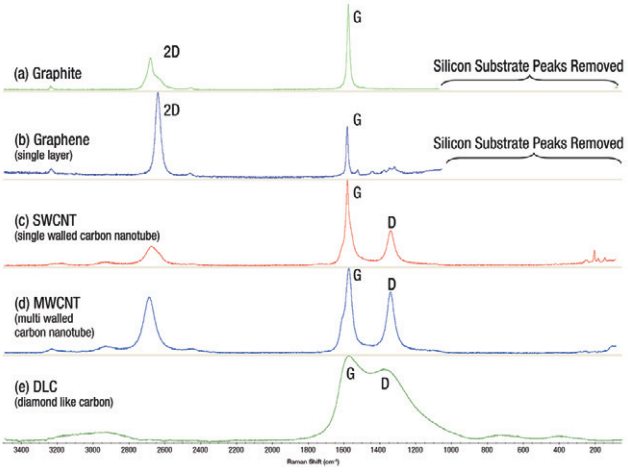

Figure 2. Raman spectra of different forms of carbon: (a) graphite, (b) single layer of graphene, (c) single-walled carbon nanotube (SWCNT), (d) multi-walled carbon nanotube (MWCNT), (d) diamond-like carbon (DLC). These spectra were obtained using a DXR Raman Microscope and a 532 nm laser.

Silicon has been studied extensively as a promising candidate as an anode material for lithium-ion batteries because of its high theoretical capacity (4,200 mAh/g).[8] However, silicon electrodes undergo a large volume expansion/contraction during cell cycling, and this volume change results in mechanical degradation of the anode and a dramatic fading of capacity. The high potential capacity of the silicon anode has lead researchers to try to modify the surface of the silicon anode and thus the solid electrolyte interface (SEI) to improve the cycling behavior. One approach that has been reported is to coat the silicon anode surface with carbon using a fullerene (C60) precursor.[9] Analysis of these thin films using a Thermo Scientific Nicolet™ Almega™ Dispersive Raman Spectrometer configured with a 633 nm laser indicated that the carbon was no longer in the fullerene form but displayed D and G bands typical of other types of carbon coatings. The G band comes from idealized graphite-type carbon structures, and the D band represents defects edges, vacancies, etc., from the graphite structure and can be either sp^2 or sp^3 hybridized carbon. The I_D/I_G ratio varied with the plasma power used to create the coating and with boron doping of the fullerene.[10,11] Boron doping lowered the I_D/I_G ratio with respect to the undoped materials with similar deposition conditions. A similar approach was also carried out using diamond-like carbon (DLC) films.[12] In the case of the DLC films, the D and G bands overlapped significantly, but they were deconvoluted into the two components. Peak-fitting software like Peak Resolve in Thermo Scientific OMNIC™ Software can be used to evaluate the relative contributions from these two types of carbon. Coating the silicon anodes with these carbon films provided more stable cycle performance along with high reversible capacity.

Tin dioxide (SnO_2) and tin disulfide (SnS_2) are both potentially useful anodic materials for lithium-ion batteries. These materials are interesting because they have high theoretical capacities, but, like silicon, they display a very large volume change during cycling and thus suffer from mechanical degradation. To address this issue, nanoscale hybrids of these materials have been investigated. In one report, nanorods of SnO_2 were combined with graphene, and, in another, SnS_2 nanosheets were combined with multi-walled carbon nanotubes.[13,14] In both of these cases, the hybrid materials displayed improved high-rate capacities and enhanced cycling behavior.

The Raman spectrum of the SnO_2/graphene composite material collected using a DXR Raman Microscope and a 532 nm laser showed both D and G bands typically associate with carbon, but the G band was slightly blue-shifted compared with the graphene sheet and graphene oxide peaks. This was taken as evidence of electronic interactions between the SnO_2 nanorods and the graphite-type structures of the graphene sheets (see Figure 3).[13]

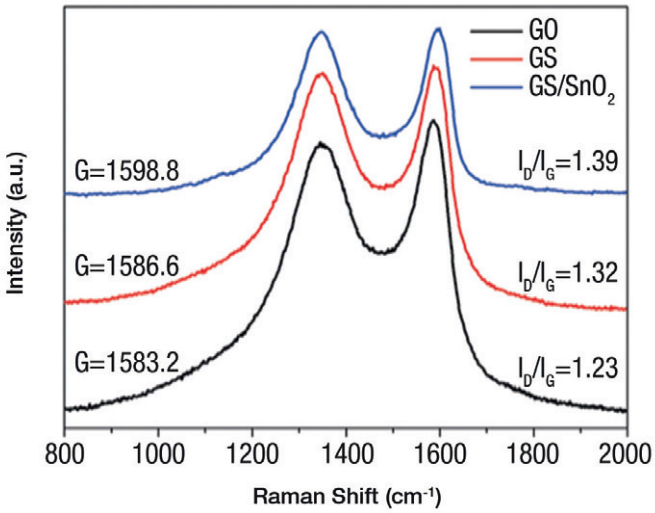

Figure 3. Hybrid anode material SnO_2 and graphene sheet (GS). Comparison of the peak location of the G band between graphene sheet (GS), graphene oxide (GO), and the hybrid anode material (GS/SnO_2). Raman spectra collected using a DXR Raman Microscope with a 532 nm laser. Adapted with permission from Chaohe Xu, Jing Sun, Lian Gao, *J. Mater. Chem.* 22, 2012, 975-979. Copyright 2012 RSC Publishing.

The composite material, as well as the starting graphene sheet, showed significant D bands, indicating substantial disorder from the idealized graphene structure. This is probably not unexpected considering that the materials were prepared hydrothermally, and there are many factors that could contribute to the defect concentration (small domains, vacancies, functionality, etc.).

The Raman spectra of the SnS_2/multi-walled carbon nanotube composite anode material displayed peaks associated with nanosheets of SnS_2 (131 (w) 212 (w), 309 peak (s), 450–650 (b) cm^{-1}) as well as peaks associated with the carbon nanotubes (D and G bands) (see Figure 4).[14] No peaks associated with SnS were observed despite the fact that SnS powder was used as the precursor. The SnS_2 nanosheet/MWCNT composites exhibited significantly better discharge capacities and cyclability compared to the SnS_2 nanosheets alone.

Lithium transition metal oxides can be used as anodes for lithium batteries as well as cathodes. $Li_4Ti_5O_{12}$ has the spinel structure and has been used as an anode material for lithium-ion batteries. It does not have, the high theoretical capacity (175 mAh/g) that materials like silicon have but it is a zero-strain insertion material, which means it shows only a very small change in volume during charge/discharge cycles.[15] It has excellent cycle characteristics; however, it has a poor rate capacity and low conductivity. Similar approaches (morphology, doping, and coating) have been reported to improve the conductivity of $Li_4Ti_5O_{12}$. One example of this was detailed in a paper on how the conductivity of $Li_4Ti_5O_{12}$ was improved by generating a carbon composite material. Raman spectroscopy was used to confirm that the structure of the $Li_4Ti_5O_{12}$ was retained in the hybrid material and that carbon had been incorporated in the material (see Figure 5).[16]

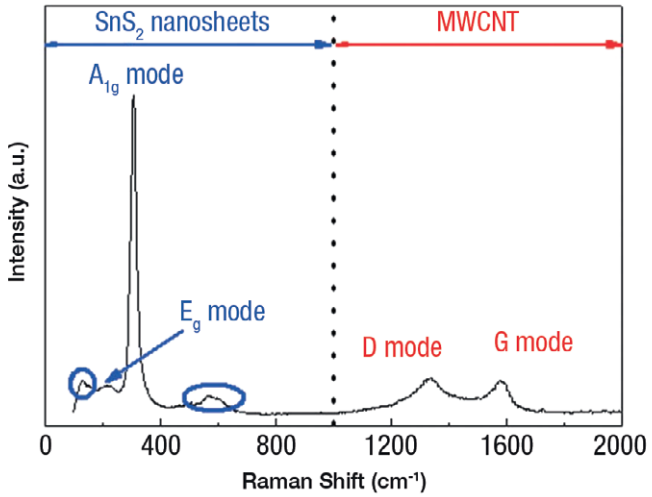

Figure 4. Raman spectrum of the SnS_2/MWCNT composite material. Peaks associated with both the SnS_2 nanosheets and the multi-walled carbon nanotubes are observed. Raman spectra collected using a Nicolet Almega Dispersive Raman Spectrometer. Adapted with permission from Jin-Gu Kang, Gwang-Hee Lee, Kyung-Soo Park, Sang-OK Kim, Sungjun Lee, Dong-Wan Kim, Jae-Gwan Park, *J. Mater. Chem.* 22, 2012, 9330-9337. Copyright 2012 RSC Publishing.

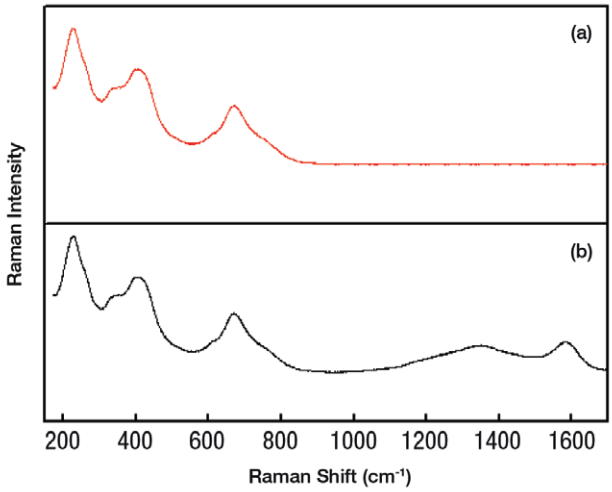

Figure 5. (a) Raman spectrum of $Li_4Ti_5O_{12}$ and (b) Raman spectrum of carbon-coated $Li_4Ti_5O_{12}$. Raman spectra were obtained using a Nicolet Almega XR Dispersive Raman Spectrometer configured with a 633 nm laser. Adapted with permission from Ju Bin Kim, Dong Jin Kim, Kyung Yoon Chung, Dongjin Byun, Byung Won Cho, *Phys. Scr.* T139, 2010. Copyright 2010 IOP Publishing.

The Raman spectra obtained using a Nicolet Almega XR Dispersive Raman Spectrometer with a 633 nm laser also showed the D and G bands typically associated with graphitic-type carbon, and disordered carbon structures were present.

These are a few examples illustrating how Raman spectroscopy can be used to analyze anode materials for lithium-ion batteries. Many anode materials involve some form of carbon, and Raman spectroscopy has proven itself very useful for the analysis of carbon-based materials. Not only can Raman spectroscopy be used to differentiate one form of carbon from another, but it also can provide detailed structural information. However, the utility of Raman spectroscopy does not stop with carbon-based materials; it can also be used to probe the structure of other materials. Transition metal oxides and tin disulfide examples were included in this application note. The versatility of use with many different types of materials and the extraordinary structural information that it can provide make Raman spectroscopy an ideal choice for the analysis of battery components. The DXR3 Raman Microscope allows for spectroscopic analysis on a microscopic scale. Advances in Raman instruments, such as the DXR3 Raman Microscope, make them easy-to-use while still providing high-quality Raman data. Easy access to high-quality Raman data is one reason for the growing number of Raman applications.

References

1. Raman Analysis of Lithium Ion battery Components –Part I: Cathodes, Thermo Scientific Application Note: 52443.
2. Raman Analysis of Lithium Ion battery Components –Part III: Electrolytes, Thermo Scientific Application Note: 52445.
3. Joe Hodkiewicz, Characterizing Carbon Materials with Raman Spectroscopy, Thermo Scientific Application Note: 51901, 2010.
4. Joe Hodkiewicz, Characterizing Graphene with Raman Spectroscopy, Thermo Scientific Application Note: 51946, 2010.
5. Joe Hodkiewicz, Technical Reference Chart for Common Calculations Involving Raman measurements with Carbon Nanomaterials, Thermo Scientific Technical Note: 51964, 2010.
6. H. Hori, M. Shikano, S. Koike, H. Sakaebe, Y. Saito, K. Tatsumi, E. Ikenaga, Abstract #117, The 15th International Meeting on Lithium Batteries, IMLB 2010, The Electrochemical Society.
7. Timothy N. Lambert, Claudia C. Luhrs, Carlos A. Chavez, Stephen Wakeland, Michael T. Brumbach, Todd M. Alam, *Carbon,* 48, 2010, 4081-4089.
8. Arenst Andreas Arie, Joong Kee Lee, *Phys. Scr.* T139, 2010.
9. Arenst Andreas Arie, Wonyoung Chang, Joong Kee Lee, *J. Solid State Electrochem.* 14, 2010, 51-56.
10. 10. Arenst Andreas Arie, Joong Kee Lee, *J. Ceramic Processing Research,* 10 (5), 2009, 614-617.
11. Arenst Andreas Arie, Joong Kee Lee, *Synthetic Metals,* 161, 2011, 158-165.
12. Sang-Ok Kim, Heung-Taek Shim, Joong Kee Lee, *J. Solid State Electrochem.* 14, 2010, 1247-1253.
13. Chaohe Xu, Jing Sun, Lian Gao, *J. Mater.* Chem. 22, 2012, 975-979.
14. Jin-Gu Kang, Gwang-Hee Lee, Kyung-Soo Park, Sang- Ok Kim, Sungjun Lee, Dong-Wan Kim, Jae-Gwan Park, *J. Mater. Chem.* 22, 2012, 9330-9337.
15. 15. Ju Bin Kim, Dong Jin Kim, Kyung Yoon Chung, Dongjin Byun, Byung Won Cho, *Phys. Scr.* T139, 2010.

Application note

Raman analysis of lithium-ion battery components Part III: Electrolytes

Authors

Robert Heintz, PhD, Thermo Fisher Scientific, Madison, WI, USA

Keywords

DXR3 Microscope, electrolytes, lithium-ion battery, Raman Spectroscopy, Solid Polymer Electrolytes (SPE)

Today's society is very mobile and this mobility comes with an increasing need for portable energy sources.

The demand for better battery technology continues to grow. Some applications use very small batteries and others, such as hybrid vehicles, use much larger batteries. The individual requirements (potential, capacity, discharge rate, etc.) vary with the intended use. Battery performance along with cost continue to be very important aspects of any new battery technology, but factors such as safety and environmental impact are becoming increasingly important.

Electrolytes are responsible for the transport of charges in batteries. If this transport is hindered then the performance of the battery is adversely affected. Electrolytes need to be able to transport the charge efficiently, but they also need to be stable under charging and discharging conditions. Side reactions of electrolytes within the battery not only reduce battery performance but shorten battery life. Improving electrolyte functionality involves not only understanding the electrolytes themselves and how they function, but also how they interact with other battery components.

Lithium-ion batteries are a particularly popular battery technology that offers some of the highest energy densities and output voltages among commercial rechargeable battery systems.[1] Various lithium salts have been investigated as electrolytes. A common example of an electrolyte used in lithium-ion batteries is lithium hexafluorophosphate ($LiPF_6$). The main issue with $LiPF_6$ is that it must be kept scrupulously dry to avoid hydrolysis to generate corrosive hydrogen fluoride (HF).[2] Other electrolytes such as lithium hexafluoroarsenate ($LiAsF_6$) are toxic.[2] Some lithium salts have low ionic conductivity (e.g., $LiSO_3CF_3$) and some form higher resistivity barriers at the electrode surfaces (e.g., $LiBF_4$).[2] None of the electrolyte choices is perfect, so the development of new electrolytes is an opportunity for improving the performance, cost, environmental impact, and safety of lithium-ion batteries.

Batteries are complex devices with a variety of different components. Because of this, the analysis of batteries requires a wide variety of analytical tools. The evaluation of battery components usually involves both electrochemical analysis and materials characterization methods. The various analytical techniques are often used together to provide a complementary and comprehensive understanding of the battery components and mechanisms. Raman spectroscopy has already been established as one of the most useful and versatile analytical techniques for the analysis of a variety of different types of materials. Previous application notes provided examples of how Raman spectroscopy can be used for the analysis of cathode and anode materials.[3,4] That coverage is expanded here to include examples of the analysis of electrolytes. These examples are not meant to be an exhaustive review of the literature, but are intended to illustrate some of the ways that Raman spectroscopy can be used and the type of information it can provide.

Commercially available Raman spectrometers have evolved into routine laboratory instruments. The Thermo Scientific™ DXR3 Raman Microscope is an example of this new class of Raman instruments that are easy to operate but provide high performance results. The DXR3 Raman Microscope is a fully integrated, high performance, research grade instrument that incorporates extensive automation that simplifies the collection of Raman data. For example, automated on-demand alignment and calibration present on the DXR3 Raman Microscope eliminates time-consuming manual realignment and calibration, providing an easy way to optimize instrument performance with a minimal amount of effort. This ease of use means it is much quicker to get started and provides confidence that you will get high performance and accurate results. This opens up the use of Raman spectroscopy for all types of users.

Raman spectroscopy probes molecular structure and local chemical environments. It is useful not only for the characterization of new electrolyte materials but it can also be used for studying more subtle changes in materials.

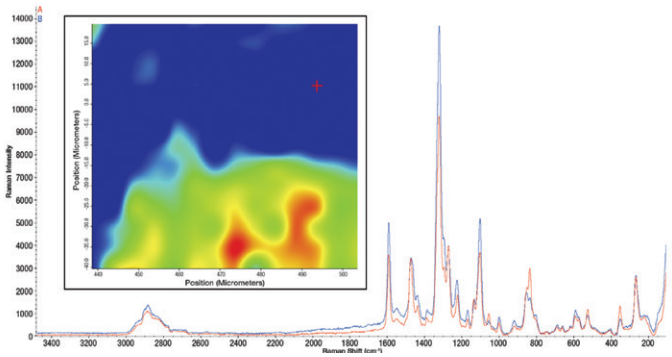

Figure 1. Spatial distribution of Cx2 in a PEO Membrane. Raman image based on the ratio of the 1600 cm-1 peak of Cx2 to the 840 cm^{-1} peak of PEO. Red indicates a higher concentration and blue represents a lower concentration of Cx2. The spectrum in blue comes from point B and the spectrum in red comes from point A. Mapping data was collected using a Nicolet Almega dispersive Raman spectrometer configured with a motorized stage and using a 780 nm laser. This figure was generated from data sent by the author.

For example, Raman spectroscopy can be used to study the degree of association of electrolyte ions in solutions and in polymer materials. The association of ions has a direct effect on the ion mobility and ion conductivity and thus affects battery performance.

Solid polymer electrolytes (SPE) offer some distinct advantages over electrolytes dissolved in organic solvents. In these composite materials the polymer matrix assumes the role of the solvent and lithium salts dispersed in the polymer are the electrolytes. With typical organic solvents there is a greater risk of leakage and organic-based solvents can be volatile and flammable. The combination of flammable solvents and highly reactive and energetic battery components represents a potentially dangerous combination if something were to happen to the battery. Overcharging or overheating of batteries can have a disastrous effect especially with volatile solvents. The use of solid polymer electrolytes reduces the risk of leakage and thus mitigates some what the danger of toxic, corrosive, or flammable electrolytes and solvents.[5]

The drawback of these solid polymer electrolytic systems is that they often display low ionic conductivity and poor transport of lithium-ions.[6] Poly ethylene oxide (PEO) is an example of a polymer that is used in solid polymer electrolytes. The low ionic conductivity of these polymer electrolytes is attributed to a crystalline phase in the polymer matrix. The low percentage of charge transfer by lithium-ions is hindered because of high anion mobility. A considerable amount of research has focused on circumventing these issues.[6]

One approach to solving the issue of low ionic conductivity has been the use of additives to suppress the crystallinity of the polymer matrix and to improve the mechanical and electrochemical properties of the resulting composite polymer electrolytes. There are reports in the literature where ceramic materials, such as alumina and titania, have been used as fillers. For example, a Thermo Scientific Nicolet™ Almega™ dispersive Raman spectrometer was used to verify the phases of these materials as well as the surface modifications of the fillers (e.g., sulfate – SO_4^{2-}).[7]

Interesting work has been done studying additives designed to partially immobilize the anions in the polymer composite electrolytes and thus improve cation charge transfer. Raman spectroscopy was not only used to characterize the additives and the electrolytes in the polymer membranes but was also used to study the distribution of the components in the membranes. Raman mapping of the polymeric materials using a Nicolet Almega dispersive Raman spectrometer with a motorized stage and a 780 nm laser, provided images based on the Raman spectra that showed the spatial distribution of the additives and electrolytes in the polymer membranes.6,8 Figure 1 shows the spatial distribution of the supramolecular additive, 5,11,17,23-tetra-p-tert-butyl-25,27-bis(((N-pnitrophenylureido) butyl) oxy)-26,28-dipropoxycalix[4]arene (Cx2), in a poly(ethylene oxide) matrix. The image is based on the ratio of a peak from the supramolecular additive (1598 cm^{-1}) to a peak associated with the PEO (840 cm^{-1}).[9]

The Thermo Scientific™ Atlμs option in the Thermo Scientific OMNIC™ software facilitated the collection and analysis of mapping data. The red color indicates a higher concentration of additive and the blue indicates a lower concentration. Representative spectra from each of the areas are displayed as well. The spectra are very similar but there are some differences.

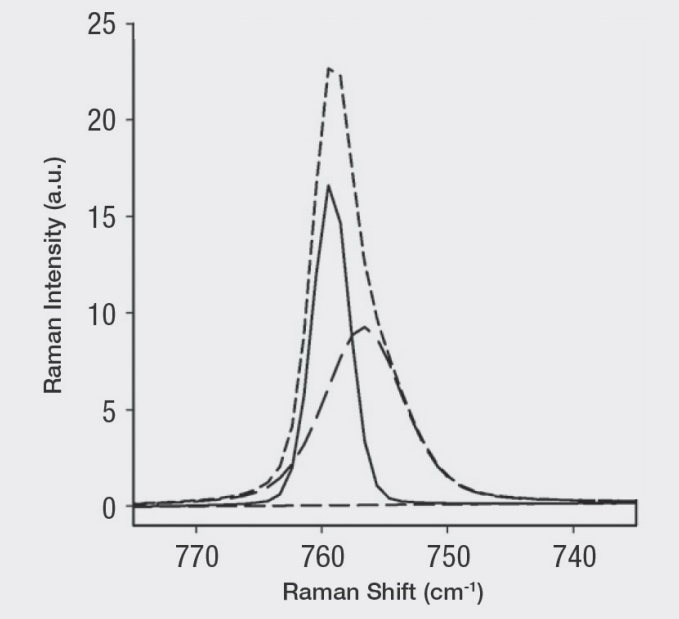

Figure 2. Deconvolution of the δsCF3 band in Raman spectrum of amorphous domains of a PEO-$LiCF_3SO_3$ membrane. The peak at 756 cm^{-1} is attributed to free ions (42%) and the peak at 759 cm^{-1} is attributed to ionic pairs (58%). Adapted with permission from Pawloska M, Zukowska GZ, Kalita M et al. (2007) *J Power Sources* 173: 755–764. Copyright 2007 Elsevier Publishing.

Raman spectroscopy can also be used to determine the degree of association of electrolyte ions in solution. This is a very interesting application that is based on the fact that the degree of association of the anions (free ion, ion pairs, and triplets) has a subtle effect on the shift of the anion peaks in the Raman spectra. This is a result of slight difference in the chemical environment due to interaction with other ions.

This type of analysis was reported as part of a paper on the development of potential electrolytes for lithium-ion batteries based on lithium salts of imidazole derived materials (e.g., lithium 4,5-dicyano-2-(pentafluoroethyl)imidazole).[10,11] The peaks associated with CN stretching in the Raman spectra were used to evaluate the relative percentages of the various ionic associations. This was achieved by careful deconvolution and peak fitting of the composite peak. This method can be used either independently or as a compliment to methods such as the Fuoss-Kraus procedure.[10] The ionic associations are of interest because the ionic conductivity is affected by the degree of association of the ions. Electrolytes with weaker associations (higher percentage of free ions) will generally display greater conductivity.

The same type of analysis can be used with other electrolytes as well. The percentages of free ions and ion pairs for lithium triflate ($LiCF_3SO_3$) in a PEO-$LiCF_3SO_3$ solid polymer electrolyte have also been determined by deconvolution and peak fitting of the CF_3 peak in the Raman spectrum of the composite material.[8] Figure 2 shows the deconvolution of the CF_3 band of the Raman spectra into bands for the free ions and ion pairs of lithium triflate in PEO-$LiCF_3SO_3$.[8] The Peak Resolve option in the OMNIC software can be used for this type of analysis.

References

1. Zhang X, Cheng F, Zhang K et al. (2012) *RSC Advances* 2: 5669–5675.
2. Niedzicki L, Kasprzyk M, Kuziak K et al. (2011) *J Power Sources* 196: 1368–1391.
3. Raman Analysis of Lithium Ion Battery Components – Part I: Cathodes, Thermo Scientific Application Note.
4. Raman Analysis of Lithium Ion Battery Components – Part II: Anodes, Thermo Scientific Application Note.
5. Syzdek JS, Armand MB, Falkowski P et al. (2011) *Chem Mater* 23: 1785–1797.
6. *Helselman, Kalita M, Plewa-Marzewska A et al. (2010) Electrochim Acta* 55: 1298–1307.
7. Sydzek J, Armand M, Marcinek M et al. (2010) *Electrochim Acta* 55: 1314–1322.
8. Pawlowska M, Zukowska GZ, Kalita M et al. (2007) *J Power Sources* 173: 755–764.
9. The Raman mapping data was supplied by Dr. Grazyna Zukowska, Warsaw University of Technology, Faculty of Chemistry.
10. Niedzicki L, Kasprzyk M, Kuziak K et al. (2009) *J Power Sources* 192: 612–617.
11. Niedzicki L, Zukowska GZ, Bukowska M et al. (2010) *Electrochim Acta* 55: 1450–1454.

TECHNICAL NOTE No. FL53370

Gas-phase FTIR for smoke toxicity measurements

Relevant Standards: EN 45545-2, EN 17084, EN 5659-2, ISO 19702

The field of Fire Science determines safety standards and sets design criteria for materials in the event of fire. Fire Science researchers analyze materials for their mechanical and chemical properties under tightly defined conditions, using dedicated Smoke Chambers or Cone Calorimeters to control the combustion parameters.

One aspect of Fire Science is Smoke Toxicity, where materials are burned to determine how dangerous their gaseous emissions are. Traditionally carbon monoxide (CO) emissions were used as the key marker of smoke toxicity, but additional gases are now also monitored for their toxicity. FTIR spectroscopy provides an ideal on-line technique to analyze gases of interest in combustion research.

New **European railway/transportation regulations now require testing by FTIR** for a variety of toxic/caustic gases, particularly dangerous acids such as HCl, HBr, HCN, and HF (See Table 1 – components list, and Figure 1 – Thermo Scientific™ OMNIC™ spectra). Thermo Fisher Scientific offers a total FTIR solution to meet the EN 45545-2 Smoke Toxicity certification requirements.

Smoke Toxicity Gases	
Compound	**Symbol**
Carbon Dioxide	CO_2
Carbon Monoxide	CO
Hydrogen Fluoride	HF
Hydrogen Chloride	HCl
Hydrogen Bromide	HBr
Hydrogen Cyanid	HCN
Sulfur Dioxide	SO_2
Nitrogen Oxide	NO
Nitrogen Dioxide	NO_2
Hydrocarbons	$C^1 – C^4$
Formaldehyde	CH_2O
Acrolein	C_3H_4O

Table 1 – Smoke toxicity gases

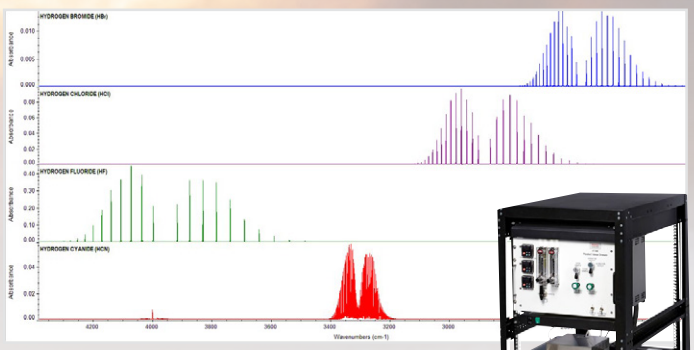

Figure 1: OMNIC spectra

Figure 2: IGS with HVD/rack

The Thermo Scientific™ Antaris™ IGS system, configured with a rack-mounted Heated Valve Drawer (HVD), provides a turnkey data acquisition and analysis package (Figure 2). Key features include:

- High sensitivity sampling of many compounds in a single measurement
- Certified Fire Science analysis method, validated to primary calibration standards
- Direct on-line sampling for real-time analysis on a second by second basis
- Ability to re-analyze stored data and/or add additional components for customized tests

The Antaris IGS/HVD system controls a constant flow of the gas sample from the smoke chamber through the FTIR gas cell. A probe is inserted into the sample “chimney,” where the smoke samples are pulled through a heated soot filter and sample transfer line using a diaphragm pump. The gas is maintained at constant temperature and pressure through the heated gas cell to eliminate sampling error and is sampled on a second-by-second basis by the FTIR.

ThermoFisher SCIENTIFIC

thermo scientific

Another key application for FTIR Fire Science measurements is the analysis of lithium ion batteries (LiB) to monitor off-gassing or chemicals released during a fire, electrical short circuit, or other hazardous conditions. These batteries generally use a lithium-fluoride salt (LiPF6 or similar) as the electrolyte to carry charge between the electrodes. These electrolytes support very high electrical charge density but can release toxic HF and other fluorinated compounds under overtaxed conditions, such as mechanical puncture in an automobile crash.

Figure 3 shows FTIR analysis of HF gas released from burning batteries under different charge states, as compared to the heat release rate (HRR) measurement. FTIR enables LiB researchers to understand key parameters in HF generation, which enables development of safer battery technologies.

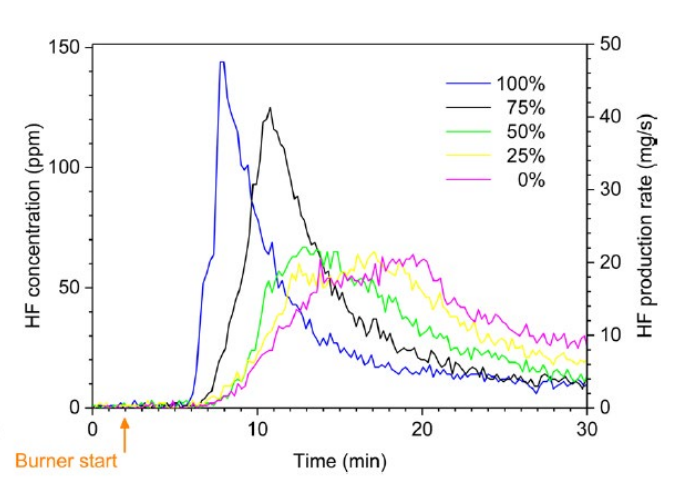

Figure 3: HF gas release from Lithium Ion Battery combustion under different charge conditions. Reference: Larsson, F., Andersson, P., **Blomqvist, P. *et al*. Toxic fluoride gas emissions from lithium-ion battery fires. *Sci Rep* 7, 10018 (2017). https://doi.org/10.1038/s41598-017-09784-z**

Summary

The Antaris IGS/HVD system is uniquely suited for analysis of toxic emissions from combustion of many materials. This system is used to meet new European regulations which specify FTIR analysis to certify material properties before they can be released onto the market. The example of HF measurement from burning lithium ion batteries shows the utility of FTIR for Fire Science safety testing.

Find out more at **thermofisher.com/igs**

ThermoFisher SCIENTIFIC

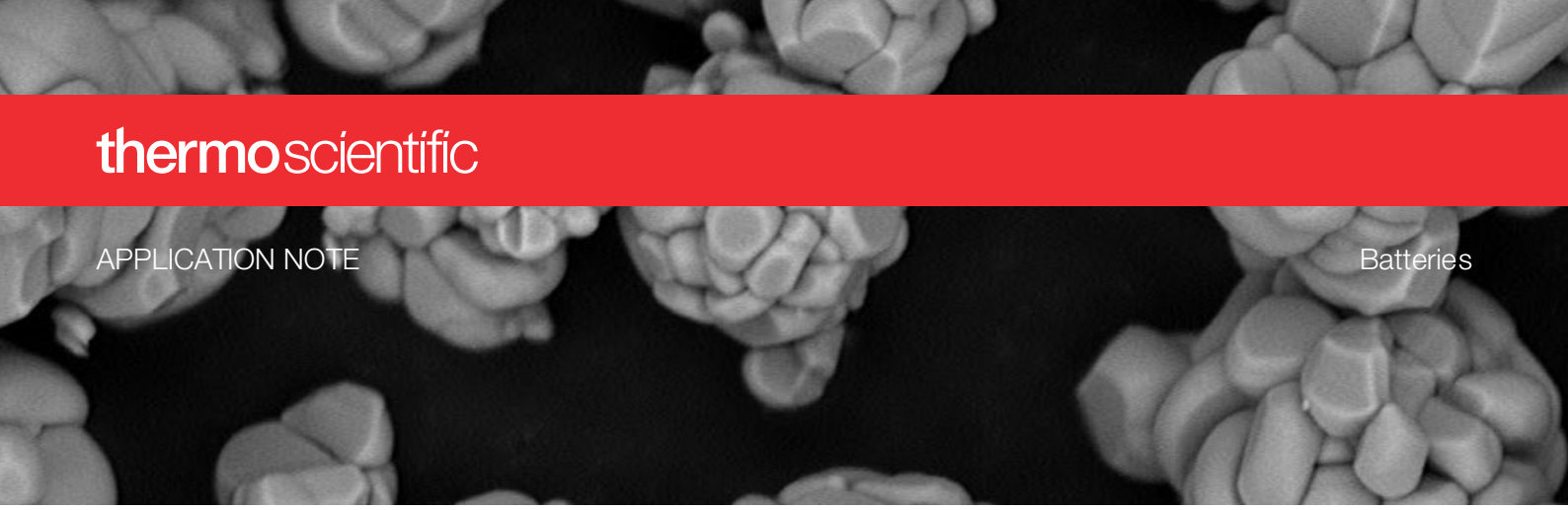

thermoscientific

APPLICATION NOTE

Batteries

Investigate batteries with a SEM for better performance

Insights on what can be revealed on batteries structure and composition with a scanning electron microscope

The secret to improving the specifications of new generation batteries is miniaturization. SEM is an unrivaled technique for inspecting and analyzing nanoscale materials, improving production processes or detecting the reasons for failure. Get some insights into how Phenom SEMs can be used to boost the performance of your products.

The battery production cycle is a long process that involves several stages. Intermediate checks are necessary to verify the quality of the production system, starting from the inspection of raw materials, to the production of intermediate components, as well as checks on the final product, requiring the system used for the investigations to be highly versatile.

The insulating materials in batteries are, by definition, non-conductive. When imaging with a SEM, this causes an accumulation of electrons on the surface of such samples, compromising the quality of the final picture and often hiding important details. In order to flawlessly image structures of interest, different solutions are available. Reducing the vacuum level in the imaging chamber can help to discharge the sample, immediately improving image quality. The value of the current that is applied can also be altered to reduce the interactions and, when dealing with very delicate samples, prevent surface damage. If both of the previously-mentioned techniques fail, a thin layer of gold can be applied on the surface, making it conductive and ready for high resolution imaging.

The advantages of electron microscopy:

- Access to nanoscale magnification;
- Integrated, non-destructive EDS analysis to measure chemical composition of the sample locally;
- Automated routines to gather data on pores, particles and fibers - quickly and without wasting the operator's time;
- 3D reconstruction of the surface to measure morphology.

With an electron microscope, you can observe:

- Size and granulometry of powders used as raw materials;
- Size and orientation of pores and fibers in insulating membranes;
- Three-dimensional structure of electrodes after production processes;
- Response of materials to electrical or thermal solicitations;
- Presence of contaminants in the battery sublayers

ThermoFisher SCIENTIFIC

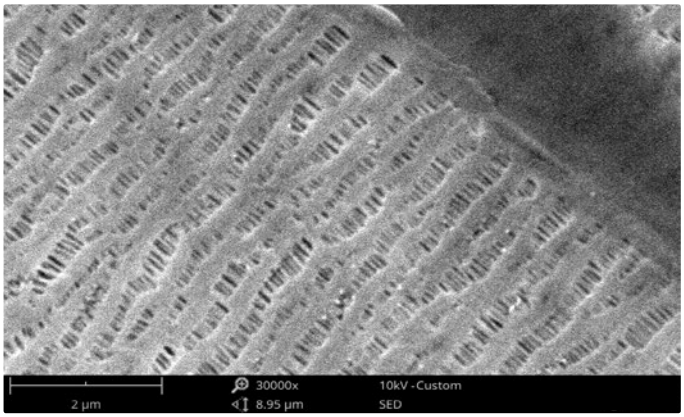

Image 1a

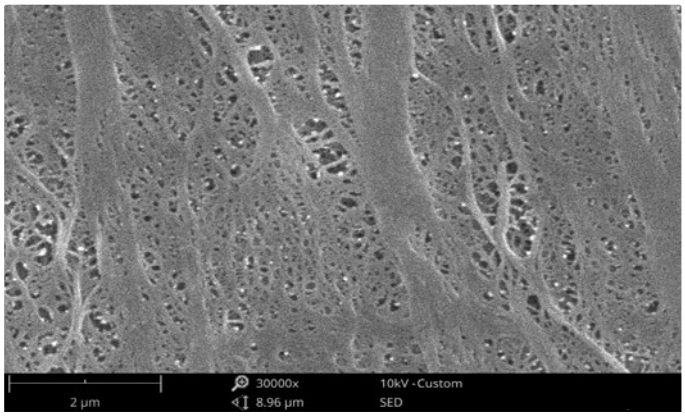

Image 1b

Image 1a and 1b: SEM images of battery insulating membranes. Highly non-conductive samples require special treatment for imaging. Operating at a different vacuum level can reduce charging effects. Coating the sample with a thin gold layer will dramatically reduce the issue.

Raw materials, such as powders, can be easily imaged at very high magnification. Particles can then be measured, to evaluate the granulometry and shape distribution within the sample. With more advanced software analysis, these measurements can be automated, providing more accurate results and saving operators a great deal of time.

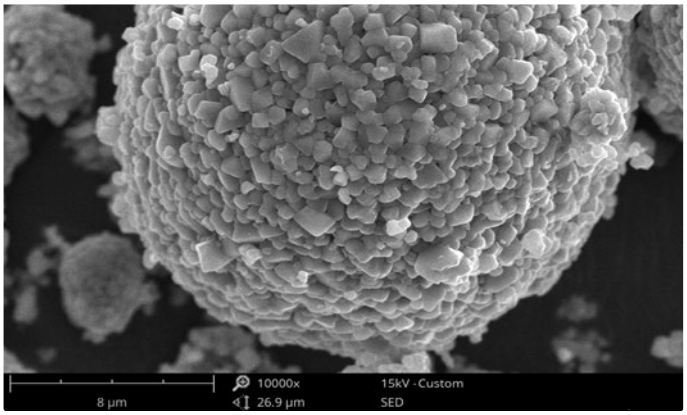

Image 2a

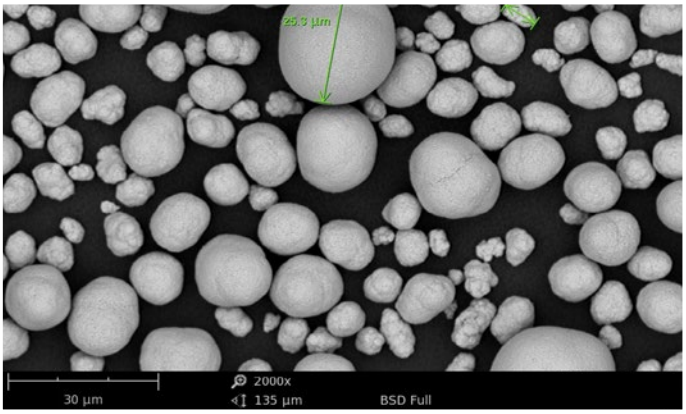

Image 2b

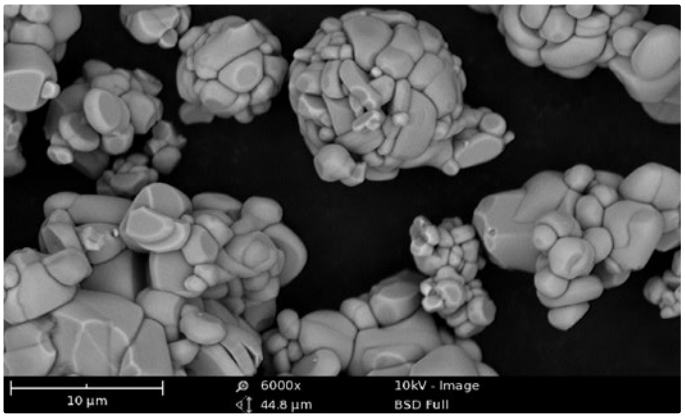

Image 2c

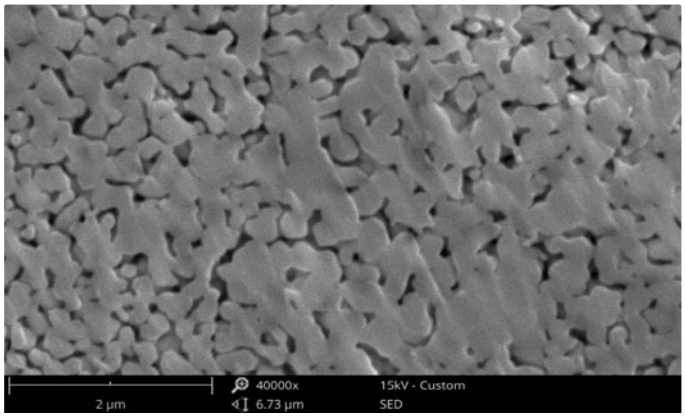

Image 2d Ion milled surface of a battery electrode. The data can be used to investigate the internal structure of the material.

Image 2a, 2b and 2c: Raw powders used in the production of cathodes. SEMs are ideal tools for investigating small particles in the range of micrometers or nanometers.

The shape and orientation of the electrodes' nanostructure is crucial to ensure that batteries have a long lasting and high efficiency. In particular, the secondary electrons detector (SED) can be used to inspect the morphology and surface topography of the sample.

thermo scientific

With a backscattered electron detector (BSD), the image will show a different contrast for areas with different compositions. It is a formidable tool, combined with the energy-dispersive detector (EDS), in the hunt for contamination and identifying which areas to analyze.

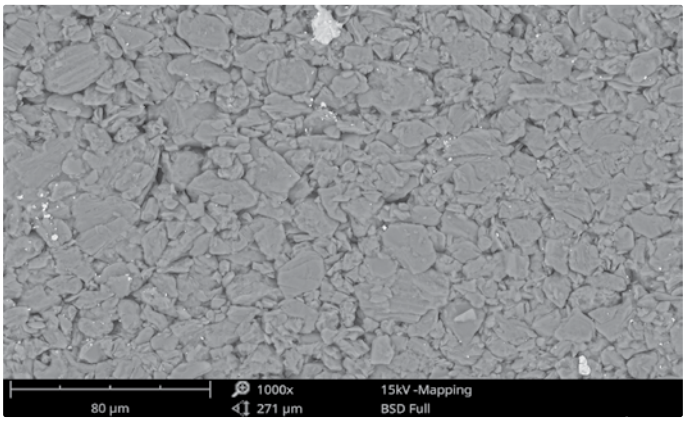

Image 3a: The structure of an electrode imaged with a BSD detector. The bright particle close to the center has a different composition compared with the rest of the sample

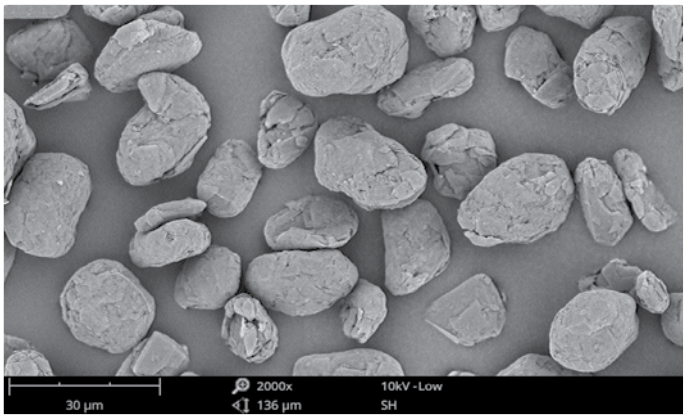

Image 3b: Powders used in the production of anodes.

Samples of interest can also be tilted and rotated, to inspect them from different points of view. *Shape from shading and stereoscopic reconstructions* can be used to create three-dimensional models of the surface and evaluate its shape and roughness.

Inspecting behavior at different temperatures, or while the sample is connected to a power supply, is also possible when using SEM. This form of testing will provide valuable information regarding the physical and chemical properties of the sample, when exposed to critical environments during its life cycle.

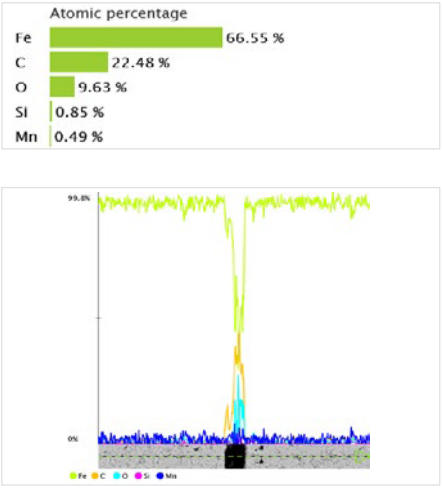

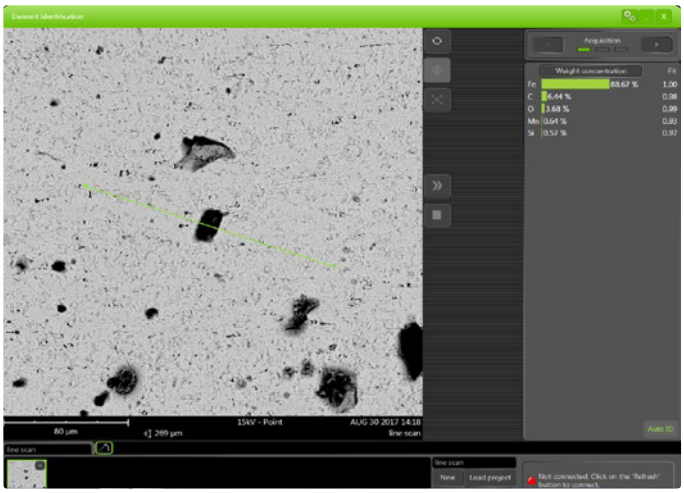

Image 4a: An example of how EDS can be used to trace how the sample composition changes along a line. Spot analysis, line scan or area map can used to monitor the distribution of different phases in a specific region of the sample.

Find out more at **thermofisher.com/phenom**

ThermoFisher SCIENTIFIC

Phenom-World B.V. Dillenburgstraat 9T, 5652 AM Eindhoven, The Netherlands.

APPLICATION NOTE

Ion spectroscopy using TOF-SIMS on a Thermo Scientific Helios DualBeam

Secondary Ion Mass Spectroscopy (SIMS)

The ionized particles that are generated by the ion beam milling process can be used for analysis, as they can be identified and quantified. Because these particles come from a very shallow depth, the technique known as Secondary Ion Mass Spectroscopy (SIMS) is considered a surface analysis technique. Discrimination is based on measurement of the time of flight (TOF), once the particles are accelerated into the drift space of the detector. A modern TOF detector is compact and suited to measuring all elements of the periodic table, including all possible isotopes. Various aspects of the technique are described in this application note.

The TOF-SIMS detector

The detector is mounted on one of the ports of the DualBeam chamber. The SIMS detector has its own vacuum chamber, electronic hardware and software, which is operated on the second monitor of the microscope PC. The detector interfaces with the DualBeam in four ways:

1. Information is exchanged between the TOF software and the microscope software via software commands. Examples are the readout of the vacuum level and the start/stop command for the FIB imaging to create a SIMS map.
2. The position of the ion beam for each pixel during a frame collection is coupled via hardware to the SIMS electronics. The SIMS system then follows the FIB scan.
3. For vacuum safety, the system protection is realized by a hardware link. If the chamber vacuum is > 10^{-4} mbar, the TOF valve cannot be opened and voltages to the ion optics extraction system cannot be applied. Similarly, if the microscope chamber is vented, the TOF valve will close and all detector voltages will drop to zero.
4. In operation, the SIMS detector is at a sample distance of 6 mm. It can be moved in and out by software control. The inserted position of the SIMS is used as an interlock for the microscope to prevent simultaneous insertion of the CBS and STEM detector.

In its retracted position the SIMS detector moves 13 mm outward so there are no restrictions for any other DualBeam task.

The detector ion optic extraction system is partially visible on the CCD camera of the microscope, just in front of the final lens of the electron column (Figure 1).

Typical ion currents for SIMS are between 40 and 300 pA. At high ion currents, such as for serial sectioning, it is good practice to retract the SIMS detector to prevent re-deposition of large amounts of material on the ion extraction system.

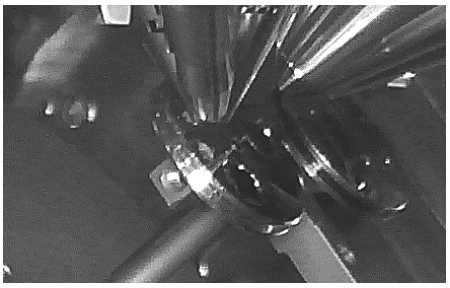

Figure 1. Ion extraction system inserted at 6 mm.

ThermoFisher SCIENTIFIC

The ion spectrum

Ions will be collected by the extractor of the ion optics of the SIMS detector at around 200 V. One of the characteristics of ion detection is the charge of the ion. The SIMS detector can detect either positive or negative ions. Some ions, such as F and Cl, exist only as negative ions, while others, such as Li, Na and K, exist only as positive ions. Some elements can be detected as either a positive ion or a negative ion. The detection mode for these ions depends mainly on the sample composition. Both detection modes can be used to detect these elements.

It should be noted that the focused ion beam itself is not blanked, and the sample is constantly sputtered. Only the ion beam ejected from the sample surface is pulsed. The timing is fully arranged by the TOF unit, providing a high-voltage pulse to induce an orthogonal movement of the ion group.

At this point, all ions will have the same energy. Due to the different masses, light element such as H will move quickly, and heavy elements such as Au will move slowly. A typical pulse width is 1 us, and a typical detection period is 9 us, adding up to a typical FIB dwell time of 10 us. The cycle is repeated at each dwell time and for each pixel the full TOF spectrum is recorded. A priori knowledge of the sample composition is not needed but is helpful to identify the different mass peaks.

A typical spectrum provides the number of counts per extraction as a function of mass, or more precisely, mass divided by charge. The spectrum cannot be used to derive quantitative information from the sample: peak heights are determined by the amount in the sample but also by the excitation conditions and the matrix effect, i.e. the enhanced or reduced ionization during milling.

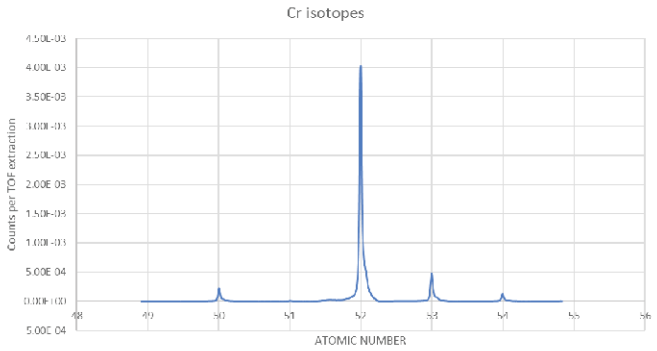

Figure 2. TOF spectrum of Cr foil.

A section of Cr spectrum is shown with the four different isotopes clearly separated (Fig. 2). The most abundant isotope is 52, and in this case, the integrated peak signal is linearly proportional to the actual abundance in the sample. In this way, the isotope ratios can be determined. The result shown compares favorably with results found in literature (Table 1).

Cr Isotope	Abundance Literature	TOF Int Intensity	Abundance from TOF
50	4.35	2.55E-03	4.339
52	83.8	4.93E-02	83.801
53	9.5	5.52E-03	9.393
54	2.37	1.45E+03	2.467

Table 1. For isotopes, this method of calculation is correct because the ionization yield for all Cr isotopes is the same.

Lateral resolution

The lateral resolution of a SIMS signal is largely dependent on the minimum ion beam diameter and the SIMS sensitivity. The BAM L200 sample is used for measuring the resolution. This sample provides a stack of GaAs and AlGaAs layers with known and different widths. It serves as a reference sample, using the aluminum signal at mass 27.

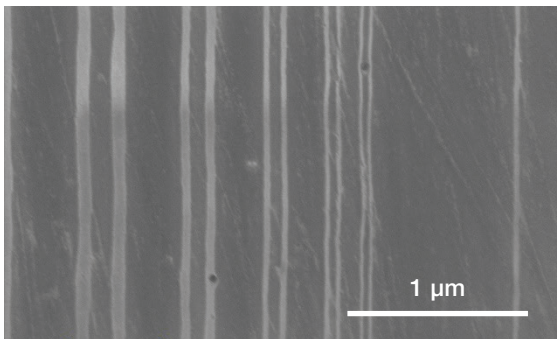

Figure 3. Electron beam image (TLD) of BAM L200. The white line pairs, left to right, refer to P4–P8. The thin line on the right is W8, with a width of 38 nm.

The white lines contain Al, and the dark area is GaAs. The ion beam has been used at 30 kV and 1.1 pA to make an image of the surface (Fig. 4).

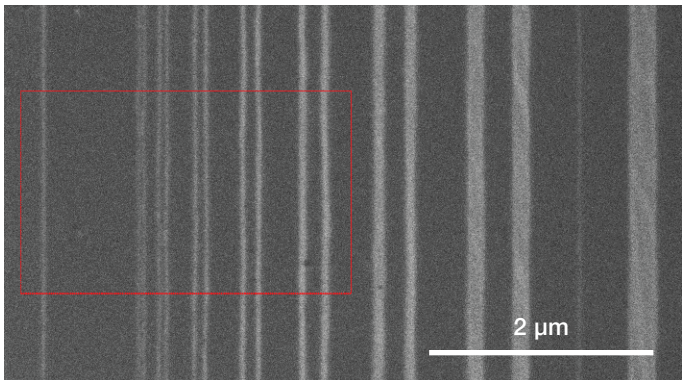

Figure 4. Ion beam image of BAM L200 at 30 kV, 1.1 pA. The area marked in red has been scanned with SIMS to collect the Al signal.

A SIMS map made on this sample has been used to plot the Al signal as a function of the distance on the sample. In this way, it can be seen to what extent the line pairs still are resolved.

From Figure 5, it is concluded that P6 (97 nm peak-peak) is well resolved. The lateral resolution is then half the peak-to- peak width, so approximately 50 nm.

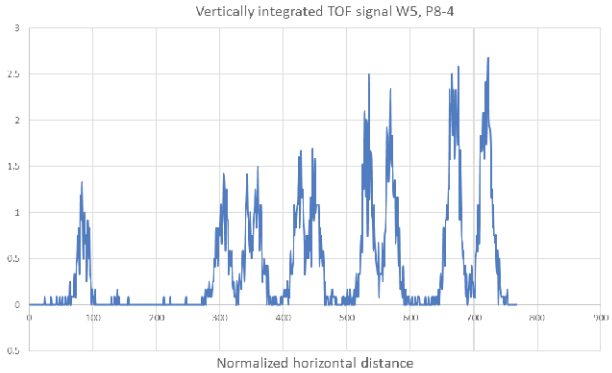

Figure 5. Al TOF signal vertically integrated showing W8 (38 nm) and P8–P4, left to right.

Depth profiling

During the milling process, whenever a new surface is revealed, a depth profile can be made of an elemental distribution in the z-direction of the sample. If we use the same BAM L200 sample, but now with the layers parallel to the ion beam, the different layers will appear when milling deeper in the sample. Depth resolution is strongly driven by the sample ion scattering process (elemental composition of the sample) and by the applied ion energy. In general, it should be taken into account that the milling process induces a forward scattering of the atoms into the material. In a layered structure, therefore, some mixing will occur during the milling process.

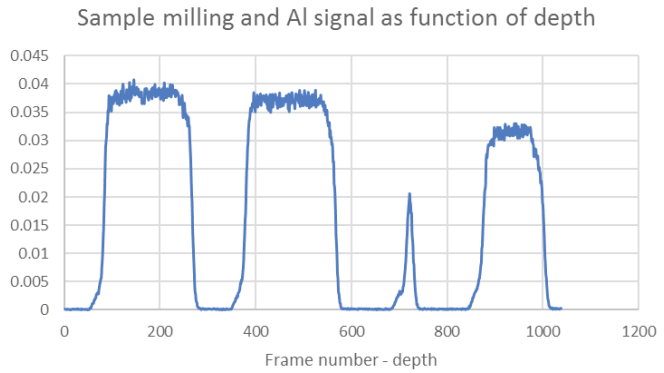

Figure 6. Depth profile milling through layers W3 (left) and W6 (right) of the BAM L200. The small peak refers to layer W5 (19.5 nm width).

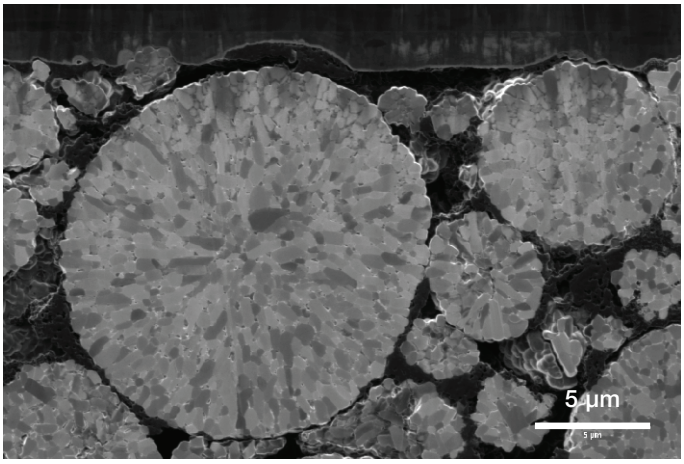

Figure 8. Cross-section of a lithium battery cathode.

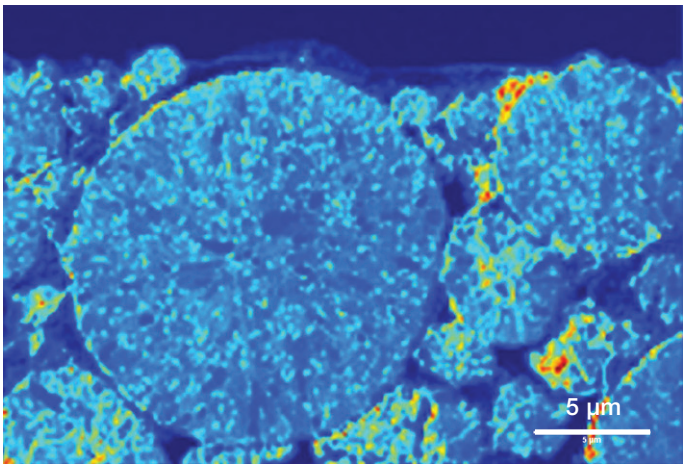

Figure 9. SIMS Map showing the Li distribution over the cross-section.

The TOF software allows users to create data from the spectral set and to obtain a profile in the z-direction of the sample.

The various layers have a very well-defined and sharp transition. It should be noted that W5 is still very visible, while the layer has a thickness of only 19.5 nm. The slope of a peak can be used to derive a depth resolution. To this extent, peak W3 (293 nm) has been magnified (Fig. 7) and used to determine the leading slope 20–80% levels. The distance between these points can be considered the depth resolution, which is 14 nm in this case.

It should be noted that the ion beam energy was set to 5 kV for this measurement, to reduce the forward scattering of substrate atoms.

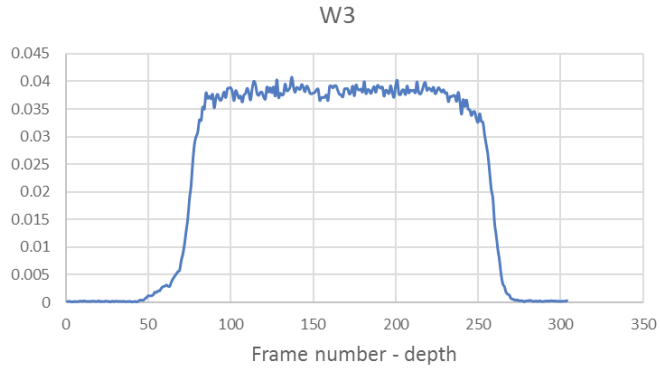

Figure 7. Magnification of the first depth profile peak W3 (193 nm).

An application example

One interesting capability of SIMS is the measurement of lithium (Li), an element frequently used in battery research, in a sample. Small particles of Li have been revealed by ion beam cross-section milling, as shown in Figures 8 & 9.

Another example is a Li-based ceramic. This sample requires a serious reduction of charging; if not, the Li signal would drop by two orders of magnitude. The absence of charging is critical for SIMS, as the signal can be reduced to zero.

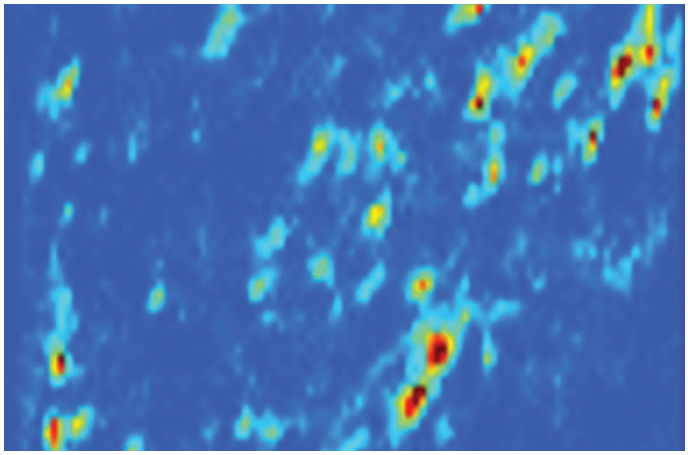

Figure 10. Li map of a ceramic. HFW = 25 um.

thermoscientific

Comparison of EDX and SIMS			
	EDX	SIMS	Remarks
Detectable elements	B and higher	H and higher	New EDX LiK at 52 eV[1]
Signal	Element specific	m/q specific	See notes [2 & 3]
Isotope separation	No	Yes	
Surface technique	No	Yes	EDX penetration depth
Detection limit	0.1%	0.001% (10 ppm)	
Quantitative	Yes, normalized	No, rough estimate	Matrix dependent
Destructive	No	Yes	Even static SIMS
Lateral resolution	200-500 nm typical	50 nm	Depends on kV and Z
Depth resolution	200-500 nm typical	20 nm	Depends on kV and Z
Chemical information	Very limited	Limited	Molecular bonds
Sensitivity to charging	Very low (< 1k V)	Very high (< 10 V)	

Notes:

1. Detection of LiKa with EDX is still very difficult due to the in situ oxidation of Li.
2. SIMS can resolve EDX line overlaps such as: MoL / SKa, BaL / TiKa, WM / SiKa and TiL / NKa.
3. Low-weight molecular fractions (e.g. (CH3)+) can be generated but strongly depend on ion type and sample. Large molecular fractions, such as from biological materials, are not created by Ga or Xe focused ion beams.

Find out more at **thermofisher.com/EM-Sales**

ThermoFisher SCIENTIFIC

APPLICATION NOTE

Multiscale Image-Based Control and Characterization of Lithium-Ion Batteries

Authors
Remi Blanc, Matthieu Niklaus, Daniel Lichau, Ali Chirazi, Patrick Barthelemy, Alex Ilitchev

Lithium-ion batteries (LIB) are the predominant energy storage device for a number of everyday applications, ranging from portable electronics to electric vehicles. This is largely because LIBs have a high energy density, low self-discharge and low memory effect, allowing for a large number of charging cycles without diminishing storage capacity.

Performance, cost and safety are now the main factors driving ongoing battery research, with variations in battery chemistry enhancing performance at a lower cost with increased safety. Direct observation, down to the micro-scale, can be a significant benefit in the research and development of batteries and fuel cells. By combining techniques such as X-ray tomography, transmission electron microscopy (TEM) as well as focused ion beam scanning transmission microscopy (FIB-SEM) or plasma FIB (PFIB), images of the whole assembly can be obtained and observed at a variety of scales.

With advanced image processing and segmentation techniques, Thermo Scientific™ Avizo™ Software is ideally suited for this multi-scale approach. At the macro level, Avizo Software can be used to assess leakage, porosity or delamination. It can also examine aging processes by monitoring the quality of the foil, cathode and anode. At the microscopic level, Avizo Software allows for the estimation of the tortuosity and permeability of the porous electrode and separator. Effective transport parameters and the cell's performance can be further analyzed with electrochemical performance simulations as well as quantification of the triple phase boundary (TPB), phase distribution and connectivity.

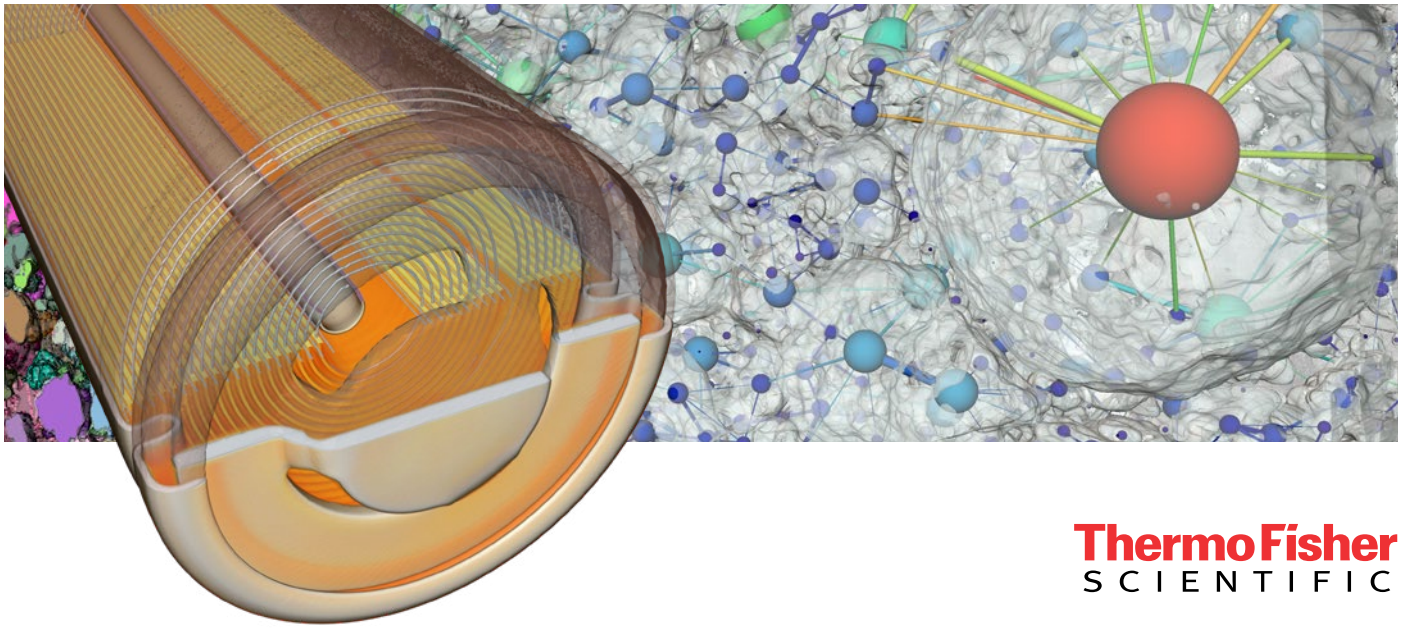

ThermoFisher SCIENTIFIC

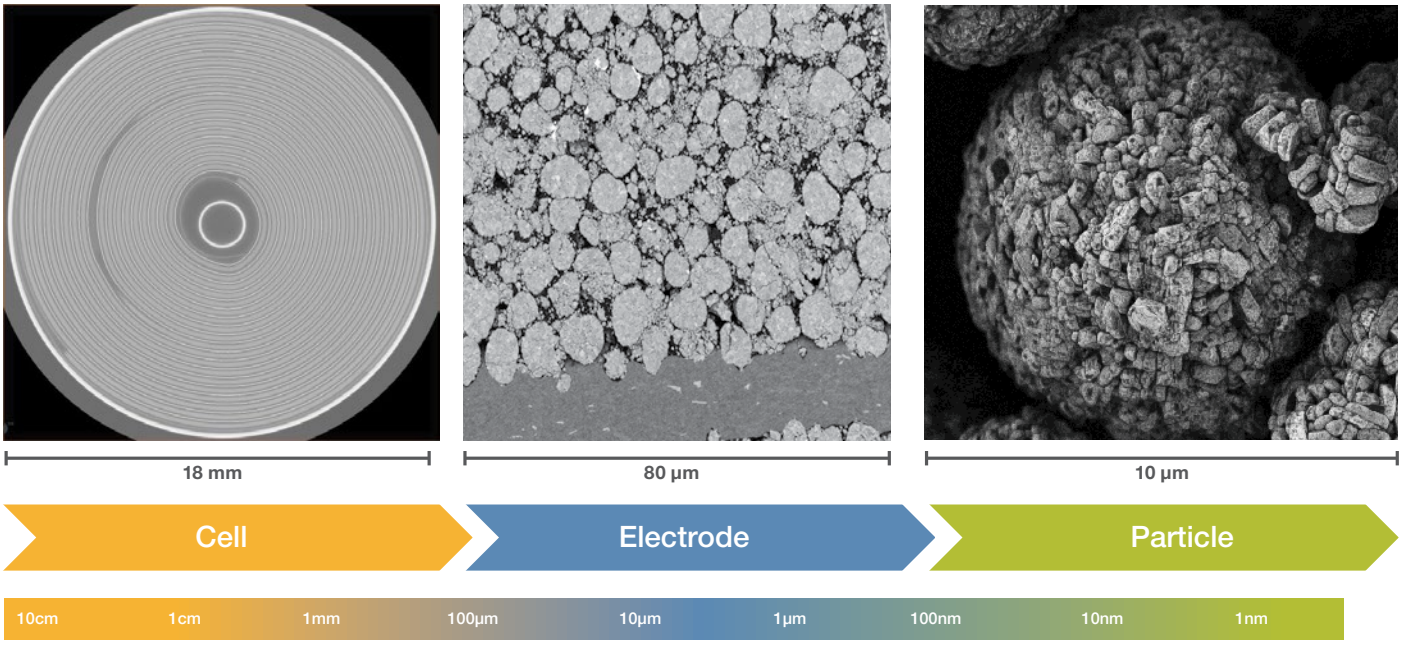

Structural analysis using microCT

Micro-computed tomography (microCT) instruments non-destructively generate 3D reconstructions of samples by placing them on a rotating stage and illuminating them with a micro-spot X-ray source. The transmitted X-rays, influenced by the material, are captured by a detector, creating a 2D projection (the tomogram). As the sample rotates a series of these projections is collected, which are subsequently recombined into a digital 3D model. MicroCT is useful in a variety of applications including;

Quality control: Non-destructive analysis of a battery can identify possible internal defects that may have occurred during manufacturing (e.g. soldering, leakage, delamination, porosity, etc.). This information can lead to more efficient and safer batteries.

Aging and degradation: Incremental changes occur to a battery during multiple charging cycles, leading to degradation. MicroCT enables non-destructive investigation of the mechanisms behind this process. The number of cycles is one of most important factors for a rechargeable battery and is impacted by changes to foil, anode and cathode morphology (length, radial distance, etc.) as well as core leakage.

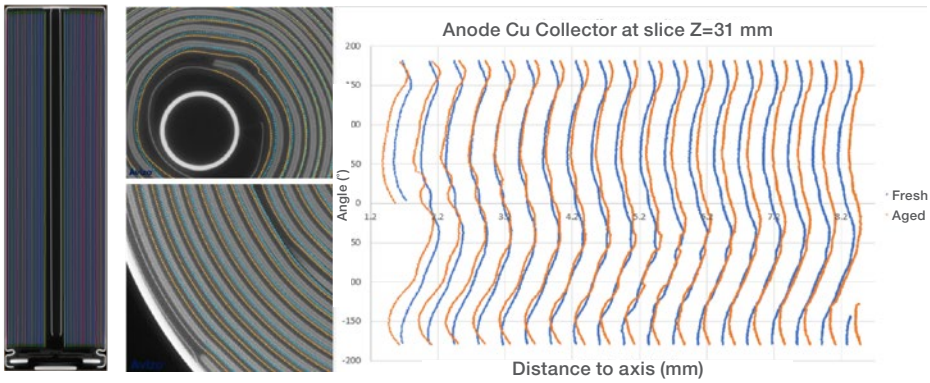

Electrode length: the structure of a lithium ion battery, changed by numerous cycles of charging and discharging. It is possible to control this degradation by monitoring the length of the electrodes. As the electrode curves the radial distance between its ends changes.

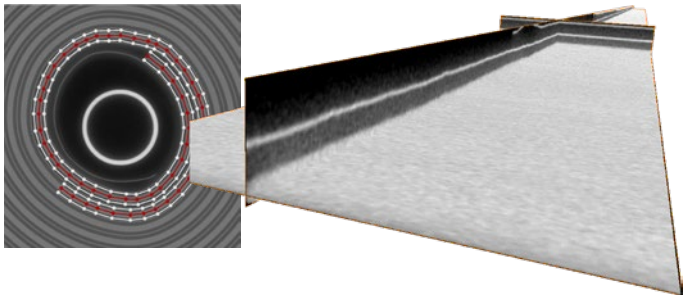

Battery unfolding: for a lithium ion cylindrical cell, the cathode can be unrolled along with the anode and separator. In order to ease the inspection of the full cathode, an unfolding algorithm specially designed to reduce distortions has been developed.[1]

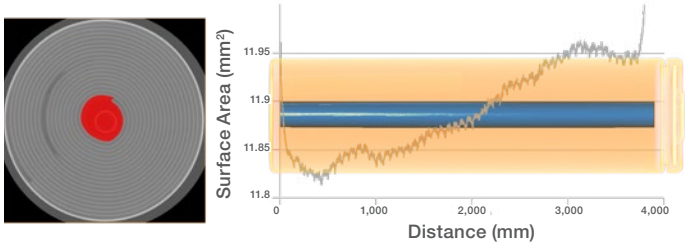

Central rod area: in order to control battery cell design, specific regions of the surface area can be segmented and measured in 3D or in 2D slices. Here the central rod of the cell is analyzed, and the results are plotted in a variation plot.

Nano-structure analysis using electron microscopy

Structural information is critical for interpretation of battery performance, influencing parameters such as the speed of charging, the total capacity as well as the rate of capacity degradation. Electron microscopes (EM) can observe structural details at the nano-scale, revealing the intricate details of particle connectivity and the porous network through which ions are transported.

Cell properties such as tortuosity, porosity, as well as pore and particle size distributions influence how effectively ions diffuse within the electrodes and the electrolyte. The electrical conductivity of an electrode is also dependent on its microstructure (the contact area between the different solids at the TPBs). Heterogeneity within the electrodes is known to contribute to cell degradation.

Our EM 3D imaging systems are essential for the analysis of transport properties (calculated from representative volumes) to understand and predict percolation in battery and fuel cell systems.

Connectivity reveals how each phase within the cell is connected and how effectively the materials are utilized. While pore connectivity informs the transport path of lithium ions, carbon phase connectivity is critical for electrode materials that do not have good electrical conductivity (e.g. $LiFePO_4$, sulfur). Phase connectivity can only be determined with 3D datasets.

Tortuosity describes the influence of morphology on electrode transport. Specifically, pore tortuosity describes the Li-ion transport capability within the electrode whereas carbon tortuosity is a critical parameter for materials that are not good electronic conductors. Tortuosity distribution analysis is useful for evaluating the homogeneity of electrode transport and can only be determined with 3D datasets.

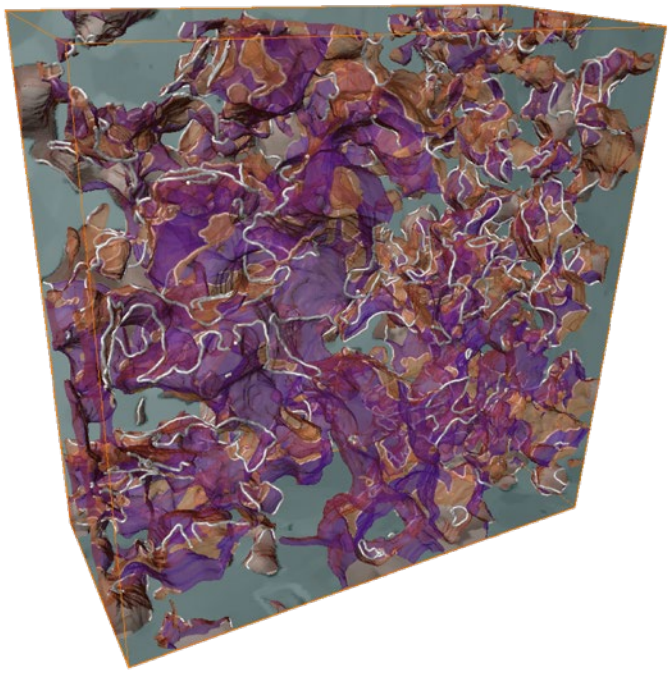

Triple phase boundary length and density is directly correlated to the rate of the electrochemical reactions and, therefore, have a direct impact on fuel cell performance.[2] With FIB-SEM these interfaces are immediately accessible after segmentation. Data courtesy of Sabanci University, Turkey.

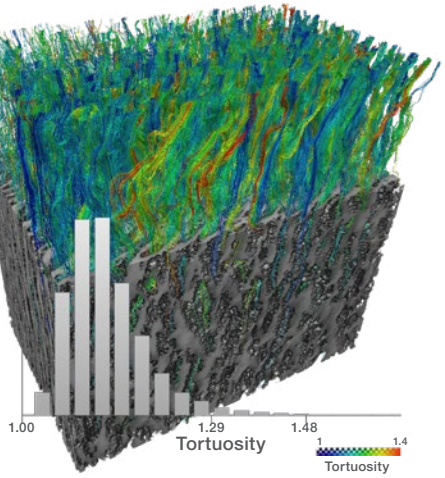

Tortuosity of the battery separator relates to electrical insulation and ion transport properties. This measurement can either be derived purely geometrically or based on simulations. Using a FIB-SEM data reconstruction, averaged 3D tortuosity and a distribution map can be obtained for a lithium ion battery separator.[3]

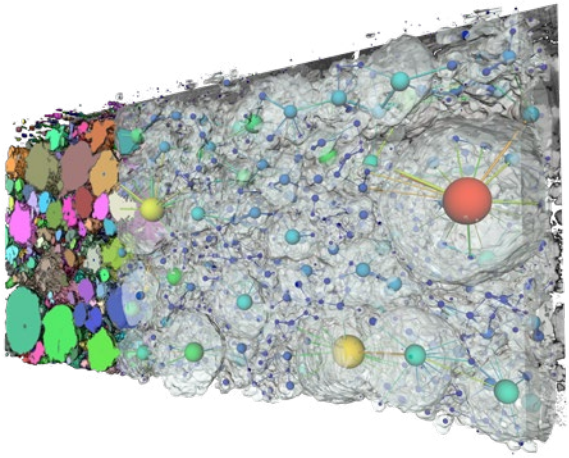

Pores and/or particles networks extraction: Connectivity of the active material with the conducting network has a critical role in the performance of a battery.[4] After identifying the activate material isolated from the binder, it is possible to generate a model of the particle network for the active material, as is shown here for a lithium-ion battery cathode. Information like particle size and contact surface area are calculated. Data acquired on a Thermo Scientific Helios PFIB DualBeam.

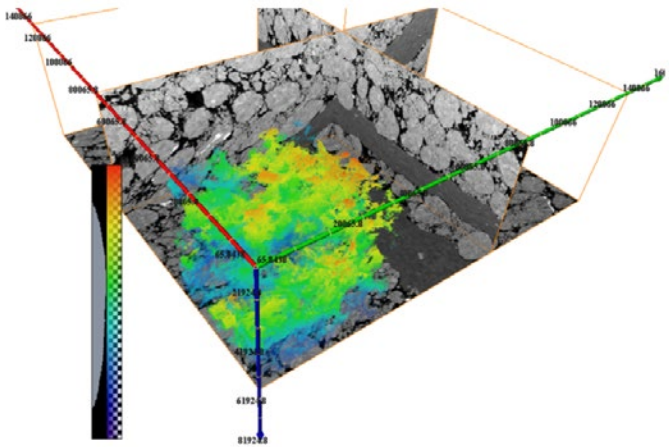

Permeability simulation and estimated pressure field generated from data acquired on the Helios PFIB DualBeam.

thermo scientific

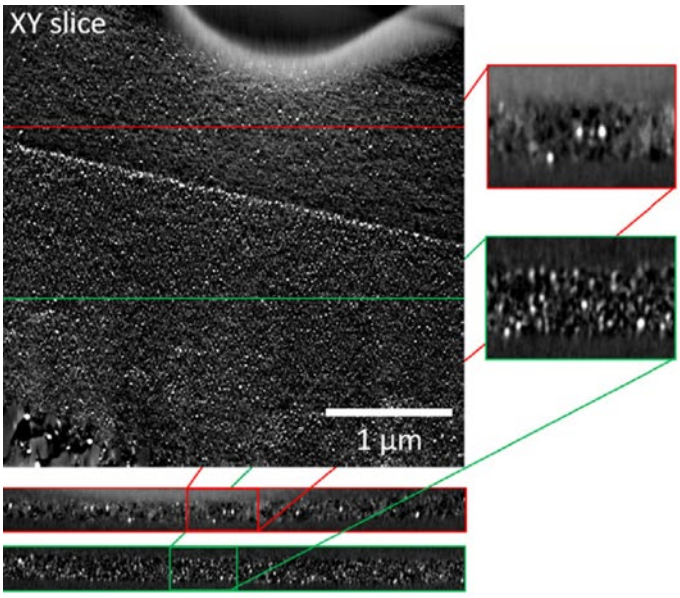

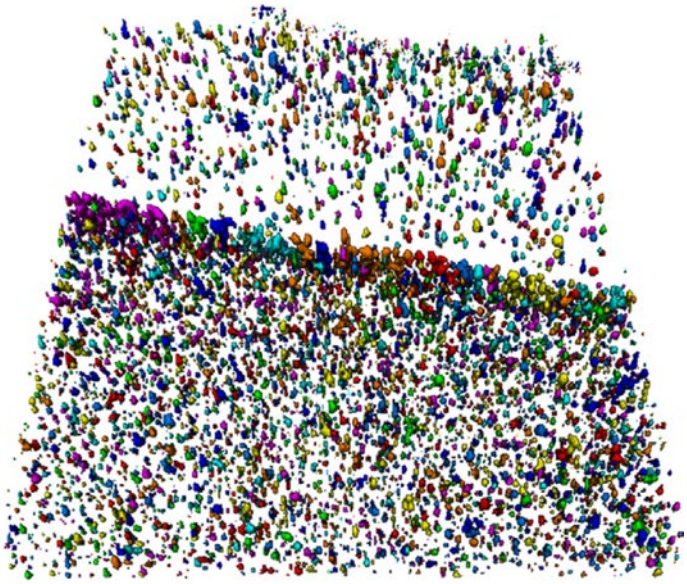

Workflow connectivity: A thin lamella was extracted from a pore-filled membrane using a Thermo Scientific Helios 660 DualBeam; subsequent STEM/EDX acquisition was performed on a Thermo Scientific Talos F200A STEM. EDX data was processed using Thermo Scientific Velox Software and 3D tomography was performed using Thermo Scientific XPlore3D Software. STEM and Velox datasets were then loaded into Avizo Software, where volume fraction and distribution of Au and Pb were computed.

Conclusions

Tomography and electron microscopy provide a vast amount of information on the material properties of battery and fuel cell samples; however, simply having this data is not enough without corresponding contextual information. Thanks to advanced image processing and segmentation techniques, Avizo Software makes it possible to take microCT and EM data and extract key quantitative parameters for materials at the micro- and macro- scales.

Avizo Software provides a reliable, fully automatable solution for material analysis in academia and industry, allowing for faster innovation, reduced time to market, and more reliable batteries/ fuel cells with enhanced performance.

References

1. Baum, Daniel, et al. “Revealing hidden text in rolled and folded papyri.” Applied Physics A, 123.3 (2017), 171.
2. Lu, Xuekun, et al. “Correlation between triple phase boundary and the microstructure of Solid Oxide Fuel Cell anodes: The role of composition, porosity and Ni densification.” Journal of Power Sources, 365 (2017), 210-219.
3. Duda, A., Koza, Z., & Matyka, M. “Hydraulic tortuosity in arbitrary porous media flow.” Physical Review E, 84(3) (2011), 036319.
4. Mendoza, Hector, et al. “Mechanical and Electrochemical Response of a LiCoO2 Cathode Using Reconstructed Microstructures.” Electrochimica Acta, 190 (2016), 1-15.

Find out more at **thermofisher.com/Avizo**

ThermoFisher SCIENTIFIC

APPLICATION NOTE

Large area automated sample preparation for batteries

Spin milling using plasma FIB-SEM

Author
Bartlomiej Winiarski, Zhao Liu, Brandon B. Van Leer, Mikhail Dutka, Herman Lemmens

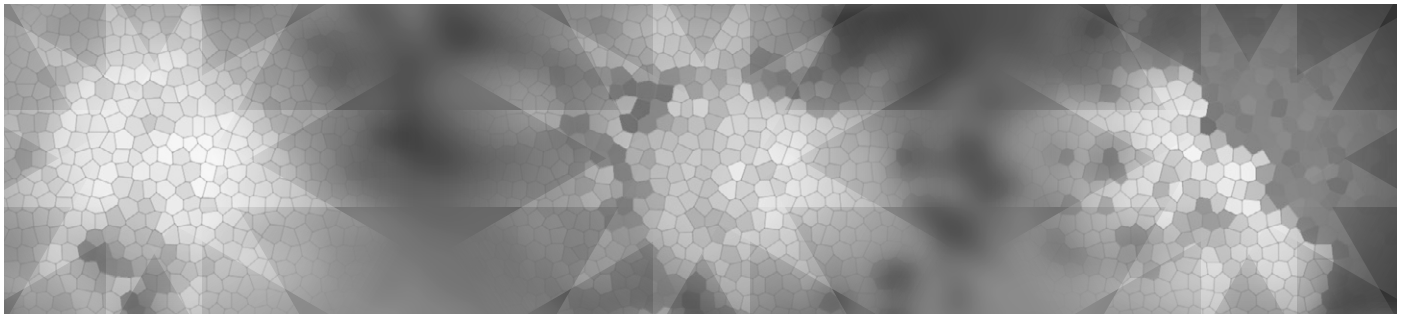

Introduction

In the past decade, the rapid growth of the consumer electronics and electric vehicle markets has focused significant attention to Li-ion batteries. Currently, two important industries, the energy and automobile industries, are involved in intensive research to improve current Li-ion battery technology and develop technology beyond Li-ion batteries [1–3]. As the energy revolution gathers pace, more advanced batteries will be needed for energy storage in order to equalize the fluctuating power production of photovoltaic solar systems or wind turbines. The trend for electromobility also creates a lot of pressure to advance battery research.

Higher energy density and better safety is achieved by a fundamental understanding of battery materials' structures and chemistry throughout the battery life cycle. In order to fully understand battery structures, multimodal information via different characterization techniques (e.g., SEM, EBSD, EDS, Raman, SIMS) is collected at multiple length scales using a correlative approach in 2D and 3D [4–6]. Although 3D analysis can provide more comprehensive structural information than 2D analysis, 3D imaging analysis usually requires a considerable amount of effort involving complex data collection and analysis procedures. In most cases, 2D characterization from a well-prepared surface area of battery material can deliver substantial quantitative and statistical information, such as phase distribution, feature size and shape, defects, and grain orientations, which are all commonly employed in batteries characterizations.

2D area preparation techniques: cross-sectional polishing vs. plasma FIB-SEM

In order to collect high-quality 2D information, an effective 2D area preparation method is essential. Broad ion beam (BIB) polishing is a well-accepted method for large 2D surface area preparation in the battery industry. An optical microscope is used for sample alignment and can prepare surface areas up to mm^2 with site preparation time (SPT) of a couple of hours via Ar ion beam polishing. Another method is a focused ion beam microscope (FIB) with integrated SEM (FIB-SEM). The introduction of plasma FIB-SEM (PFIB-SEM) opened up fast access to cross-sections of hundreds of microns wide and deep, allowing collection of multimodal information with nanometer resolution. Compared to BIB polishing, PFIB-SEM performs both milling and imaging at the same location, which reduces sample transfer steps and provides high accuracy for locating regions of interest on the sample. In this current study, a new large area ($\leq$1 mm^2) or large volume acquisition technique, namely plasma FIB spin milling (PFIB-SM), is introduced and shown to polish areas of a Li-ion battery sample comparable to what can be achieved in the BIB [7].

ThermoFisher SCIENTIFIC

Experimental method and results

As an example, a generic NMC cathode from a Li-ion battery cell was mounted on a regular SEM flat stub and spin mill polished in a PFIB-SEM via focused ion beam using 30 kV high tension and 60 nA (Xe^+) and 120 nA (Ar^+) currents, where areas of 500 µm in diameter were prepared within dozens of minutes. Figure 1 illustrates the experimental setup. The SEM stub with specimen is mounted on a spin mill post positioned in the center of the stage rotation axis, where the plasma ion beam is positioned at the glancing angle of 0.5–1 degree to the sample surface. During the PFIB-SM process, the stage rotates to several stationary positions at which the ion beam mills the sample. The FIB polishes superficial layers of the specimen surface and requires only minimum SPT (~50 min - Xe and ~35 min - Ar). The PFIB-SM technique allows collection of data from on-axis of the SEM stub (Figure 1 (a)) and off-axis location via compucentric stage rotation (Figure 1 (b)), enabling access to areas of about 50 mm^2. The geometry of EDS and EBSD measurements on the prepared sample are shown in Figure 1 (c)–(d). Figures 2 and 3 show the PFIB-SM results. The spin milling process results in a flower-like pattern on the sample surface. SEM images and EBSD maps revealing the high-quality flat surface prepared via FIB-SM technique are presented in Figures 2 (d)–(e) and 3. Argon PFIB-SM at higher beam currents reduces the site preparation time by about 30%, while keeping similar quality of the microstructure as obtained by Xe^+ beam (as indicated by EBSD data in Fig. 3). Such a well-prepared, large, 2D area with short SPT enables multimodal information collection with statistics for electrode structural-performance analysis.

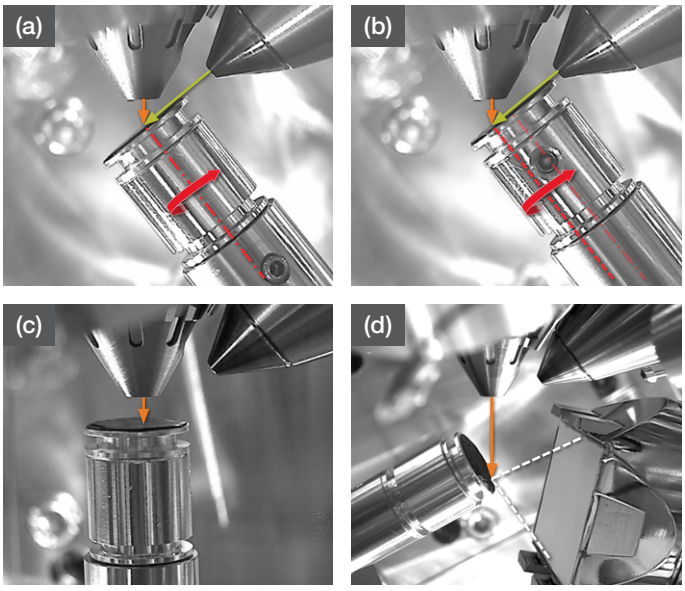

Figure 1. The experimental setup of PFIB spin milling. (a) Stage on-axis rotation and (b) off-axis compucentric rotation; (c) SEM/EDS data collection and (d) EBSD data collection geometries.

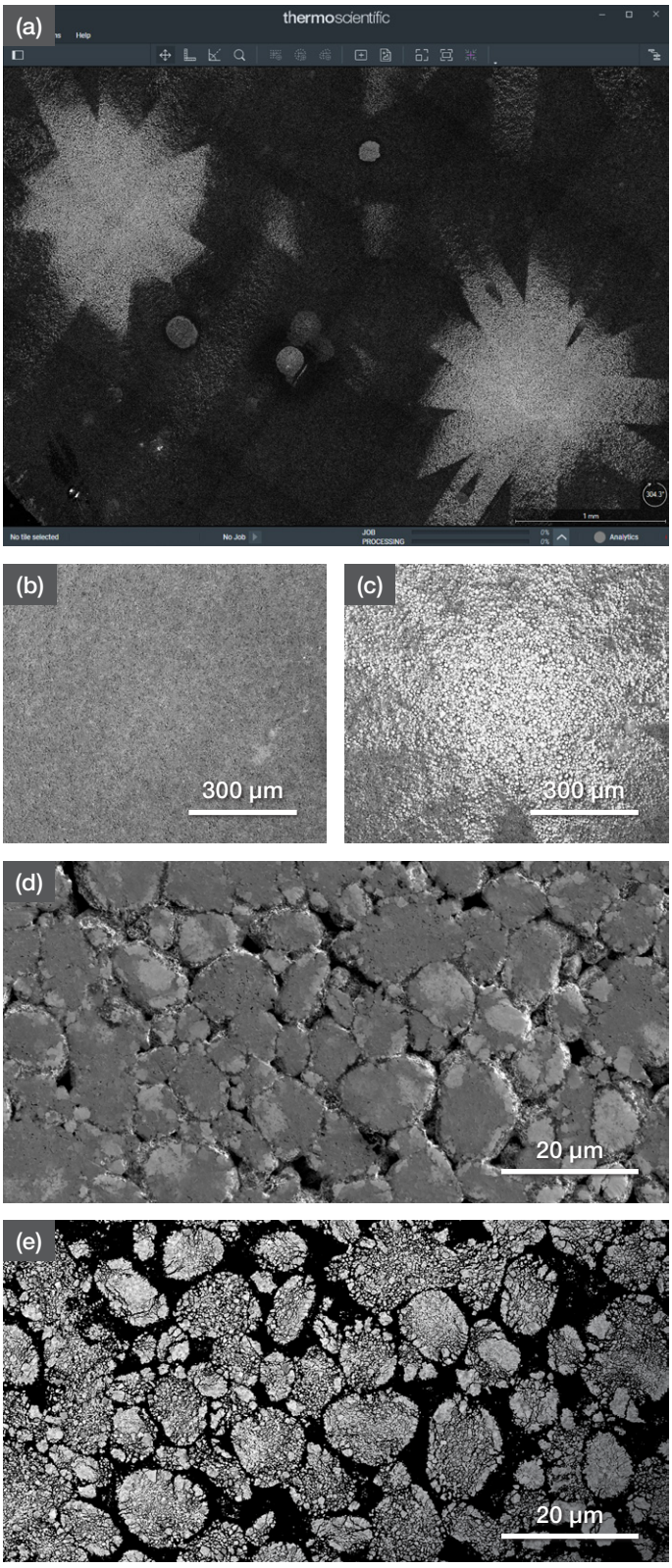

Figure 2. Xe PFIB spin milling results. (a) SEM data is collected in a Thermo Scientific Maps™ Software project; the cathode before (ETD-BSE) (b) and after spin milling (ETD-BSE) (c) at 30 keV, 60 nA, 0.5° glancing angle, total data collection time <60 min; (d) SEM ETD-SE 2keV, 0.8nA; (e) SEM CBS 5 keV, 1.6 nA.

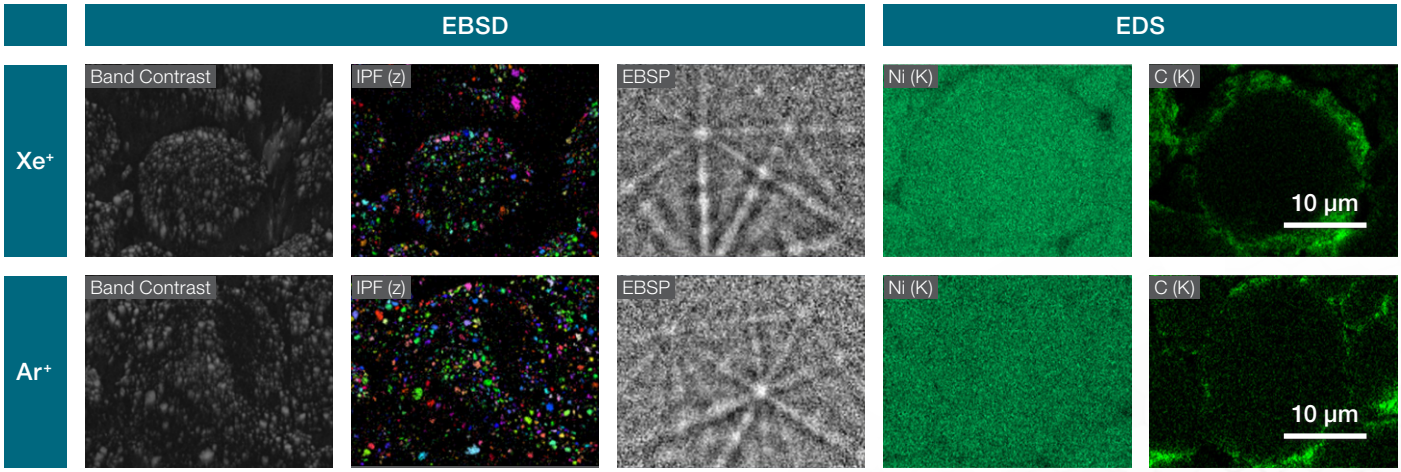

Figure 3. Comparison results of EBSD (left) and EDS (right) after xenon (top) and argon (bottom) PFIB spin milling on NMC cathode.

Conclusion

This work presents the application of the PFIB-SM method for battery research. It is a powerful technique that is well suited for rapid polishing of large area surfaces and allows acquisition of multimodal information. Argon at higher beam currents reduces the site preparation time by about 30%, while keeping similar quality of the microstructure as obtained by Xe^+ beam. Furthermore, the latest Thermo Scientific™ Helios™ 5 Hydra PFIB features the capability for fast switching between different primary ions (Xe^+, Ar^+, O^+, N^+), thus giving even more control for surface preparation strategies based on different types of battery material needs.

Keywords
Plasma FIB-SEM, spin milling, lithium-ion battery, cathode

Acknowledgements
Sample courtesy of Dr. Philipp Müller, BASF SE, Ludwigshafen am Rhein, Germany

Reference

[1] J Nanda, C Wang, et al. MRS Bulletin 43(10):740-745.
[2] G Blomgren. Journal of The Electrochemical Society 164(1): A5019-A5025.
[3] M Liu, P Zhang at al. Nature Communications, (2019) 10:3917.
[4] R Moroni, M Börner at al. Scientific Reports 2016; 6: 30109.
[5] B Winiarski, G Pyka, at al. Microscopy and Microanalysis, Nano Supp, Dec 2017.
[6] B Winiarski, G Pyka, at al. Microscopy and Microanalysis 24(S1) 2018:366-367.
[7] B Winiarski, C Rue, at al. Microscopy and Microanalysis 25(S2) 2019:350-351.

Find out more at **thermofisher.com/HeliosPFIB**

APPLICATION NOTE

Strategies for accurate imaging on battery separator structure

Author: Devin Wu, Zhao Liu, Herman Lemmens, Brandon van Leer

Introduction

As one of the major components in a Li-ion battery, the battery separator plays a key role in preventing physical contact between electrodes as well as facilitating the ion transport within the cell [1]. Because the battery separator structure is closely correlated with its performance, an in-depth understanding of its structure is essential [2]. 2D and 3D imaging are effective approaches to characterize the separator structure; however, due to the intrinsic beam sensitivity of the separator, appropriate imaging techniques are needed to accurately characterize its structure [3-4]. In this application note, strategies for using scanning electron microscopy (SEM) and DualBeam™ technology, also known as focused ion beam-scanning electron microscopy (FIB-SEM), to image the battery separator structure are presented.

Discussion and Results

A commercial polypropylene (PP) separator was used for SEM imaging. The accelerating voltage effects on imaging are explored on the Thermo Scientific™ Apreo SEM (Figure 1). At a 1.5 keV acceleration voltage, clear beam damage effects are observed on the PP separator, where the polymer shows melting and distortion of the pore shapes. Decreasing the voltage to 100 eV minimizes the beam damage and maintains pore structure and features on the polymer. This result indicates the importance of optimizing accelerating voltage in imaging the battery separator. Low-energy imaging is recommended to preserve the separator structure for accurate characterization.

Besides characterizing the separator surface morphology, the cross-section of the separator is also of interest for understanding the structure of the component. Broad ion beam (BIB) polishing under cryogenic temperature is a well-accepted method for 2D cross-section preparation of separator components. Sample preparation to final image collection usually takes 6–8 hours per sample. Compared to BIB polishing, the DualBeam instrument performs both milling and imaging at the same location, which reduces the sample transfer steps. In addition, since the focused ion beam can effectively cut a separator cross-section with tens-of-micron width as a representative sample, it opens up fast access to the separator cross-section within an hour.

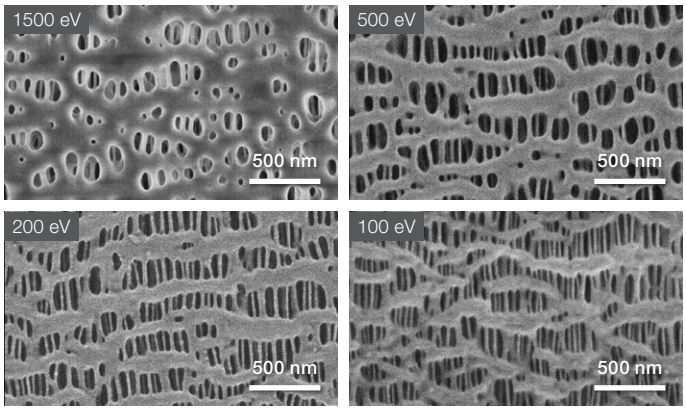

Figure 1: Accelerating voltage effects on battery separator morphology.

Figure 2 shows the ceramic-coated composite separator cross-section prepared at different temperatures using the Thermo Scientific Scios™ 2 DualBeam. The cross-section preparation at room temperature shows severe ion beam damage during the FIB milling process (Figure 2 (a)). The entire polymer structure is deformed, and there is a delamination between the ceramic layer and polymer layer on the edge. Figure 2 (b) and (e) shows the separator milled and imaged at -80°C via cryo-FIB milling. At this temperature, the separator structure is well maintained, and the contrast among different phases is clearly visible. However, when decreasing the cryo FIB-milling temperature to -180°C, inferior image quality due to redeposition on the cross-section has been observed, where the contrasts among phases is no longer clear.

ThermoFisher SCIENTIFIC

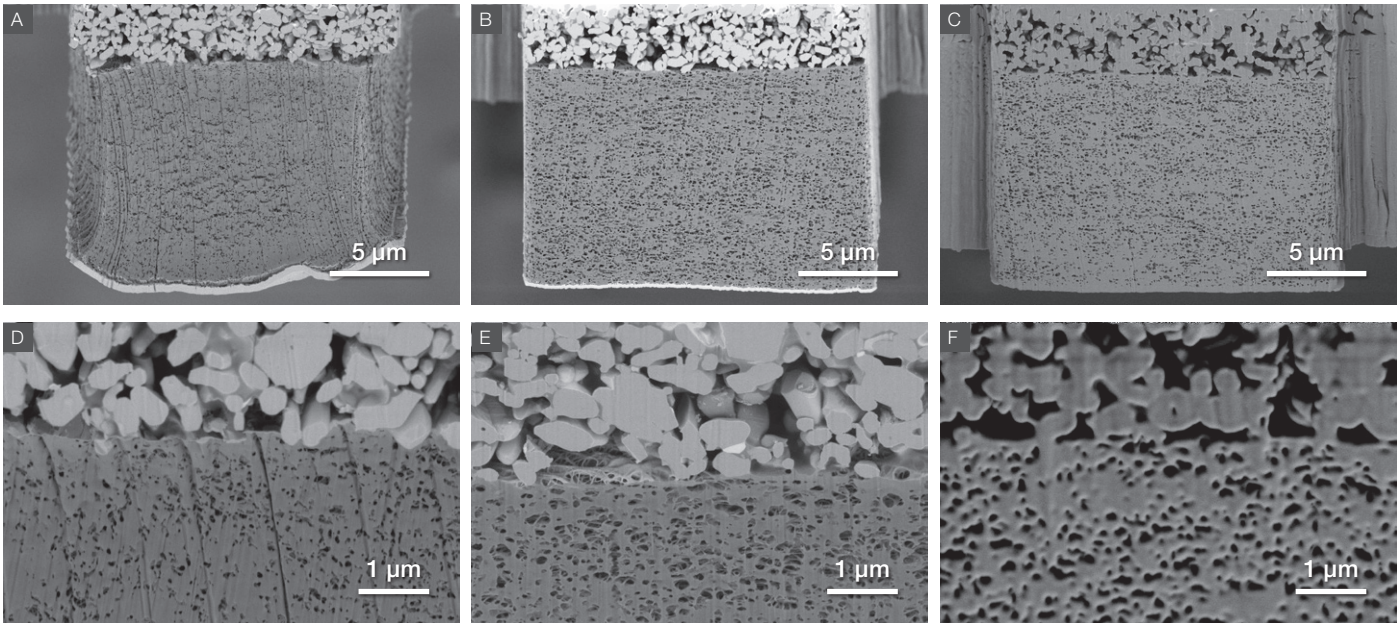

Figure 2: FIB cross-section preparation at different temperature (a) and (d) room temperature; (b) and (e) -80°C; (c) and (f) -180°C.

These results show the critical role of cryo-FIB milling for preparing separator sample cross-sections and defining the optimized temperature range for best imaging quality.

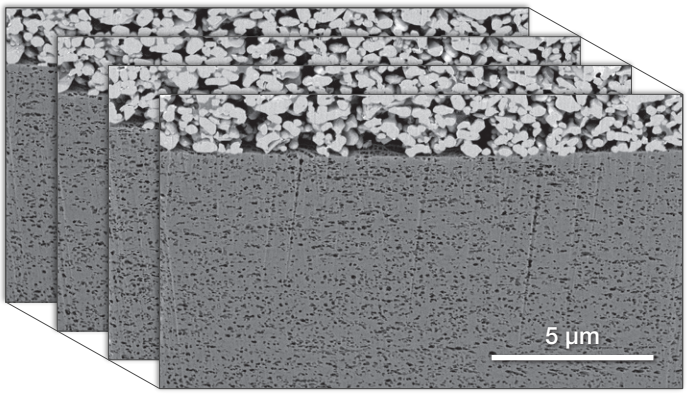

Figure 3: A series of 2D cross-section images collected via Auto Slice and View 4 Software for 3D reconstruction and analysis.

In addition to 2D cross-section imaging, the cryo-DualBeam can perform 3D imaging analysis via FIB serial sectioning tomography (FIB-SST). Figure 3 shows a stack of 2D images automatedly acquired via Thermo Scientific Auto Slice and View™ 4 Software for 3D data analysis. The 3D analysis on this data set allows for further extraction of key microstructural parameters such as closed/open pore volume fraction, pore connectivity, and tortuosity for separator transport property analysis.

Conclusion

The intrinsic beam sensitivity of the battery separator causes characterization challenges for the electron microscope; however, these challenges can be overcome by employing strategies such as low-energy imaging and cryo-FIB milling to accurately characterize the structure of the battery separator. The as-developed strategy for separator imaging will help scientists and engineers to make battery separator with safer feature and higher performance to enable better batteries.

Reference

[1] P. Arora, J. Zhang et al. Chemical Reviews, 2004; 104, 10, 4419-4462
[2] N. P. Deng, et al, Journal of Power Sources, 2016, 331, 132-155
[3] M. F. Lagadec, et al. Nature Energy, 2019, 4, 16-25
[4] M. F. Lagadec, et al. Journal of Electrochemical Society, 2016, 163 (6) A992 – A994

Key words

Li-ion battery, Separator, SEM, DualBeam, Cryo-FIB, 3D imaging, FIB-SST, SST, Serial sectioning tomography

Find out more at **thermofisher.com/battery-research**

ThermoFisher SCIENTIFIC

APPLICATION NOTE

Assessment of contaminants within battery materials via Axia ChemiSEM

Introduction

Contamination is a major issue in the battery manufacturing process. From production of the cathode, anode, and battery cell to battery module assembly and testing, contaminants are a concern at every stage of the process. The existence of contaminants in the battery can cause a wide range of problems—lowering materials usage efficiency, accelerating cell degradation, and even causing internal shorts. As a result, it is essential for materials scientists to obtain a thorough understanding of the contaminants that enter the battery manufacturing process.

The combination of a scanning electron microscope (SEM) and energy dispersive X-ray spectroscopy (EDS) can be used to probe both structure and elemental information of contaminants in battery materials. However, battery contaminants generally have a low concentration level, and image acquisition times can be long when studying these contaminants using conventional EDS. In this application note, we introduce a fast and simple method for characterizing these contaminants via the Thermo Scientific™ Axia™ ChemiSEM, a new SEM platform designed to bring speed and simplicity to materials micro-structural analysis and defect discovery.

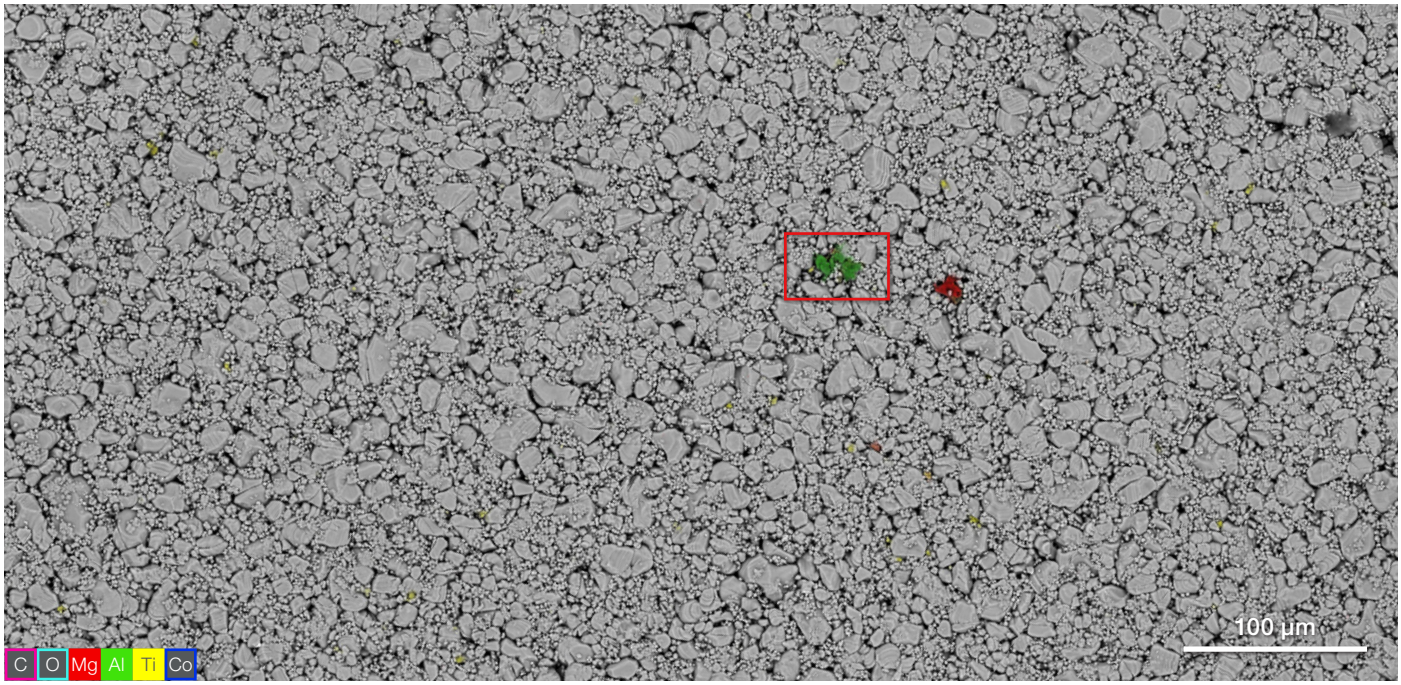

Figure 1. Large-scale navigation montage image obtained by collecting neighboring frames to generate a low magnification image for point-and-click navigation. 750 µm x 370 µm. Acquisition parameters: acc voltage 20 keV, beam current 0.13 uA.

ThermoFisher SCIENTIFIC

Large-scale navigation

With the Axia ChemiSEM, identification of the presence of contaminants can be rapidly achieved within a large field of view—thanks to the system's full integration of different imaging modalities including live-quantitative elemental mapping and conventional SEM imaging. The image in Figure 1 shows a navigation image acquired on the surface of a lithium cobalt oxide ($LiCoO_2$) cathode via Axia ChemiSEM.

This large-scale overview of the sample with EDS data included is collected within 15 minutes. Traditionally, a grayscale image with morphological information and contrast based on backscattered electron signal cannot provide enough information to identify regions of interest for contamination analysis. The main reason for this limitation is that a backscattered electron image only provides a compositional contrast based on the atomic number, and oftentimes the compositional contrast between two different elements is too similar to be observed in grayscale.

With the quantitative elemental information provided by Axia ChemiSEM, however, the large-scale overview already shows some foreign elements, such as magnesium (Mg), aluminum (Al), and titanium (Ti), as well as their position. The large-scale overview serves as a navigation image that can be used to easily move to the region of interest where the contaminants are present to run a more detailed characterization.

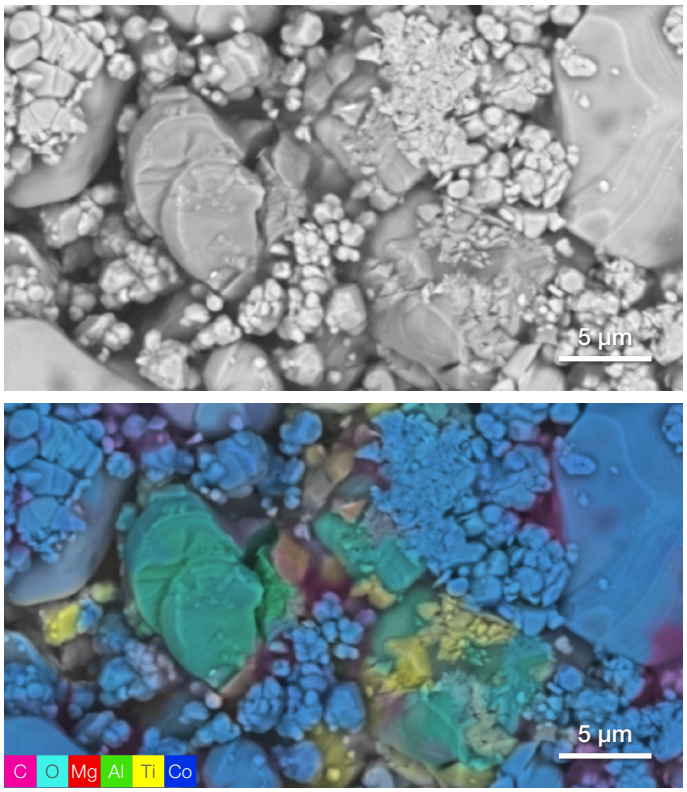

Figure 2. Traditional backscattered electron image (top) of the region of interest and quantitative elemental mapping (bottom) obtained with an acquisition of 80 seconds. (Acquisition parameters: acc voltage 10 keV, beam current 0.76 nA, dwell time 5 us).

Combined SEM-EDS analysis

Using the navigation image as a reference, the user can simply click on the point of interest to drive the stage to it. This process significantly decreases time-to-data for each suspected contaminant. To further demonstrate this ability to hone in on specific regions, the characterization of one area of interest highlighted in Figure 1 is presented in Figure 2. Using conventional SEM imaging, the backscattered electron image, which offers a first level of feedback on the composition, does not provide enough information to identify the contaminant.

By contrast, Axia ChemiSEM provides near instant access to quantitative elemental information every time a grayscale image is acquired since X-ray detection is always on. X-rays are acquired and processed in the background during the acquisition of the grayscale image to obtain quantitative elemental information, different from the raw signal usually acquired from a traditional EDS gross counts mapping analysis. This constant access to elemental information translates to a seamless characterization experience where no time is wasted waiting for data.

The quantitative elemental map presented in Figure 2 was collected simultaneously during the conventional SEM image acquisition. To view this result, the user simply needs to activate the quantitative elemental view. There is no need to re-acquire the data as one would need do with a conventional EDS system.

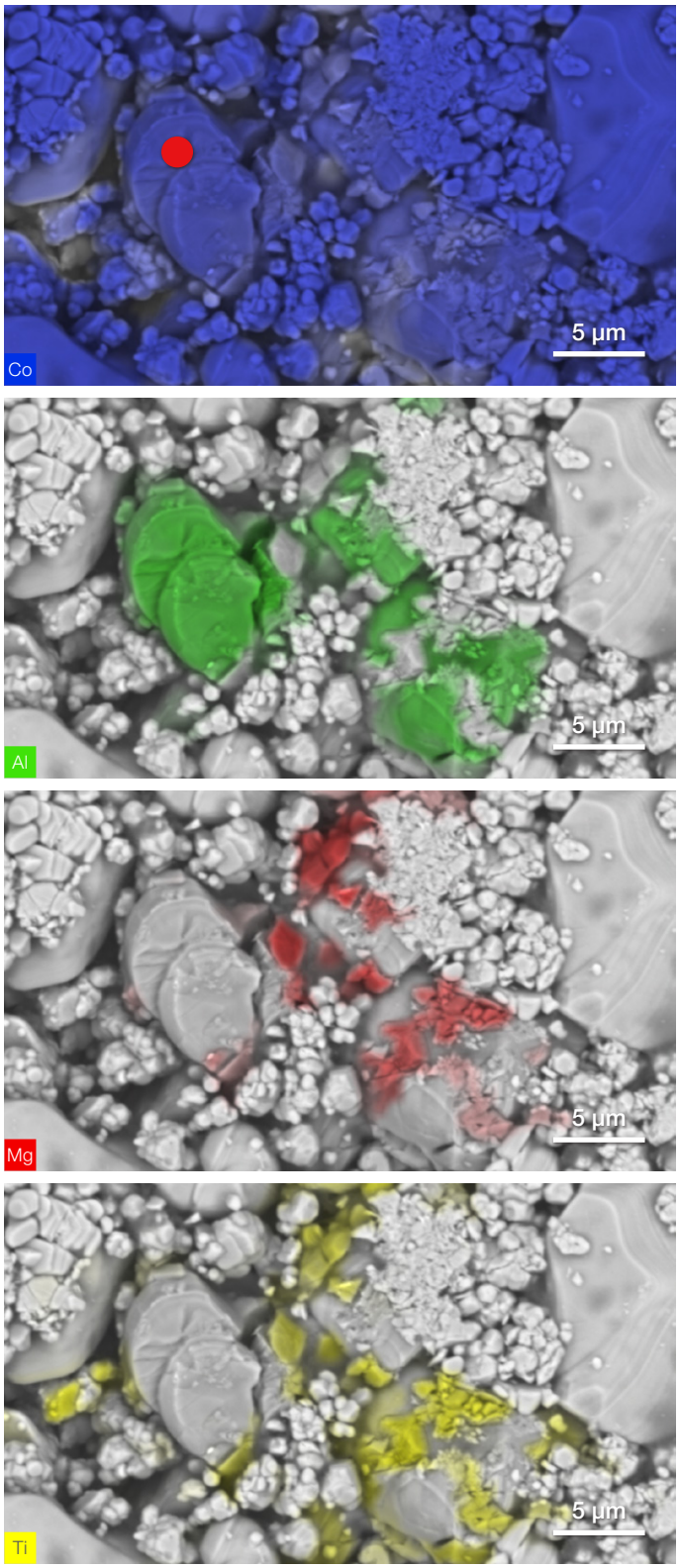

Figure 3. The first image on the top shows the distribution of the cobalt (Co) which is part of the battery matrix. The other three images highlight the distribution of aluminum (Al), magnesium (Mg) and titanium (Ti) contamination, respectively. The red dot in the top image shows the location where further analysis will be performed.

To obtain a better view of the distribution of each element, the user can generate a complete set of images highlighting one element at a time, as shown in Figure 3. Besides Co, the main element from $LiCoO_2$, the results also show the presence of the elements Al, Mg, and Ti within the electrode, which are unexpected. These contaminants could have been introduced during the cathode materials synthesis, mixing, or coating processes as the battery was manufactured. The user stays focused on searching for the odd elements, which easily stand out, leading to a more intuitive and accurate discovery process.

Point analyses

To further identify these contaminants, point analyses have been executed to obtain the exact quantification of the elements present in the contamination with the focus on Al as an example. All of the conventional EDS functions are fully integrated into the Axia ChemiSEM user interface with no need to switch to a different software. (The location of the point analyzed is shown with a red dot in the first image from the top of Figure 3.)

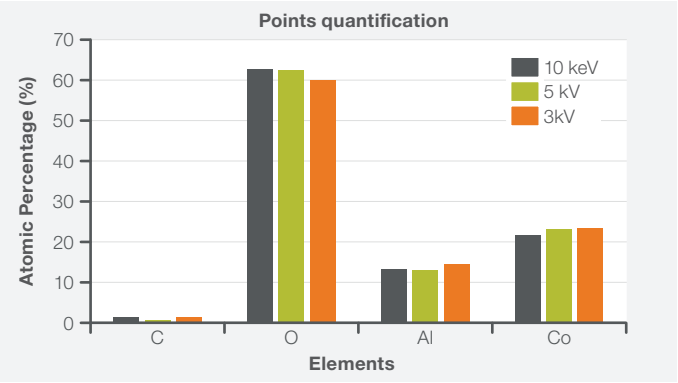

Figure 4. Contamination composition quantified at different acquisition conditions (10 keV and 0.76 nA, 5 keV and 0.28 nA, 3 keV and 0.16 nA).

In order to exclude the interaction volume effects on the quantitative results of the contaminant's composition, both accelerating voltage and beam current have been reduced and the same point analysis has been performed. The purpose is to exclude the interaction volume effects on the quantitative results of the contaminant's composition. Figure 4 compares the analysis of that point as a function of acceleration voltage.

Axia ChemiSEM's enhanced graphical user interface provides automated system alignments, allowing the user to change the analysis parameters without manual adjustments for fast and easy analyses. In short order, point analyses using three different characterization conditions have been acquired, lowering the accelerating voltage up to the minimum required to identify the contaminant's composition and excite the Al k-line (1.4866 keV), as shown in Figure 4. The obtained results are comparable, regardless of accelerating voltage.

The fact that the contaminant's composition remains consistent proves that a certain amount of Al is embedded in the $LiCoO_2$, which likely means that the Al element was reacting with the precursor used to synthesize $LiCoO_2$ during the sintering process. As a result of this analysis, the researcher would be able to determine that the raw materials for $LiCoO_2$ synthesis or the equipment involved in the sintering process need to be carefully examined to eliminate this contaminant.

Conclusion

A thorough assessment of the contaminants within battery materials is critical to assuring battery quality and performance. Using the Thermo Scientific Axia ChemiSEM, large-scale SEM-EDS mapping was employed to quickly and easily identify contaminants and then move directly into detailed quantitative EDS analysis to more precisely pinpoint the distribution of each contaminant. Point analyses were then performed to obtain the exact quantification of each element present in the contamination.

With the Axia ChemiSEM, SEM imaging and EDS are no longer separate workflows, but an integrated process designed to rapidly move from discovery to analysis that generates accurate results. Live EDS technology together with the Axia ChemiSEM's automatic alignment function allows for a smooth user experience and efficient characterization of the battery electrode. Using the Axia ChemiSEM for fast and simple SEM-EDS contaminant analysis, battery manufacturers can improve the efficiency of their research—reducing contaminants during the manufacturing process and improving battery performance.

Find out more at **thermofisher.com/Axia-ChemiSEM**

ThermoFisher SCIENTIFIC

APPLICATION NOTE

Environmental Transmission Electron Microscopy

In situ characterization application examples in heterogeneous catalysis research

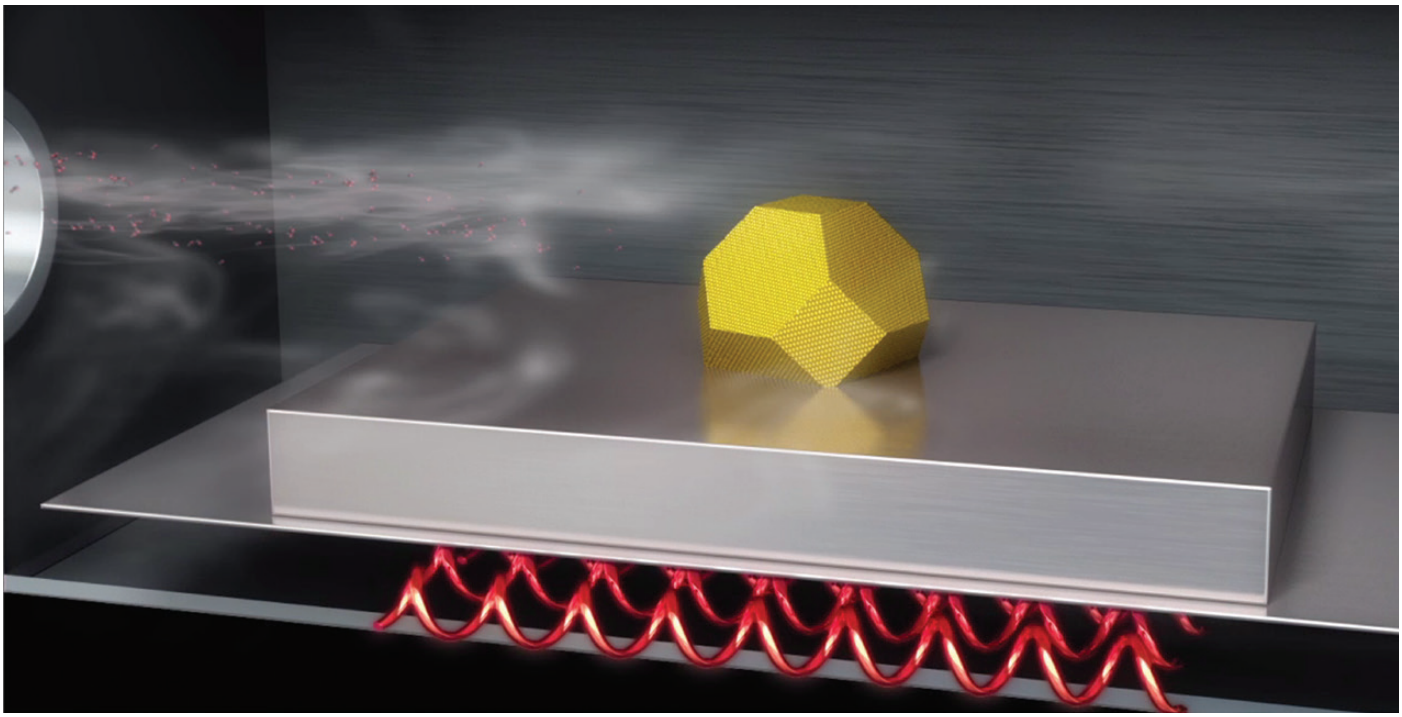

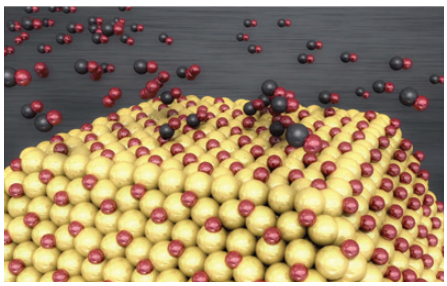

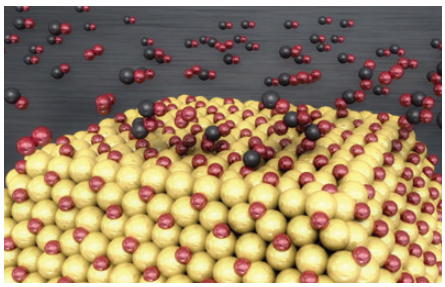

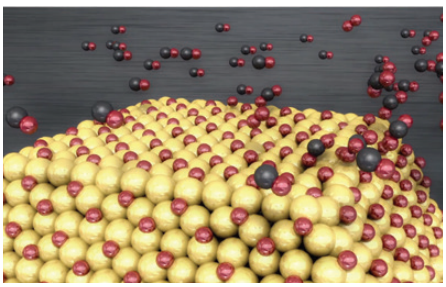

ThermoFisher SCIENTIFIC

The continuing dependence on non-renewable fossil fuels, as well as the demand for new unconventional renewable fuel and feedstock resources for energy, transportation and industry, requires a continuing effort in materials research, particularly catalysis research, at the nanoscale.

As part of this research, it is necessary to characterize existing functional nanomaterials or apply rational design strategies to new catalysts. This requires a detailed understanding of structure-performance relationships and atomic-scale insight into the geometric and electronic structure, and chemical composition. Transmission Electron Microscopy (TEM) is often used for these applications, but the instruments have required significant modification in order to be safely used for catalysis research.

Themis ETEM

The Thermo Scientific™ Themis™ ETEM is the dedicated atomic-resolution Scanning/Transmission Electron Microscope (S/TEM) solution for time-resolved studies of the behavior of nanomaterials during exposure to reactive gas environments and elevated temperatures. Designed specifically for *in situ* dynamic experiments in catalysis, Themis ETEM features a unique, innovative differentially pumped objective lens for window- free imaging, and gas inlets for safe application of inert and reactive gas.

Gas pressures in ETEM experiments can be accurately preset from 10^{-3} Pa up to 2000 Pa (for N_2). The new software-controls offer a range of settings to accommodate both handling by novice (automatic mode) as well as advanced (manual control) operators. The ETEM is equipped with a mass spectrometer for determining gas composition in either the gas inlet system or the specimen area. A built-in plasma cleaner allows for cleaning of the specimen area after using a gas. In addition, compatibility with regular Themis TEM holders for easy sample insertion, and space for full double tilt capability for applications like 3D tomography further extend the functionality of the ETEM to other materials

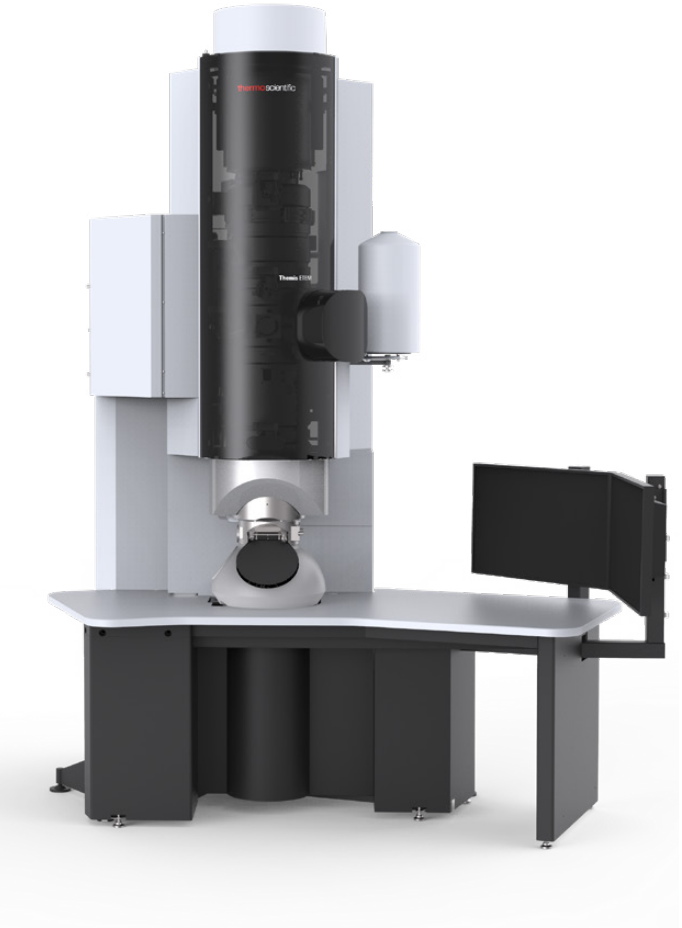

Key Benefits
Observe functional nanomaterials' time-resolved (dynamic) response to gas and temperature stimuli
Study gas-solid interactions at the nanometer and atomic scale, including shape and morphology, and interaction at surfaces and interfaces
Gain insight at the atomic-scale into the geometric and electronic structure, and chemical composition of functional nanomaterials

Nanoparticle size, shape and structure: visualize nanocatalysts in operando

Catalysis is the change in rate of a chemical reaction due to the participation of a substance called a catalyst. Unlike other reagents that participate in the chemical reaction, a catalyst is not consumed by the reaction itself. A catalyst may participate in multiple chemical transformations.

In general, catalysts positively influence a chemical process to achieve a higher selectivity, a higher yield, or fewer amounts of side products while consuming less energy. Some examples of catalyst and support materials are metals, metal oxides, and zeolites.

Substances that slow a catalyst's effect in a chemical reaction are called inhibitors. Substances that increase the activity of catalysts are called promoters, and substances that deactivate catalysts are called catalytic poisons.

Nearly 90% of all chemical processes use catalysts; therefore, it is indispensable to develop a fundamental understanding of the functionality of catalysts.

The catalytic activity of catalysts seems to, among other influences, depend strongly on their size, shape, and structure. While *ex situ* characterization offers important insight to the catalyst's structure and composition, this observation might not provide the information about changes to the catalyst's structure and properties while in its operating state. This is fundamental to describing the catalyst's structure – property relationships because in operado, the catalyst undergoes significant changes in size, shape, structure and composition to become active (see Figures 1 & 2).

For this reason it is very important to obtain the structural information about the catalyst under reactive conditions, like elevated temperatures and pressures to understand and to improve the catalytic activity and functionality of new catalysts.

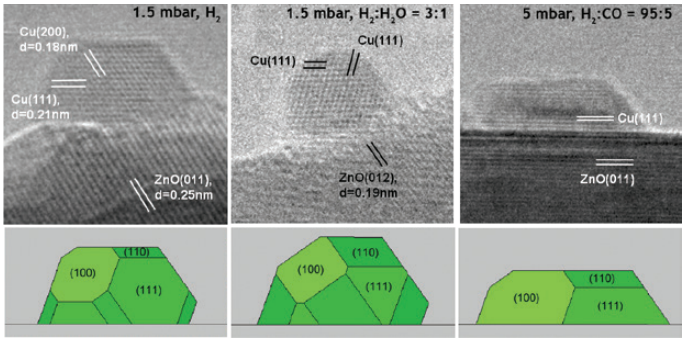

Figure 1. *In situ* HRTEM images of a methanol synthesis catalyst consisting of Cu nanocrystals on ZnO in various gas environments at a temperature of 220°C. Below the corresponding Wulff constructions of the Cu nanocrystals. The HRTEM images have been recorded in situ at a pressure of 1.5 mbar of H_2; and at a total pressure of 1.5 mbar in a gas mixture of H_2:H_2O = 3:1; and at a total pressure of 5 mbar in a gas mixture of H_2 (95%) and CO (5%), respectively.

Ref. P. L. Hansen et. al., Science vol 295 (2002) 2053-2055

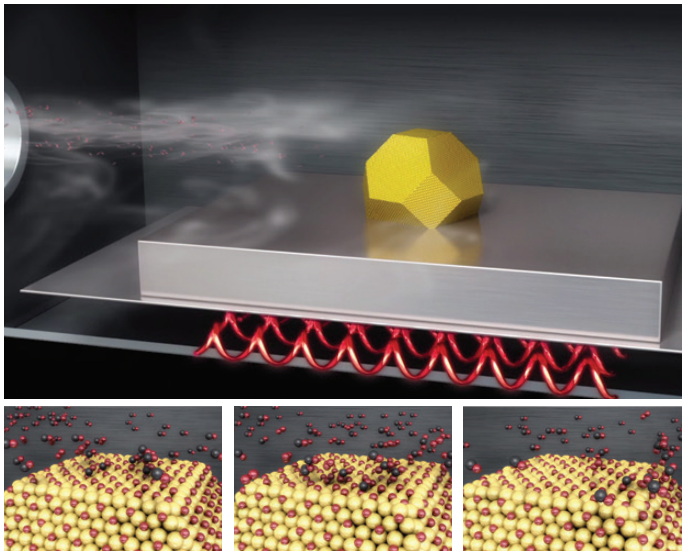

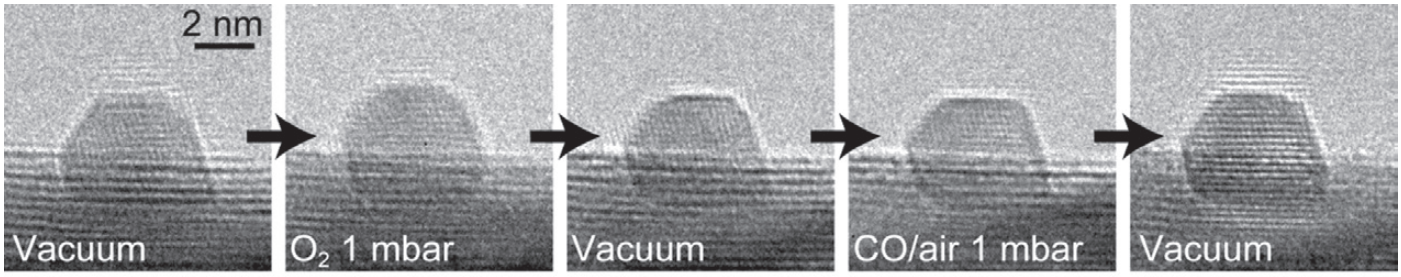

Figure 2. Reversible change in the morphology of a gold nanoparticle supported on CeO_2 between vacuum and gas environments (O_2 and 1 vol% CO/air gases). After introducing the O_2 gas in vacuum, the morphology of the gold nanoparticle changed from faceted to a roundish morphology. After removing the O_2 gas, the gold nanoparticle morphology reverted back to a faceted morphology. Subsequently, 1 vol% CO/air was introduced under vacuum. The major {111} and {100} facets appeared clearly in 1 vol% CO/air. After removing 1 vol% CO/air, the morphology of the gold nanoparticle appeared to be faceted as in the proceeding observations in vacuum.

Ref. T. Uchiyama et. al., Angew. Chem. (2011), 123, 10339 –10342

NOTE: Certain gases may be not approved for use with the ETEM or their use may be restricted. Please contact Thermo Fisher Scientific for additional information on approved gases and our gas approval process.

Nanoparticle size, shape and structure: visualize nanocatalysts in operando

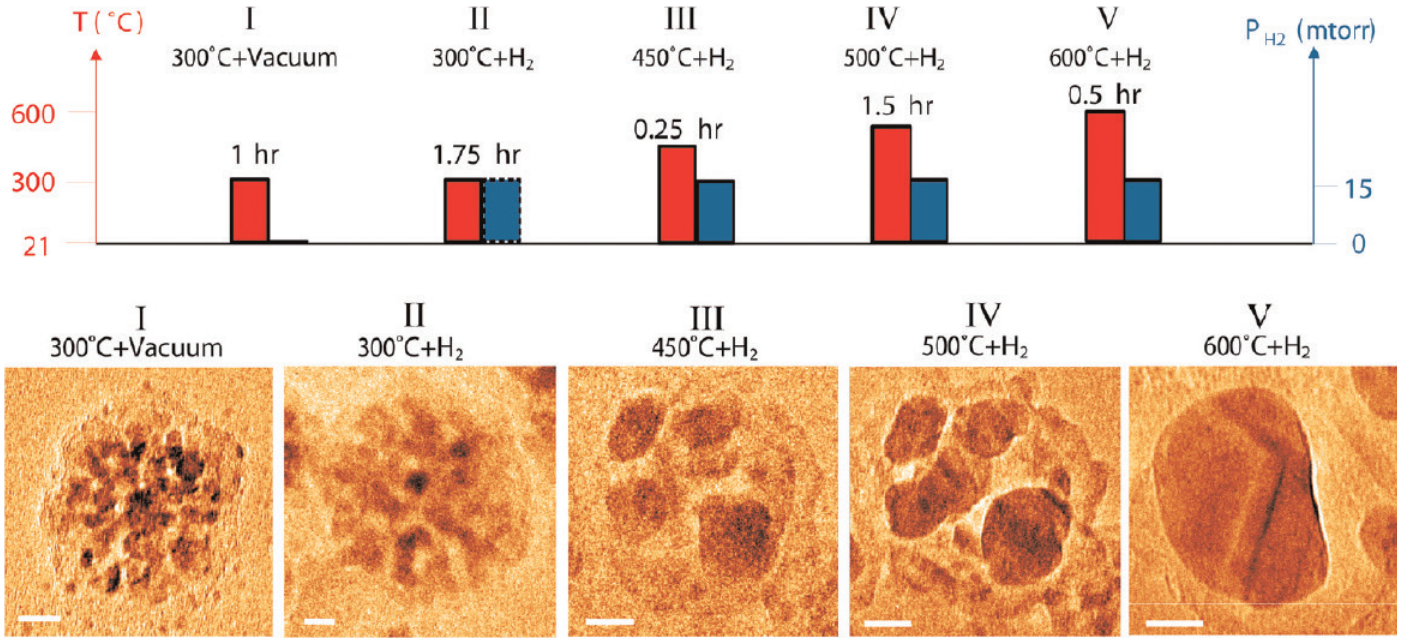

Figure 3. *In situ* observation of structural changes of Co/CoOX catalysts at different reduction conditions. Nanoporous cobalt/silica catalysts relevant to Fischer-Tropsch synthesis, an industrial reaction that converts syngas (mixture of hydrogen and carbon monoxide) to liquid fuels. (Upper image) Heating and H_2 gas environmental conditions and their durations. For a period of 30 minutes, the H_2 gas pressure was raised to ~6.5 Torr. (Lower image) *In situ* ETEM images of the nanocomposites under the corresponding environmental treatments. Scale bars are 10nm. The CoOX reduction into metallic cobalt results in an increase of an effective particle size of the porous structure.

Ref. H. L. Xin et.al., ACS Nano, 2012, 6 (5), pp 4241–4247, DOI: 10.1021/nn3007652

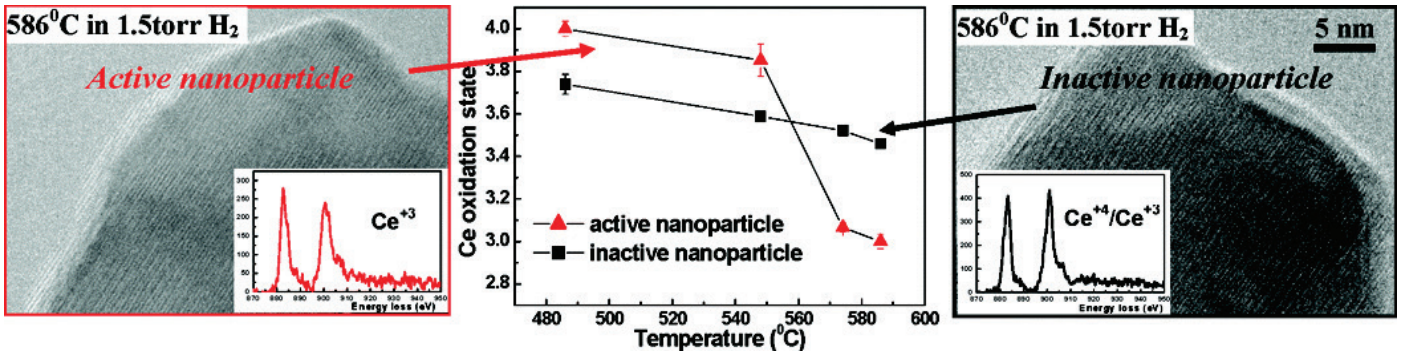

Figure 4. Nanoscale ceria zirconia particles are a critical component in the modern automotive three-way catalytic converter and have potential applications in other areas such as fuel cells, where redox functionality is important. *In situ* studies allow following the dynamic redox process taking place in individual ceria zirconia nanoparticles with changes in the oxygen chemical potential. Considerable variability in the redox activity have been observed with correlation of these differences to nanoscale structural and compositional measurements. The more active structure has predominantly disordered cations and shows no evidence for oxygen vacancy ordering during reduction. (Left and right) In situ HRTEM observations from nominally identica ceria zirconia nanoparticles recorded at 586°C in 1.5 Torr of H_2 The in situ EELS (insets) show that the particle on the right is more strongly reduced than the particle on the left. (Center) Oxidation state for same two particles as a function of temperature.

Ref. R. Wang, et. al., Nano Lett., (2008) Vol. 8, No. 3, 962-967

Production of syngas by partial oxidation of methane: Ni catalyst activation process

Synthesis gas (Syngas) is a mixture containing certain amounts of carbon monoxide (CO) and hydrogen (H_2). Production methods are steam reforming of natural gas or liquid hydrocarbons, and the gasification of coal or biomass.

Syngas is used as intermediate in creating synthetic natural gas. The hydrogen in syngas is used in refinery and in fuel cells, and is the base for the production of ammonia (NH_3). Syngas is an essential base product in the chemical industry and is used in the Fischer–Tropsch process to produce alkanes such as diesel fuel, synthetic petroleum, or is converted to methanol (CH_3OH).

As an example, partial oxidation of methane (CH_4) is an important reaction for the production of syngas:

$$CH_4 + ½\ O_2 \rightarrow 2\ H_2 + CO$$

Because of its slight exothermic nature, and the obtained product syngas ratio of H_2: CO=2 is beneficial as input for Fischer–Tropsch synthesis:

$$(2n+1)\ H_2 + n\ CO \rightarrow C_nH_{(2n+2)} + n\ H_2O$$

The process of partial oxidation of methane may also be useful for other energy-related processes, such as fuel reforming for high-temperature fuel-cell applications.
Noble metals are very efficient and stable as catalysts for converting methane to syngas; however, noble metals are costly for large-scale applications. Supported Ni catalysts, as less expensive options, have shown high conversion efficiencies (see Figure 5) at low cost, although deactivation by coke formation and sintering can be problematic.

Figure 6 shows the development of the structure, composition and morphologies in model Ni/SiO_2 catalyst during ramp-up for partial oxidation of methane under high conversion conditions. The gas composition along the catalyst bed varied in space and time during ramp-up. Essentially there was no single "reactor condition" in this case and the variation in the gas composition had to be taken into account in the design of experiments so that the correct structure property relations could be determined.

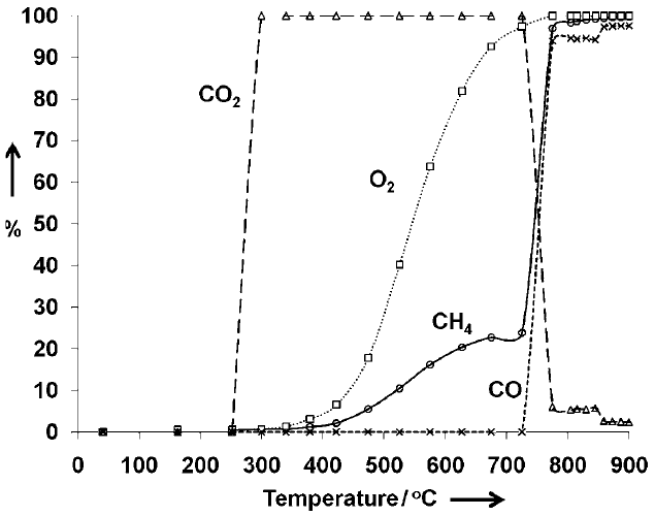

Figure 5. Conversion and selectivity for partial oxidation of methane over a model 2.5 wt% Ni/SiO_2 catalyst.

Ref. S. Chenna, R. Banerjee, and Peter A. Crozier, ChemCatChem (2011), 3, 1051 – 1059

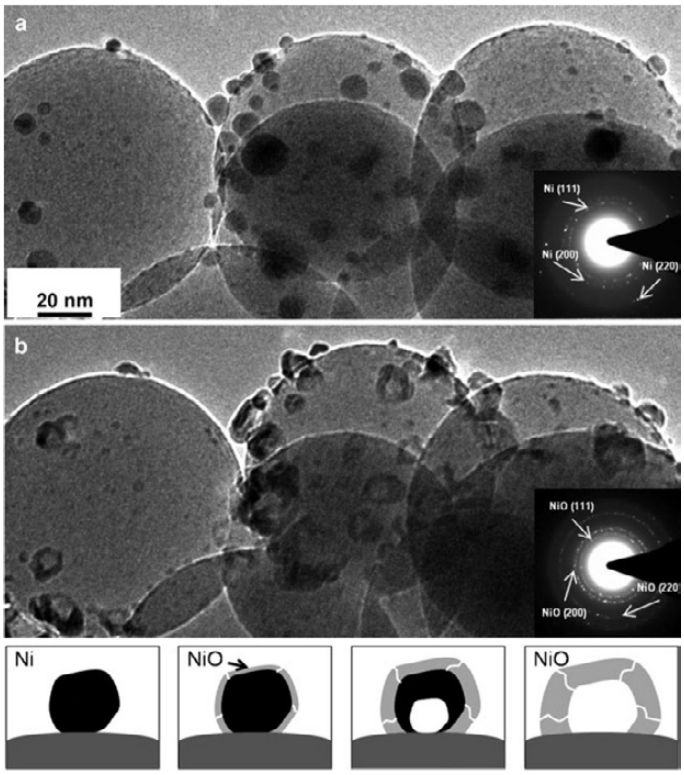

Figure 6. (Upper image) Partial oxidation of methane catalyst Ni/SiO_2 in presence of 1 mbar of H_2 at 400°C. (Middle image) same catalyst in presence of 1 mbar of mixture of CH_4 and O_2 in 2:1 ratio at 400°C.

(Lower image) Diagram of NiO void formation by Kirkendall effect.

Ref. S. Chenna, R. Banerjee, and Peter A. Crozier, ChemCatChem (2011), 3, 1051 – 1059

NOTE: Certain gases may be not approved for use with the ETEM or their use may be restricted. Please contact Thermo Fisher Scientific for additional information on approved gases and our gas approval process.

Catalyst deactivation by carbonaceous layer growth

In a vast number of commercially relevant catalytically chemical processes, the deposition of coke (carbon) is a by-product of the underlying reactions. This causes catalyst deactivation and can lead to reduced process efficiency.

There is an ongoing interest in stabilizing the activity of supported catalytical nanoparticles and to understand the processes by which carbon-base layers, forms and accumulates on their surface.

Natural gas conversion into synthesis gas: steam reforming catalyst Ni/$MgAl_2O_4$

Steam reforming is a fuel reforming process that produces hydrogen or other useful products from fossil fuel such as a natural gas, mainly methane CH_4. As described previously, hydrogen is a renewable fuel source and an important reactant in a large number of chemical processes.

There is a tremendous research effort in designing affordable catalyst heterostructures. In addition to revealing the structure-function relationship, this research is leading to understanding and preventing catalyst deactivation that occurs when carbon-layer growth that covers the active sites. Direct visualization, such as *in situ* HRTEM, plays an essential role in this (see Figure 7).

Alkane dehydrogenation: alkene producing catalyst Pt/MgO

Dehydrogenation is widely used for the transformation of alkanes (hydrocarbons with carbon-carbon single bond) to alkenes (olefins, carbon-carbon double bond). The simplest example of this reaction is the catalytic dehydrogenation of ethane to ethene:

$$C_2H_6 \rightarrow C_2H_4 + H_2$$

The catalytic alkane dehydrogenation process has the advantages of a high selectivity of valuable alkenes and the formation of hydrogen as a by-product (see Figure 8). Alkenes are essential building blocks in the petrochemical industry. The C-C double bond in alkenes gives them the ability to undergo polymerization to form a huge variety of polymers (plastics). Alkenes are also an important starting material in organic synthesis, forming products such as alcohols, aldehydes, epoxide, or amines. All of these compounds/chemicals are the base for products such as adhesives, fertilizers, carpets and paints

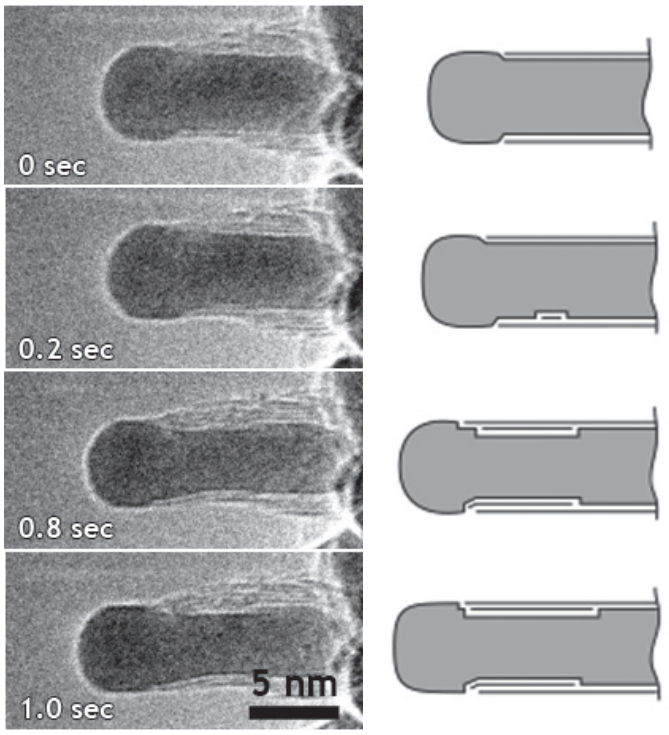

Figure 7. Carbon nanofiber growth by catalytic decomposition of methane over a catalyst consisting of Ni nanoclusters supported on $MgAl_2O_4$. Image sequence (Left) and drawings (Right) illustrate the positions and effect of mono-atomic Ni step edges at the C–Ni interface. Dynamic *in situ* ETEM study with CH_4:H_2 = 1:1 at a total pressure of 2.1 mbar with the sample heated to 536°C.

Ref. S. Helveg, et. al., NATURE (2004) VOL 427, 426-429

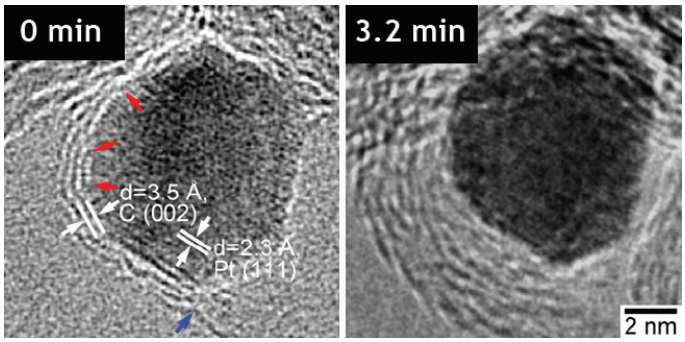

Figure 8. Dynamic *in situ* ETEM study (1.3 mbar C_4H_8, 475°C) with atomic-scale resolution Carbon layer growth during catalytic dehydrogenation over a catalyst consisting of Pt particles supported on MgO. Surface-step are identified as growth centers for graphene.

Ref. Zhenmeng Peng, et. al., Journal of Catalysis 286 (2012) 22–29

Catalytic low temperature CO oxidation

Low temperature carbon monoxide (CO) oxidation is needed in various applications, such as in indoor air purification, safety devices (e.g., in laboratories using CO), submarine ventilation systems, and catalytic converters for cold-start emissions control of automotive exhausts. Another important application is the purification of hydrogen H_2. H_2 gas is used in fuel cells. And H_2-rich gas mixtures are an essential feedstock for chemical and energy-generating processes, including in petrochemical refineries and the production of chemicals (such as ammonia, methanol, etc.).

The H_2-rich gas mixture obtained for instance by steam reforming of a hydrocarbon fuel:

$$CH_4 + H_2O \rightarrow CO + 3\,H_2$$

usually contains by-products, mainly CO in the range of concentrations of typically ~1 vol%, even after the water-gas shift reaction:

$$CO + H_2O \rightarrow CO_2 + H_2$$

Unfortunately this small amount of CO present in the reformed gas mixture poisons the active sites of a catalyst, for instance, the electrodes of a fuel cell. Among the many approaches selective catalytic oxidation ($CO + \frac{1}{2}\,O_2 \rightarrow CO_2$) has been found to be the most effective way to remove the trace amount of CO from hydrogen. An efficient CO oxidation catalyst is thus necessary. It should be highly selective, because H_2 oxidation should be minimized, and the catalyst must be resistant to CO_2 and H_2O deactivation. In ongoing research efforts, supported noble metal catalysts on transition metal oxides show interesting performances.

Temperature dependence of CO conversation rate: catalyst for automobile exhaust gas treatment Pt/CeO_2

Platinum (Pt) nanoparticles supported on CeO_2 (Pt/CeO_2) are currently used as a component in three-way catalysts for automobile exhaust gas treatment and Pt/CeO_2 shows catalytic activity for CO oxidation.

CO conversion over the Pt/CeO_2 catalysts increases rapidly at around 40°C (see Figure 9). As the temperature increases starting from room temperature (RT) in CO/air, the round Pt nanoparticles become partially faceted (see Figure 10). By comparing the shape of Pt nanoparticles under various conditions, it is possible to understand the mechanism for the shape change, and thereby the CO conversion rate which is dependent on temperature. It is proposed that the change in shape of the Pt nanoparticles is induced by the adsorption of CO molecules and O atoms.

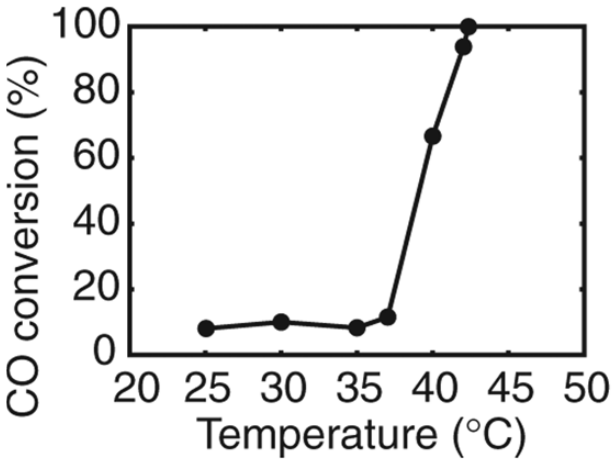

Figure 9. CO conversion over Pt/CeO_2 catalysts as a function of temperature.

Ref. H. Yoshida, et. al., Applied Physics Express 4 (2011) 065001. DOI: 10.1143/APEX.4.065001

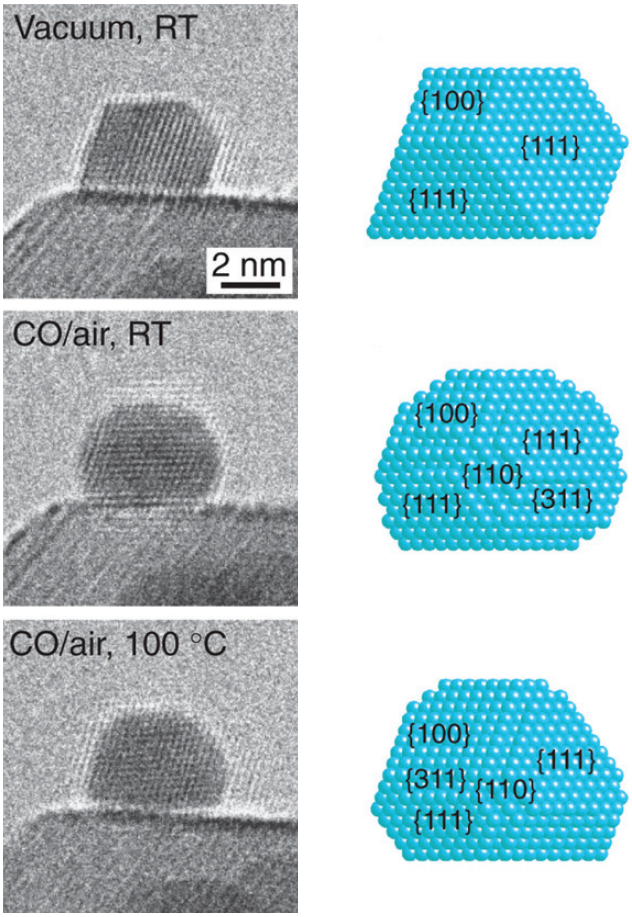

Figure 10. ETEM images of a Pt nanoparticle supported on CeO_2 in vacuum at RT and under realistic reaction conditions: at 1 mbar CO/air at RT (when the catalytic activity is low) and at 1 mbar CO/air at 100°C (when the catalytic activity is high). The corresponding three-dimensional atomic models of the Pt nanoparticle are based on the ETEM images and Wulff constructions.

Ref. H. Yoshida, et. al., Applied Physics Express 4 (2011) 065001. DOI: 10.1143/APEX.4.065001

NOTE: Certain gases may be not approved for use with the ETEM or their use may be restricted. Please contact Thermo Fisher Scientific for additional information on approved gases and our gas approval process.

Catalytic low temperature CO oxidation: CO oxidation at room temperature—catalyst Au/CeO_2

Bulk gold, as a noble metal, is rather unreactive, but gold nanoparticles behave much differently. Particularly surprising is the catalytic activity of gold clusters/nanoparticles supported on various metal oxides. For example, gold, when supported in the form of nanoparticles on crystalline metal oxides such as CeO_2, is quite active towards the conversion of carbon monoxide to carbon dioxide, even at and below ambient temperatures (see Figure 11).

One crucial step of catalytic oxidation is the activation of the oxygen molecule, a cleavage of the O-O bond resulting in the formation of oxygen atoms. Another reaction step is the transfer of the oxygen atom to the carbon monoxide. To understand reaction mechanisms direct visualization of surface facets, surface reconstructions, atoms, and ideally of adsorbed gas molecules is vital (see Figures 12 & 13).

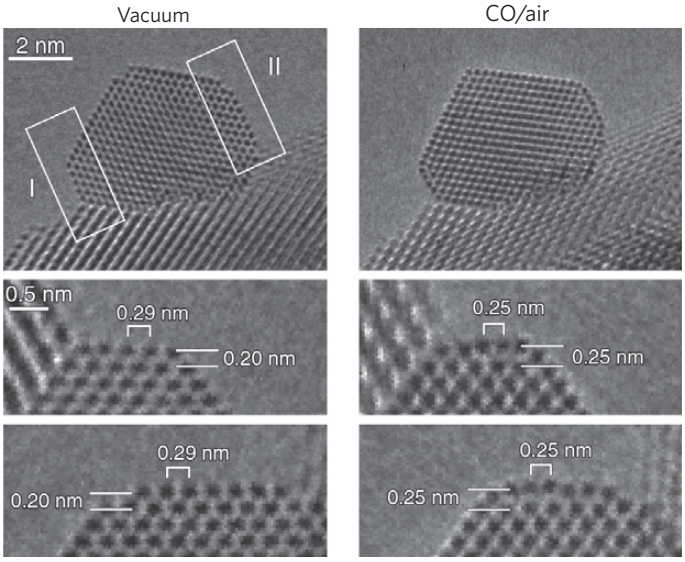

Figure 12. A gold nanoparticle supported on CeO2 in a vacuum and in a reaction environment for CO oxidation (1 volume% CO in air gas mixture at 0.45 mbar at room temperature). Under catalytic conditions the gold nanoparticle exhibits Au {100}–hex reconstructed surface structures. Two {100} facets are present in the rectangular regions indicated by I and II. In vacuum, the distance between the topmost and the second topmost {100} surface layers of 0.20 nm was the same as the interplanar distance of the {200} planes in crystalline bulk gold. In the reaction environment, both the average distance of the adjoining Au atomic columns and the interplanar distance changed to 0.25 nm.

Ref. H. Yoshida, et. al., Science (2012) Vol. 335 no. 6066 317-319 DOI: 10.1126/science.1213194

Ref. T. Uchiyama, et. al., Angew. Chem. 2011, 123, 10339 –10342, DOI: 10.1002/ange.201102487

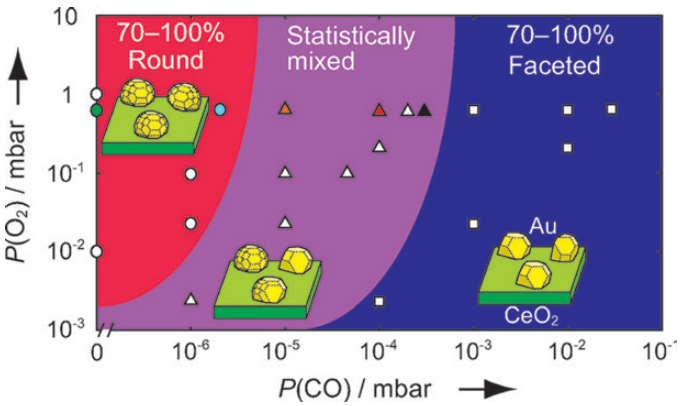

Figure 11. Morphology of gold nanoparticles supported on CeO_2, as a function of the partial pressures of CO and O_2 in CO/air gaseous mixtures. The squares, triangles and circles represent faceted, statistically mixed, and rounded (dynamic multi-faceted) morphologies, respectively.

Ref. T. Uchiyama, et. al., Angew. Chem. 2011, 123, 10339 –10342, DOI: 10.1002/ange.201102487

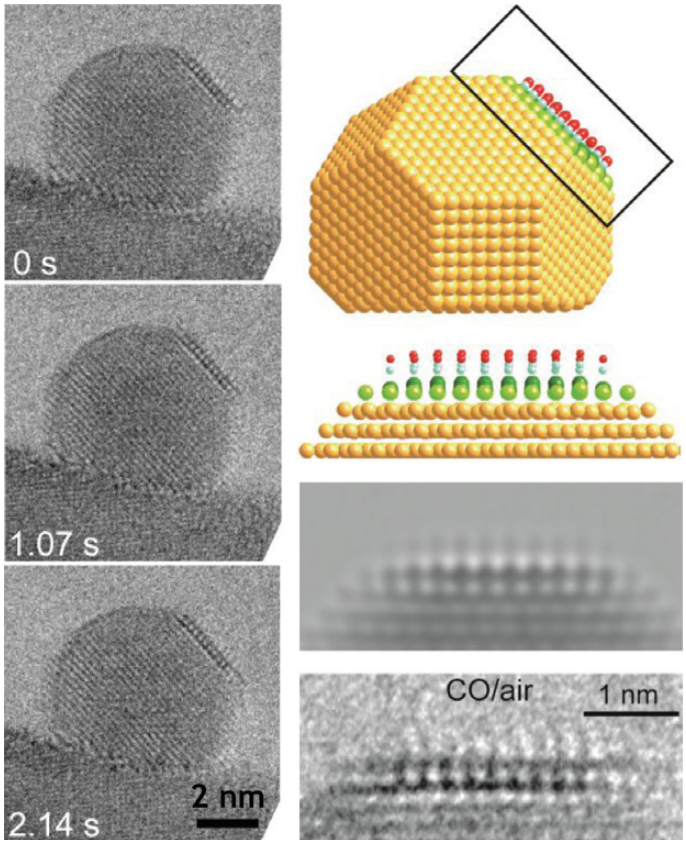

Figure 13. (Left) A gold nanoparticle supported on CeO_2 observed in reaction environment for CO oxidation (1 vol% CO in air gas mixture at 1 mbar at room temperature). An unusual image feature appeared on the upper-right part of the gold nanoparticle. (Right) Gold nanoparticle model with a Au {100}–hex reconstructed surface and adsorbed CO molecules for TEM image calculations. The rectangular area (box) is enlarged and shown just below the model. Comparison between the corresponding calculated TEM image and the experimentally observed image in CO/air confirm the presence of the Au {100}–hex reconstructed surface with adsorbed CO molecules.

Ref. H. Yoshida, et. al., Science (2012) Vol. 335 no. 6066 317-319 DOI: 10.1126/science.1213194

Catalyst deactivation by sintering

Metal nanoparticles dispersed on a porous support materia are used as efficient heterogeneous catalysts for diverse applications in energy conversion, chemical supply, and environmental protection.

However, the high-surface area of the nanoparticles is associated with an excess surface energy, so the nanoparticles represent a meta-stable solid state. Given sufficient thermal activation, the nanoparticles will sinter into larger particles. This coarsening causes an unwanted reduction in the metal surface area, which may affect the catalyst performance.

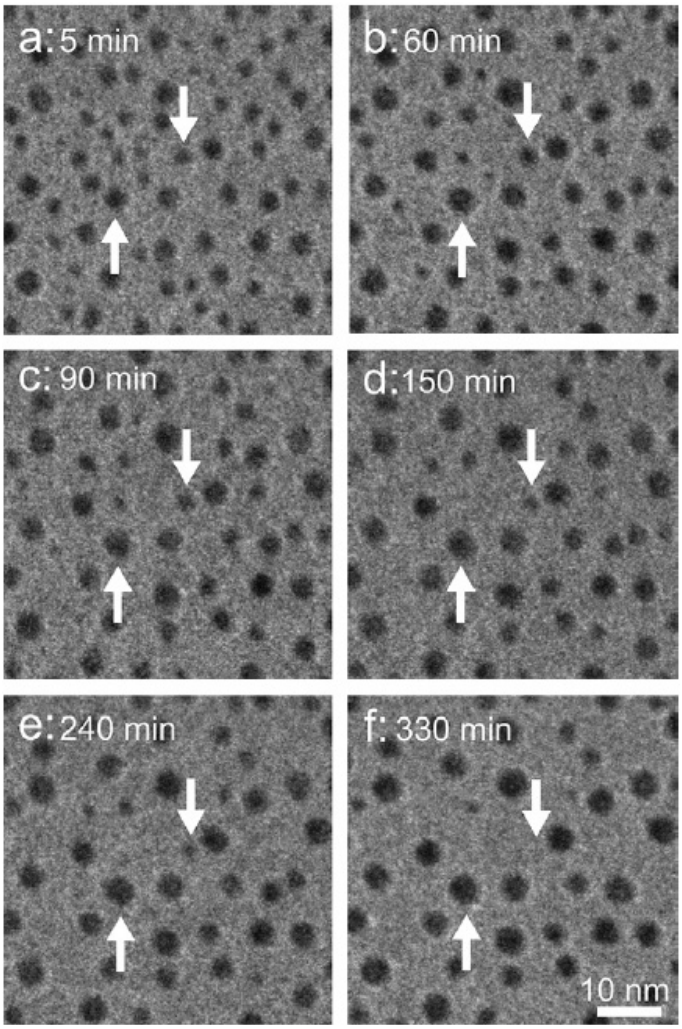

Figure 14. Observations of a Pt/SiO_2 model catalyst during exposure to 10 mbar air at 650°C to reveal unique mechanical and kinetic information on Pt nanoparticle ripening. This information enables a detailed comparison of the temporal evolution of the nanoparticle sizes with predictions made from different ripening models. Arrows indicate examples of a growing and of a decaying particle.

Ref. S. B. Simonsen, et. al., Journal of Catalysis 281 (2011) 147–155

Sintering on supported metal catalysts involves complex physical and chemical phenomena that make the understanding of the mechanisms of sintering difficult. At the microscopic level, the sintering is attributed to the transport of atomic species at surface of the nanoparticle or the support material (see Figures 14 & 15). The specific transport pathways for the atomic species are often considered to reflect the following generic sintering mechanisms:

- particle migration, in which the nanoparticles diffuse over the support and eventually coalesce with other nanoparticles, and;
- atom migration, in which atomic species are emitted from one nanoparticle, diffuse over the support, then attach to another nanoparticle.

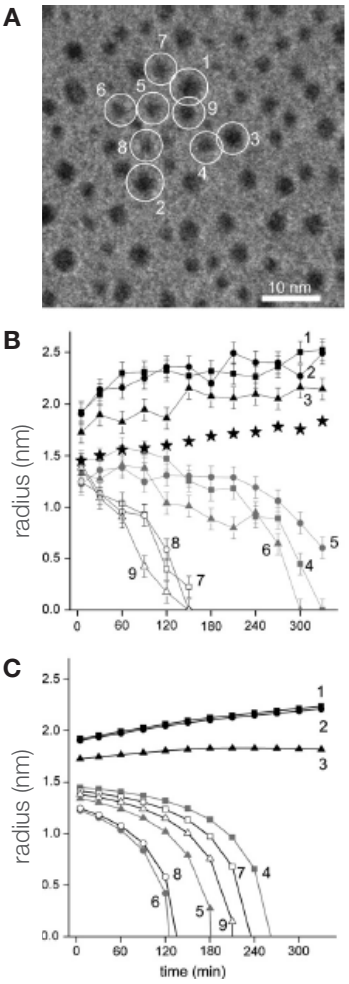

Figure 15. (A) An outline of the nine selected particles (white circles). (B) The particle radii for the particles 1–9 (A) as a function of time in the experiment. The mean radius for the whole TEM image (stars) is also presented. (C) Calculated time-dependent particle radii for the particles 1–9. The calculations used the interface-controlled ripening model based on the mean-field assumption.

Ref. S. B. Simonsen, et. al., Journal of Catalysis 281 (2011) 147–155

NOTE: Certain gases may be not approved for use with the ETEM or their use may be restricted. Please contact Thermo Fisher Scientific for additional information on approved gases and our gas approval process.

Reduction–oxidation cycle: SOFC fuel cell anode

A fuel cell is an energy conversion device that converts chemical energy from a fuel into electricity through an electrochemical reaction. The most commonly used fuel for this purpose is hydrogen (H_2) gas, but hydrocarbons such as natural gas and alcohols (e.g. methanol) can also be used.

Solid oxide fuel cells (SOFC) are a class of fuel cell characterized by the use of a solid oxide material as the electrolyte. Advantages of SOFCs include flexibility of the used fuel, for example CO, H_2, CH_4 (see **Figure 16**), delocalization of energy production, reduction of pollutants such as mono-nitrogen oxides (NOx) and sulfur oxides (SOx). SOFCs also offer high efficiency, long-term stability, low emissions, and relatively low cost.

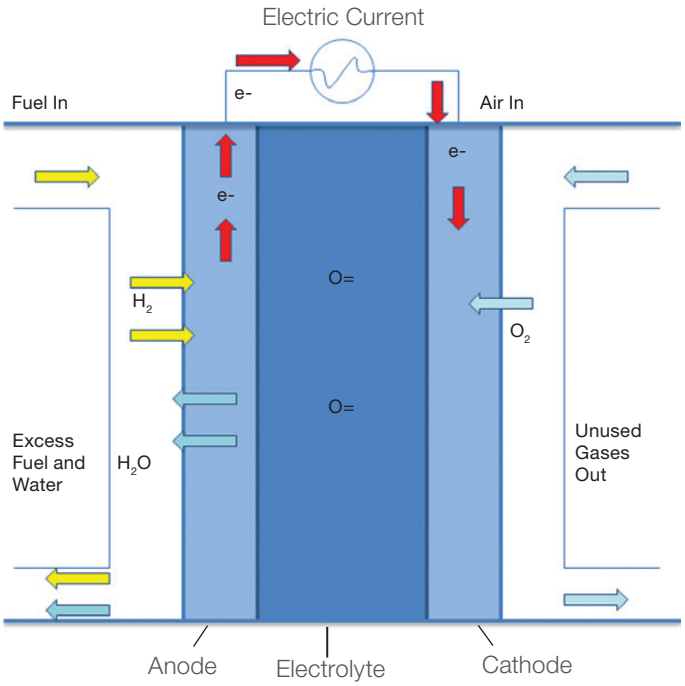

Figure 16. Reduction–oxidation cycle in a SOFC fuel cell anode.

A standard solid oxide fuel cells design is based on an anode made of porous ceramic–metal composite yttria(Y_2O_3) stabilized zirconia (YSZ) and nickel (Ni) (see **Figure 17**).

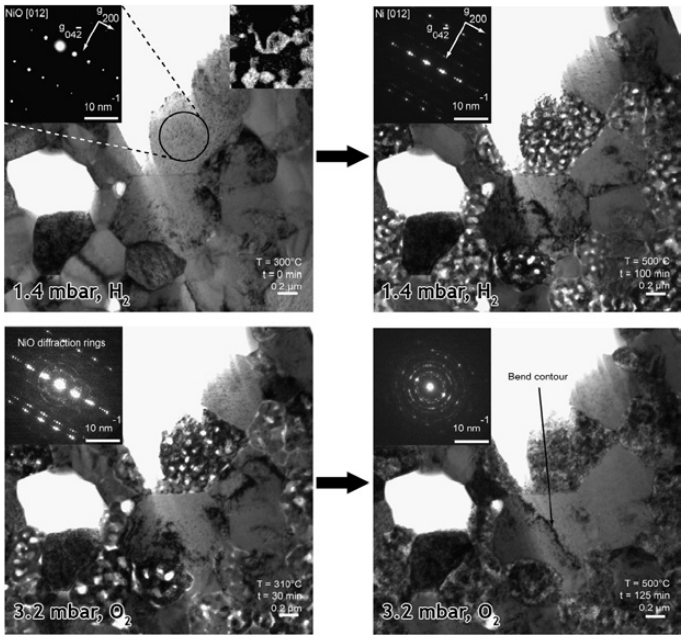

Figure 17. Understanding decreasing performance behaviors of the fuel cells due to structural changes on the anode. Evolution of the microstructure of the fuel cell anode made of yttria(Y_2O_3)-stabilized zirconia (YSZ) and nickel oxide (NiO) during *in situ* reduction and reoxidation. (Upper images) *In situ* reduction of a NiO–YSZ anode precursor in 1.4 mbar of H_2. Nanoporosity is observed to form in the NiO grains to accommodate the volume shrinkage that results from the reduction of NiO to Ni. (Lower images) *In situ* reoxidation in 3.2 mbar O_2. With increasing temperature, the nanoporosity that was created during *in situ* reduction is filled now by polycrystalline NiO. This occupies a larger volume than that of the as-sintered grains. Stress is observed in the YSZ phase, accumulating over successive redox cycles.

Ref. Q. Jeangros, et. al., Acta Materialia 58 (2010) 4578–4589

Diesel automotive exhaust clean-up: soot oxidation

Carbonaceous nanoclusters, such as soot particles from the exhaust of diesel-driven engines, have an influence on our climate and also pose potential health risks. The awareness of soot abatement is increasing due to new environmental legislation for exhaust specifications.

Soot particles could be reduced either by optimizing the combustion inside the engine or by removing the carbonaceous particles from the gaseous exhaust stream. These particles can be removed using a particulate filter. One approach to effectively regenerate the filters onboard is to functionalize the filters for catalytic oxidation of the deposited soot. Ceria(CeO_2)-based materials are widely adopted for this purpose and have been the subject of several investigations (see Figures 18 & 19).

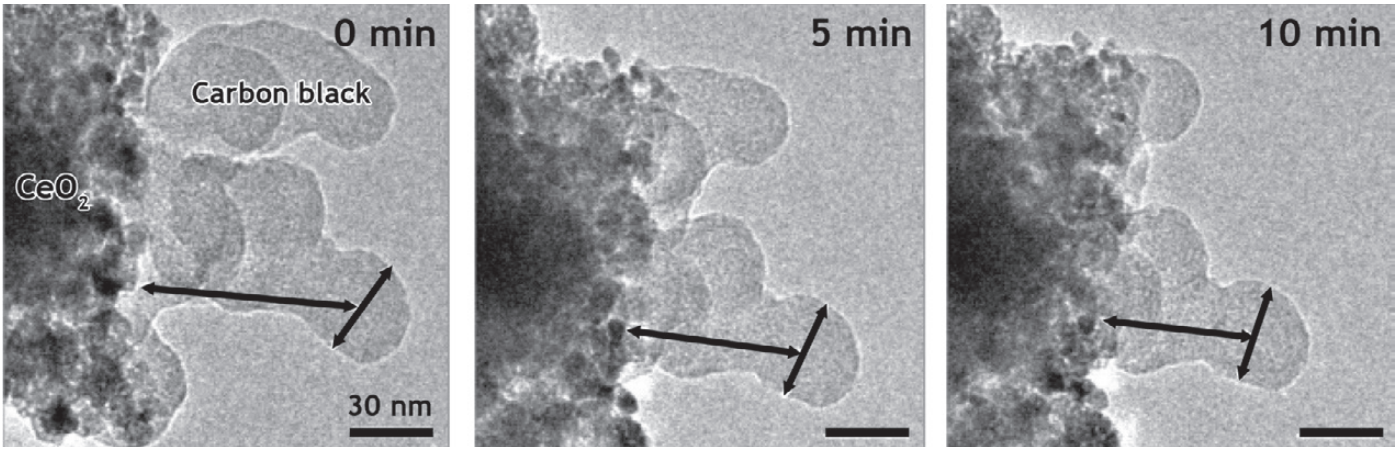

Figure 18. In situ study of the oxidation of an agglomerate of carbon black particles (diesel soot) attached to CeO_2 by exposure to 2 mbar O_2 at 475°C. The constant diameter of a carbon black particle, not the. reduction of the carbon black–CeO_2 distance indicates that the oxidation occurs near the CeO_2 surface.

Ref. S. B. Simonsen, et. al., Journal of Catalysis 255 (2008) 1–5

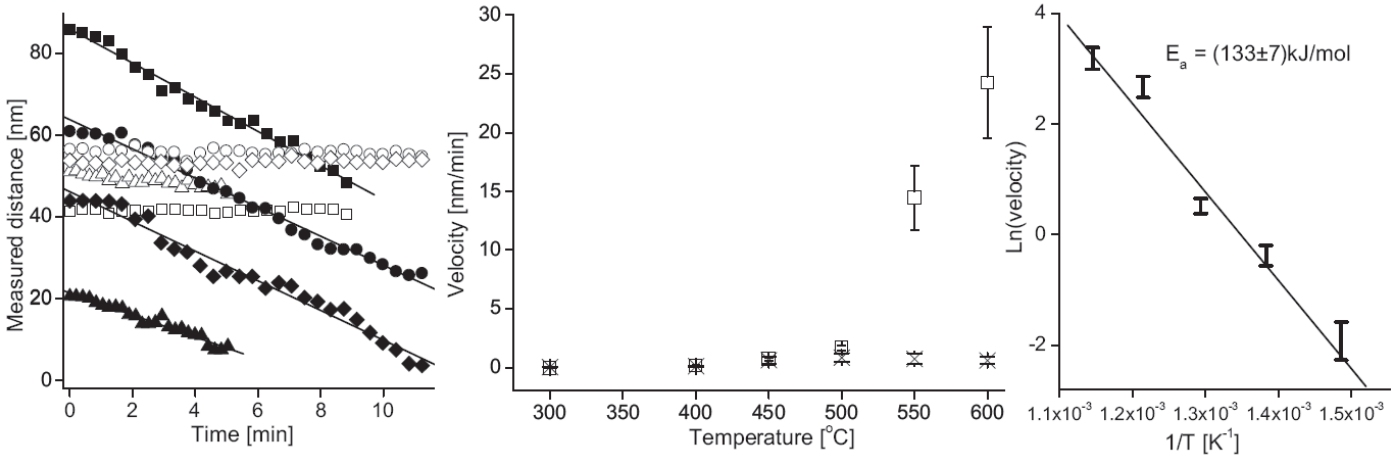

Figure 19. Several carbon black particles have been monitored and their diameter and their distance to the catalyst have been mapped out. (Left) Diameters (open symbols) of different carbon black particles particles and distances from the particle centers to the catalyst edge (filled symbols) as a function of time during exposure to 2 mbar O_2 at 475°C. (Middle) The mean velocity of carbon black particles relative to CeO_2 (□) and Al_2O_3 (×) presented for different temperatures. For each temperature, the average velocity and the standard deviation are obtained from observations of 10 particles in different agglomerates. (Right) Arrhenius plot of the mean velocities between carbon black particles relative to CeO_2.

Ref. S. B. Simonsen, et. al., Journal of Catalysis 255 (2008) 1–5

NOTE: Certain gases may be not approved for use with the ETEM or their use may be restricted. Please contact Thermo Fisher Scientific for additional information on approved gases and our gas approval process.

thermo scientific

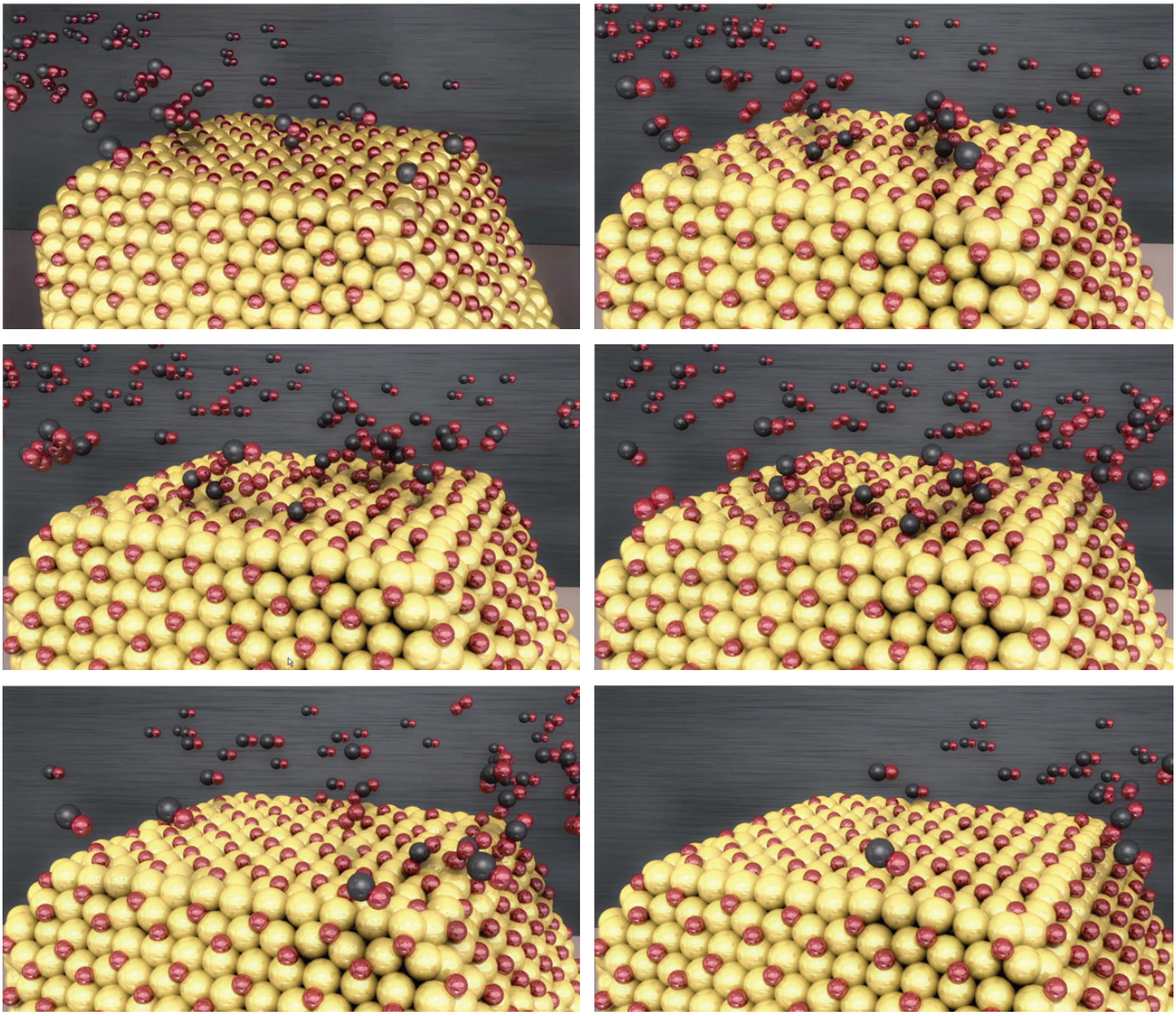

Find out more at **thermofisher.com/EM-Sales**

ThermoFisher SCIENTIFIC

APPLICATION NOTE AN52615

Analysis of electrode materials for lithium ion batteries

Author
Tim Nunney
Thermo Fisher Scientific
East Grinstead, West Sussex, UK

Keywords
K-Alpha, Nexsa, air-sensitive, anode, cathode, electrodes, inert transfer, Li-ion battery, lithium, NMC, vacuum transfer

Description

The Thermo Scientific™ Nexsa™ XPS System was used to analyze the surface of lithium-ion battery electrodes. Due to the air-sensitive nature of these materials, the Nexsa vacuum transfer module was used to safely transport the samples from a glove box to the instrument without exposure to ambient atmosphere. This ensured that the surface was as representative of the electrode material as removed from the cell.

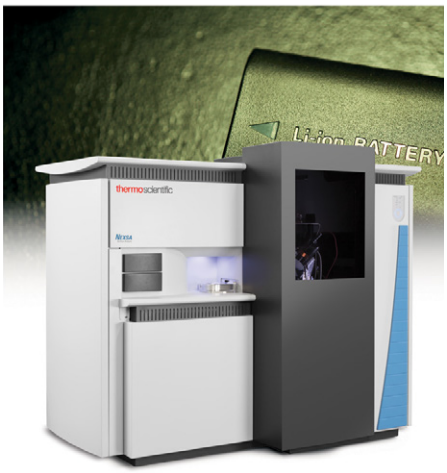

Introduction

For a large number of applications, from automobiles to portable electronics, lithium-ion battery assembles have become the energy storage solution of choice. Lithium ion (Li-ion) battery cells are lightweight compared to other battery technology, which makes them appropriate for transport applications when combined with their relatively high energy density, and can mitigate against their higher cost. Further improving the performance of Li-ion cells, for example to increase energy density, reduce weight, decrease costs, and improve recharge times, involves developing improvements to at least one of the core components of the cell, shown in Figure 1.

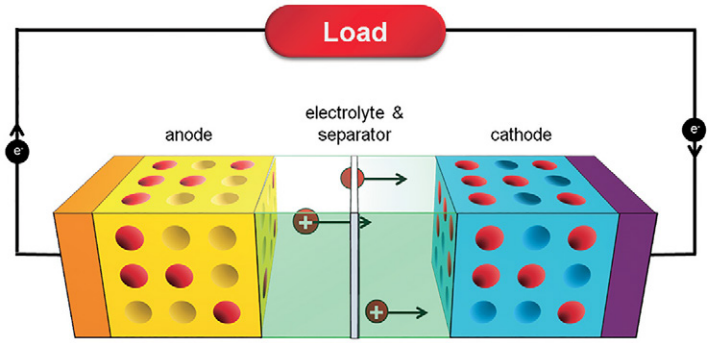

Figure 1: Li-ion cell in operation

When operating, lithium stored in the anode is oxidized, and the Li^+ ions created transport through the electrolyte and separator film to the cathode. In the cathode, it is the anion that is oxidized, creating a compound that can store the arriving lithium ions. When the cell is recharged after use, the flow of ions is in the opposite direction, and they are reduced back to lithium metal to be stored in the anode. The anode is typically made from graphite, with lithium intercalated into the graphite structure. The cathode is comprised of a lithium metal oxide, the exact composition of which varies depending upon the required characteristics of the cell. The most commonly used cathode materials are $LiCoO_2$ (LCO – lithium-cobalt), $LiMn_2O_4$ (LMO – lithium-manganese), $LiFePO_4$ (LFP – lithium-phosphate), and $Li(NiMnCo)O_2$ (NMC – nickel manganese cobalt). These oxides change in stoichiometry depending on whether the cell is charged or discharged; i.e., if the flow of Li^+ is to or from the cathode.

ThermoFisher SCIENTIFIC

A by-product of the charge and discharge process is the formation of the solid-electrolyte interphase (SEI) layer on the anode. The formation and development of the SEI layer competes with the reversible lithium intercalation process, and over the lifetime of the battery the presence of the SEI will contribute to the lowering of capacity, and is a contributing factor to the ultimate failure of the cell. Understanding the SEI layer is an area of significant interest, so that it can be controlled and therefore improve cell performance. XPS depth profiling offers a way of chemically characterizing the complex mix that makes up the interphase layer, allowing an identification of the chemistries that comprise the SEI.

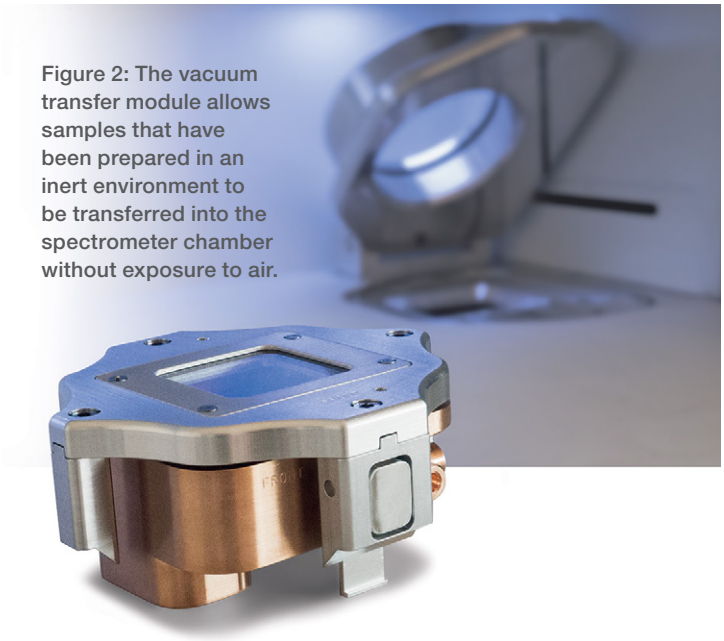

Figure 2: The vacuum transfer module allows samples that have been prepared in an inert environment to be transferred into the spectrometer chamber without exposure to air.

Method or experiment

Lithium is very sensitive to air and moisture, and so to analyze the electrode materials successfully it needs to be introduced into the XPS system without air exposure. To do this, the samples are loaded into the Vacuum Transfer Module (VTM) in a glove box. The VTM (Figure 2), compatible with the K-Alpha and Nexsa instruments, is evacuated in the glove box antechamber, and then transported to the XPS system. As the VTM is held together by air pressure, it automatically opens during the pump-down cycle in the system load-lock and is therefore integrated into the standard, automated, sample transfer process.

In these experiments, two cathode samples were investigated. One sample was a pristine, unused sample; the other sample was from a cell that had been through several chargedischarge cycles, and was in a charged state when the cell was disassembled.

Results

Survey spectra collected from the as received cathode samples are shown in Figure 3. The cathode material is $Li(Ni_xMnyCoz)O_2$, prepared using a binder medium to hold the material together. The binder is a mixture of fluorine and oxygen containing polymers, and for the pristine sample is evident as a significant amount of residue on the surface. This could be important during the first use of the cathode, if the binder residue is mobile in the electrolyte, or reacts to begin the formation of a surface layer which impedes ion transport.

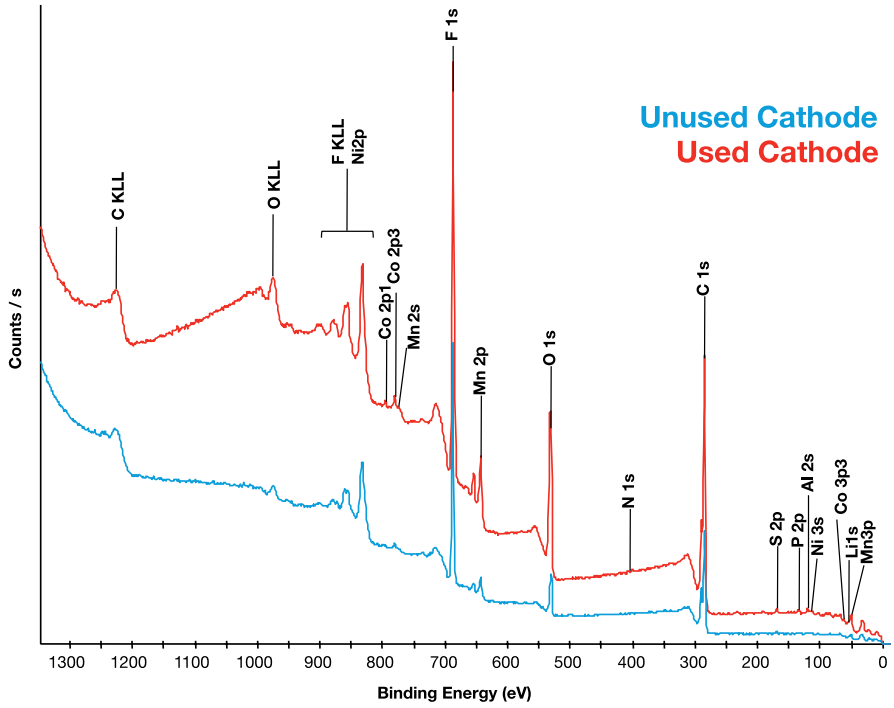

Figure 3: Survey spectra from pristine cathode (blue) and cycled cathode (red) samples

The cycled cathode still shows the presence of the binder, and also evidence of residue from the electrolyte at the surface. Figure 4 shows the variation in the NMC components of the two samples (excluding oxygen). The relative intensities of the Ni, Mn, and Co components are very similar between the two samples, but the amount of Li detected is around 40% of that seen in the pristine cathode. This is as expected in a sample from a charged cell, where the Li ion transport has been towards the anode and away from the cathode, resulting in a depleted level of lithium in the cathode.

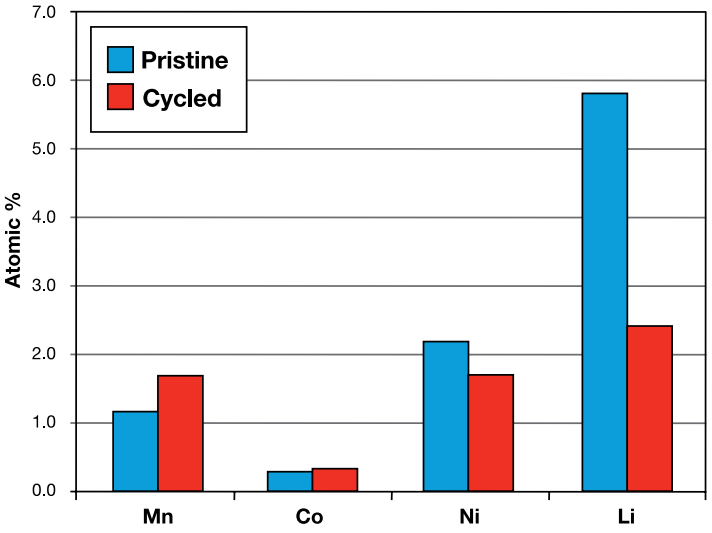

Figure 4: Composition variation for the NMC components

Summary

By using the vacuum transfer module and the Nexsa XPS System it is possible to analyze Li-ion battery components. Analysis of unused and cycled cathode samples determined the expected variation in lithium content.

Acknowledgements

We would like to thank Dr. Harry Meyer III (HTML, Oak Ridge National Lab., TN, USA), Dr. David Wood III, and Dr. Debasish Mohanty (NTRL, Oak Ridge National Lab., TN, USA) for the supply of samples, facilities and help with this analysis.

Application note | 70399

Ion chromatography

Determination of tetrafluoroborate, perchlorate, and hexafluorophosphate in a simulated electrolyte sample from lithium ion battery production

Authors

Thunyarat Phesatcha[1], Suparerk Tukkeeree[1], Jeff Rohrer[2]

[1]Thermo Fisher Scientific, Bangkok, Thailand;

[2]Thermo Fisher Scientific, Sunnyvale, CA, USA

Keywords

lithium ion batteries, aging, ion chromatography, electrolytes, ionic liquids

Introduction

Lithium ion batteries are commonly used in portable consumer electronic devices. The electrolyte solution in these batteries consists of a lithium salt in an organic solvent. Commonly used salts are lithium hexafluorophosphate ($LiPF_6$), lithium perchlorate ($LiClO_4$), lithium tetrafluoroborate ($LiBF_4$), lithium hexafluoroarsenate ($LiAsF_6$), lithium hexafluorosilicate ($LiSiF_6$), and lithium tetraphenylborate ($LiB(C_6H_5)_4$). Some organic solvents used in the electrolyte solution are ethylene carbonate, diethyl carbonate, dimethyl carbonate, ethyl methyl carbonate, propylene carbonate, methyl formate, methyl acrylate, methyl butylate, and ethyl acetate. The electrolyte in lithium batteries may have a mixture of these lithium salts and organic solvents. The electrolyte's concentration in the solvent ranges from 0.1 to 2 mol/L, with an optimal range of 0.8–1.2 mol/L. The anions of the added lithium salts can be determined by ion chromatography (IC) to ensure that the solutions have been prepared at the proper concentrations.

Here, the authors prepare simulated samples that contain either lithium tetrafluoroborate, lithium perchlorate, or lithium hexafluorophosphate in an equal mixture of ethylene carbonate, diethyl carbonate, and propylene carbonate, and demonstrate that the anionic content can be determined accurately using a Reagent-Free™ IC (RFIC™) system. The RFIC system allows the analyst to avoid the problems encountered in eluent preparation. The RFIC system also delivers excellent retention time reproducibility for easy and reproducible quantification in the analysis of lithium ion battery electrolyte solutions.

Equipment

- Thermo Scientific™ Dionex™ ICS-3000* system:
  - DP Dual Pump
  - DC Detector/Chromatography module with dual-temperature zone equipped with 6-port valve
- EG Eluent Generator module
- Thermo Scientific™ Dionex™ Chromeleon™ Chromatography Data System Software Version 6.80 SR7

*This application can be conducted with any Dionex RFIC system.

Reagents and standards

- Deionized water (DI), Type I reagent grade, 18 MΩ-cm resistivity or better
- Lithium tetrafluoroborate ($LiBF_4$, Sigma-Aldrich)
- Lithium perchlorate ($LiClO_4$, Sigma-Aldrich)
- Lithium hexafluorophosphate ($LiPF_6$, Sigma-Aldrich)
- Ethylene carbonate, 98% ($C_3H_4O_3$, Sigma-Aldrich)
- Diethyl carbonate, 99% ($C_5H_{10}O_3$, Sigma-Aldrich)
- Propylene carbonate ($C_4H_6O_3$, Sigma-Aldrich)

Chromatographic conditions	
Columns:	Thermo Scientific™ Dionex™ IonPac™ AS20, 4 × 250 mm (P/N 063148)
Guard:	Dionex IonPac AG20, 4 × 50 mm (P/N 063154)
Eluent source:	Thermo Scientific™ Dionex™ EluGen™ EGC II KOH Column (P/N 058900) with Thermo Scientific™ Dionex™ CR-ATC Continuously Regenerated Anion Trap Column (P/N 060477)
Gradient steps:	Potassium hydroxide; 15 mM from –7 to 10 min 15 to 80 mM (Curve 4) from 10 to 13 min and 80 mM from 13 to 26 min
Flow rate:	1.2 mL/min
Sample volume:	10 µL
Column oven:	35 °C
Pressure:	~2200 psi
Detection:	Suppressed conductivity, Thermo Scientific™ Dionex™ ASRS™ 300 Anion Self-Regenerating Suppressor, 4 mm (P/N 060554) Thermo Scientific™ Dionex™ CRD 200 Carbonate Removal Device, 4 mm (P/N 062983), Recycle mode
Suppressor current:	238 mA

Preparation of solutions and reagents

Stock standard solutions

Dissolve 0.093, 0.112, and 0.105 g of lithium tetrafluoroborate, lithium perchlorate, and lithium hexafluorophosphate, respectively, in DI water in separate 100 mL volumetric flasks. Dilute to volume with DI water.

Calibration standard solutions

Prepare mixed calibration standard solutions by diluting a mixture of defined volumes of 1000 mg/L stock standard solutions with DI water in a 10 mL volumetric flask. The volumes of each 1000 mg/L stock standard solution and the prepared calibration standard concentrations are shown in Table 1.

Table 1. Volumes of 1000 mg/L stock standard solutions used to prepare calibration standards at the listed concentrations

Concentration of each Anion (mg/L)	Volume of each 1000 mg/L Stock standard solution (µL)	Final Volume (mL)
5	50	10
10	100	10
20	200	10

Eluent

The eluent generator (EG) produces the eluent using the Dionex EluGen EGC II KOH cartridge and DI water (18 MΩ-cm resistivity or better) supplied by the pump. The eluent concentration is controlled by the Chromeleon Chromatography Data System software. The Dionex EluGen cartridge requires at least 14 MPa (2000 psi) of system backpressure, which ensures optimal removal of electrolysis gas from the eluent produced by the generator. See the Dionex ICS-3000 Operator's Manual (Document No. 065031-04) for instructions on adding backpressure.

Mixture of Three Carbonate Solvents (1:1:1)

Thoroughly mix 10 g each of ethylene carbonate, diethyl carbonate, and propylene carbonate.

Simulated Electrolyte Sample

To simulate samples from lithium ion batteries, prepare three samples. Two samples are 1 M solutions of lithium tetrafluoroborate and lithium perchlorate prepared in the mixture of three carbonate solvents. The third sample is a 1 M solution of lithium hexafluorophosphate prepared in DI water. Later, this sample will be diluted 1:1 with the mixture of three carbonate solvents. This preparation is necessary because lithium hexafluorophosphate does not dissolve in the mixture of three carbonate solvents. Table 2 shows details of the sample preparation for these three samples.

Table 2. Preparation of simulated samples.

Simulated sample	Weight of Lithium Salt (g)	Solvent	Final Volume (mL)
1 M lithium tetrafluoroborate	0.938	Mixture of three carbonate solvents	10
1 M lithium perchlorate	1.068	Mixture of three carbonate solvents	10
1 M lithium hexafluorophosphate	1.519	DI water	10

Sample preparation

Tetrafluoroborate and Perchlorate sample

Dilute 1 M lithium tetrafluoroborate and lithium perchlorate solutions 10,000 times with DI water.

Hexafluorophosphate sample

Mix 1 M lithium hexafluorophosphate with the mixture of three carbonate solvents in a 1:1 ratio. Dilute this solution 5,000 times with DI water.

Results and discussion

Chromatography

The analyte anions in this application—perchlorate, tetrafluoroborate, and hexafluorophosphate—are classified as polarizable anions. These anions tend to be strongly retained and have poor peak shapes with typical anion-exchange columns. With anion-exchange columns, analysts often include organic additives in the eluent (for example, p-cyanophenol) to improve the peak shapes of polarizable anions. This is undesirable because it increases eluent costs, eluent complexity, waste disposal costs, and decreases detection sensitivity. To address this problem, we designed the Dionex IonPac AS16 column and later, the IonPac AS20 column. These are high-capacity, hydroxide-selective, anion-exchange columns designed for polarizable anions. The stationary phases in these columns allow easy elution of polarizable anions with good peak shapes while requiring no organic solvent in the eluent. The high capacity allows the determination of polarizable anions in the presence of high concentrations of other anions.

In the analysis presented here, the authors used the Dionex IonPac AS20 column because it has higher column capacity than the AS16 column (310 µeq/column compared to 160); however, the AS16 column can also be used with different hydroxide eluent concentrations. Because both columns can be used with hydroxide eluents, they can be paired with an eluent generator (EG). An EG, the key component of an RFIC system, produces error-free pure hydroxide eluent. This translates to highly reproducible analyte retention times for reproducible determination without the labor involved in manually preparing hydroxide eluents. Figure 1 shows the separation of three mixed standard solutions (used for method calibration) of the three analytes of interest: perchlorate, tetrafluoroborate, and hexafluorophosphate. The three anions were well separated in about 25 min, with the first analyte, tetrafluoroborate, eluting at about 13 min. The first 12 min of the separation were included to allow most common inorganic anions to elute so that they did not interfere with the determination of the three analytes. Tetrafluoroborate eluted between sulfate and phosphate, while perchlorate and hexafluorophosphate eluted after phosphate. Table 3 shows the calibration information for each analyte.

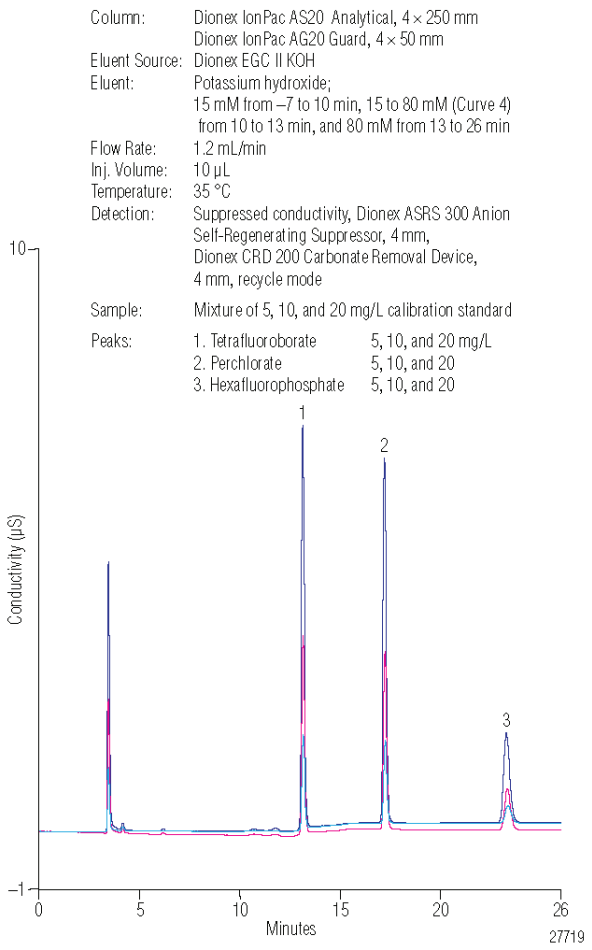

Figure 1. Overlay of chromatograms of the calibration standards

Table 3. Concentrations of calibration standards and the calibration results reported by the Chromeleon software

Analyte	Concentration (mg/L)			Result		
	Level 1	Level 2	Level 3	% Coeff.Det.	Offset (µS*min)	Slope (µS*min)/mg/L
Tetrafluoroborate	5	10	20	100.00	–0.0485	0.0606
Perchlorate	5	10	20	99.99	–0.0597	0.0623
Hexafluorophosphate	5	10	20	99.91	–0.0449	0.0296

Sample Analysis

Here, three simulated lithium ion battery electrolyte samples were prepared. One molar solution each of lithium tetrafluoroborate and lithium perchlorate was prepared in a mixture of three carbonate solvents. One molar lithium hexafluorophosphate was prepared in DI water and then diluted 1:1 with the mixture of three carbonate solvents. The first two samples were diluted 1 to 10,000 and the third sample was diluted 1:5,000 with DI water prior to analysis by IC. Figure 2 shows the chromatography of each of the three samples. The Dionex CRD 200 Carbonate Removal Device was used to eliminate any possible interference from sample carbonate. Short-term reproducibility was measured by making five injections of each sample. The data in Table 4 show good reproducibility for the amount measured in each sample. To judge accuracy, the authors compared measured concentration to the calculated concentration (Table 5) and found that the measured concentration was between 97.4, 104, and 109% of the calculated concentration for perchlorate, hexafluorphosphate, and tetrafluoroborate, respectively. As a second test of accuracy, the simulated samples were spiked with 2 mg/L of the same anion prior to dilution. The data in Table 5 also show good recoveries for each anion, suggesting method accuracy.

Conclusion

This application demonstrates an IC method that uses an RFIC system to easily assay the anions in the simulated lithium ion battery electrolyte samples. The results show that this method is both accurate and reproducible.

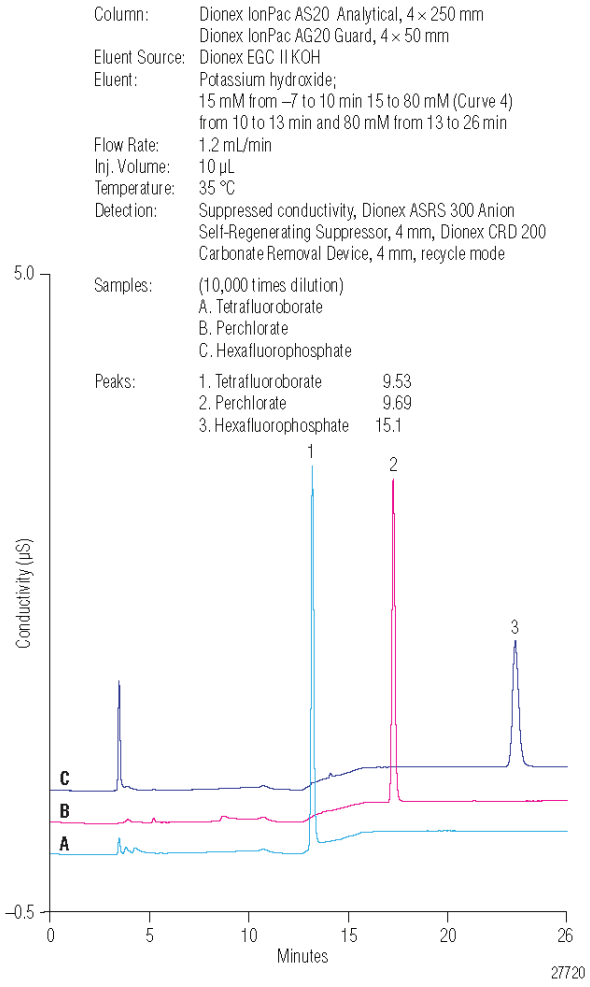

Figure 2. Chromatograms of samples (10,000 times dilution)

Table 4. Assay results for the samples and spiked samples

Injection No.	Amount (mg/L)					
	Tetrafluoroborate		Perchlorate		Hexafluorophosphate	
	Sample	Spiked sample	Sample	Spiked sample	Sample	Spiked sample
1	9.57	11.3	9.74	11.9	15.1	16.7
2	9.45	11.3	9.68	11.9	15.1	16.8
3	9.58	11.1	9.75	11.7	15.1	16.7
4	9.55	11.3	9.69	11.8	15.1	16.8
5	9.48	11.2	9.57	11.8	15.2	16.8
Average	**9.53**	**11.3**	**9.69**	**11.8**	**15.1**	16.8
RSD	**0.62**	**0.55**	**0.74**	**0.64**	**0.30**	**0.26**

Table 5. Assay results for the samples and spiked samples

Ion	Calculated concentration after 10,000 times dilution (mg/L)	Average found concentration (mg/L)	Recovery (%)	Spiked concentration (mg/L)	Average found concentration in spiked sample (mg/L)	Recovery (%)
Tetrafluoroborate	8.70	9.53	109	2	11.3	88.5
Perchlorate	9.95	9.69	97.4	2	11.8	106
Hexafluorophosphate	14.5	15.1	104	2	16.8	85.0

Learn more at **thermofisher.com/ic**

APPLICATION NOTE

Determination of Dissolved Manganese in Lithium/Manganese Oxide Battery Electrolyte

Authors
Chanita Chantarasukon,[1] Suparerk Tukkeeree,[1] and Jeff Rohrer[2]
1Thermo Fisher Scientific, Bangkok, Thailand; [2]Thermo Fisher Scientific, Sunnyvale, CA USA

Key Words
Lithium-Ion Battery, Cathode, Dionex IonPac CS12A Column, Reagent-Free Ion Chromatography System

Introduction

Lithium-ion batteries are widely used in products such as portable consumer electronic devices and electric vehicles. Many different materials are used to make the cathode in lithium batteries, including those that are manganese-, cobalt-, and nickel-based. Lithium-ion batteries that are manganese-based are more environmentally friendly, have a good safety record, and can be made at a lower cost; however, they have a shorter lifetime than other types of lithium-ion batteries. One of the reported causes of lifetime loss is the dissolution of manganese from the cathode into the electrolyte during cycling (i.e., charging/discharging). Lithium/lithium manganese oxide ($Li/LiMn_2O_4$) is a type of battery that has a manganese-based cathode.

In Thermo Scientific Application Note (AN) 258, ion chromatography (IC) was applied to determine the anions tetrafluoroborate, perchlorate, and hexafluorophosphate in a simulated electrolyte solution for lithium-ion batteries.[1] AN 258 used a Reagent-Free™ IC (RFIC™) system, and it is also possible to use an RFIC system to determine manganese in a simulated electrolyte solution for lithium-ion batteries. There is one report of an IC method that uses manually prepared eluents and direct conductivity detection to determine dissolved manganese in the electrolyte of a $Li/LiMn_2O_4$ battery.[2] However, that method has poor sensitivity, which is inherent with direct conductivity detection. Even with a three-component (tartaric acid, dipicolinic acid, and ascorbic acid) mobile phase, the manganese peak exhibits extreme tailing on the chosen column. A better IC cation column will improve peak shape and therefore improve integration precision and method accuracy, while suppressed conductivity detection will improve method sensitivity.

The work shown here uses an RFIC system with suppressed conductivity detection to quantify dissolved manganese in the simulated electrolyte of a $Li/LiMn_2O_4$ battery. The method uses the Thermo Scientific™ Dionex™ IonPac™ CS12A column set, which was designed to deliver good peak shapes for cations such as manganese(II) (Mn^{2+}), with a simple methanesulfonic acid (MSA) eluent produced by an eluent generator. The combination of the RFIC system and a quality IC column yields a method that is sensitive, accurate, reproducible, and easy to execute, requiring only the addition of deionized water to the RFIC system.

Goal

To develop an IC method that accurately determines dissolved manganese in the electrolyte of a Li/LiMn2O4 battery using an RFIC system

ThermoFisher SCIENTIFIC

Equipment

- Thermo Scientific Dionex ICS-2100 Integrated RFIC system,* including a Thermo Scientific Dionex AS-AP Autosampler
- Thermo Scientific™ Dionex™ Chromeleon™ Chromatography Data System (CDS) software version 6.80, SR9 or higher

*Any Thermo Scientific RFIC system may be used.

Reagents and Standards

- Deionized (DI) water (H_2O), Type I reagent grade, 18 MΩ-cm resistivity or better
- Ethylene Carbonate ($C_3H_4O_3$), 99% (Fisher Scientific P/N 50-700-5617)
- Ethyl Methyl Carbonate ($C_4H_8O_3$), 99% (Sigma-Aldrich® P/N 754935)
- Vinylene Carbonate ($C_3H_2O_3$), 97% (Fisher Scientific P/N 50-751-1840)
- Lithium Hexafluorophosphate ($LiPF_6$), 98% (Fisher Scientific P/N 21324-40-3)
- Manganese(II) Sulfate, Monohydrate ($MnSO_4.H_2O$) (Fisher Scientific P/N 10034-96-5)

Preparation of Solutions and Reagents

Mixture of Ethylene Carbonate and Ethyl Methyl Carbonate, 1:1 (w/v)

Dissolve 10 g of ethylene carbonate in 10 mL of ethyl methyl carbonate.

Manganese Stock Standard Solution, 1000 mg/L

Place 0.308 g of manganese(II) sulfate monohydrate in a 100 mL volumetric flask, dissolve in DI water, bring to volume with DI water, and mix.

Working standard solution

Add the appropriate volumes of 1000 mg/L manganese stock standard solution into separate 100 mL volumetric flasks, bring to volume with DI water, and mix. The volumes of manganese stock standard solution used for the preparation of working standard solutions are shown in Table 1.

Level	Volume of Manganese Stock Solution (1000 mg/L) Used for a 100 mL Preparation (mL)	Concentration (mg/L)
1	0.010	0.10
2	0.020	0.20
3	0.040	0.40
4	0.080	0.80
5	0.100	1.00

Table 1. Preparation of working standards.

Sample Preparation

Preparation of a Simulated Sample

Prepare 1.12 M of LiPF6 and 2 wt % of vinylene carbonate in the mixture of ethylene carbonate and ethyl methyl carbonate by placing 1.7 g of LiPF6 and 0.2 g of vinylene carbonate in a 10 mL volumetric flask; dissolve, then bring to volume with the mixture of ethylene carbonate and ethyl methyl carbonate. Prepare a 1 to 50 dilution of this simulated sample using DI water prior to injection. This is the same dilution used in the published method.2

Spiked Sample Simulation

Prepare 5 mg/L of manganese, 1.12 M of LiPF6, and 2 wt % of vinylene carbonate in the mixture of ethylene carbonate and ethyl methyl carbonate by placing 1.7 g of LiPF6, 0.2 g of vinylene carbonate, and 50 µL of 1000 mg/L manganese stock standard solution in a 10 mL volumetric flask; dissolve, then bring to volume with the mixture of ethylene carbonate and ethyl methyl carbonate. Prepare a 1 to 50 dilution of this spiked simulated sample using DI water prior to injection.

Chromatographic Conditions

Columns:	Dionex IonPac CG12A Guard, 4 × 50 mm (P/N 046074) Dionex IonPac CS12A Analytical, 4 × 250 mm (P/N 046073)
Eluent Source:	Thermo Scientific Dionex EGC III MSA Eluent Generator Cartridge (P/N 074535) with Thermo Scientific Dionex CR-CTC II Continuously Regenerated Cation Trap Column (P/N 066262)
Eluent Concentration:	20 mM MSA
Flow Rate:	1.0 mL/min
Inj. Volume:	20 µL
Temperature:	35 °C
Detection:	Suppressed Conductivity, Thermo Scientific™ Dionex™ CSRS™ 300 Cation Self-Regenerating Suppressor, 4 mm (P/N 064556), Recycle Mode, Current 60 mA
Total Conductivity:	~0.34 µS

Analyte	Concentration (mg/L)					Calibration Results			
	Level 1	Level 2	Level 3	Level 4	Level 5	Points	r^2	Offset	Slope
Manganese	0.1	0.2	0.4	0.8	1.0	15	0.9997	-0.0046	0.1617

Table 2. Working standard concentrations and calibration results.

Results and Discussion

Separation

Manganese is a divalent cation that can be separated from six common cations using the Dionex IonPac CS12A column set with isocratic elution. As shown in Figure 1, manganese is well separated from the other common divalent cations—magnesium and calcium—using a 20 mM MSA eluent. Figure 1 also shows that manganese is well resolved from other common cations. Note the good peak shape for manganese and the other cations. The MSA eluent is automatically produced by pumping DI water through the eluent generator cartridge with the concentration controlled by Chromeleon CDS software.

Method Calibration

The method was calibrated before sample analysis using five concentrations of manganese ranging from 0.1 to 1.0 mg/L. The method showed a linear relationship between analyte concentration and peak area of manganese. The coefficient of determination (r2) for the line was 0.9997. Figure 2 shows the overlay of chromatograms of the working (calibration) standards, and Table 2 shows the concentrations of the working standards and the calibration result. Note that a 20 µL injection of the 0.1 mg/L standard produced a peak of significant size and good peak shape, whereas the nonsuppressed method in Reference 2 produced a small tailing peak for a 1 mg/L standard (though only a 10 µL injection). This highlights the expected sensitivity benefit of using suppressed rather than nonsuppressed conductivity detection.

Columns: Dionex IonPac CS12A Guard, 4 × 50 mm
Dionex IonPac CG12A Analytical, 4 × 250 mm
Eluent Source: Dionex EGC III MSA Cartridge with Dionex CR-CTC Column
Eluent: 20 mM MSA
Flow Rate: 1.0 mL/min
Inj. Volume: 20 µL
Temperature: 35 °C
Detection: Suppressed Conductivity, Dionex CSRS 300 Suppressor, 4 mm, Recycle mode, Current 60 mA
Sample: Standard Mixture

Peaks:		
	1. Lithium	1.0 mg/L
	2. Sodium	1.0
	3. Ammonium	1.0
	4. Potassium	1.0
	5. Magnesium	1.0
	6. Manganese	1.0
	7. Calcium	1.0

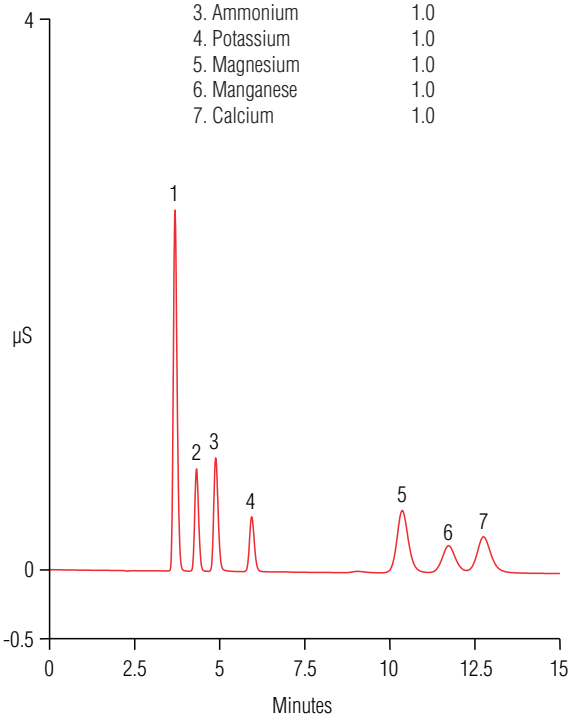

Figure 1. Chromatogram of a standard containing six common cations and manganese.

Columns: Dionex IonPac CS12A Guard, 4 × 50 mm
Dionex IonPac CG12A Analytical, 4 × 250 mm
Eluent Source: Dionex EGC III MSA Cartridge with Dionex CR-CTC Column
Eluent: 20 mM MSA
Flow Rate: 1.0 mL/min
Inj. Volume: 20 µL
Temperature: 35 °C
Detection: Suppressed Conductivity, Dionex CSRS 300 Suppressor, 4 mm, Recycle mode, Current 60 mA
Sample: Calibration Standard

Peak:		
	1. Manganese	0.1, 0.2, 0.4, 0.8, and 1.0 mg/L

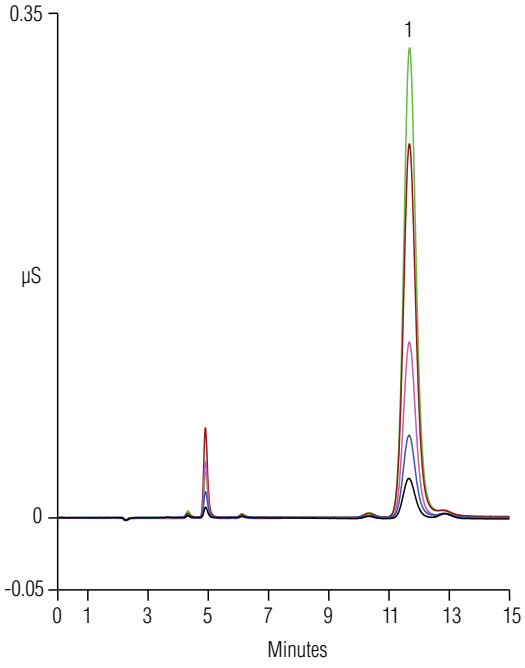

Figure 2. Overlay of chromatograms of the calibration standards.

thermo scientific

Sample Analysis

An electrolyte sample was simulated as described in the Sample Preparation section and diluted 1 to 50 with DI water. Five sample injections were made and, as expected, no manganese was found in the simulated sample. A sample was then prepared to simulate manganese cathode dissolution in the electrolyte. This simulated sample had a manganese concentration of 0.1 mg/L after dilution. Five injections of the diluted spiked simulated sample were made to quantify manganese. The measured concentrations were then compared to the prepared concentration. This analysis yielded a manganese recovery of 103% with an RSD of 0.15% (Table 3).

Figure 3 shows the overlay of chromatograms of the simulated and spiked simulated samples. Note that the magnesium and calcium peaks—eluting before and after manganese, respectively—do not interfere with the quantification of manganese. Overall, the results indicate that this is an accurate and reproducible method for determining manganese in Li/LiMn2O4 battery electrolyte.

Conclusion

This study demonstrates an accurate and reproducible IC method that uses suppressed conductivity detection to determine manganese in the simulated electrolyte of a Li/LiMn2O4 battery. The method uses an RFIC system and requires only 15 min per analysis with a simple isocratic separation using an MSA eluent. The eluent is produced by an eluent generator to preclude the labor and potential error associated with eluent preparation.

References

1. Thermo Scientific Application Note 258: Determination of Tetrafluoroborate, Perchlorate, and Hexafluorophosphate in a Simulated Electrolyte Sample from Lithium Ion Battery Production. Sunnyvale, CA, 2010. [Online] www.dionex.com/en-us/webdocs/88116-AN258-IC-Lithium-Battery-AN70399_E.pdf (accessed Apr. 5, 2013).
2. Doh, C.; Lee, J.; Lee, D.; Jin, B.; Moon, S. The Quantitative Analysis of the Dissolved Manganese in the Electrolyte of Li/LiMn2O4 Cell Using by Ion Chromatography. Bull. Korean Chem. Soc. 2009, 30 (10), 2429–2432.

Columns:	Dionex IonPac CS12A Guard, 4 × 50 mm Dionex IonPac CG12A Analytical, 4 × 250 mm
Eluent Source:	Dionex EGC III MSA Cartridge with Dionex CR-CTC Column
Eluent:	20 mM MSA
Flow Rate:	1.0 mL/min
Inj. Volume:	20 µL
Temperature:	35 °C
Detection:	Suppressed Conductivity, Dionex CSRS 300 Suppressor, 4 mm, Recycle mode, Current 60 mA
Samples:	Sample Spiked Sample
Peak:	1. Manganese 0.1033 mg/L

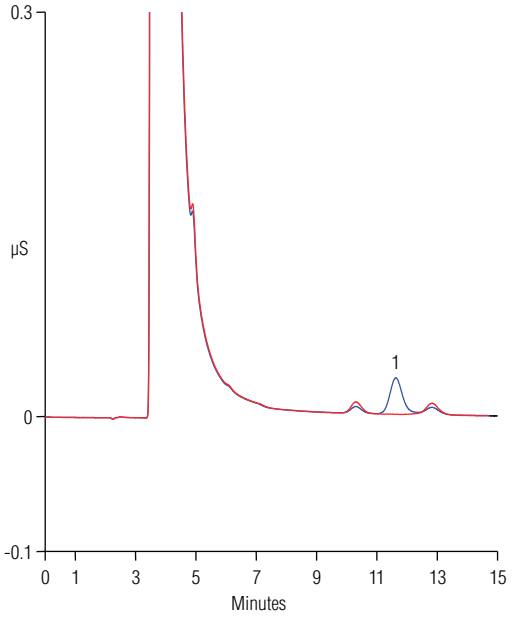

Figure 3. Overlay of chromatograms of unspiked and spiked samples.

Injection No.	Amount in Sample (mg/L)	Amount in Spiked Sample, Spiked Conc 0.1 mg/L (mg/L)
1	ND	0.1030
2	ND	0.1034
3	ND	0.1033
4	ND	0.1034
5	ND	0.1033
Average	ND	**0.1033**
RSD (%)	—	**0.15**
Recovery (%)	—	**103**

Table 3. Sample and spiked sample results.

Find out more at **thermofisher.com/dionex**

ThermoFisher SCIENTIFIC

Application note | 000243

Industrial analysis

Robust and sensitive measurement of trace element impurities in $LiPF_6$ electrolyte solutions using ICP-OES

Authors

Sukanya Sengupta, Bhagyesh Surekar, and Daniel Kutscher

Thermo Fisher Scientific, Bremen, Germany

Keywords

Battery production, ICP-OES, robustness, method validation, sensitivity, limits of quantification, analytical testing

Goal

To demonstrate the capabilities of the Thermo Scientific™ iCAP™ PRO XP ICP-OES Duo for sensitive, robust, fast, and straightforward analysis of trace elements in lithium hexafluorophosphate electrolyte samples

Introduction

Lithium ion (Li-ion) batteries are increasingly being used in electronic devices and electric vehicles (EV). The demand for electric vehicles is expected to grow significantly in the next years, as they can be a viable alternative to fossil fuel driven vehicles and help to rapidly decrease CO_2 emission from traffic. These developments have led to a growing industry demand for Li-ion batteries globally that is complemented by significant efforts in research and development, dedicated to providing efficient and cost-effective solutions[1]. For production, especially in the ramp-up phase, regular and rigorous quality control of all components, including the lithium salt, anode and cathode material, and electrolyte, of an Li-ion battery is crucial. The electrolyte plays an important role in the charging and discharging performance of the battery, and hence needs to be checked for potential impurities. At the same time, the electrolyte is also a sample type that allows the investigation of ageing processes, as degradation products from all components of the battery can accumulate within it over time. Finally, once the battery is at the end of its life, all components must be thoroughly screened to ensure that potential environmental contamination and injury risks to personnel disassembling the batteries are minimized.

One of the most common electrolytes in Li-ion batteries is lithium hexafluorophosphate ($LiPF_6$) dissolved in a binary or ternary mixture of ethylene carbonate (EC) and linear carbonates, such as diethyl carbonate (DEC) and ethyl-methyl carbonate (EMC). It is a popular electrolyte material in the industry due to its high energy density and power properties.[2,3] At the moment, there is only one standard method available for the analysis of electrolytes for lithium-ion batteries, based on the Chinese Standard HGT/ 4067-2015,[4] which requires method detection limits of 1 mg·L^{-1} in the final $LiPF_6$ electrolyte samples. The Thermo Scientific™ iCAP™ PRO ICP-OES Series can be the instrument of choice for this analysis, delivering detection limit performance well within the required range and providing a robust setup that can accurately characterize $LiPF_6$ electrolyte sample materials.

Experimental

Instrument parameters and experimental conditions

An iCAP PRO XP ICP OES Duo instrument was used in this study to carry out measurements of 15 trace elements that may be present as impurities in electrolyte samples. The instrument was operated using intelligent full range (or iFR) mode, allowing a complete screening of the UV as well as the visible part of the spectrum in one single exposure. Due to the sensitivity requirement, the plasma was observed axially.

The nature of the samples, a unique combination of organic solvents with traces of HF formed due to the partial hydrolysis of the PF_6^- anion, demands careful selection of a compatible sample introduction system. Every component must be fully compatible with the chemistry of the sample and the matrix, so an inert nebulizer and spray chamber, as well as a ceramic torch and an alumina-based injector, were used. Details of the sample introduction setup and instrument parameters are listed in Table 1. Use of personal protective equipment, including gloves, laboratory glasses, and coat, while handling the samples is essential. A suitable cover for the autosampler containing the samples is also required.

$LiPF_6$ in organic solvents can be challenging to handle and analyze, particularly over longer measurement sessions spanning several hours. The high carbon content, coming both from the diluent and the organic carbonates present in the matrix, along with the presence of HF, leads to analytical challenges including high background signals, injector blockage, and high plasma load, leading to instability or even extinguishing of the plasma. The optimized experimental parameters developed in this method, together with the inherent robustness of the iCAP PRO Series ICP-OES overcome these challenges and ensure stable, sensitive, and accurate analysis with low sample measurement times. The iCAP PRO XP ICP-OES Duo brings advantages like full flexibility for method development and the option to use the extended UV (or eUV) mode for even more sensitive observation in the UV range, making it an ideal choice of instrument for this method.

Table 1. Instrument configuration and typical operating parameters

Instrument parameter	Setting
Spray chamber	PTFE HF resistant spray chamber
Nebulizer	Burgener PEEK MiraMist™
Center tube	1.0 mm alumina injector
Torch	Demountable ceramic D-Torch
Pump speed	30 rpm
Pump tubes	Phthalate-free Solva orange/white Phthalate-free Solva white/white
Uptake time	70 s
Wash time	70 s
Nebulizer gas flow	0.30 L·min^{-1}
Auxiliary gas flow	0.5 L·min^{-1}
Coolant gas flow	15 L·min^{-1}
RF power	1,250 W
Repeats	3
Exposure time	10 s Axial iFR

Sample preparation

Three different electrolyte samples were measured in this exercise. These were fresh unused $LiPF_6$ electrolyte solutions in organic solvent mixtures like EC + EMC and EC + DEC. Approximately 2.5 g (~2 mL) of electrolyte samples were accurately diluted in 50 mL of an organic diluent consisting of 5% (v/v) EMC and 20% (v/v) ethanol in 18 MΩ·cm ultra-pure water.

Standards and reference materials

A calibration blank and a set of calibration and linearity standards containing the 15 target elements up to 1,000 µg·L^{-1} concentration (0, 50, 200, 500, and 1,000 µg·L^{-1}) were prepared in the same diluent as the samples using single element standards (1,000 mg·L^{-1}, SPEX™ CertiPrep Group, Metuchen, US) of individual analytes. 5 mg·L^{-1} yttrium was added as an internal standard to all samples and calibration solutions in order to track and compensate for matrix effects.

Quality control and method validation

The 200 µg·L^{-1} calibration solution was used as a quality control (QC) standard to ensure that good analytical precision was achieved throughout the analysis. To ensure method validity, selected samples were spiked with 50 µg·L^{-1} of the target elements and analyzed by the same method used for all other analyses in this study (Table 1). Spiked samples were also included in a robustness test to estimate analytical accuracy and precision over a long session of measurements.

Data acquisition and data processing

The Thermo Scientific™ Qtegra™ Intelligent Scientific Data Solution™ (ISDS) Software was used for data acquisition, processing, and reporting. Qtegra ISDS Software contains a full feature set for quality control tests performed during the analysis.

Results and discussion

Selectivity, sensitivity, and linearity

Wavelengths with the highest sensitivities in the high carbon matrix of the samples were selected for the analysis. Qtegra ISDS Software provided the flexible option to select background and peak positions freely and even remove background positions from one side or the other of a peak in case of any interference, which ensured accurate calculation of the concentrations of all elements in the solutions being analyzed.

The limit of detection/instrument detection limit (LOD/IDL) and method detection limit (MDL) were calculated based on repeat measurements of blank and low concentration calibration standards and the dilution factor used for sample preparation. The LODs and MDLs for each element are listed in Table 2.

The calibration linearity of the developed method was tested up to concentration levels of 1,000 µg·L^{-1} for all elements. The calibration curves for the different wavelengths gave R^2 values of between 0.9991 and >0.9999 over the entire calibration range (some examples of calibration curves are shown in Figure 1).

Table 2. List of suitable wavelengths, lowest limits of detections (LOD), R^2 values, and method detection limits (MDL) for individual elements

Element	Wavelength (nm)	Mode	LOD (µg·L^{-1})	R^2	MDL (mg·L^{-1})
Al	167.079	Axial-iFR	0.50	0.9998	0.010
As	193.759	Axial-iFR	7.57	0.9998	0.151
Ca	393.366	Axial-iFR	3.52	0.9991	0.070
Cd	214.438	Axial-iFR	0.18	0.9999	0.004
Co	238.892	Axial-iFR	0.34	0.9998	0.007
Cr	283.563	Axial-iFR	0.06	0.9997	0.001
Cu	324.754	Axial-iFR	0.60	0.9994	0.012
Fe	238.204	Axial-iFR	0.46	0.9999	0.009
Hg	253.652	Axial-iFR	6.28	0.9999	0.126
K	766.490	Axial-iFR	1.28	0.9998	0.026
Mg	279.553	Axial-iFR	0.05	0.9997	0.001
Na	589.592	Axial-iFR	3.88	0.9991	0.078
Ni	231.604	Axial-iFR	0.70	0.9998	0.014
Pb	220.353	Axial-iFR	4.92	0.9999	0.098
Zn	213.856	Axial-iFR	1.56	0.9997	0.031

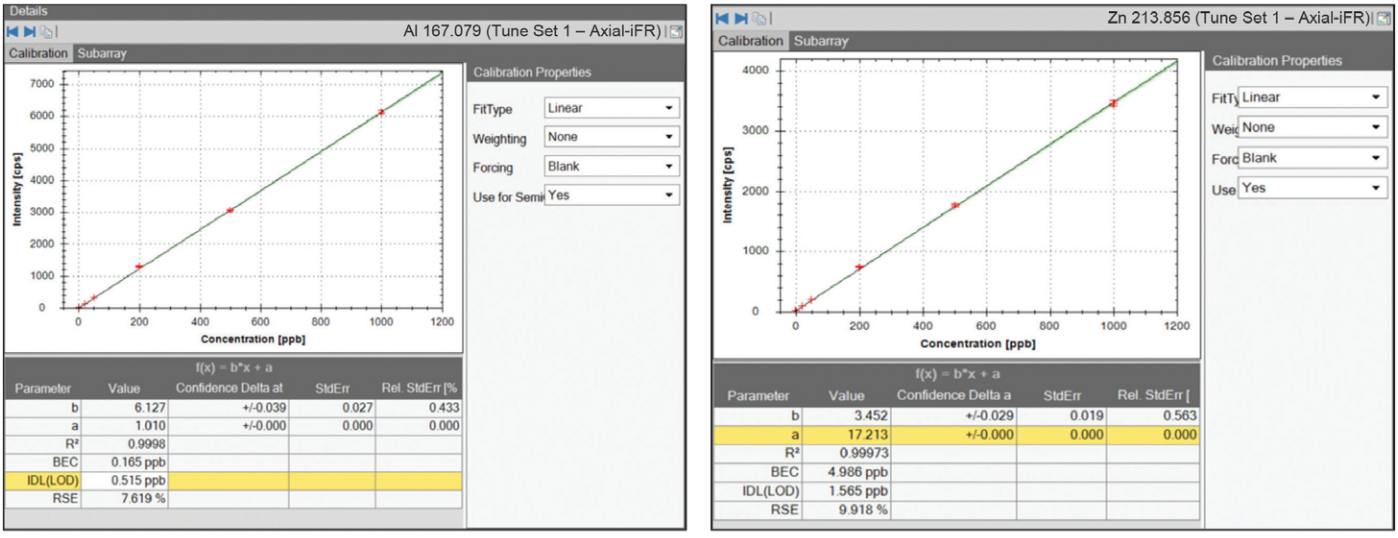

Figure 1. Examples of calibration curves obtained using the developed method

Accuracy

The accuracy and precision of the method was assessed by monitoring the concentration recoveries of two fresh electrolyte samples spiked with 50 µg·L^{-1} of the target elements. Recoveries were found to be within the accepted range of 80 to 120%, with most elements showing >90% (Table 3). A recovery of the internal standard (5 mg·L^{-1} yttrium) of around 90% in fresh electrolyte sample matrices demonstrated low matrix suppression, further ensuring data accuracy.

Robustness validation over a typical working day

The developed method was tested for its robustness, i.e., its ability to deliver accurate and precise results when longer sequences are run in a laboratory, as may occur in a production facility environment. The samples described above (native and spiked solutions of the two fresh electrolytes) were set up as an uninterrupted measurement over several hours, repeated on different days. The objective of this test was to prove that the sample matrix (containing significant amounts of ethanol as part of the diluent) can be run without the occurrence of signal drift or interruptions due to failure of applicable QC checks or limits set for the recovery of the internal standard. The sequence started with the calibration block, including blanks and standards, followed by an initial QC check (ICV = Initial Calibration Verification). The QC sample was regularly analyzed after every 20 unknown samples. A spiked sample was also measured occasionally throughout the robustness test.

The internal standard recovery, QC sample concentration recovery, and spiked concentration recoveries all remained stable throughout the experiment. Internal standard recovery was consistently between 85 and 90% for a measurement sequence of longer than 6 hours, as shown in Figure 2. The slightly lower recovery of the internal standard in real samples (compared to the calibration solutions) is due to the additional matrix contribution from the electrolyte samples (organic carbonates and elevated lithium content). However, despite the slight suppression the application of the internal standard allowed these matrix effects to be fully overcome (as demonstrated by the accuracy of the spike recovery test), and, more importantly, the sample matrix could be analyzed for an extended period of time (greater than 6 hours) without drift of the analytical system occurring. The QC recoveries were also found to be within a narrow range of 80–100% for all analytes, with the exception of sodium, which showed a slightly lower recovery of 76–78% for some samples in the test. The results of all QC checks analyzed as part of the study are shown in Figure 3. The recovery of the 100 µg·L^{-1} spike in the spiked electrolyte samples demonstrated very good accuracy (86–103%) and stability (RSD 1.5–4.7%) throughout the robustness test (Figure 4).

The trace elemental compositions of the electrolyte samples, corrected for the sample dilution, are presented in Table 4

Table 3. Spike recoveries on fresh electrolyte samples. Concentrations are in sample solutions that were measured directly, with no dilution factors applied.

			Concentrations (µg·L^{-1})			Concentrations (µg·L^{-1})		
Element	Wavelength (nm)	Mode	Sample 1 measured value	50 µg·L^{-1} spiked Sample 1	Spike recovery %	Sample 2 measured value	50 µg·L^{-1} spiked Sample 2	Spike recovery %
Al	167.079	Axial-iFR	<DL	50.6	97.7	<DL	48.5	93.9
As	193.759	Axial-iFR	<DL	50.2	115.6	<DL	52.4	94.1
Ca	393.366	Axial-iFR	15.8	59.7	87.8	<DL	57.9	112.3
Cd	214.438	Axial-iFR	<DL	48.2	96.7	<DL	45.6	91.3
Co	238.892	Axial-iFR	<DL	49.0	98.0	0.1	46.6	93.1
Cr	283.563	Axial-iFR	0.6	50.2	99.3	0.8	48.2	94.7
Cu	324.754	Axial-iFR	<DL	53.9	108.0	<DL	52.7	106.6
Fe	238.204	Axial-iFR	2.2	48.6	92.8	3.8	49.6	91.6
Hg	253.652	Axial-iFR	<DL	40.7	83.5	<DL	40.2	80.1
K	766.490	Axial-iFR	29.3	73.6	88.5	12.9	N.A.	N.A.
Mg	279.553	Axial-iFR	4.4	54.2	99.5	2.5	52.0	98.9
Na	589.592	Axial-iFR	29.3	73.6	88.5	11.2	69.7	117.0
Ni	231.604	Axial-iFR	2.7	45.9	86.4	<DL	42.1	86.6
Pb	220.353	Axial-iFR	<DL	50.5	107.1	1.3	50.4	98.2
Zn	213.856	Axial-iFR	10.9	59.3	96.9	2.5	56.7	108.3

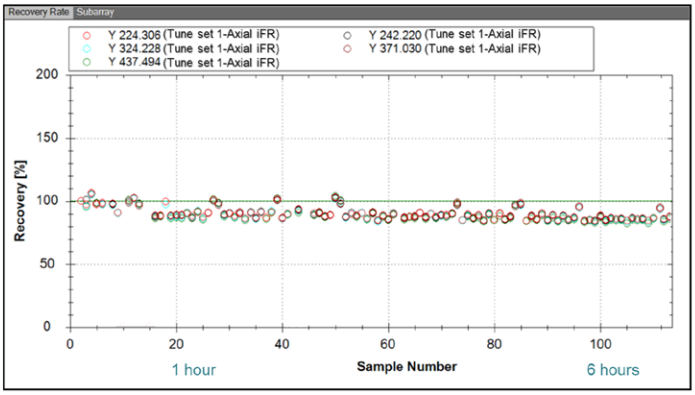

Figure 2. Internal standard recovery in samples and standards during an extended measurement sequence covering more than 6 hours

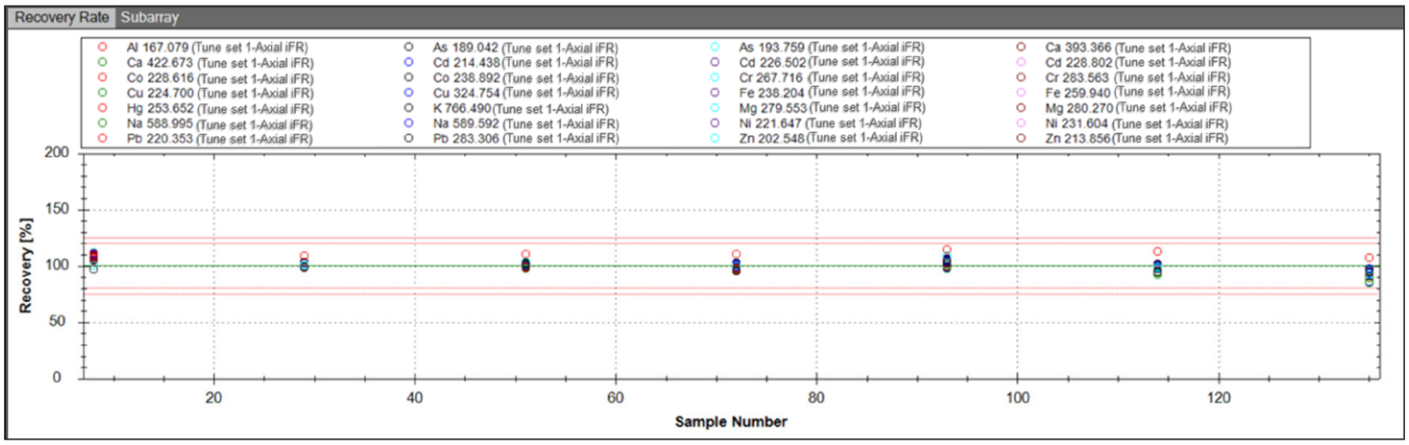

Figure 3. Robustness data demonstrating CCV (continuous calibration verification) recoveries of target elements in a QC standard (200 µg·L^{-1}) during a 7-hour experiment. The red lines mark the acceptable QC recoveries of between 80 and 120%. This figure is a direct export from the software for quick and easy data visualization.

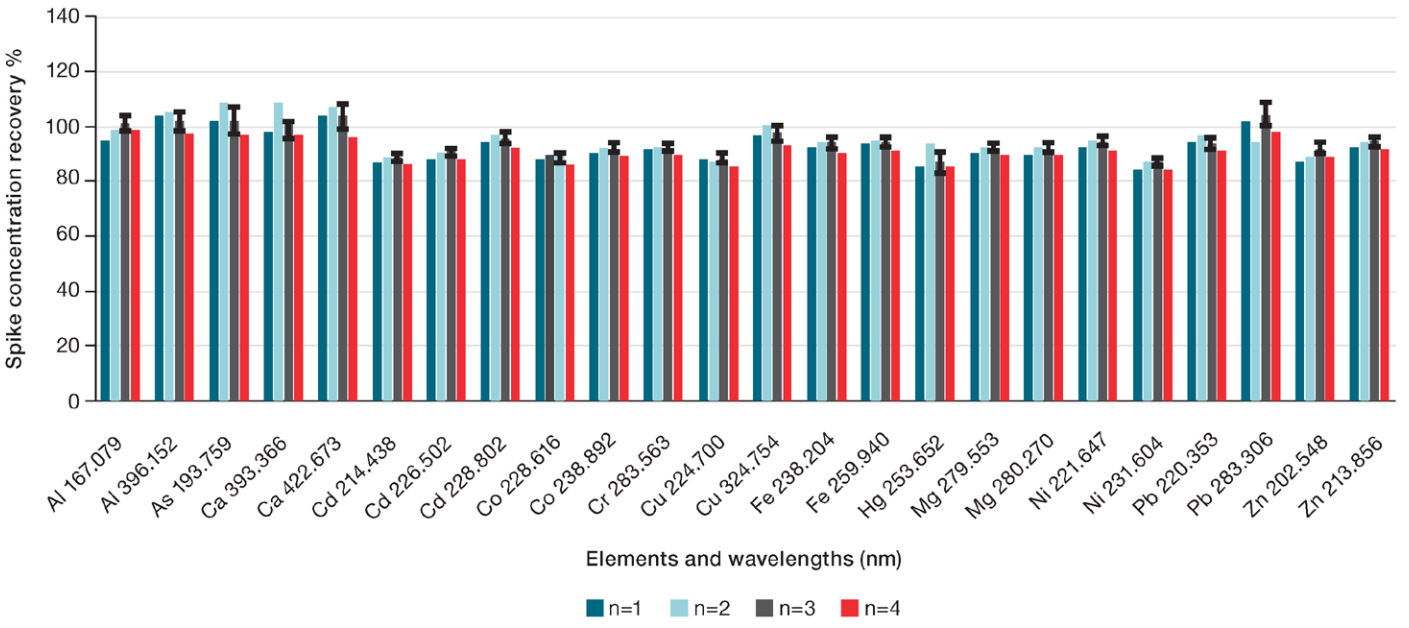

Figure 4. Concentration recoveries of a spiked electrolyte sample during the robustness test. The spiked sample was run on 4 occasions throughout a 7-hour sequence.

Table 4. Trace elemental composition of the fresh electrolyte samples (dilution corrected). Only elements detected in the quantifiable range have been reported here.

Element	Sample 1		Sample 2		Sample 3	
	Concentration (µg·L^{-1})	SD (1σ)	Concentration (µg·L^{-1})	SD (1σ)	Concentration (µg·L^{-1})	SD (1σ)
Al	<DL	-	<DL	-	<DL	-
Ca	316	13.1	<DL	-	<DL	-
Cr	12	2	16	0.15	10.0	1.9
Fe	44	0.5	76	0.12	100	3.1
K	<DL	-	260	0.35	321	8.7
Mg	12	2.7	50	0.004	6.6	3
Na	666	5.7	227	0.21	273	10.1
Ni	54	-	<DL	-	<DL	-
Zn	218	8.0	<DL	-	<DL	-

Conclusions

This study has demonstrated the performance of the iCAP PRO XP ICP-OES Duo system for highly sensitive and accurate analysis of impurities in electrolyte solutions containing $LiPF_6$ and organic carbonates, such as ethyl carbonate and ethyl methyl carbonate. The proposed method allowed for fast sample turnaround times combined with high reproducibility and robustness, allowing reliable analysis of long sequences over multiple days of analysis.

A summary of the main results and conclusions is presented below:

- Excellent sensitivity, sufficient for detecting impurities in $LiPF_6$ electrolyte samples (in the low µg·L^{-1} (ppb) range), was achieved for all the target elements using the Axial iFR mode of the instrument. A large linear dynamic calibration range of up to 1,000 µg·L^{-1} was also obtained. The linear dynamic range could be further expanded, if required, by adding standard solutions with higher concentrations. This would be beneficial when analyzing, for example, used electrolyte samples for battery ageing studies or failure diagnostic purposes.
- The accuracy of the method was verified by successfully recovering known spiked concentrations in fresh electrolyte samples in spite of the challenges arising from the sample matrix composition.
- Excellent system robustness and reproducibility was demonstrated over multiple days, proving the reliability of the method, with accuracy over long measurement runs validated by analysis of QC solutions, spiked samples, and internal standards.
- Daily continuous measurements of more than 6 hours are possible with the described method. Using a short exposure time of 10 s ensured not only fast analysis (3 min 6 s/sample), but also high sensitivity. A total of more than 100 samples could be measured daily following this approach. This high sample turnaround with consumption of low sample volumes, minimal downtime, and no need for extensive sample preparation or user interaction positions the iCAP PRO XP ICP-OES Duo system as an effective choice of instrument for quality control and characterization of trace elements in fresh electrolyte samples.

References

1. Lithium Batteries — new materials, developments and perspectives; Pistoia, G., Ed.; Elsevier Science: Amsterdam, 1994.
2. Scrosati, B., Insertion Compounds for Lithium Rocking Chair Batteries. In *Electrochemistry of Novel Materials;* Lipkowski, J.; Ross, P.N., Eds.; VCH: New York, 1993, pp 111-140.
3. Wu, W.; Yang, X.; Zhang, G.; Chen, K.; Wang, S. Experimental investigation on the thermal performance of heat pipe-assisted phase change material based battery thermal management system. *Energy Convers. Manag.* **2017**; 138, 486–92.
4. Cell liquor of lithium hexafluorophosphate. **https://www.chinesestandard.net/PDF/English.aspx/HGT4067-2015**

Learn more at **thermofisher.com**

Determination of elemental impurities in lithium iron phosphate using ICP-OES

Authors: Jingfang He,[1] Xiaobo Li,[1] Fei Wang,[1] Miao Jing,[1] and Jianfeng Cui[2]
[1]Thermo Fisher Scientific, Shanghai, China
[2]Thermo Fisher Scientific, Bremen, Germany

Keywords: Lithium iron phosphate, iCAP PRO ICP-OES, lithium battery, cathode material

Goal

This application note describes the analysis of lithium iron phosphate using the Thermo Scientific™ iCAP™ PRO Series ICP-OES. The note describes the method development as well as presenting key figures of merit, such as detection limits and stability.

Introduction

Lithium iron phosphate has properties that make it an ideal cathode material for lithium-ion batteries. The material is characterized by a large discharge capacity, low toxicity, and low cost. The first large capacity lithium iron phosphate battery was produced in China in 2005, and the life cycle performance characteristics of the battery were unmatched by other batteries of a similar classification. An ideal application for batteries with a lithium iron phosphate cathode is in series in electric vehicles where frequent charging and discharging of the batteries takes place.

The purity of the cathode material is critical, and changes in the raw material processing and synthesis can cause the introduction of impurities in the final cathode material. These impurities impact the lifetime and energy storage capacity of the battery, and in extreme cases may affect the integrity of the crystal structure of the battery, causing safety issues. Therefore, accurate analysis of the cathode material is key to the performance and safety of lithium batteries made using these materials.

Experimental

Sample and standard preparation

The sample (customer supplied) was weighed (0.2000 g) into a polytetrafluoroethylene beaker. Perchloric acid (10 mL, concentrated) was added, and the beaker was heated on a hot plate until the sample was completely dissolved. When cooled, the sample was transferred to a volumetric flask (50 mL); a blank was prepared using the same method. This solution was analyzed directly to determine elemental impurities. For the matrix elements, a further dilution (factor of 50) with ultrapure water was carried out prior to analysis.

ThermoFisher SCIENTIFIC

Standards were prepared by diluting stock solutions (1,000 mg/L) to the required concentrations. For impurity analysis, these were 0.05, 0.10, 0.50, and 1.0 mg/L, and, for the matrix elements, these were 2, 5, 10 mg/L for Li, and 10, 20, 50 mg/L for P and Fe.

Instrument, method development, and analysis

The Thermo Scientific iCAP PRO Radial ICP-OES instrument, fitted with a fully demountable extended matrix tolerance (EMT) quartz torch, was used for the analysis. This instrument is ideal for the analysis of complex matrix samples, such as lithium iron phosphate, due to the pre-optimized radial view. The iCAP PRO ICP-OES has continuous wavelength coverage from 167 to 852 nm. Combined with the CID detection of 2,048 × 2,048 pixels, this allows the spectral line library to have more than 50,000 optional spectral lines. Therefore, the iCAP PRO ICP-OES can flexibly use a variety of other spectral lines to avoid interference.

The Thermo Scientific™ Qtegra™ Intelligent Scientific Data Solution™ (ISDS) software was used to create a LabBook and control the instrument. Wavelengths were selected in the LabBook based on their potential to be free from interferences, method parameters were set (Table 1), and the analysis was carried out. The instrument was calibrated, the unknown samples determined, spikes of the impurity elements (at 0.2 mg/L) were analyzed, and a two-hour stability test was carried out for the matrix elements, measuring one sample every two hours. After the data collection, the sub-array spectrum overlay function was used to examine the spectra of each wavelength. This can be used to determine if any interferences are present and optimize the central integration area and background correction points.

Results and discussion

Calibrations with excellent linearity were obtained for all 26 elements analyzed, as shown in Table 2. For the 23 impurity elements, the concentrations found in the sample (corrected for the dilution factor) ranged from below the detection limit of the method for Cd, Mo, Se, and W up to 240 mg/kg for Mn (Table 3). Detection limits achieved for the impurity elements were in the µg/L range in the solutions measured and in the sub-mg/kg to low mg/kg range for the solid sample (Table 3). Spike recoveries for the impurity elements (all spiked at 0.2 mg/L) ranged from 90 to 110% of the spiked concentration, as shown in Figure 1. Finally, excellent precision (<0.8% RSD over seven repeat analyses) was achieved for the 2-hour measurement stability test of the matrix elements Li, Fe and P (Table 4).

Table 1. Instrument parameters used for the analysis

Parameter	Setting
Instrument model	iCAP PRO Radial
Observation method	Radial
Plasma torch	Demountable EMT torch
Injector	2.0 mm quartz injector
Spraychamber	Glass concentric
Nebulizer	Glass concentric
Peristaltic pump speed	50 rpm
Plasma RF power	1,150 W
Nebulizer gas flow	0.6 L/min
Auxiliary gas flow	0.5 L/min
Cool gas flow	12 L/min

Table 2. Correlation coefficient R^2 of the standard curve of each element

Element and wavelength (nm)	R^2	Element/wavelength (nm)	R^2
Al 396.152	0.9997	Na 589.592	0.9999
As 189.042	0.9999	Ni 231.604	0.9999
Ba 455.403	0.9999	P 177.495	0.9997
Ca 393.366	0.9999	Pb 168.216	1.0000
Cd 228.802	0.9999	S 180.731	1.0000
Co 228.616	0.9999	Sb 206.833	0.9999
Cr 206.157	0.9999	Se 196.090	0.9991
Fe 271.441	0.9999	Si 212.412	0.9999
K 766.490	0.9996	Sn 189.989	1.0000
Li 670.791	0.9996	Ti 323.452	1.0000
Mg 285.213	0.9999	V 309.311	0.9998
Mn 257.610	0.9999	W 207.911	1.0000
Mo 202.030	1.0000	Zn 213.856	0.9999

Table 3. Impurity elements test results: the detection limit of the method is based on the weighed sample (0.2 g) and the constant volume of 50 mL; ND = not detected

	Sample (mg/kg)	Solution detection limit (µg/L)	Method detection limit (mg/kg)
Al 396.152	110.08	6.18	1.54
As 189.042	6.16	11.21	2.8
Ba 455.403	0.55	0.19	0.05
Ca 393.366	37.23	0.09	0.02
Cd 228.802	ND	1.45	0.36
Co 228.616	7.51	2.09	0.52
Cr 206.157	8.19	2.2	0.55
K 766.490	21.94	35.87	8.97
Mg 285.213	119.54	0.71	0.18
Mn 257.610	240.22	0.21	0.05
Mo 202.030	ND	2.46	0.62
Na 589.592	167.64	34.79	8.70
Ni 231.604	2.69	2.24	0.56
Pb 168.216	9.48	20.8	5.2
S 180.731	24.54	7.69	1.92
Sb 206.833	20.54	13.35	3.34
Se 196.090	ND	15.48	3.87
Si 212.412	13.76	11.29	2.82
Sn 189.989	1.38	3.21	0.8
Ti 323.452	228.11	0.56	0.14
V 309.311	17.78	1.37	0.34
W 207.911	ND	9.91	2.48
Zn 213.856	97.98	0.53	0.13

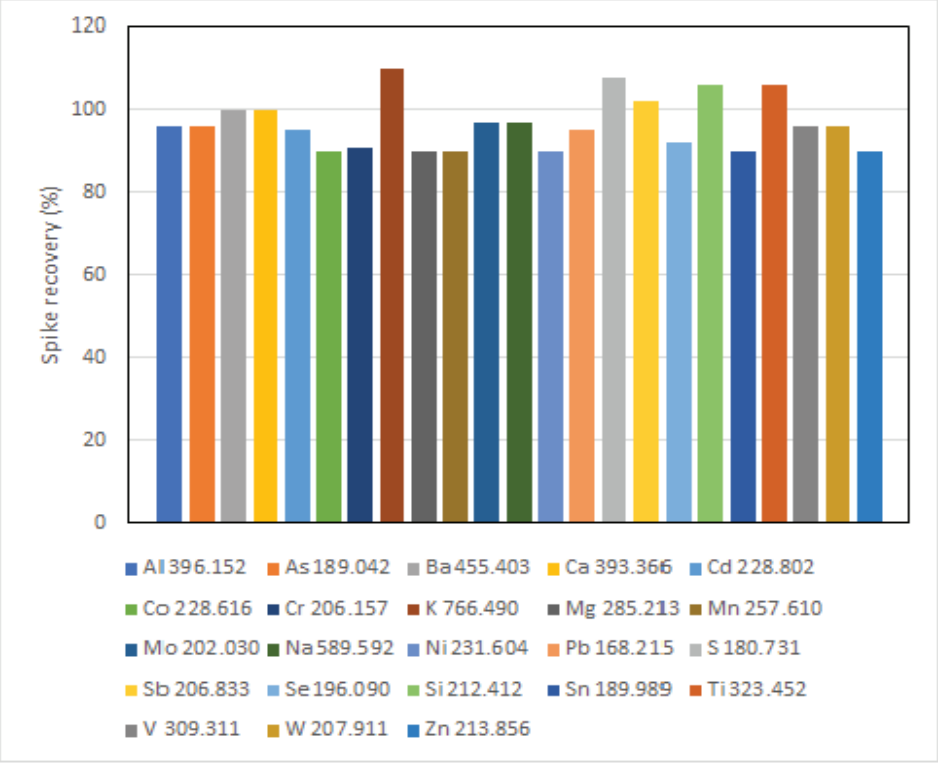

Figure 1. Spike recovery results for samples spiked with 0.2 mg/L of the 23 impurity elements

Table 4. Results of matrix elements analysis and 2-hour stability test (measured every 20 minutes for 2 hours, 7 times in total, unit %)

	Measured concentration (mg/L)		
Sample/element	Fe 271.441 nm	P 177.495 nm	Li 670.791 nm
1–1	34.69	19.33	4.42
1–2	34.87	19.55	4.44
1–3	34.67	19.48	4.43
1–4	34.47	19.51	4.41
1–5	34.33	19.47	4.37
1–6	34.63	19.62	4.43
1–7	34.20	19.47	4.35
Average value	34.55	19.49	4.41
Standard deviation	0.23	0.09	0.03
Relative standard deviation %	0.66	0.46	0.76

Conclusion

This application note demonstrates the effective application of the iCAP PRO Radial ICP-OES instrument for analysis of elemental impurities in lithium iron phosphate, a commonly used cathode material in lithium-ion batteries. A total of 23 key impurity elements were accurately and sensitively measured, as demonstrated by the results obtained for the customer supplied sample and the quantitative spike recoveries obtained for each element spiked into the sample. The instrument not only has the capability to measure elemental impurities at low concentrations, but also has the linear range to determine matrix elements accurately over a typical analysis sequence, as demonstrated by the high precision results achieved for the matrix element stability test. Use of the robust, fully demountable EMT torch design for this application ensures low operating consumable costs and this, coupled with excellent stability and sensitivity, makes the iCAP PRO ICP-OES an ideal choice for accurately measuring a range of matrix and impurity elements in materials for the lithium battery industry.

Find out more at **thermofisher.com/icp-oes**

ThermoFisher SCIENTIFIC

APPLICATION NOTE 000466

Determination of elemental impurities in graphite powder for lithium-ion battery anodes

Author: Thermo Fisher Scientific Inc.

Keywords: Lithium ion batteries, elemental impurities, ICP-OES, graphite, anode

Goal

To develop a robust and reliable method for the determination of elemental impurities in graphite powder samples for lithium-ion battery anodes, using the Thermo Scientific™ iCAP™ PRO X ICP-OES Duo instrument. This note will demonstrate the performance of the method with respect to calibration linearity for 13 trace element impurities (target $R^2 > 0.999$) and quantification of these elements. It will also illustrate the robustness of the method developed through spike recovery analysis of the microwave digested samples.

Introduction

For lithium-ion batteries, the negative electrode (anode) material is generally made from graphite powder. Graphite powder is suitable for this application primarily because it is an easily molded, chemically stable, and non-metallic material with good electrical conductivity and high temperature, oxidation, and corrosion resistance. It also has a large lithium-ion diffusion coefficient with a high lithium insertion capacity and does not change volume with insertion of lithium ions. In addition, graphite powder can be modified through various oxidation and pyrolysis processes to generate a core-shell structure that can improve its charging/discharging performance and increase the anode lifetime. Graphite powder has become the main lithium-ion battery anode material in use today in smaller consumer goods, such as mobile phones, as well as in electrical vehicles.

Through optimization of the sample pre-treatment process and plasma parameters, together with rigorous selection of the most suitable analyte emission lines, a robust, accurate and reliable ICP-OES analytical method for the determination of 13 trace elements in graphite powder materials for lithium ion batteries was developed.

ThermoFisher SCIENTIFIC

Experimental

Instruments and reagents

For this work, an iCAP PRO X ICP-OES Duo instrument was used (Figure 1). For sample preparation, ultrapure water (18.2 MΩ·cm resistivity), nitric acid, and hydrochloric acid (Merck) were used. Sample digestions were carried out using a microwave digestion system (ETHOS™ One, Milestone, Italy).

Figure 1. Thermo Scientific iCAP PRO X ICP-OES Duo

Calibration solution and sample preparation

Multi-element calibration solutions containing all 13 elements of interest at blank, 0.05, 0.20, and 0.50 µg/mL concentrations were prepared from a stock solution made from single element standards (1,000 µg/mL, National Standard Material Research Centre). Three raw material briquetting charcoal materials were analyzed in this study. Portions of each sample (0.5 g, accurately weighed) were mixed with 3 mL HNO_3 and 9 mL HCl in PTFE vessels and microwave digested at 190 °C for 30 minutes. After digestion was complete, the samples were diluted with ultrapure water to 50 mL and filtered prior to analysis. Microwave digestion reagent blank samples were also prepared using the same method. Finally, spike recovery tests were performed on all three briquetting charcoal samples, with each digested and diluted sample spiked at 0.20 µg/mL using the multi-element stock solution.

Instrument parameters and method optimization

The instrument configuration parameters used for the analysis are given in Table 1 and the wavelengths selected for each element are shown in Table 2.

Table 1. Instrument configuration parameters

Instrument parameter	Setting
Injection pump tubing	PVC, orange/white, i.d. 0.64 mm
Drain pump tubing	PVC, white/white, i.d. 1.02 mm
Pump speed	50 rpm
Nebulizer	Glass concentric nebulizer
Nebulizer gas flow	0.6 L/min
Spray chamber	Baffled glass cyclonic
Torch center tube	2.0 mm center tube
Observation method	Axial
RF power	1150 W
Auxiliary gas flow	0.5 L/min
Exposure time	15 s
Repeats	3

Table 2. Wavelength selection for the 13 elements analyzed

Element	Wavelength (nm)	Element	Wavelength (nm)
As	189.042	Mo	202.030
Be	313.042	Ni	231.604
Cd	214.438	Pb	220.353
Co	228.616	Sb	206.833
Cr	267.716	V	309.311
Cu	213.598	Zn	213.856
Mn	257.610		

Results and discussion

Linear calibrations (R^2 > 0.9999) were obtained for all 13 trace elements measured. The concentrations found for each element in the three raw material briquetting coal materials, calculated back to the solid samples, are presented in Table 3. The spike recovery test results for each sample are shown in Table 4. Table 4 shows that quantitative spike recoveries (from 93 to 104%) were achieved for all the trace elements measured in this study.

Table 3. Raw material briquetting charcoal sample results (mg/kg)

Sample	As	Be	Cd	Co	Cr	Cu	Mn
Briquetting charcoal 1	3.09	5.40	0.12	12.60	15.61	10.18	132.9
Briquetting charcoal 2	3.34	10.39	0.08	13.10	13.57	6.45	90.15
Briquetting charcoal 3	2.54	5.34	0.14	9.85	9.80	4.07	194.3

Sample	Mo	Ni	Pb	Sb	V	Zn
Briquetting charcoal 1	1.24	24.68	15.62	2.23	24.56	10.03
Briquetting charcoal 2	0.91	30.71	13.50	1.85	36.55	12.64
Briquetting charcoal 3	0.56	26.28	17.39	1.66	13.54	10.67

Table 4. Spike recovery results

	As	Be	Cd	Co	Cr	Cu	Mn
Sample 1 (µg/mL)	0.031	0.0540	0.001	0.126	0.156	0.102	1.329
Spike result (µg/mL)	0.218	0.257	0.189	0.321	0.355	0.297	1.532
Spike (µg/mL)	0.200	0.200	0.20	0.200	0.200	0.200	0.200
Spike recovery (%)	94	101	94	97	99	98	102
	As	Be	Cd	Co	Cr	Cu	Mn
Sample 2 (µg/mL)	0.033	0.104	0.001	0.131	0.136	0.065	0.902
Spike result (µg/mL)	0.225	0.312	0.192	0.332	0.343	0.263	1.107
Spike (µg/mL)	0.200	0.200	0.200	0.200	0.200	0.200	0.200
Spike recovery (%)	96	104	96	101	103	99	103
	As	Be	Cd	Co	Cr	Cu	Mn
Sample 3 (µg/mL)	0.025	0.053	0.001	0.099	0.098	0.041	1.943
Spike result (µg/mL)	0.221	0.254	0.193	0.294	0.298	0.234	2.132
Spike (µg/mL)	0.200	0.200	0.200	0.200	0.200	0.200	0.200
Spike recovery (%)	98	100	96	98	100	97	95

	Mo	Ni	Pb	Sb	V	Zn
Sample 1 (µg/mL)	0.012	0.247	0.156	0.022	0.246	0.100
Spike result (µg/mL)	0.210	0.434	0.345	0.223	0.441	0.288
Spike (µg/mL)	0.200	0.200	0.200	0.200	0.200	0.200
Spike recovery (%)	99	93	94	101	97	94
	Mo	Ni	Pb	Sb	V	Zn
Sample 2 (µg/mL)	0.009	0.307	0.135	0.019	0.366	0.126
Spike result (µg/mL)	0.212	0.502	0.324	0.222	0.568	0.316
Spike (µg/mL)	0.200	0.200	0.200	0.200	0.200	0.200
Spike recovery (%)	101	97	94	102	101	95
	Mo	Ni	Pb	Sb	V	Zn
Sample 3 (µg/mL)	0.006	0.263	0.174	0.017	0.135	0.107
Spike result (µg/mL)	0.203	0.455	0.369	0.220	0.330	0.297
Spike (µg/mL)	0.200	0.200	0.200	0.200	0.200	0.200
Spike recovery (%)	99	96	98	102	97	95

thermoscientific

Conclusion

This application note has demonstrated the performance of the iCAP PRO X ICP-OES Duo instrument for quantitative trace element impurity analysis in graphite powder samples (derived from briquetting coal) used for lithium-ion battery anode production. Using the ASTM D6357-2004 and GB/T24533-2009 (Appendix H) standards as a guide, a robust sample preparation method based on microwave digestion of the samples was developed. Concentrations were determined for all 13 trace elements in the three raw material briquetting charcoal samples, and the robustness of the analysis was confirmed by the achievement of quantitative spike recoveries of the measured elements (in the range 93 to 104%).

The iCAP PRO X ICP-OES Duo provides the advantages of high sensitivity, good stability, fast analysis speed and low operating costs required for all aspects of elemental analysis in the lithium ion battery workflow. From quantifying lithium concentrations in ores and brine to routinely confirming the composition of cathode active materials in a QA/QC environment, the iCAP PRO X ICP-OES Duo offers the performance and flexibility required to meet the analytical demands of this rapidly growing sector.

Find out more at **thermofisher.com/icp-oes**

ThermoFisher SCIENTIFIC

Application note | 000602

Industrial

Determination of lithium and other elements in brine solutions using ICP-OES

Authors

Bhagyesh Surekar[1], Simon Nelms[2]

[1]Thermo Fisher Scientific, Bremen, Germany
[2]Thermo Fisher Scientific, Hemel Hempstead, UK

Keywords

iCAP PRO Series, ICP-OES, Li-ion battery, brine solutions, robustness, lithium extraction

Goal

To develop a robust methodology for the determination of a wide concentration range of lithium together with trace level measurement of other critical elemental contaminants in brine solutions using the Thermo Scientific™ iCAP™ PRO Series ICP-OES.

Introduction

As part of the global initiative on sustainability and green energy, battery electric vehicles (BEVs) are rapidly gaining in popularity and their share of the vehicle market is expected to increase at least 10-fold over the next decade. After a few years of rapid growth, there are now more than 10 million electric cars on the road globally, and this is anticipated to rise to about 40 million in 2030 and up to 300 million by 2050.[1]

Currently, electric vehicles most often use batteries based on lithium-ion technology because of the high energy density of such batteries relative to their weight, their ability to undergo multiple charge / discharge cycles before significantly losing performance, and their relatively low cost. Since the late 1990s, advances in the performance of lithium-ion battery technology have mainly been driven by demand from portable electronics, laptop computers, mobile phones, and power tools. However, the rapid rise of BEVs and hybrid electric vehicles (HEVs) has intensified research and development of a new generation of batteries with greater robustness and higher charge capacity to significantly increase the achievable range of these vehicles between each charging cycle.

The rapidly increasing demand for Li-ion batteries has led to a critical need for exploration and development of additional natural resources of lithium as well as other commonly used elements in battery manufacturing, such as manganese, nickel, and cobalt. In addition to mineral sources, such as spodumene ore, underground brine reserves are also rich sources of lithium. There are various methods for extracting lithium from brine, including precipitation, liquid-liquid extraction, selective membrane separation, electrodialysis, and ion exchange adsorption.[2] With cost and efficiency taken into consideration, extraction of lithium ions from solutions by ion exchange adsorption is one of the most effective methods. The abundance of lithium in brine solutions can vary significantly in the concentration range of 10 mg·L^{-1} or less to about 4,000 mg·L^{-1} or more depending upon the geography of the source.

To assess the quality of brine solutions from the perspective of their lithium content and to determine the cost-effectiveness and efficiency of the extraction process, it is important to accurately measure lithium concentrations in brine extracts prior to establishing the extraction process. The concentration of other trace impurity elements present in the original brine itself, the lithium salts extracted from the brine, and the waste brine once the lithium has been extracted must also be determined, as these have an adverse impact on the quality of the material extracted during the process and can also have negative environmental impacts.

In this work, a comprehensive analytical method was developed and tested for analysis of brine solutions using the Thermo Scientific™ iCAP™ PRO XP ICP-OES Duo instrument, operated using the Thermo Scientific™ Qtegra™ Intelligent Scientific Data Solution™ (ISDS) Software. The main objective of this application note is to present the performance of the method developed in the study for laboratories working in the lithium extraction area or otherwise involved in measuring concentrated salt solutions such as brine.

Experimental

Instrument parameters and experimental conditions

In this study, an iCAP PRO XP ICP-OES Duo instrument equipped with a ceramic D-Torch and operated in axial Intelligent Full Range (iFR) and Radial iFR modes was used to analyze 19 analytes including lithium. Lithium was measured using radial viewing mode while the other trace elements were measured using the higher sensitivity axial view of the ICP-OES. Details of the sample introduction system components and instrument parameters used are given in Table 1. Automated sample introduction was carried out using a Teledyne CETAC ASX-560 autosampler.

A 10 mg·L^{-1} yttrium internal standard solution, prepared in a matrix of 0.5% (v/v) nitric acid, was added online to correct for any drift or physical interferences such as signal suppression.

Table 1. Instrument configuration and operating parameters

Instrument parameter	Setting
Spray chamber	Baffled cyclonic
Nebulizer	Burgener Mira Mist
Pump tubing	Sample uptake: Tygon™ orange/white Drain: Tygon™ white/white
Torch injector tube	2.0 mm (ceramic)
Torch	Ceramic D-Torch Duo
Pump speed	45 rpm
Flush pump speed	100 rpm
Nebulizer gas flow	0.55 L/min
Auxiliary gas flow	1.5 L/min
Coolant gas flow	12.5 L/min
Additional argon gas flow	0.15 L/min
Plasma RF power	1,350 W
Replicates	3
Exposure time	Axial iFR – 10 s Radial iFR – 10 s
Radial viewing height	6 mm

Brine solutions containing 25% (w/w) sodium chloride were analyzed in this study. The analysis of samples containing high dissolved solids is often a challenge for ICP-OES instruments, and particularly so for dual view systems, because of problems such as salting up (leading to a blocked nebulizer or torch injector) and sample deposition on optical components (leading to signal drift and the need for increased instrument maintenance). However, innovative hardware adaptions for the iCAP PRO Series ICP-OES Duo instrument, such as its optimized vertical torch configuration, offer significantly improved matrix tolerance with an achievable robustness that is similar to that of radial view only instruments. The ability to also optimize the radial plasma viewing height for radially viewed elements enables accurate and precise measurement of analytes in the presence of high amounts of easily ionizable elements such as sodium in the sample matrix. Deposition of salts at the nebulizer tip during long analytical runs was avoided by using a Burgener Mira Mist™ nebulizer, and to prevent salting up of the torch injector, an additional flow of argon gas was introduced at a flow rate of 0.15 L·min^{-1} around the sample aerosol with the help of a sheath gas adaptor (for more information on the instrument configuration used, please refer to application note AN44470).[3]

Sample and standard preparation

The samples used in this study were prepared using commercially available sodium chloride salt. To simulate the typical matrix of brine solutions, a 25% (w/w) solution of sodium chloride was prepared by dissolving 25 g of salt in 100 g of distilled water. All samples were then acidified at 0.5% (v/v) using nitric acid prior to analysis.

To tackle matrix-related challenges and avoid physical and spectral interferences, the approach of matrix-matched calibration standards was followed in the study. All calibration standards were prepared in the same matrix as the samples using a 25% (w/w) solution of pure sodium chloride. A mixed stock solution of 10 mg·L^{-1} of the trace level analytes was prepared in 2% (v/v) nitric acid, which was then gravimetrically diluted to yield calibration standards with the concentrations given in Table 2. A lithium standard stock solution of 10,000 mg·L^{-1} concentration was added appropriately in the same calibration solutions to prepare lithium standard solutions with the concentrations given in Table 2. Trace level analytes were calibrated in the concentration range of 0.01 to 1 mg·L^{-1}, while lithium was calibrated in the range of 10 mg·L^{-1} to 5,000 mg·L^{-1}.

Calibration linearity and instrument detection limits

Instrument detection limits and calibration line correlation coefficients for all the measured analytes obtained during the linearity study are given in Table 3, together with the wavelength and plasma viewing mode used for each analyte. Instrument detection limits were calculated based on 10 replicate measurements of the calibration blank solution and the slope achieved for each individual analyte calibration line. Excellent detection limits and calibration linearity were achieved for all the analytes measured, as shown in Table 3. In this case, all brine samples were analyzed directly without any sample preparation steps or any sample dilution performed prior to analysis. Hence, the instrument detection limits achieved also represent the method detection limits (MDLs).

Table 2. List of target elements and their concentrations in the calibration standards (mg·L^{-1})

Elements	Standard 1	Standard 2	Standard 3	Standard 4	Standard 5	Standard 6	Standard 7
Al, As, Ba, Cd, Ca, Cr, Co, Cu, Fe, Pb, Mg, Mn, Hg, Ni, Si, Sr, S, Zn	0.01	0.05	0.1	0.25	0.5	1	-
Li	10	100	1,000	2,000	3,000	4,000	5,000

Table 3. List of analytes, wavelengths, measurement mode, correlation coefficients, and method detection limits (mg·L^{-1})

Element	Wavelength (nm)	Plasma view	R^2	MDL (mg·L^{-1})
Al	167.079	Axial	0.9998	0.0011
As	189.042	Axial	0.9995	0.0141
Ba	455.403	Axial	0.9996	0.0001
Cd	226.502	Axial	0.9994	0.0010
Ca	393.366	Axial	0.9993	0.0011
Cr	267.716	Axial	0.9998	0.0014
Co	228.616	Axial	0.9999	0.0041
Cu	324.754	Axial	0.9995	0.0017
Fe	238.204	Axial	0.9996	0.0003
Pb	220.353	Axial	0.9997	0.0151
Mg	279.553	Axial	0.9996	0.0014
Mn	257.610	Axial	0.9997	0.0005
Hg	184.950	Axial	0.9999	0.0023
Ni	231.604	Axial	0.9997	0.0066
Si	251.611	Axial	0.9995	0.0061
Sr	421.552	Axial	0.9998	0.0001
S	180.731	Axial	0.9999	0.0981
Zn	213.856	Axial	0.9997	0.0008
Li	610.362	Radial	0.9994	0.0578

Method accuracy

The accuracy of the entire analytical setup was assessed by measuring an independently prepared QC standard containing 0.5 mg·L^{-1} of the trace level analytes and 3,000 mg·L^{-1} of Li. The QC sample was analyzed every 10 samples throughout the entire analytical run of 11 hours. Figure 1 shows the percentage accuracy level for all the measured trace level analytes, and Figure 2 presents the accuracy of the Li measurement in the periodically analyzed QC samples. As can be seen, the accuracy observed for all analytes was found to be in the range of 90% to 110% throughout the whole analytical run.

To check the method performance against its intended purpose of accurate Li measurement over a wider range of concentrations, Li was spiked into unknown brine samples at relatively low concentration levels of 10 mg·L^{-1} and 100 mg·L^{-1} and the percent recovery calculated. Accurate measurement of Li at lower concentrations in brine is as important as being able to measure high Li concentrations, as the ability to achieve lower-level detection is vital for ensuring that efficient Li extraction has been achieved after processing the brine solutions. Extraction efficiency can be easily assessed by analyzing the original brine solution after the extraction process. Table 4 shows spiked concentrations and percent recovery observed for lithium in this additional study. The recovery presented is the average value calculated from six replicate measurements of each spiked sample analyzed at different intervals over the 11-hour duration of the analytical run. The observed average recovery for Li was found to be in the range of 100±5% with a relative standard deviation of less than 5%.

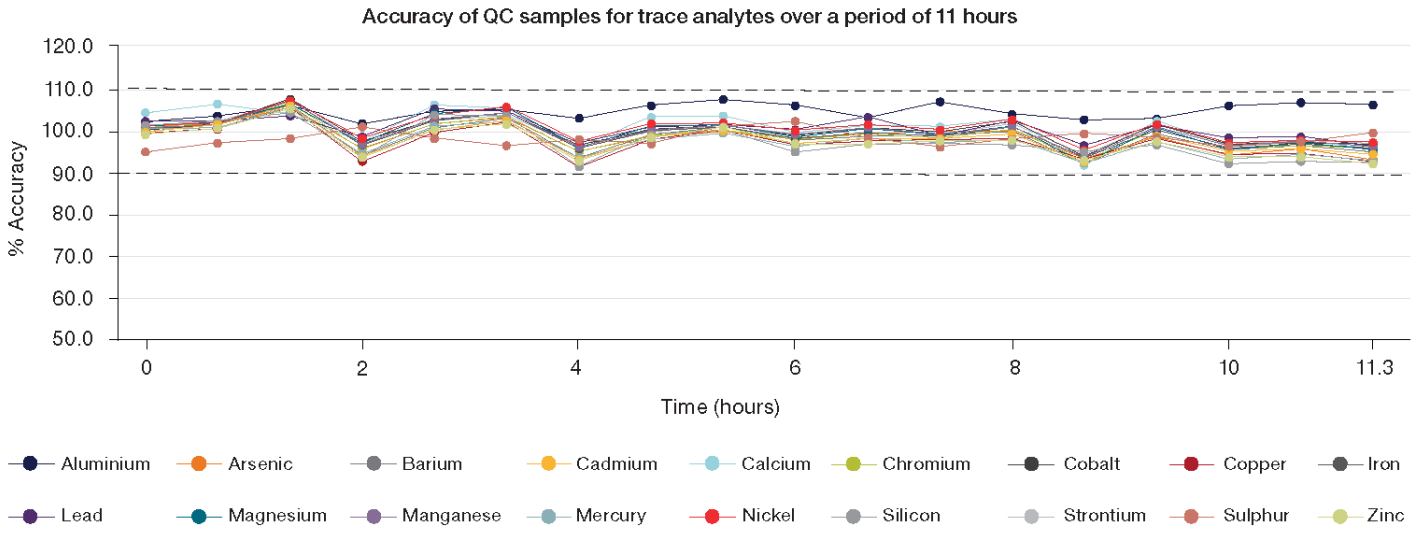

Figure 1. Percent accuracy observed for QC standards containing 0.5 mg·L^{-1} of the trace level analytes

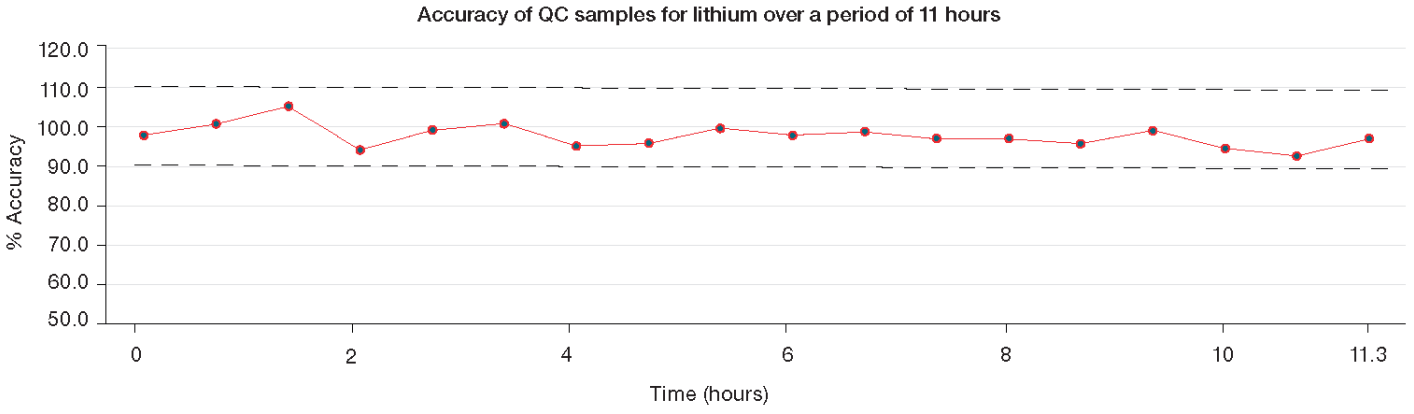

Figure 2. Percent accuracy observed for QC standards containing 3,000 mg·L^{-1} of lithium

Table 4. Spiked concentrations of Li and average percent recovery (n=6)

Spiked concentration of Li ($mg \cdot L^{-1}$)	Recovered concentration ($mg \cdot L^{-1}$)	%Recovery	%RSD
10	10.5	105.0	4.0
100	100.3	100.3	2.2

System robustness

Since analysis of high dissolved solids containing samples such as brine solutions with ICP-OES is a challenge, the proposed method was assessed thoroughly for matrix tolerance and its performance robustness. An internal standard solution containing 10 $mg \cdot L^{-1}$ of yttrium (Y) was added online throughout the analytical batch of over 11 hours of continuous measurement where more than 200 brine samples were analyzed. Three different wavelengths of Y were measured in both axial and radial view, and their response was monitored against the initial intensity of each wavelength recorded at the beginning of the analytical batch. Figure 3 shows a graphical representation of the internal standard response directly taken from the Qtegra ISDS Software. This figure shows that all internal standard wavelengths read back in the range of between 90% and 115% of their initial values, indicating that the proposed analytical setup has excellent robustness and is suitable for longer batch analysis containing these types of challenging matrices.

Upon completion of the long-term measurement, sample introduction system components such as the nebulizer, spray chamber, injector, and torch were examined carefully for salt deposition or any possible damage. There was no significant salt deposition observed anywhere in the sample introduction components and no damage or deterioration of these components was visible.

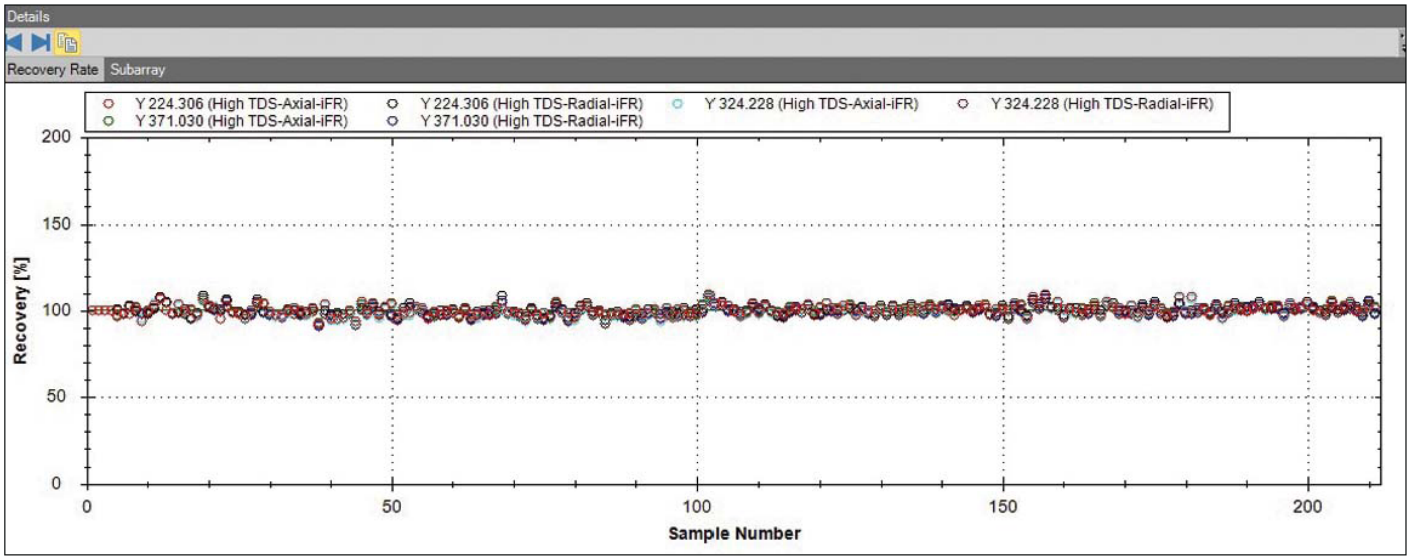

Figure 3. Signal stability of the internal standard wavelengths during the more than 11-hour analytical run

Summary and conclusions

- The quality of the analytical data observed in this study shows that the iCAP PRO XP ICP-OES equipped with a Burgener Mira Mist nebulizer and sheath gas adaptor is a reliable and robust analytical solution for the analysis of brine solutions and similar, equally challenging samples.
- The wide linear dynamic range established for lithium (up to 5,000 mg·L^{-1}) together with the high degree of accuracy and precision across this linear range enables reliable quantification of lithium with varying concentrations, without the need for sample pre-treatments such as dilution. This enables quick sample turnaround, increasing the overall productivity of analytical laboratories involved with analysis of brine and other similar high matrix samples.
- The iCAP PRO series ICP-OES Duo instrument, with its vertical torch configuration and sheath gas adaptor, offers great flexibility for analyzing a wide range of analytes at both higher concentrations and trace levels in a single analytical measurement with robustness equivalent to that of radial ICP-OES instruments.
- The axial mode of the iCAP PRO Series ICP-OES provides significantly lower detection limits and consistently accurate analytical data while analyzing samples with high dissolved solids, enabling reliable measurement of analytes with emission wavelengths distributed across the entire wavelength range.
- The Qtegra ISDS Software simplifies method optimization through various available auto-tune options and provides useful analytical information with customizable report templates, reducing the manual effort required for data evaluation, re-processing, and results reporting.

References

1. Electric Vehicles, IEA Report, November 2021, **https://www.iea.org/reports/electric-vehicles**
2. Lithium Recovery from Brines Including Seawater, Salt Lake Brine, Underground Water and Geothermal Water, January 2020, **https://www.intechopen.com/chapters/70887**
3. Thermo Scientific Application Note 44470: High matrix tolerance of the Thermo Scientific iCAP PRO XP ICP-OES Radial and Duo equipped with a ceramic torch and sheath gas adapter, **https://assets.thermofisher.com/TFS-Assets/CMD/Application-Notes/an-44470-icp-oes-metals-brine-ceramic-torch-sheath-an44470-en.pdf**

Learn more at **thermofisher.com/icp-oes**

Sensitive determination of elements in lithium batteries using the Thermo Scientific iCAP PRO XP ICP-OES

Authors: Jingfang He,[1] Xiaobo Li,[1]
Fei Wang,[1] Miao Jing,[1] and Jianfeng Cui[2]
[1]Thermo Fisher Scientific, Shanghai, China
[2]Thermo Fisher Scientific, Bremen, Germany

Keywords: Lithium battery, iCAP PRO XP ICP-OES, cathode material, ternary materials, fast detection, robust analysis, quantification

Goal

This note demonstrates a fast analytical method for the determination of major and trace elements in the ternary cathode material of lithium batteries using the Thermo Scientific™ iCAP™ PRO Series ICP-OES.

Introduction

The continuous development of lithium-ion batteries and the research into their materials is at the forefront of the energy sector as it moves away from fossil fuels. To regulate the quality of production, the Chinese national standard method YS/T 798-2012 was established. All new lithium battery developments must meet the requirements of these standards. The ternary material of lithium batteries typically contains lithium, nickel, cobalt, and manganese, and potassium aluminate as its cathode material. In recent years, lithium batteries using ternary materials as cathode materials have gradually replaced nickel-metal hydride batteries, lithium cobalt batteries and lithium-ion phosphate batteries. This is due to the high capacity, good cycle stability (battery life), and moderate cost of the new battery type. The proportion and content of the main elements in the ternary cathode material can affect the performance and cost of the lithium battery significantly and the content of impurities in the ternary material alters the safety of the battery. Therefore, the accurate determination and quantification of the main elements, as well as trace impurities in the ternary cathode material, becomes particularly important.

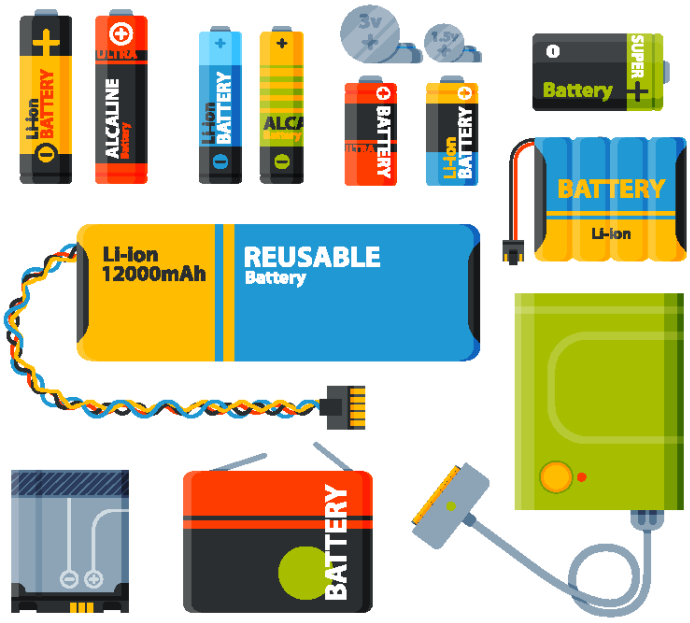

ThermoFisher SCIENTIFIC

Experimental

Standards and sample preparation

A series of calibration standards were prepared to determine the elemental impurities and major elements within the lithium battery material. Multi-element standard solutions were prepared by diluting single-element stock standards with 2% hydrochloric acid (elements in this solution are listed in Table 2, on page 3). The standard concentrations of analytes defined as impurities were 0, 0.05, 0.10, 0.50, 1.0, and 5.0 mg·L^{-1} in a mixed standard solution To determine the concentration of major elements, calibration standards containing lithium at 0, 2, 5, and 10 mg/L and Co, Ni, and Mn at 0, 10, 20, and 50 mg/L were prepared.

To prepare the sample, an aliquot of 0.25 g of ternary cathode material was weighed into a polytetrafluoroethylene beaker. A volume of 10 mL hydrochloric acid (37%, Sinopharm) was added, and the mixture was heated on a hot plate for digestion at just below the boiling point of the acid until all the sample powder dissolved to a clear solution. After the sample cooled, it was transferred to a 50 mL volumetric flask and filled to volume with ultrapure water with a resistivity of 18.2 MΩ·cm (Barnstead™ water purification system, Thermo Scientific™) A preparation blank was also prepared using the same method. For the analysis of elemental impurities, the sample solution was analyzed undiluted, while for the analysis of major elements, the sample solution was diluted 50-fold.

Instrument parameters and method optimization

The iCAP PRO XP ICP-OES Radial system was selected for the application, the lower detection limits offered by the axial view of a dual view system were not required for this application. The system utilizes intelligent Full Range (iFR) mode and captures the complete spectrum in the range of 167 to 852 nm in one exposure. This not only reduces the overall analysis time, but also the operational cost as the argon gas consumption is also reduced. The parameters used for the analysis are shown in Table 1. The standard and the sample solutions were introduced into the plasma to collect the spectral data information of all elemental impurities. After data collection was completed, each spectrum was displayed by the subarray spectrum overlay functionality of the Thermo Scientific™ Qtegra™ Intelligent Scientific Data Solution™ (ISDS) Software (Figure 1). Using the wavelength library in the Qtegra ISDS Software, potential interferences can be avoided. The adjustment and optimization of the array position allows for more reasonable data collection points.

Table 1. Instrument parameters used for the analysis

Parameter	Setting
Peristaltic pump speed	50 rpm
RF power	1150 W
Nebulizer gas	0.6 L·min^{-1}
Auxiliary gas	0.5 L·min^{-1}
Cooling gas	12 L·min^{-1}
Viewing mode	Radial
Nebulizer	Glass concentric nebulizer
Torch	EMT quartz torch
Injector	2.0 mm quartz injector
Spraychamber	Glass cyclonic spraychamber
Radial viewing height	10 mm
Exposure time	10 s
Analysis mode	iFR

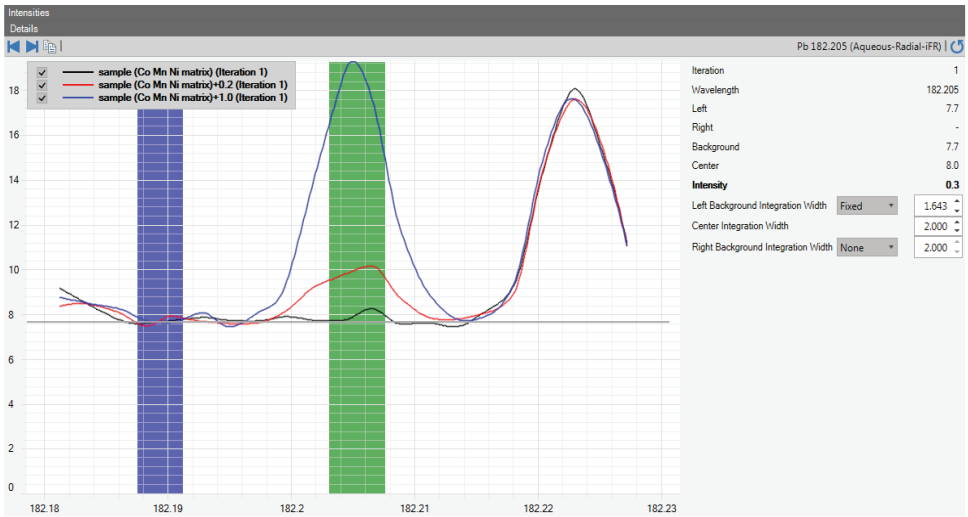

Figure 1. Spectrum of Pb at 182.205 nm, showing no interference in the central observation area

Results and discussion

The correlation coefficients R^2 of the obtained calibration curves were higher than 0.9995 for all analytes, indicating excellent linearity of the wavelengths selected (Table 2).

Table 2. Correlation coefficients (R^2) determined from calibration curves of each analyte and concentration range.

Element and wavelength (nm)	Correlation coefficient R^2	Concentration range (mg·L^{-1})
Al 396.152	0.9997	0–5
As 189.042	>0.9999	0–5
Ba 455.403	>0.9999	0–5
Ca 393.366	>0.9999	0–5
Cd 214.438	>0.9999	0–5
Cr 206.157	>0.9999	0–5
Cu 324.754	>0.9999	0–5
Fe 259.940	>0.9999	0–5
K 766.490	0.9995	0–5
Mg 285.213	>0.9999	0–5
Mo 204.598	>0.9999	0–5
Na 589.592	0.9995	0–5
P 213.618	>0.9999	0–5
Pb 182.205	0.9995	0–5
S 180.731	>0.9999	0–5
Sb 206.833	>0.9999	0–5
Si 212.412	0.9995	0–5
Sn 189.989	>0.9999	0–5
Ti 334.941	>0.9999	0–5
V 309.311	>0.9999	0–5
Zn 206.200	>0.9999	0–5
Li 670.791	>0.9999	0–10
Mn 191.510	>0.9999	0–50
Ni 221.647	>0.9999	0–50
Co 228.616	>0.9999	0–50

The unspiked ternary cathode material sample was analyzed for impurities and the results are shown in Table 3.

The sample was spiked with 1.0 mg·L^{-1} of Al and S and 0.2 mg·L^{-1} of all other elements. The recoveries are all in the range of 90% to 110% as shown in Figure 2.

Table 3. Quantification of detected elemental impurities in an unspiked ternary cathode sample as well as instrument and method detection limits. <LOD stands for values below the detection limit.

Element and wavelength (nm)	Concentration in the solid sample (mg·kg^{-1})	Instrument detection limit in solution (mg·L^{-1})	Method detection limit in solid (mg·kg^{-1})
Al 396.152	1067	0.0098	1.959
As 189.042	2.06	0.0082	1.631
Ba 455.403	19.16	0.0001	0.020
Ca 393.366	62.13	0.0001	0.010
Cd 214.438	0.37	0.0003	0.064
Cr 206.157	1.26	0.0015	0.304
Cu 324.754	1.64	0.0025	0.500
Fe 259.940	18.62	0.0012	0.243
K 766.490	30.85	0.0090	1.808
Mg 285.213	103	0.0006	0.124
Mo 204.598	<LOD	0.0052	1.035
Na 589.592	102	0.0052	1.030
P 213.618	<LOD	0.0054	1.088
Pb 182.205	7.02	0.0142	2.838
S 180.731	805.39	0.0073	1.461
Sb 206.833	<LOD	0.0192	3.835
Si 212.412	65.39	0.0102	2.039
Sn 189.989	2.41	0.0065	1.296
Ti 334.941	4.54	0.0008	0.166
V 309.311	<LOD	0.0014	0.275
Zn 206.200	1.19	0.0007	0.147

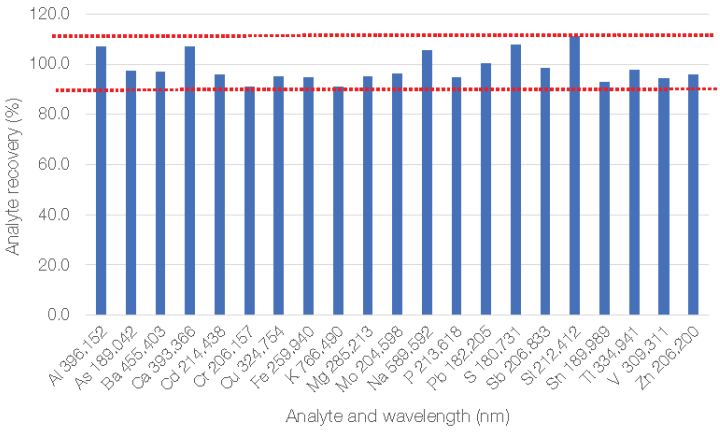

Figure 2. Calculated recoveries (%) for target analytes in the spiked ternary material samples. Spiked at 1.0 mg·L^{-1} for Al and S and with 0.2 mg·L^{-1} for all other elements.

thermoscientific

A stability test was conducted on the major elements in the sample by analyzing the stability test sample every 20 minutes over a period of 2 hours. The RSDs are well below 1% for all analytes and no drift is observed (Table 4).

Table 4. Major element concentration (in mg·kg^{-1}), average values, standard deviation (SD) values as well as repeatability data as % RSD (n=7) of the test sample

Measurement Nr/Element	Li 670.791	Mn 191.510	Ni 221.647	Co 228.616
1	6.99	11.06	34.56	12.33
2	7.01	11.08	34.07	12.16
3	6.95	11.24	34.54	12.34
4	7.06	11.20	34.66	12.34
5	7.05	11.17	34.62	12.29
6	7.03	11.11	34.43	12.34
7	6.98	11.21	34.81	12.46
Average	7.01	11.15	34.53	12.32
SD	0.040	0.068	0.234	0.089
RSD%	0.574	0.613	0.677	0.721

Conclusion

In this application note, a Thermo Scientific iCAP PRO XP ICP-OES Radial system was used to establish a rapid detection method for the determination of major elements and trace impurities in a ternary cathode material used in lithium batteries.

For the impurity elements, recovery values of between 90% and 110% were achieved, as calculated from the spiked samples. For interferences from complex matrices, such as cobalt-nickel-manganese-lithium matrix and the spectral interference of elements, such as nickel and manganese, the iCAP PRO XP ICP-OES system uses a high-resolution optical system that can obtain accurate test results for each element.

All performance specifications meet the testing requirements specified by the national standard method YS/T 798-2012.[1] The iCAP PRO XP ICP-OES system has an ultra-high sensitivity and stability for the detection of elements with characteristic wavelengths in the far ultraviolet region (e.g., S 180.731 nm, Pb 182.205 nm).

The iCAP-PRO XP ICP-OES system performance for major elements, such as nickel, cobalt, manganese, and lithium, demonstrated excellent levels of precision (with % RSD <1%) and accuracy (spike recoveries with the range 90% to 110%).

Overall, the analytical solution employed in this study with the iCAP PRO XP ICP-OES system meets all analytical requirements for routine or research laboratories that aim to analyze elements in ternary materials of lithium batteries.

Reference

1. YS/T 798-2012: China National non-ferrous metal industry standards, Lithium nickel cobalt manganese oxide, Ministry of Industry and Information Technology of the People's Republic of China.

Find out more at **thermofisher.com/ICP-OES**

ThermoFisher SCIENTIFIC

thermo scientific

CASE STUDY
MEET BATTERY RESEARCH CENTER

Orbitrap GC-MS Technology Provides New Insight into Lithium Ion Battery Degradation

"We can see many more compounds that we hadn't seen before—including intermediates from the start of the reaction—which helps us establish reaction mechanisms."

—Dr. Sascha Nowak, Head of the Analytics and Environment Division, MEET Battery Research Center, University of Münster

Advancing lithium-Ion battery technology

From consumer electronics to electric vehicles, the growing demand for better-performing, safer, and less costly batteries has led researchers to focus on improving several aspects of lithium ion battery technology. Münster Electrochemical Energy Technology (MEET), the battery research center at Münster University, aims to address electrolyte aging, a major factor affecting lithium ion battery life. Using the Thermo Scientific™ Q Exactive™ GC Orbitrap™ GC-MS/MS system, MEET's Analytics and Environment division gains a broader and deeper understanding of their samples that in turn provides new insight into the complex reaction mechanisms involved in electrolyte aging. Ultimately these insights will enable the research team to identify additives to curtail, or even halt, electrolyte aging.

ThermoFisher SCIENTIFIC

Electrolyte aging

Of the basic components of a lithium-ion battery, the electrolyte provides a conductive medium for lithium ions to move between electrodes. It consists of conducting solids, which are highly fluorinated, and various solvents. Lithium hexafluorophosphate ($LiPF_6$)-based electrolytes with mixtures of aprotic organic carbonate solvents are commonly used. As the electrolyte degrades, several decomposition complex products are formed, such as fluorophosphates and organoflurophosphates. Using a variety of analytical approaches, researchers at MEET's Analytics and Environment division identify and quantify these compounds as they are generated during aging.

> "We have solvents that are highly concentrated, and the Q Exactive instrument is robust enough to handle these very well; such that we can do trace analysis."
>
> —Dr. Sascha Nowak

Research challenges

There are significant challenges associated with this research. To begin, the degradation mechanisms, and the resulting degradation products, are often unknown and not described in published literature. Thus there are no reference materials available, and research published thus far has used low-resolution gas chromatography—mass spectrometry techniques (GC-MS)[1, 2], nuclear magnetic resonance (NMR)[3], and other techniques to identify compounds. Often these approaches do not provide sufficient structural information or sensitivity to detect and identify all compounds of interest. Moreover, some of the analytes are very small, low-molecular-weight molecules that, if fragmented, would be below the detection range of standard triple quadrupole GC-MS systems.

Another challenge is the complexity of the sample matrices studied, which are rich in highly fluorinated compounds and concentrated solvents. Matrix effects can lead to interferences, reduce instrument sensitivity, and increase instrument maintenance requirements.

© WWU/MEET

"Because we've seen so many more compounds, the Q Exactive GC reduces the time it takes us to establish complete reaction mechanisms. And though in the future we will spend more time identifying all of these compounds; because we get additional fragmentation information from the Q Exactive, we will be able to do it much faster."

—Dr. Sascha Nowak

Q Exactive GC Orbitrap GC-MS/MS solution

Using the Q Exactive GC Orbitrap GC-MS/MS system, MEET is now able to obtain lower detection limits and richer information in the form of accurate mass fragment ions and molecular ions produced by chemical ionization (CI). Compared to other approaches, this additional information enables MEET to detect and identify many more electrolyte degradation products. This in turn has enabled MEET to determine previously unknown, or confirm suspected, reaction mechanisms.[4]

High-capacity component detection with low limits of detection and matrix tolerance

Using other GC-MS technology, MEET typically detected about eight or nine decomposition products. When the same samples were analyzed with the Q Exactive GC Orbitrap GC-MS/MS system, MEET detected over forty compounds, a remarkable increase. MEET also found never-before-detected non-fluorinated hydrogen, carbon and oxygen-based compounds that improve their understanding of previously unknown mechanisms of solvent decomposition.

The new compounds, many of which were previously unknown early intermediates, were detected due to the sensitivity and selectivity of the Orbitrap GC-MS/MS instrument. Compared to other GC-MS approaches, the Q Exactive GC Orbitrap GC-MS/MS system improved detection limits from low mg/L to low ng/L levels, even in complex lithium-ion battery matrices.

Though the samples are rich in highly fluorinated compounds and concentrated solvents, the Q Exactive GC Orbitrap system provided exceptional robustness for trace-level analysis under these conditions. Continuous operation over the duration of research projects is commonly achieved.

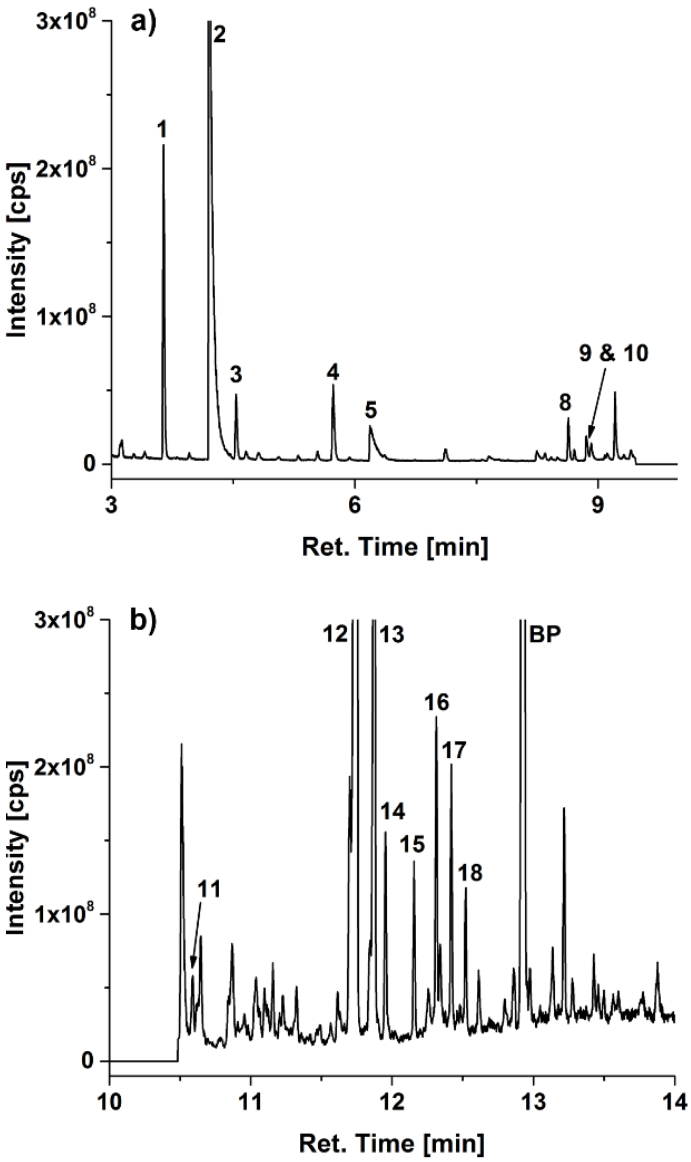

Q Exactive GC Orbitrap GC-MS/MS system chromatograms of electrolyte extracted from an 18650 cell cycled at 20 °C diluted 1:10 in DCM with focus on the retention time from 3 to 10 min (a) and 10 to 14 min (b).

Conclusion

The Q Exactive GC Orbitrap system brings together the power of high-resolution GC and high-resolution accurate-mass (HRAM) Orbitrap MS to provide more comprehensive characterization of samples in discovery analysis. With the Q Exactive GC-MS/MS system, MEET accesses the exact mass information of more compounds, at significantly lower levels. The result is a broader and deeper understanding of the complex reaction mechanisms involved in electrolyte aging.

About Sascha Nowak

Sascha Nowak studied chemistry at the University of Münster, and obtained his Ph.D. in Analytical Chemistry.
In 2009, Dr. Nowak joined the working group of Prof. Winter at the MEET Battery Research Center at Münster University as a postdoctoral researcher where he established the Analytical Department. From 2010—2012, he headed the competence areas Analytics and Recycling, and since 2012, has headed MEET's Analytics and Environment division, which mainly focuses on electrolyte aging, transition metal migration, and surface investigations, recycling, second life, and toxicological investigations.

About Münster Electrochemical Energy Technology (MEET)

Münster Electrochemical Energy Technology (MEET) is the battery research center at Münster University. It comprises an international team of about 150 scientists who work on the research and development of innovative electrochemical energy storage devices with high energy density, longer durability, and maximum safety. The aim is to improve batteries for use in electric cars and stationary energy storage systems at the lowest possible cost. MEET strives to further enhance the competitiveness of its partners in battery research—in particular on lithium-ion technology—both regionally and nationally.

The Analytics and Environment division is one of the three divisions at MEET. An important area of research for this division is electrolyte aging, which includes examination of electrolytes and migration of active material into the electrolyte, formation and properties of potentially toxic substances, and re-deposition of the migrated active material on the anode surfaces. The division also deals with the evaluation and development of recycling and second-life procedures to allow recovery and reuse of individual battery components or complete batteries.

References

1. Mönnighoff, X.; Murmann, P.; Weber, W.; Winter, M.; and Nowak, S. Post-Mortem Investigations of Fluorinated Flame Retardants for Lithium Ion Battery Electrolytes by Gas Chromatography with Chemical Ionization. Electrochimica Acta. 2017. 246: 1042–1051.
2. Mönnighoff, X.; Friesen, A.; Konersmann, B.; Horsthemke, F.; Grützke, M.; Winter, M.; Nowak, S. Supercritical Carbon Dioxide Extraction of Electrolyte from Spent Lithium Ion Batteries and its Characterization by Gas Chromatography with Chemical Ionization. Journal of Power Sources. 2017. 352, 56–63.
3. Wiemers-Meyer, S.; Winter, M.; and Nowak, S. Phys. Mechanistic insights into lithium ion battery electrolyte degradation–a quantitative NMR study. Phys. Chem. Chem. Phys. 2016.18, 26595–26601.
4. Horsthemke, F.; Friesen, A.; Mönnighoff, X.; Stenzel, Y.P.; Grützke, M.; Andersson, J.; Winter, M.; Nowak, S.; 2017. Fast Screening Method to Characterize Lithium Ion Battery Electrolytes by Means of Solid Phase Microextraction–Gas Chromatography-Mass Spectrometry. RSC Advances. 2017. 7: 46989–46998.

Find out more at **thermofisher.com/OrbitrapGCMS**

ThermoFisher SCIENTIFIC

APPLICATION NOTE 000394

Analysis of electrolyte components of lithium-ion batteries using gas chromatography-mass spectrometry

Author: Thermo Fisher Scientific Inc.

Keywords: Single quadrupole GC-MS, ISQ 7000 single quadrupole mass spectrometer, Li-battery electrolyte, TraceGOLD TG-5MS column, carbonates

Goal

At present, methods and literature references for determining electrolyte composition are limited. The purpose of this work is to establish a simple and efficient gas chromatography–mass spectrometry detection method for a sensitive and fast determination of lithium-ion battery electrolyte composition and content.

Introduction

The electrolyte in a lithium-ion battery is the carrier of positive lithium ions between the cathode and anode. It is generally made of lithium salts dissolved in organic solvents. Electrolyte solutions must enable the Li-ions to transport freely, requiring both high dielectric constant and low viscosity. For this reason, suitable electrolyte solutions are a mixture of cyclic and linear carbonate esters, in which the exact composition plays a key role in the performance of lithium-ion batteries.

Gas chromatography–mass spectrometry can be used to provide the qualitative and quantitative composition of the Li-battery electrolyte, with a direct injection of diluted samples. In this study, a simple GC-MS method has been developed to detect ester compounds in a concentration range of 3.0 µg/L to 30.0 µg/L.

Experimental

Instrumentation

A Thermo Scientific™ TRACE™ 1310 GC connected to a Thermo Scientific™ ISQ™ 7000 single quadrupole mass spectrometer with an electron impact (EI) ionization source was used. A Thermo Scientific™ AS1310 liquid autosampler performed the injection.

The separation of the ester compounds was achieved on a Thermo Scientific™ TraceGOLD™ TG-5MS, 30 m, 0.25 mm i.d., 0.25 µm film thickness, capillary column (P/N 26098-1420).

Reagents and standards

A standard mixture of ester compounds at ≥97% concentration was used to prepare diluted standard solutions in ethyl acetate at five levels of concentration: 4, 10, 20, 50, and 100 mg/L.

ThermoFisher SCIENTIFIC

Sample preparation

The sample preparation consisted of dilution of the electrolyte sample to a suitable concentration with ethyl acetate for direct injection into the GC-MS.

GC-MS experimental conditions

The GC-MS experimental conditions are reported in Tables 1 and 2.

Table 1. GC-MS method parameters

GC-MS method parameter	Value
GC column	TraceGOLD TG-5MS 30 m, 0.25 mm i.d., 0.25 µm film thickness (P/N 26098-1420)
GC oven temperature	50 °C (3 min), 10 °C/min to 240 °C (3 min)
Injector	SSL
Injector temperature	280 °C
Injection mode	Split 50:1
Injection volume	1 µL
Carrier gas	Helium at 1 mL/min constant flow
MS ion source temperature	EI source at 300 °C
Transfer line temperature	280 °C
Acquisition mode	Full scan 40–200 *m/z*

Table 2. Standard mixture composition, retention times, and selected ions

#	Compound	RT (min)	Quant ion	Qual ion
1	EMC (ethyl methyl carbonate)	2.70	45	77
2	VC (vinylene carbonate)	3.38	86	42
3	DEC (diethyl carbonate)	3.96	91	45
4	PP (n-propyl propionate)	4.41	75	57
5	FEC (fluoroethylene carbonate)	5.28	62	106
6	EC (ethylene carbonate)	7.38	88	43
7	PC (propylene carbonate)	7.80	57	87
8	PS (1,3-propane sultone)	11.03	58	122

Results and discussion

Different dilution solvents, including ethyl acetate, acetone, hexane, toluene, ethanol, and trichloromethane, were compared with respect to their dissolving power. The dissolving effect for the target ester compounds was acceptable only with ethyl acetate, which was selected as the dilution solvent for this study. Five levels of concentration were prepared (4, 10, 20, 50, and 100 mg/L) and used to verify the linear response, the limit of detection (LOD), the limit of quantitation (LOQ), and the area counts repeatability (RSD%). An example of the total ion chromatogram of the standard mixture at 20 mg/L is shown in Figure 1.

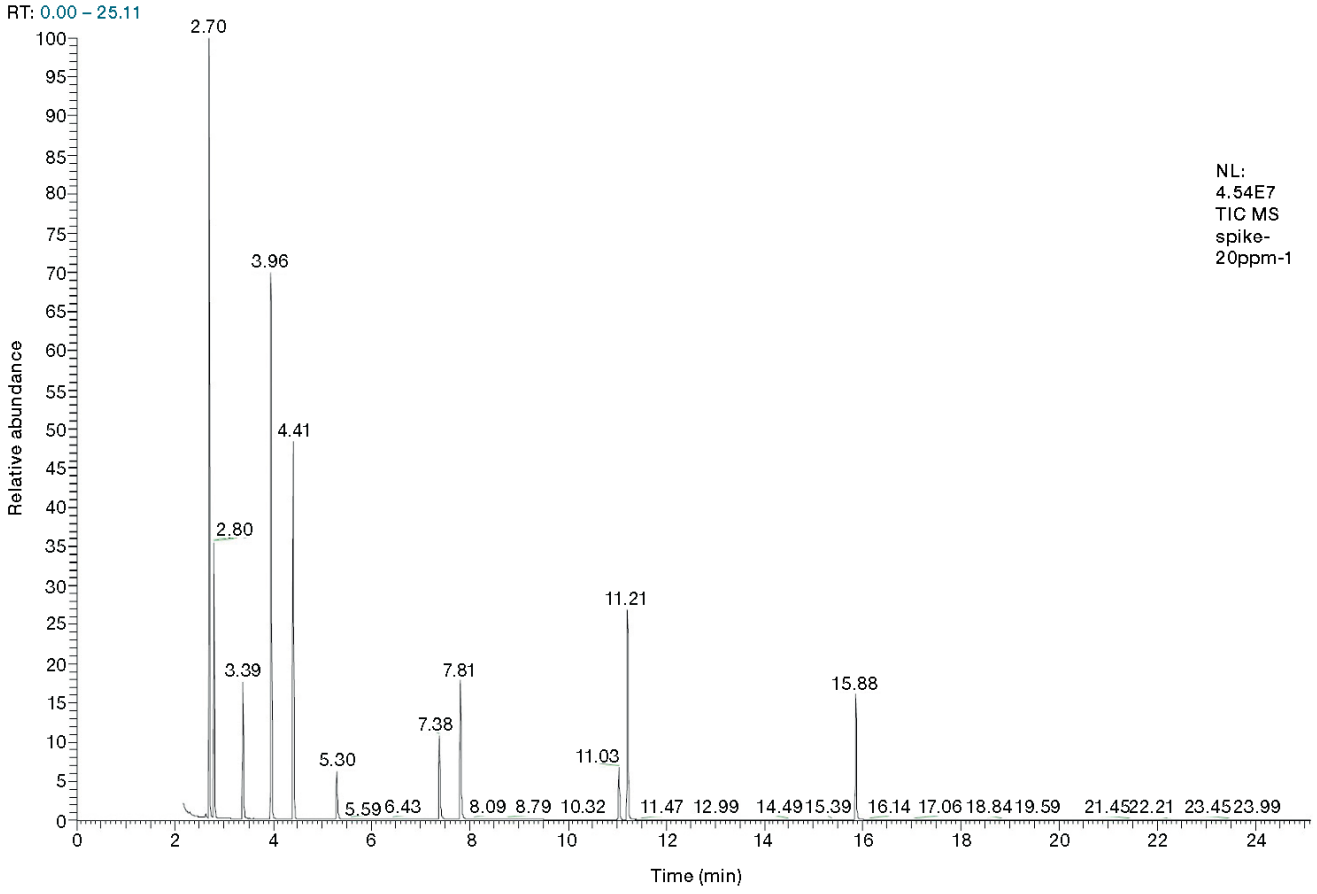

Figure 1. Total ion chromatogram of the standard mixture of esters at 20 mg/L

The linear calibration curves obtained for the ester compounds are reported in Figure 2, showing an excellent linear relationship with correlation coefficients >0.999 between 4.0 and 100.0 mg/L (Table 3).

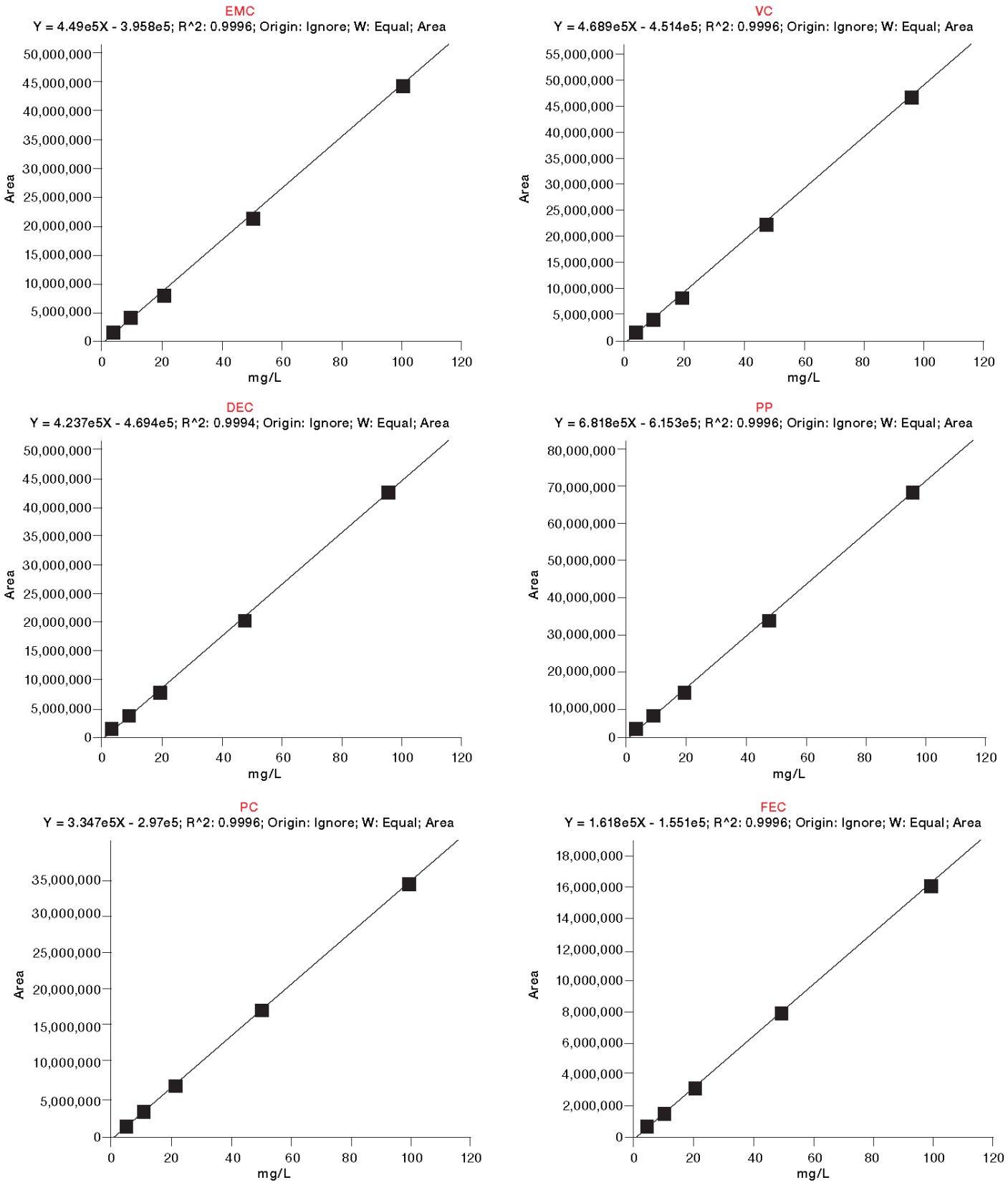

Figure 2. Linear relationship plots for the ester compounds under study

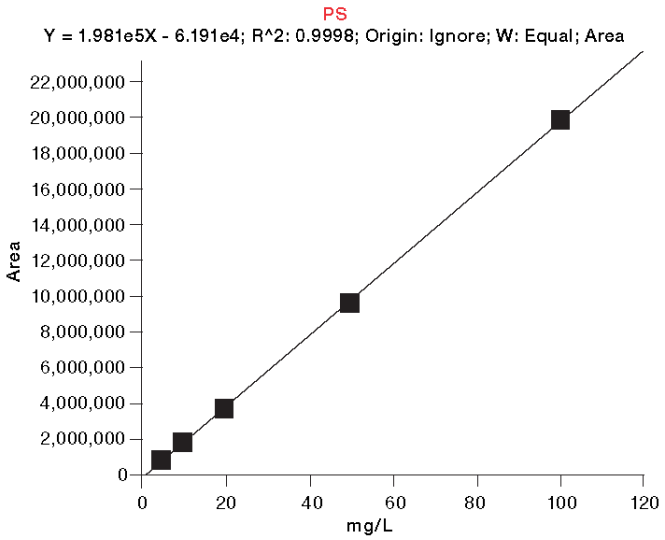

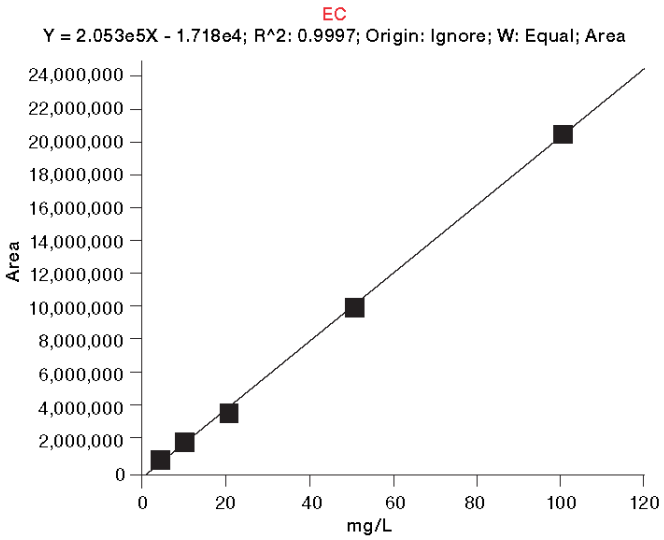

Figure 2 continued. Linear relationship plots for the ester compounds under study

Table 3. Retention time, response linearity, and limit of detection (LOD) for the target analytes

#	Compound	RT (min)	Linear range (mg/L)	Correlation coefficient (R^2)	LOD (µg/L)
1	EMC (ethyl methyl carbonate)	2.70	4.0–100.0	0.9996	3.0
2	VC (carbonated ethyl carbonate)	3.38	4.0–100.0	0.9996	9.0
3	DEC (diethyl carbonate)	3.96	4.0–100.0	0.9994	4.0
4	PP (propylene acid)	4.41	4.0–100.0	0.9996	4.5
5	FEC (fluorocarbonate olesters)	5.28	4.0–100.0	0.9996	28.0
6	EC (ethylene carbonate)	7.38	4.0–100.0	0.9997	32.0
7	PC (acrylic carbonate)	7.80	4.0–100.0	0.9996	19.0
8	PS (1,3-propylene sulfonate lactone)	11.03	4.0–100.0	0.9998	25.0

The limit of detection was extrapolated on the extracted quantification ion, considering a signal-to-noise ratio (S/N) of 3. The LODs for the target ester compounds are reported in Table 3. Full scan acquisition was applied for electrolyte composition screening. However, the sensitivity for the target compounds can be lowered by 1–2 orders of magnitude if necessary by acquiring the signal in Selected Ion Monitoring (SIM) mode.

Sample analysis

Using the established analysis method, the lithium-ion battery electrolyte was diluted with ethyl acetate and spiked with the 20 mg/L standard mixture to evaluate the recovery and the repeatability over six repeated injections, as reported in Table 4.

Table 4. Target analyte recovery and repeatability (n=6)

#	Compound	Recovery (%)	RSD (%)
1	EMC (ethyl methyl carbonate)	105.3	3.96
2	VC (carbonated ethyl carbonate)	101.6	1.34
3	DEC (diethyl carbonate)	104.6	3.74
4	PP (propylene acid)	95.2	3.62
5	FEC (fluorocarbonate olesters)	96.3	3.21
6	EC (ethylene carbonate)	94.3	4.16
7	PC (acrylic carbonate)	92.4	4.14
8	PS (1,3-propylene sulfonate lactone)	97.4	3.15

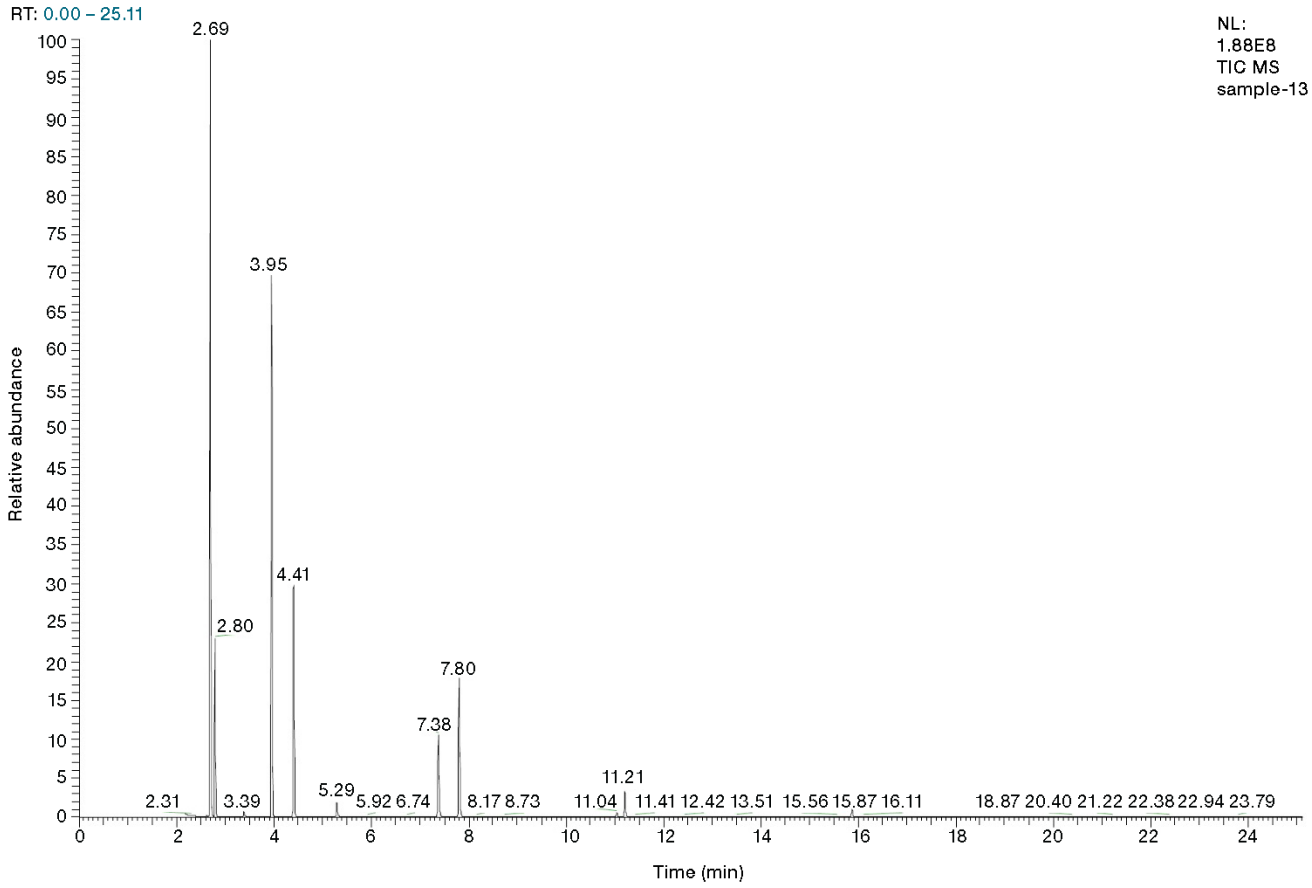

Figure 3. Total ion chromatogram of a diluted electrolyte sample

Conclusion

The GC-MS method is a simple, reliable, and accurate approach for lithium-ion battery electrolyte composition analysis and quality control requirements. The samples can be simply diluted with a suitable solvent and directly injected into the GC-MS system.

The results show very good recovery for the target ester compounds of 92.4.3–105.3%, demonstrating the high accuracy of the method. The excellent precision of the method was also demonstrated, with an RSD value ≤4.16% over six repeated injections.

Full scan acquisition can be applied with good sensitivity. SIM acquisition can be utilized to lower the limits of detection for the method.

References

1. Lei, Y. Some organic additives are positive for the full-molytan liquid flow battery. Study on the effects of electrolyte properties. Central South University.
2. Sun, S. New separation for lithium-ion batteries. Research on sub-liquid electrolytes. Harbin University of Technology.

Find out more at **thermofisher.com**

ThermoFisher SCIENTIFIC

Technical note | 000413

Mass spectrometry

Identification of lithium-ion battery degradation products using GC Orbitrap mass spectrometry

Authors

Christoph Peschel[1], Sascha Nowak[1], and Dominic Roberts[2]

[1]Münster Electrochemical Energy Technology (MEET), University of Münster, Germany
[2]Thermo Fisher Scientific, Hemel Hempstead, United Kingdom

Keywords

Lithium-ion battery, electrolyte degradation products, Orbitrap Exploris GC, Orbitrap technology, high resolution accurate mass, mass accuracy, gas chromatography, research

Goal

To demonstrate the identification of characteristic carbonate substructures and electrolyte solvent degradation in lithium-ion batteries using the Thermo Scientific™ Orbitrap Exploris™ GC mass spectrometer.

Introduction

From consumer electronics to electric vehicles, the growing demand for better-performing, safer, and less costly batteries has led researchers to focus on improving several aspects of lithium-ion battery technology. The experiments shown in this study by Münster Electrochemical Energy Technology (MEET) aim to investigate electrolyte aging, a major factor affecting lithium-ion battery life. Using gas chromatography coupled to high-resolution accurate-mass mass spectrometry (GC-HRAM-MS), MEET's Analytics and Environment division gains the flexibility and data quality to have a deeper understanding of their samples. This in turn provides detailed insight into the complex reaction mechanisms involved in electrolyte aging. Ultimately these discoveries will enable the research team to identify additives to curtail, halt, or even tailor electrolyte aging.

Of the basic components of a lithium-ion battery, the electrolyte provides a conductive medium for lithium ions to move between electrodes. It consists of conducting salts, which are highly fluorinated, and various solvents. Lithium hexafluorophosphate ($LiPF_6$)-based electrolytes dissolved in mixtures of aprotic organic carbonate solvents are commonly used. As the electrolyte degrades, several decomposition complex products are formed, such as carbonate oligomers, fluorophosphates, and organoflurophosphates. Using a variety of analytical approaches, researchers at MEET's Analytics and Environment division identify and quantify these compounds as they are generated during aging.

There are significant challenges associated with this research. To begin, the degradation mechanisms and the resulting degradation products are often unknown and not described in published literature. Thus, there are no reference materials available, and research published to date has used low-resolution gas chromatography–mass spectrometry techniques (GC-MS),[1-3] nuclear magnetic resonance (NMR),[4] and other techniques to identify compounds. Often these approaches do not provide sufficient structural information or sensitivity to detect and identify all compounds of interest. Another challenge is the complexity of the sample matrices studied, which are rich in highly fluorinated compounds and concentrated solvents. Matrix effects can lead to interferences, reduce sensitivity, and increase instrument maintenance requirements. Instrument sensitivity is a significant benefit as it allows a high split or dilution to be applied to protect the system from high concentration components, while allowing detection of the trace levels of decomposition species of interest in electrolyte aging.

In this study the identification of known carbonate dimers using GC-HRAM-MS is shown as part of a targeted analysis in an aged electrolyte matrix. Subsequently, the identification of unknown related carbonates identified from similar retention and fragmentation profiles is investigated and confirmed using both electron ionization (EI) and positive chemical ionization (PCI) with GC Orbitrap mass spectrometry.

Experimental

Sample and standard preparation

The pure aged electrolyte was collected by centrifugation of the separator and negative electrode of the battery after cell formation. For precipitation of the GC-harmful $LiPF_6$ conducting salt, the electrolyte was diluted in dichloromethane (1/100; v/v) and stored at 3 °C overnight. The supernatant was taken for analysis.

Instrument and method setup

Automatic sample injection was performed using a Thermo Scientific™ TriPlus™ RSH autosampler, and chromatographic separation was performed using a Thermo Scientific™ TRACE™ 1310 GC system fitted with a Thermo Scientific™ TraceGOLD™ TG-5SilMS 30 m × 0.25 mm i.d. x 0.25 µm film capillary column with a 5 m integrated guard (P/N 26096-1425). Finally, a Thermo Scientific Orbitrap Exploris GC-MS was used for accurate mass measurements in full-scan mode at 60,000 mass resolution (FWHM at *m/z* 200). Data processing processing was performed using Thermo Scientific™ FreeStyle™ software. Additional details of instrument parameters are displayed in Tables 1–3.

Table 1. GC and injector conditions

TRACE 1310 GC system parameters			
Injection volume	1.0 µL		
Liner	Thermo Scientific™ LinerGOLD™ Split/splitless with quartz wool (P/N 453A2265)		
Inlet	250 °C		
Carrier gas, flow	He, 1.16 mL/min		
Inlet module and mode	SSL, Split		
Split ratio	100 (EI), 10 (PCI)		
Purge flow	2 mL/min		
Column	TraceGOLD TG-5SilMS 30 m × 0.25 mm i.d. x 0.25 µm film (P/N 26096-1425)		
Oven temperature program	**Rate (°C/min)**	**Target temperature (°C)**	**Hold time (min)**
Initial	-	40	1.0
Ramp 1	3.0	60	0
Ramp 2	30.0	260	2.0
Run time	16.3	-	-

Table 2. Orbitrap Exploris GC-MS parameters (EI)

Orbitrap Exploris GC mass spectrometer parameters	
Transfer line	250 °C
Ionization type	EI
Ion source	200 °C
Electron energy	70 eV
Acquisition modes	Full-scan
Mass range	35–500 Da
Resolving power	60,000 (FWHM at *m/z* 200)

Table 3. Orbitrap Exploris GC-MS parameters (PCI)

Orbitrap Exploris GC mass spectrometer parameters	
Transfer line	250 °C
Ionization type	PCI
Ion source	300 °C
CI reagent gas	Ammonia (3.5 purity)
CI gas flow rate	2.5 mL/min
Acquisition modes	Full-scan
Mass range	50–500 Da
Resolving power	60,000 (FWHM at *m/z* 200)

Results and discussion

The objective of the experiments was to identify carbonate substructures by detection of known species, followed by screening for lower abundance related compounds by inspection of similar accurate mass fragmentation and chromatographic features. The presence of carbonate substructures is indicative of electrolyte solvent degradation, and information on elemental composition provides information about the possible mechanisms.

Targeted carbonate substructures

Figure 1 shows the EI extracted ion chromatogram of dimethyl, ethyl methyl, and diethyl carbonate structures containing dimers in the aged electrolyte. The marker fragments for methyl carbonate mainly correspond to *m/z* 103.0389 ($C_4H_7O_3$), *m/z* 77.0233 ($C_2H_5O_3$) and for ethyl carbonate *m/z* 63.0076 (CH_3O_3). The accurate mass fragmentation patterns observed in the full scan data in Figure 2 provides reliable confirmation of which substructure is present. When determining these compounds in unknown samples, these accurate mass ions provide the selectivity to extract against a complex chemical background and certainty in the detection. The mass accuracy of the ions in the spectra in Figure 2 are all <2 ppm even at these relatively low masses (<105 Da).

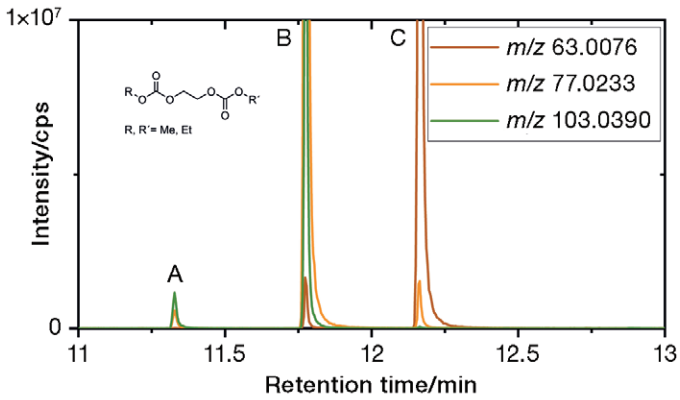

Figure 1. Overlaid EI extracted ion chromatogram of *m/z* 103.0389 ($C_4H_7O_3$), *m/z* 77.0233 ($C_2H_5O_3$), and *m/z* 63.0076 (CH_3O_3). Peaks labeled (A) dimethyl carbonate, (B) ethyl methyl carbonate, and (C) diethyl carbonate. For ethyl methyl species both *m/z* 103.0389 and *m/z* 63.0076 are detectable.

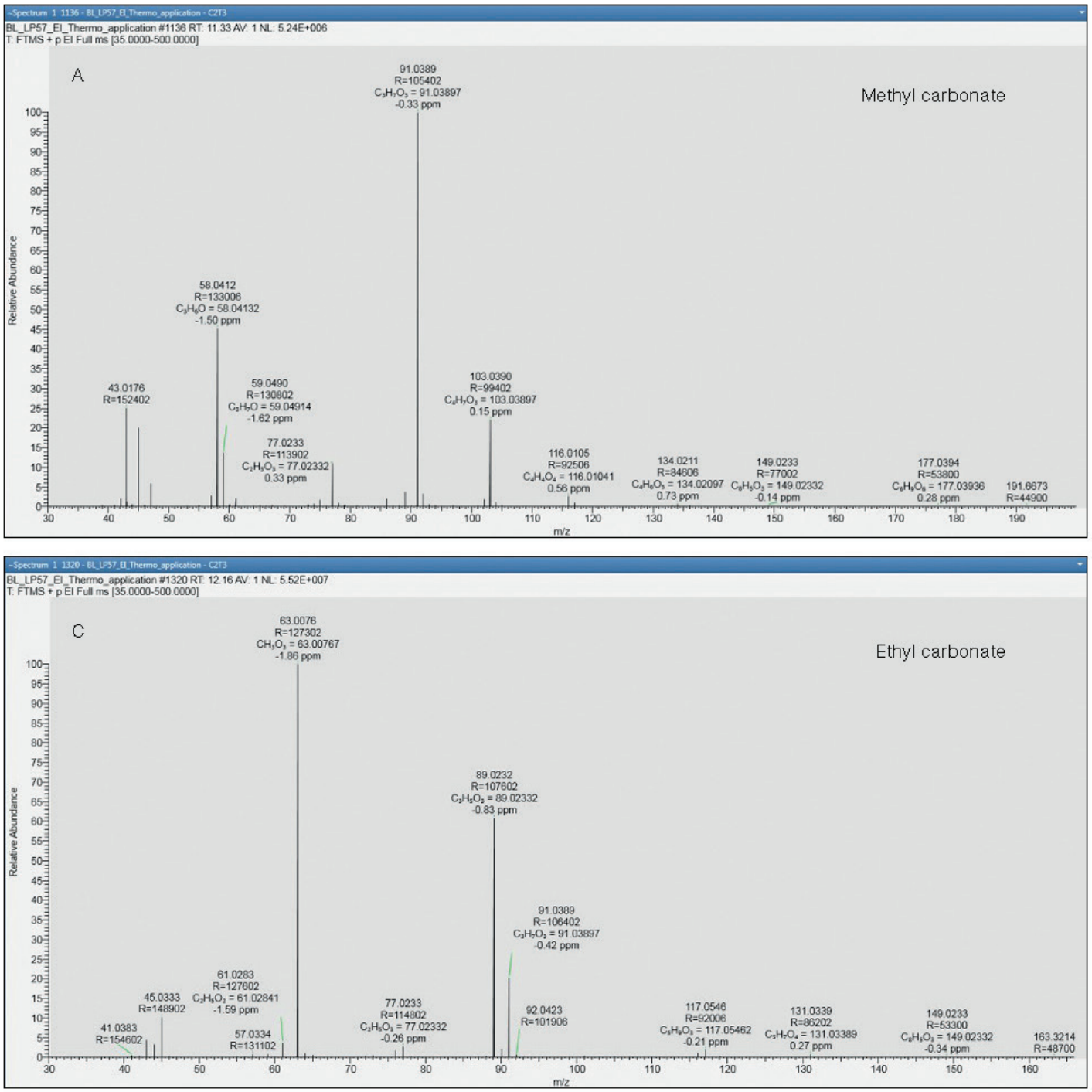

Figure 2. Full scan accurate mass spectra of dimer peaks at 11.3 and 12.2 minutes, peaks A and C. Upper spectrum shows characteristic fragmentation for methyl carbonate (*m/z* 103.0390), and lower spectrum for ethyl carbonate (*m/z* 63.0076).

Identification of unknown carbonate substructures

The extraction of the accurate mass ions in the targeted analysis of methyl and ethyl carbonate revealed the presence of peaks later in the chromatogram at 13.9, 14.1, and 14.4 minutes (Figure 3) with similar fragmentation and elution patterns. This similarity led to the suspicion that these were structurally related to the known compounds and therefore of interest in the context of electrolyte degradation. As such, it was important that the peaks could be identified with a high degree of certainty. With no certified standards, the accurate mass information provided a pathway to proposing an identify based on their elemental formula.

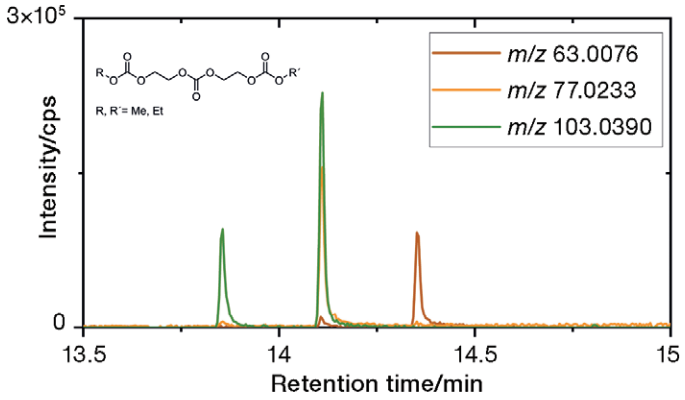

Figure 3. Overlaid EI extracted ion chromatogram of *m/z* 103.0389 ($C_4H_7O_3$), *m/z* 77.0233 ($C_2H_5O_3$), and *m/z* 63.0076 (CH_3O_3). The chromatographic pattern at 13.9, 14.1, and 14.4 minutes is similar to the known carbonate dimers, and therefore the peaks are interesting to this study of electrolyte degradation.

Due to strong fragmentation behavior of organic carbonates with electron ionization, molecular ion information was not obtained by this analysis. Furthermore, carbonate dimers and trimers also fragment when methane is used as a chemical ionization reagent gas. Therefore, soft PCI with ammonia was performed as it was critical to identify the molecular ion of the peaks through a chemical ionization acquisition. The Orbitrap Exploris GC is capable of switching from EI to PCI without breaking the system vacuum, enabling a change within minutes. This provides a quick route to identification of the molecular ion by inspection of the spectrum of known adducts. Positive chemical ionization data was acquired using ammonia as the reagent gas to generate $[M+H]^+$ and $[M+NH_4]^+$ ions in the spectrum. The mass adducts identify which is the molecular ion in the spectrum to then propose an accurate elemental composition. The better the mass accuracy, the lower the number of possible elemental compositions that need to be evaluated.

The zoomed spectrum of the peak at 13.9 minutes is shown in Figure 4 (upper) showing the $[M+H]^+$ and $[M+NH^4]^+$ ions at *m/z* 267.07106 and *m/z* 284.09761, respectively. The proposed elemental composition corresponds to $C_9H_{15}O_9$ when using the elements C 1-50, H 1-50, O 1-20, P 0-10, and F 0-10. The importance of good mass accuracy is demonstrated in Figure 5 where <1 ppm mass accuracy suggests only two possible elemental compositions. Whereas, with poor mass accuracy at 5 or 10 ppm there are up to 11 formulae that would fit. This means it takes longer to work through each suggested composition, and the certainty in the result is not as high as with the sub 1 ppm mass accuracy provided by Orbitrap-based mass spectrometry. The two suggested elemental compositions can be quickly reviewed with the correct answer—$C_9H_{15}O_9$ fitting with -0.51 ppm and the alternative $C_{10}H_{18}O_3FP_2$ with -0.18 ppm. The latter can be excluded because the ratio of P, O, and F does not fit for PF_6 originating species and the previously observed EI fragment ions cannot be matched with these elements.

Ethyl and methyl carbonate structures have three possible termination species; the peaks at 14.1 and 14.4 minutes align with these to show a trimer and therefore agree with the pattern observed in literature known dimers.[2] For peaks at 14.1 and 14.4 minutes, both $[M+H]^+$ and $[M+NH^4]^+$ ions are observed as seen in Figure 4 with excellent mass accuracy to support elemental proposals of $C_{10}H_{17}O_9$ and to $C_{11}H_{19}O_9$, respectively. This information can either be applied as a targeted screen of future samples or used to support further understanding of the mechanisms of electrolyte degradation.

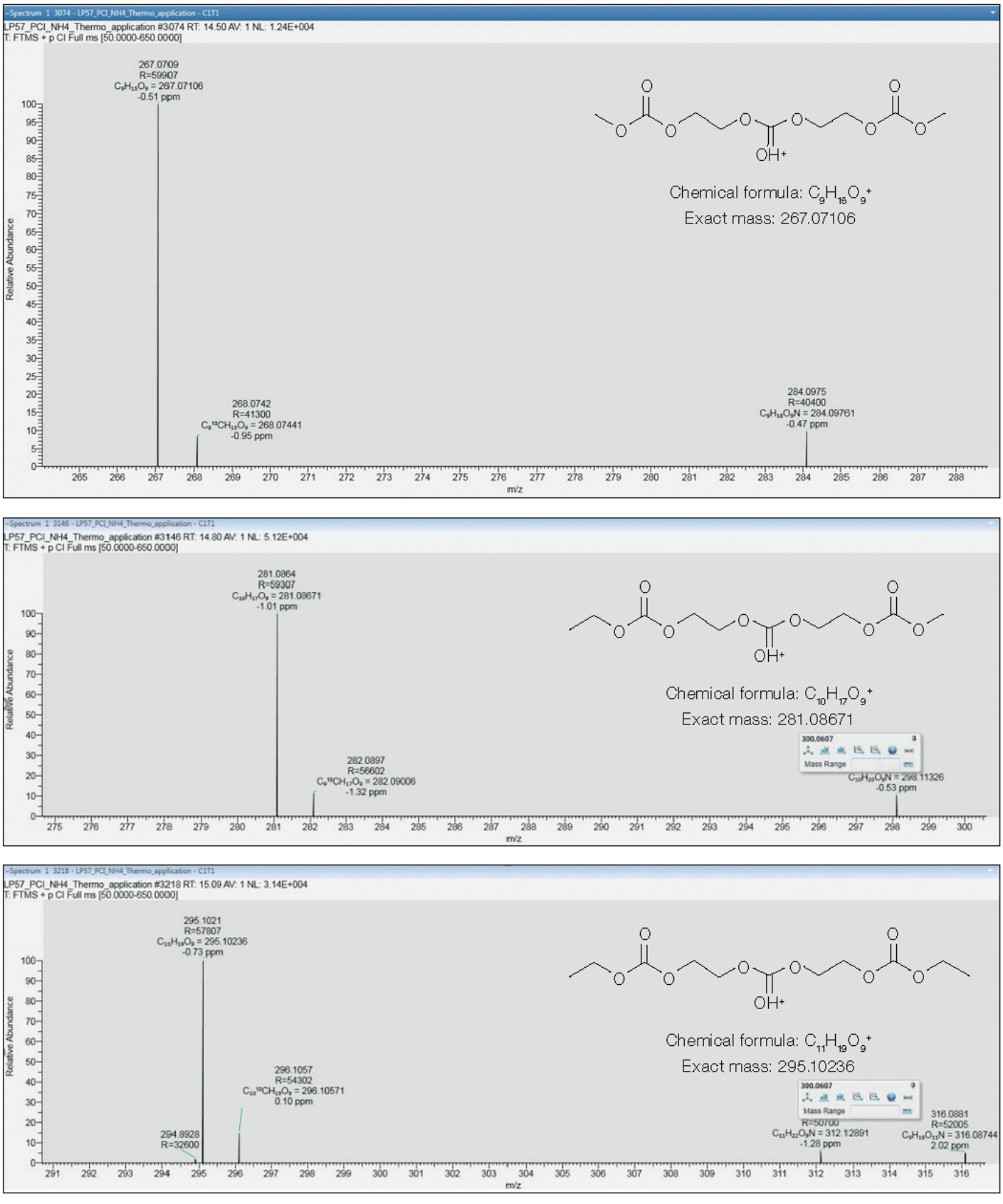

Figure 4. Zoomed positive chemical ionization spectra of peaks at 13.9 (upper), 14.1 (middle,) and 14.4 (lower) minutes. $[M+H]^+$ and $[M+NH^4]^+$ ions are labeled with theoretical accurate mass, proposed elemental formula, and ppm mass accuracy. The R value corresponds to the mass resolution of the ion.

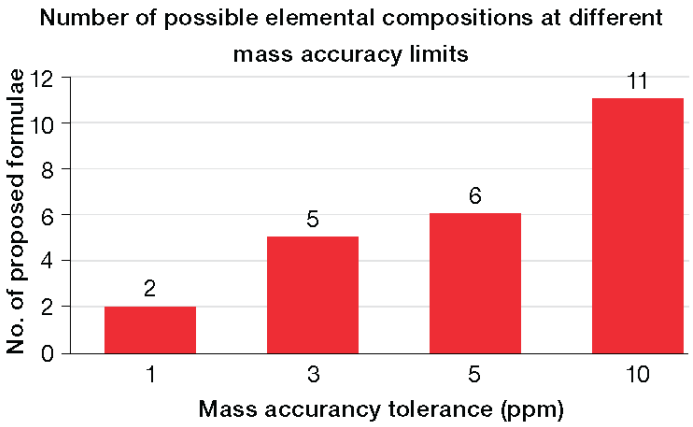

Figure 5. Bar chart showing the number of possible elemental compositions with increasing mass accuracy. The expected sub 1 ppm mass accuracy of the GC Orbitrap system shows only two possible formulae, meaning that identification can be achieved in a shorter time and with a higher degree of confidence.

Conclusions

The results of this study demonstrate that the benchtop Orbitrap Exploris GC mass spectrometer provides a powerful tool for the detailed characterization of lithium-ion battery electrolytes.

- Target compounds, ethyl carbonate and methyl carbonate, could be accurately determined against a complex chemical background through identification of unique fragmentation profiles including *m/z* 103.0389 ($C_4H_7O_3$), *m/z* 77.0233 ($C_2H_5O_3$), and *m/z* 63.0076 (CH_3O_3). The mass resolving power of 60,000 enabled chromatographic peaks to be extracted with narrow windows, providing clear detection of target compounds from background chemical interferences.
- GC unknown trimer peaks exhibiting similar elution profiles to known compounds could be identified through EI and PCI data acquisitions that provided information on the elemental composition of mass adduct ions in the spectra. The ability to change between in EI and CI without breaking system vacuum enables a convenient route to obtain this important structural information.
- Good mass accuracy ensured that the correct elemental composition $C_9H_{15}O_9$, $C_{10}H_{17}O_9$, and $C_{11}H_{19}O_9$ could be proposed for unknowns without an extensive workload and that proposals could be made with a high degree of certainty. This information can then be used as part of a targeted screening analysis or to understand electrolyte aging mechanisms.

References

1. Mönnighoff, X.; Murmann, P.; Weber, W.; Winter, M.; and Nowak, S. Post-Mortem Investigations of Fluorinated Flame Retardants for Lithium Ion Battery Electrolytes by Gas Chromatography with Chemical Ionization. *Electrochimica Acta.* **2017**, *246*, 1042–1051.
2. Mönnighoff, X.; Friesen, A.; Konersmann, B.; Horsthemke, F.; Grützke, M.; Winter, M.; Nowak, S. Supercritical Carbon Dioxide Extraction of Electrolyte from Spent Lithium Ion Batteries and its Characterization by Gas Chromatography with Chemical Ionization. *Journal of Power Sources.* **2017**, *352*, 56–63.
3. Horsthemke, F.; Friesen, A.; Mönnighoff, X.; Stenzel, Y.P.; Grützke, M.; Andersson, J.; Winter, M.; Nowak, S.; 2017. Fast Screening Method to Characterize Lithium Ion Battery Electrolytes by Means of Solid Phase Microextraction–Gas Chromatography Mass Spectrometry. *RSC Advances.* **2017**, *7*, 46989–46998.
4. Wiemers-Meyer, S.; Winter, M.; and Nowak, S. Phys. Mechanistic insights into lithium ion battery electrolyte degradation–a quantitative NMR study. *Phys. Chem. Chem. Phys.* **2016**, *18*, 26595–26601.

Learn more at thermofisher.com

Application note | 001124

Industrial

Comprehensive analysis of electrolyte solutions for lithium-ion batteries using gas chromatography-mass spectrometry

Authors

Nicholas A. Warner[1], Adam Ladak[2], Simon Nelms[2], and Daniel Kutscher[1]

[1]Thermo Fisher Scientific, Bremen, Germany

[2]Thermo Fisher Scientific, Hemel Hempstead, United Kingdom

Keywords

Electrolytes, additives, degradation products, GC-MS, single quadrupole MS, full scan, selected ion monitoring (SIM)

Goal

The goal of this application note is to demonstrate the Thermo Scientific™ ISQ™ 7610 Single Quadrupole GC-MS capabilities for accurate quantitation and characterization of lithium battery electrolyte components.

Introduction

The development of the lithium-ion battery (LIB) over the past three decades has led to groundbreaking advancements in energy storage. This comes at an opportune time as the world's current and ever-growing energy demands have reached a critical point. Traditional petroleum-based energy sources (i.e., oil, natural gas) are dwindling, while strict mandates have been initiated by governments to reduce petroleum-based carbon emissions under the Paris Agreement by 2030. In addition, recent geopolitical factors have made access to traditional energy sources in Europe highly volatile and unstable, further driving the need for new sources of energy. While renewable energy sources (i.e., solar, hydro, wind) could be a viable alternative, storage of energy is a limiting factor for larger scale use.

The biggest impact of LIBs can be seen in the transport sector with their implementation in electric vehicles. However, the longevity of LIB operation is a crucial factor to become a suitable energy replacement to petroleum in motor vehicles. The durability of LIBs is attributed to the thermodynamics of the battery electrolyte. The most common electrolyte used in LIBs is lithium hexfluorophosphate ($LiPF_6$) salt mixed with organic carbonate solvents (i.e., dimethyl carbonate, ethyl methyl carbonate, diethyl carbonate).

Upon the first cycling of the LIB, reduction of the electrolyte at the anode surface produces a conductive film known as the solid electrolyte interface (SEI), where current (i.e., Li^+) can pass through while simultaneously preventing further reduction of the electrolyte. However, the $LiPF_6$ is thermodynamically unstable at elevated operating temperatures (>60 °C) causing the organic carbonate solvents to be further reduced. As a result, a thicker and more resistive SEI is formed, limiting current flow and LIB charging capacity. In addition, thermal dissociation of the $LiPF_6$ to PF_5 causes deterioration of the SEI through side reactions, resulting in continued electrolyte degradation as it comes in contact again with the anode surface.[1]

The addition of electrolyte additives can help reduce electrolyte degradation in LIB batteries. These chemicals are preferentially reduced at higher potentials, helping prevent further electrolyte degradation under such operating conditions. Differences in additive functional groups will alter the properties of the SEI. Thus, knowledge of electrolyte composition and byproducts formed during battery operation is key for future development of more efficient, stable, and high performing LIBs.

In this application note, an analytical method for the compositional analysis of LIB electrolytes is demonstrated. Extraction and analysis of LIB electrolytes for 16 different electrolyte solvent, additive, and degradation compounds were performed using the Thermo Scientific™ TRACE™ 1610 gas chromatograph coupled to the Thermo Scientific™ ISQ™ 7610 single quadrupole GC-MS system. High linearity was observed over an extended calibration range with trace level detection possible at $\mu g \cdot L^{-1}$ levels. Quantification, confirmation, and identification were achieved using full scan together with selected ion monitoring (SIM) acquisition for accurate determination of LIB electrolyte composition.

Experimental

Standard and sample preparation

Individual standard stock solutions of different organic carbonate solvents (Sigma-Aldrich, USA), electrolyte additives (Sigma-Aldrich, USA) and dioxahexane acid dimethyl ester (abcr chemicals, Germany) were weighed and diluted in dichloromethane (Honeywell, USA) to a concentration of 10 $g \cdot L^{-1}$. A secondary stock solution containing all analytes was prepared in dichloromethane at a concentration of 500 $mg \cdot L^{-1}$ followed by serial dilution to produce a 7-point calibration curve (0.1, 1.0, 10, 25, 50, 100, 200 $mg \cdot L^{-1}$).

For sample preparation, 20 µL aliquots of LIB electrolyte material were diluted with 1 mL of dichloromethane. Sample dilutions were centrifuged for 5 min at 8,500 rpm using a Thermo Scientific™ Sorvall™ ST 8R centrifuge (P/N 75007203) for removal of the $LiPF_6$ salt to avoid detrimental effects to the GC column. The supernatant was then diluted by factors of 10, 100, and 1,000 (total sample dilution of 500, 5,000, and 50,000, respectively) for analysis by GC-MS using external calibration.

Instrument and method setup

Analysis was carried out using the ISQ 7610 GC-MS. Automatic sample injection was performed using a Thermo Scientific™ TriPlus™ RSH autosampler with chromatographic separation obtained using a TRACE 1610 GC equipped with a Thermo Scientific™ TraceGOLD™ TG-35MS 30 m × 0.25 mm i.d. × 0.25 µm film capillary column (P/N 26094-1420). Sample analysis was performed in full scan and selected ion monitoring (SIM) acquisition modes. Additional instrument parameters are displayed in Table 1 and Table 2.

Table 1. GC injection and column conditions

Trace 1610 GC system parameters	
Injection volume (µL)	1
Liner	Thermo Scientific™ LinerGold™ Precision liner (P/N 453A1255-UI)
Injection mode	Split
Split ratio	1:20
Injector temperature (°C)	250
Carrier gas, ($mL \cdot min^{-1}$)	He, 1.0 (constant flow)
Oven temperature program	
Initial temperature (°C)	35
Hold time (min)	3
Temperature 1 (°C)	160
Rate (°C·min-1)	10
Hold time (min)	0
Temperature 2 (°C)	200
Rate ($°C \cdot min^{-1}$)	20
Hold time (min)	5
Total run time (min)	23

Table 2. Mass spectrometer conditions for using simultaneous full scan and timed acquisition (t-SIM)

ISQ single quadrupole GC-MS parameters	
Transfer line (°C)	280
Thermo Scientific™ Exactabrite™ ion source (°C)	260
Ionization mode	EI
Electron energy (eV)	70
Full scan range (*m/z*)	35–500
Full scan time (s)	0.2
SIM time (s)	0.6
Minimum baseline peak width (s)	6
Desired peak scans	10

Results and discussion

Chromatography

Using the TraceGOLD TG-35MS capillary column, separation of targeted analytes was achieved within 16 minutes (Figure 1, Table 3). Potential interferences due to coelution between diethyl carbonate and propyl propionate are avoided using mass spectrometric detection, where selective mass separation is achieved. This eliminates the need for an extended oven temperature program for chromatographic separation, providing faster and more efficient analyses.

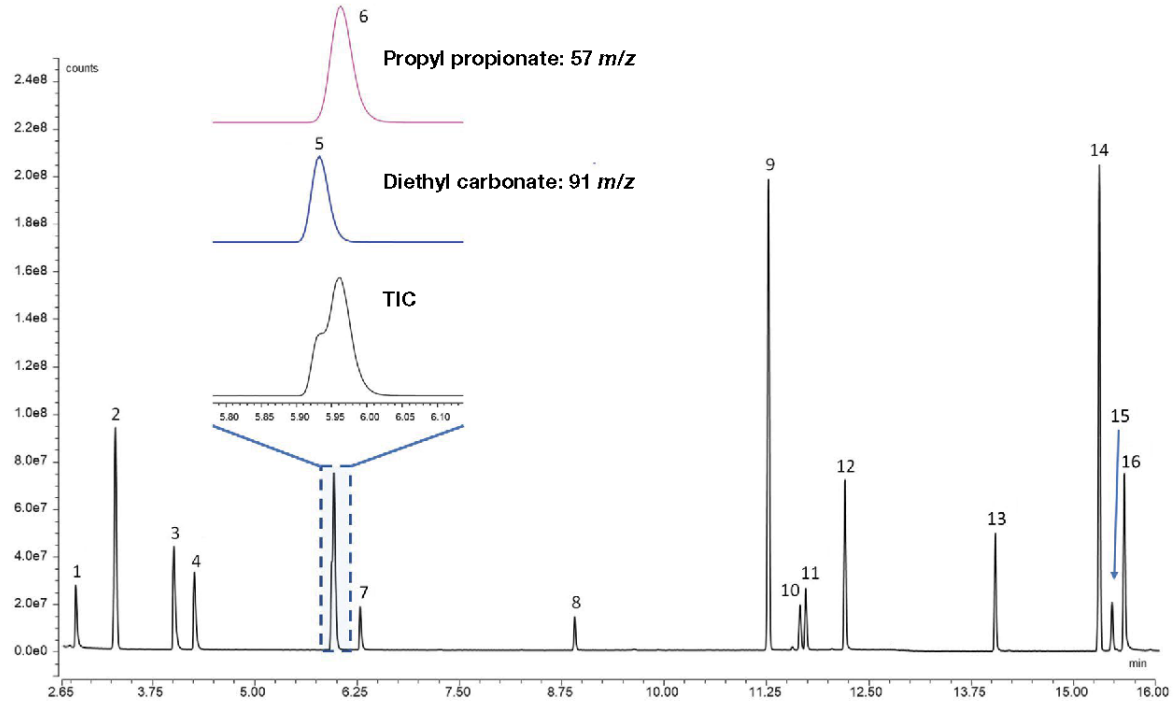

Figure 1. Full scan acquisition of 10 mg·L^{-1} standard of LIB electrolyte solvent, additive, and degradation compounds.
A full list of all compounds is given in Table 3.

Table 3. Compound retention time, acquisition ions, and calibration correlation coefficients acquired in full scan (0.1–200 mg·L^{-1}) and t-SIM (0.1–100 mg·L^{-1}) acquisition modes

Compound	Electrolyte component	Retention time (min)	SIM ions (*m/z*)[a]	Full scan (0.1–200 mg·L^{-1})	SIM (0.1–100 mg·L^{-1})
				r^2	r^2
1. Dimethyl carbonate	Solvent	2.80	**45**, 51, 90	0.9993	0.9997
2. Fluorobenzene	Co-solvent	3.29	**96**, 70, 95	0.9958	0.9992
3. Ethyl propionate	Additive/co-solvent	4.00	**57**, 102, 74	0.9952	0.9990
4. Ethyl methyl carbonate	Solvent	4.26	**77**, 45, 59	0.9998	0.9998
5. Diethyl carbonate	Solvent	5.94	**91**, 45, 63	0.9962	0.9962
6. Propyl propionate	Additive/co-solvent	5.97	**57**, 87, 75	0.9906	0.9991
7. Vinylene carbonate	Additive	6.28	**86**, 44, 58	0.9997	0.9990
8. Flouroethylene carbonate	Additive	8.92	**62**, 44, 106	0.9326	0.9992
9. 1,1–dimethylpropylbenzene	Additive	11.29	**119**, 91, 148	0.9825	0.9992
10. Ethyl carbonate	Solvent	11.67	**88**, 102, 43	0.9998	0.9982
11. Propyl carbonate	Solvent	11.75	**57**, 43, 87	0.9969	0.9988
12. Succoinitrile	Additive	12.22	**53**, 79, 80	0.9969	0.9993
13. 2,5 Dioxaheznedioc acid dimethyl ester	Degradation product	14.04	**59**, 91, 102	0.9986	0.9936
14. Phenylcyclohexane	Additive	15.28	**160**, 104, 117	0.9961	0.9993
15. 1,3-propanesultone	Additive	15.43	**58**, 57, 122	0.9996	0.9983
16. Adiponitrile	Additive/co-solvent	15.58	**68**, 54, 55	0.9922	0.9985

[a]Bold text represents the quantification ion

Linearity

Calibration analysis showed all compounds, with exception of fluoroethylene carbonate, displayed linear correlation from 0.1 to 200 mg·L^{-1} with full scan acquisition (Table 3), demonstrating the high dynamic linear range of the new Thermo Scientific™ XLXR™ electron multiplier detector. In SIM acquisition mode, correlation coefficients for all compounds improved, including fluoroethylene, with all compounds displaying linear response between 0.1 and 100 mg·L^{-1}.

Sensitivity

Analytical variation observed in replicate analysis (n=10) of the lowest calibration standard was used to determine instrument detection (IDL: 3 × standard deviation) andquantification (IQL: 10 × standard deviation) limits (Table 4). Detection and quantification limits were compound dependent, with IDLand IQL of 0.021 and 0.07 mg·L^{-1} or lower for all compounds, respectively.

Table 4. Instrument detection (IDL) and quantification (IQL) limits for electrolyte solvents and additives. Relative standard deviation (% RSD) based on replicate injection (n = 10) of 0.1 mg·L^{-1} standard.

Compounds	IDL	IQL	%RSD
Dimethyl carbonate	0.010	0.035	2.6
Fluorobenzene	0.006	0.019	2.5
Ethyl propionate	0.004	0.015	2.0
Ethyl methyl carbonate	0.006	0.020	2.5
Diethyl carbonate	0.007	0.023	2.8
Propyl propionate	0.011	0.037	2.4
Vinylene carbonate	0.006	0.021	3.2
Fluoroethylene carbonate	0.015	0.049	6.3
1,1-Dimethylpropylbenzene	0.004	0.014	1.9
Ethylene carbonate	0.005	0.017	2.2
Propyl carbonate	0.021	0.070	2.0
Succoninitrile	0.010	0.034	5.0
Dioxahexane acid dimethyl ester	0.007	0.023	4.6
Phenylcyclohexane	0.003	0.011	2.2
1,3-propanesultone	0.004	0.014	1.9
Adiponitrile	0.003	0.009	1.8

Electrolyte composition and unknown determination

Full scan acquisition of both new and cycled LIB electrolytes showed differences in their composition (Figure 2).

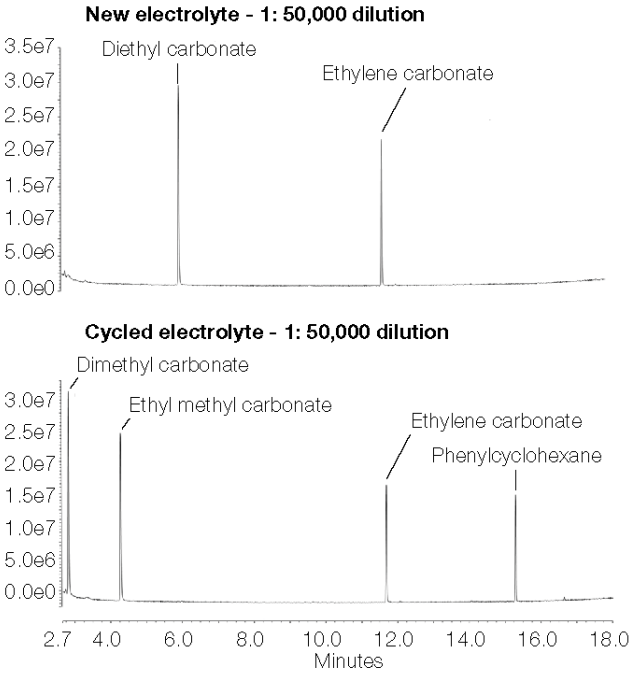

Figure 2. Full scan acquisition of new and cycled electrolyte solutions at 1:50,000 dilution

Such differences are not unexpected as composition will differ depending on their source of production. Analysis of three new electrolyte solutions showed similar composition between electrolyte samples 1 and 2 (i.e., diethyl carbonate and ethylene carbonate dominated), but differed in that observed in electrolyte 3 (i.e., ethyl methyl carbonate and ethylene carbonate dominated) (Table 5). Composition analysis of cycled electrolytes showed dimethyl carbonate, ethyl methyl carbonate, ethylene carbonate, and phenylcyclohexane were dominate components.

In addition to the electrolyte solvent and additive compounds detected in cycled electrolytes, several other minor peaks were observed close to the chromatographic baseline. NIST spectral library search of the full scan acquisition identified one of these peaks as biphenyl, a common additive in LIBs for its flame retardant properties[1] (Figure 3). To confirm these findings, a 1:5,000 dilution of the cycled electrolyte was analyzed. Not only was biphenyl confirmed to be present but also dioxahexane acid dimethyl ester, a known degradation product of LIB electrolytes[2] (Figure 4.)

An additional peak was identified as 1,4-meracapto-2,3-butanediol prior by the NIST search library. However, the low probability score (24.6%) indicates further investigation using a standard to confirm spectra and retention time is needed

Table 5. Composition analysis (mg·L^{-1}) of LIB electrolyte solutions at 1:5000 dilution

Compound[a]	Electrolyte 1 (new)	Electrolyte 2 (new)	Electrolyte 3 (new)	Electrolyte 4 (cycled)	Electrolyte 5 (cycled)
Dimethyl carbonate	0.08	0.10	0.04	64.0	71.9
Ethyl propionate	ND	ND	ND	0.01[b*]	0.02
Ethyl methyl carbonate	ND	0.06	102	43.9	46.9
Diethyl carbonate	77.8	114	ND	0.25	0.31
Vinylene carbonate	ND	ND	ND	0.01[b*]	ND
Ethylene carbonate	89.2	129	128	63.4	59.9
Dioxahexane acid dimethyl ester	ND	ND	ND	0.21	0.30
Phenylcyclohexane	ND	ND	ND	4.25	4.25

[a]Compounds reported if both confirmation ion ratios passed

[b]Detected in 1:500 dilution of electrolyte sample

*Above IDL but below IQL

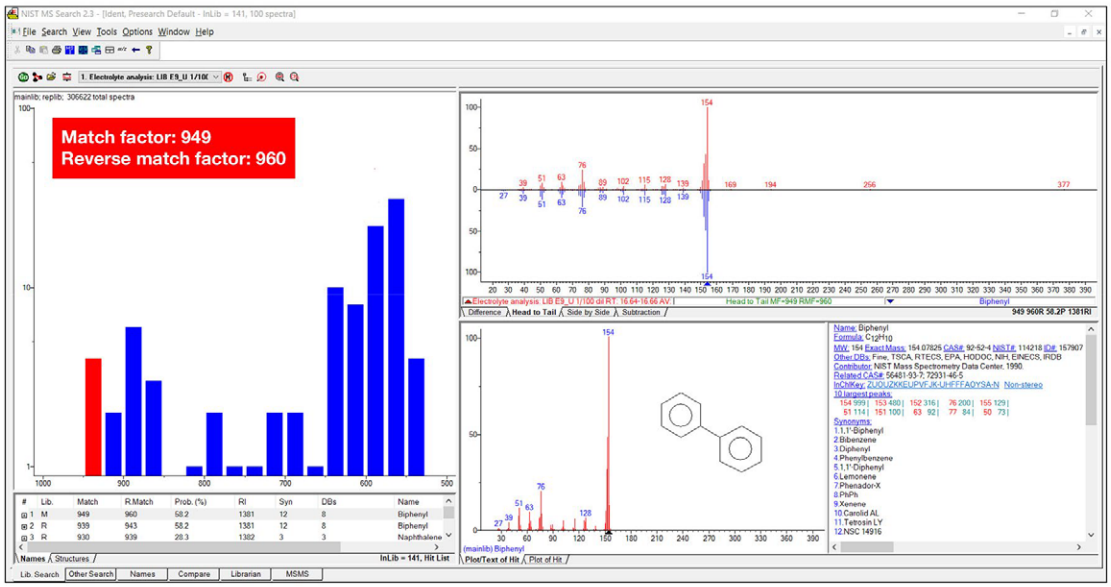

Figure 3. NIST library identification of unknown peak as biphenyl

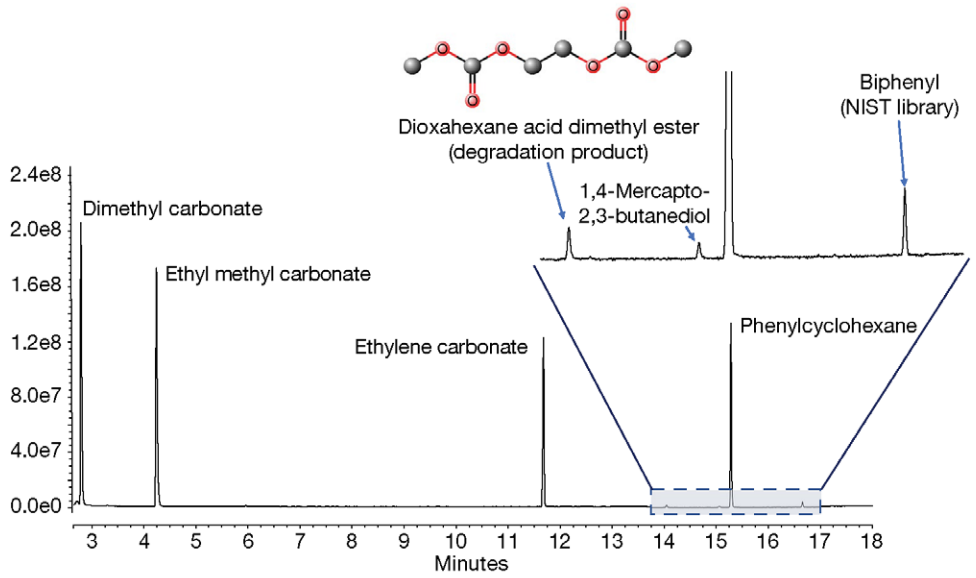

Figure 4. Full scan acquisition of cycled LIB electrolyte at 1:5,000 dilution

Additive confirmation with SIM analysis

Complete composition analysis of LIB electrolytes is challenging due to the wide concentration range of the different components. The organic carbonate solvents (i.e., dimethyl carbonate, diethyl carbonate, ethyl methyl carbonate, ethylene carbonate) are present at high concentrations (vol%) and require high dilution ratios to be analyzed by MS. Meanwhile, electrolyte additives or products of side reactions may be present at much lower concentrations and risk avoiding detection with high dilution ratios. Analysis using SIM acquisition can aid detection by reducing overall signal noise encountered in full scan analysis through selective ion acquisition for targeted analytes present at low concentrations. An example of this can be seen in the full scan and SIM acquisition of vinylene carbonate in cycled electrolyte sample diluted 1:500 (Figure 5). In full scan, the quantification ion for vinylene carbonate was not detected. However, the quantification ion and both confirmation ions for vinylene carbonate were detected using SIM acquisition. Moreover, ion ratios for both confirmation ions were within the expected ion ratio criteria (± 20%) based on the standard fragmentation, confirming the presence of vinylene carbonate. Ethylene propionate was also detected in both cycled electrolytes using SIM analysis (Table 5). Traces of fluorobenzene were also observed in several electrolyte samples with confirmation ratios passing criteria but were below IDL. Results from the compositional analysis of analyzed LIB electrolytes are reported in Table 5.

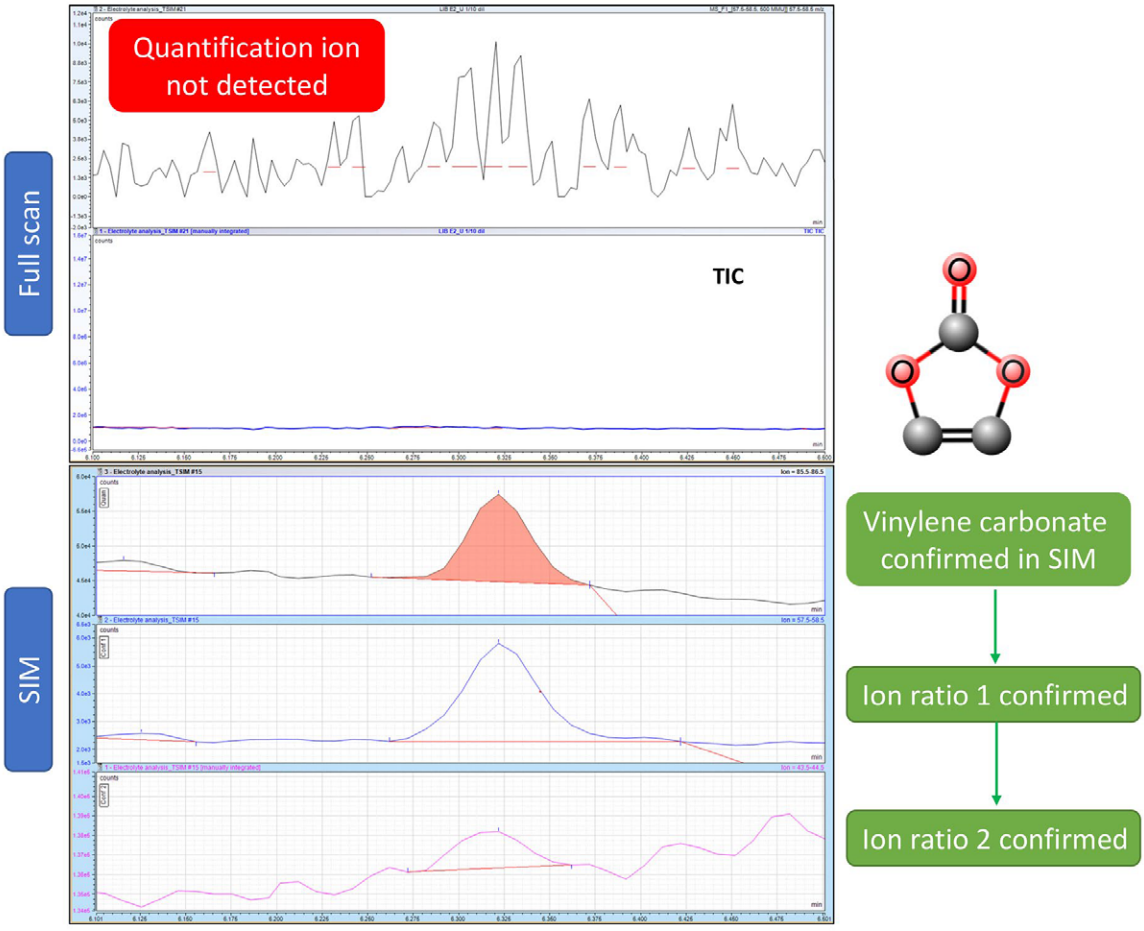

Figure 5. Full scan and SIM acquisition of vinylene carbonate in cycled LIB electrolyte at 1:500 dilution

Conclusion

This application demonstrates the ISQ 7610 MS equipped with the new XLXR detector provides a high linear dynamic range for quantification of LIB electrolyte components over varying concentration ranges.

- Efficient separation of various electrolyte components was achieved within 16 min.
- Full scan analysis provided characterization of unknown additives present in electrolyte samples while t-SIM acquisition provided confirmation of electrolyte additives not achievable with full scan acquisition.
- Linear dynamic range of over 4 orders of magnitude was achieved using the XLXR detector.
- Detection of LIB electrolyte components were achievable at $\mu g \cdot L^{-1}$ levels with IDLs ranging from 0.003 to 0.021 $\mu g \cdot L^{-1}$.

References

1. Campion, C. L. Thermal Decomposition of $LiPF_6$-Based Electrolytes for Lithium-Ion Batteries. *J. Electrochem. Soc.* **2005,** *152,* A2327 – A2334. https://doi.org/10.1149/1.2083267
2. Zhang, S. S. A review on electrolyte additives for lithium-ion batteries. *J. Power Sources* **2006,** *22,* 1379–1394. https://doi.org/10.1016/j.jpowsour.2006.07.074
3. Horsthemke, F.; Friesen, A.; Mönnighoff, X.; Stenzel, Y. P.; Grützke, M.; Andersson, J.T.; Winter, M.; Nowak, S. Fast screening method to characterize lithium-ion battery electrolytes by means of solid phase microextraction – gas chromatography – mass spectrometry. *RSC Adv.* **2017,** *7,* 46989 – 46998. https://doi.org/10.1039/C7RA08599K

Learn more at **thermofisher.com/gc-ms**

APPLICATION BRIEF 000401

Battery drum pack gas analysis through a multi-valve, multi-column GC system

Author: Thermo Fisher Scientific Inc.

Keywords: Gas analysis, TRACE 1310 GC, TRACE 1310 Auxiliary Oven, Li-battery

Goal

The purpose of this application brief is to report a multi-column, multi-valve gas chromatographic solution for the analysis of gases producing Li-battery swelling.

Introduction

Initial charge/discharge processes in batteries produce a variety of gas components that have an impact on battery performance after long-term use. Additionally, some flammable gases create a security risk. Therefore, the gas composition produced by batteries provides important information about possible deterioration and the performance of different battery formulations.

However, there are two main difficulties in analyzing the composition of battery gas. Firstly, the gas composition produced by batteries is highly complex. There are three categories:

- Permanent gases such as hydrogen, methane, carbon monoxide, carbon dioxide, etc.
- Short-chain hydrocarbons (C2-C5)
- Other volatile compounds

These components are difficult to fully separate on a single gas chromatographic column for systematic analysis, and

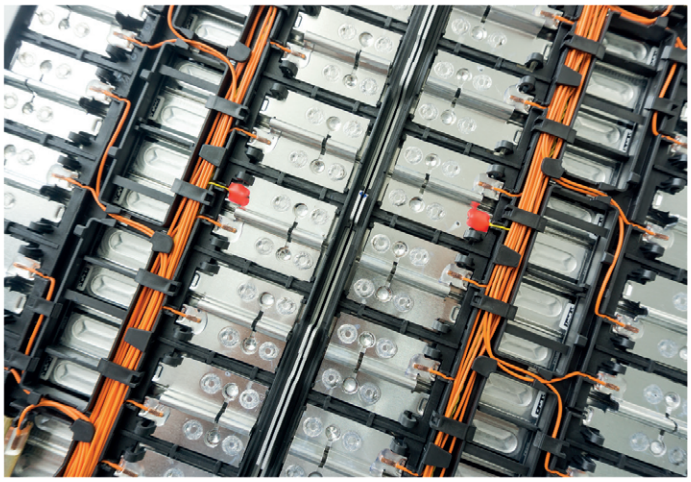

a multi-column GC configuration is required. Secondly, in many cases, in addition to the qualitative identification of the gases produced by the battery, the concentration of the produced gases is required.

In this work, a multi-valve, multi-column GC equipped with two detectors was used to analyze samples from a battery drum package and detect permanent gases and light hydrocarbons up to C6+. The components in the sample were quantitatively measured by the external standard method.

Experimental

A Thermo Scientific™ TRACE™ 1300 Series GC gas chromatograph equipped with a Thermo Scientific™ iConnect SSL injector and an iConnect FID detector was connected to a Thermo Scientific™ 1310 Auxiliary Oven housing a 10-port and two 6-port switching valves and an iConnect TCD detector.

ThermoFisher SCIENTIFIC

The following capillary columns were used and connected as shown in the schematic diagram (Figure 1):

- Thermo Scientific™ TracePLOT TG-BOND Q GC column, 30 m, 0.53 mm i.d., 20 µm th. (P/N 26004-6090)
- Agilent® J&W® CP6938, PLOT Moleseive, 25 m, 0.53 mm i.d.
- Thermo Scientific™ TraceGOLD™ TG-WaxMS A GC column, RT-12454, 30 m, 0.32 mm i.d., 1 µm th. (P/N 26087-2970)
- Restek® Al_2O_3, 25 m, 0.32 mm i.d., 8 µm th.
- Thermo Scientific™ TraceGOLD™ TG-1MS GC column 30 m, 0.32 mm i.d., 3.0 µm th. (P/N 26099-4840)

Sampling method: 1 mL of gas was injected through the SSL injector using a gas-tight syringe.

A gas standard mixture in nitrogen was used as the external standard. Its composition is reported in Table 1.

Two detectors were configured for a simultaneous detection of the permanent gases (TCD channel) and the light hydrocarbons (FID channel).

The operative conditions of the system are reported in Table 2.

Table 1. Gas standard mixture composition

Compound	Conc. (%,V/V)
Methane	5.99
Ethane	5.13
Ethylene	2.99
Propane	7.93
Cyclopropane	0.51
Propylene	3.01
Isobutane	2.72
Butane	2.07
Propandiene	0.95
Acetylene	0.12
trans-Butene	1.54
Butene	1.00
Isobutylene	0.80
cis-Butene	1.23
Isoprene	0.11
Pentane	0.14
1,3-butadiene	1.53
Propyne	0.47
trans-2-pentene	0.20
2- Methyl-2-butene	0.15
1-pentene	0.10
cis-2-pentene	0.14
Hexane	0.10
Hydrogen	14.93
Oxygen	0.53
Carbon monoxide	1.50
Carbon dioxide	3.00
Nitrogen bulk gas	

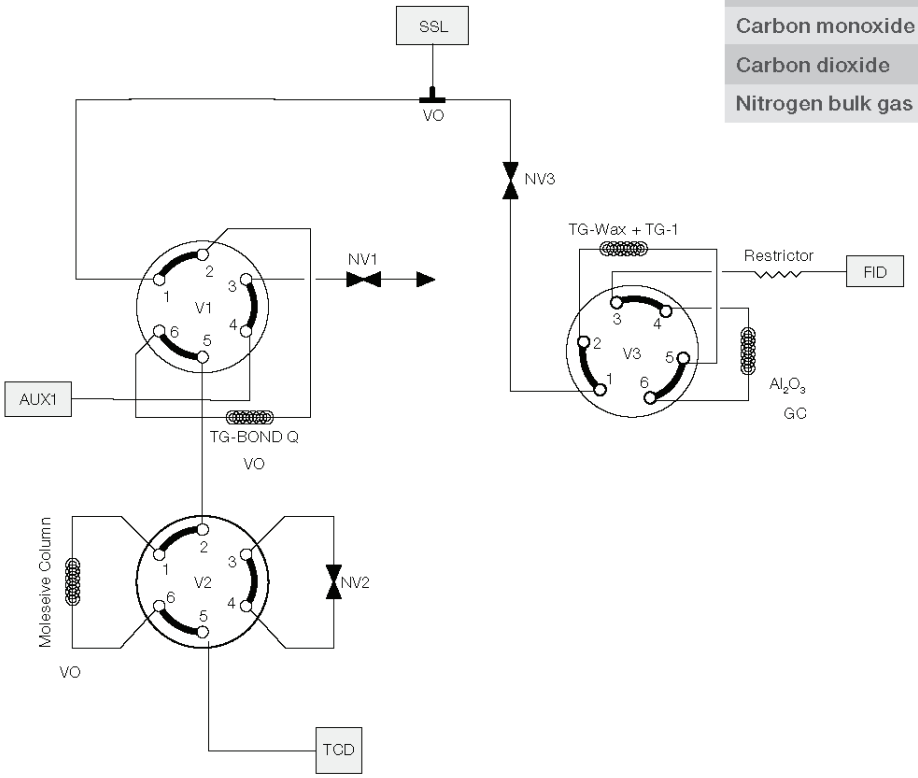

Figure 1. Valve diagram of the multi-column GC configuration

Table 2. Operative conditions of the configured GC system

Carrier gas (Argon)	
Flow mode	Constant pressure
Front SSL	123 kPa
Carrier AUX	78 kPa
Detector TCD (Aux-Left)	
Temperature	200 °C
Filament temperature	300 °C
Reference flow	1 mL/min (Ar)
Detector FID (Back)	
Temperature	250 °C
Ignition threshold	1.0 pA
Air	350 mL/min
H_2	35 mL/min
Make up gas (N_2)	30 mL/min
GC oven	
Initial temperature	60 °C
Initial time	1.20 min
Ramp 1	15 °C/min
Final temperature 1	100 °C
Final time 1	1.00 min
Ramp 2	30 °C/min
Final temperature 2	180 °C
Final time 2	1.00 min
Auxiliary oven	
Temperature	70 °C

Results

A gas sample of 500 µL was taken with a 1 mL gastight syringe directly from the battery drum pack and injected manually into the GC system for separation and detection. A single injection allowed for qualitative and quantitative determination of H_2, O_2, N_2, CO, CO_2, C1-C5, and C6+ in the battery drum pack gas.

The switching valves were activated at a specific timing to cut the fraction and divert the sample components onto the appropriate columns for their separation. Components H_2, O_2, N_2, CO, and CO_2 were then measured by the TCD, while the components of C1-C5 and C6+ were detected by the FID.

The six-port valve V3 allowed the backflush of the heavier compounds, detected as C6+, while the C1-C5 were separated onto the alumina (Al_2O_3) column. The six-port valve V1 allows the backflush of heavier gases preventing contamination of the molecular sieve column. The system configured with backflush operation effectively shortened the analysis time and extended the life of the alumina and MolSieve columns.

Five samples from two separate batches were analyzed and the components quantified against the external standard mixture.

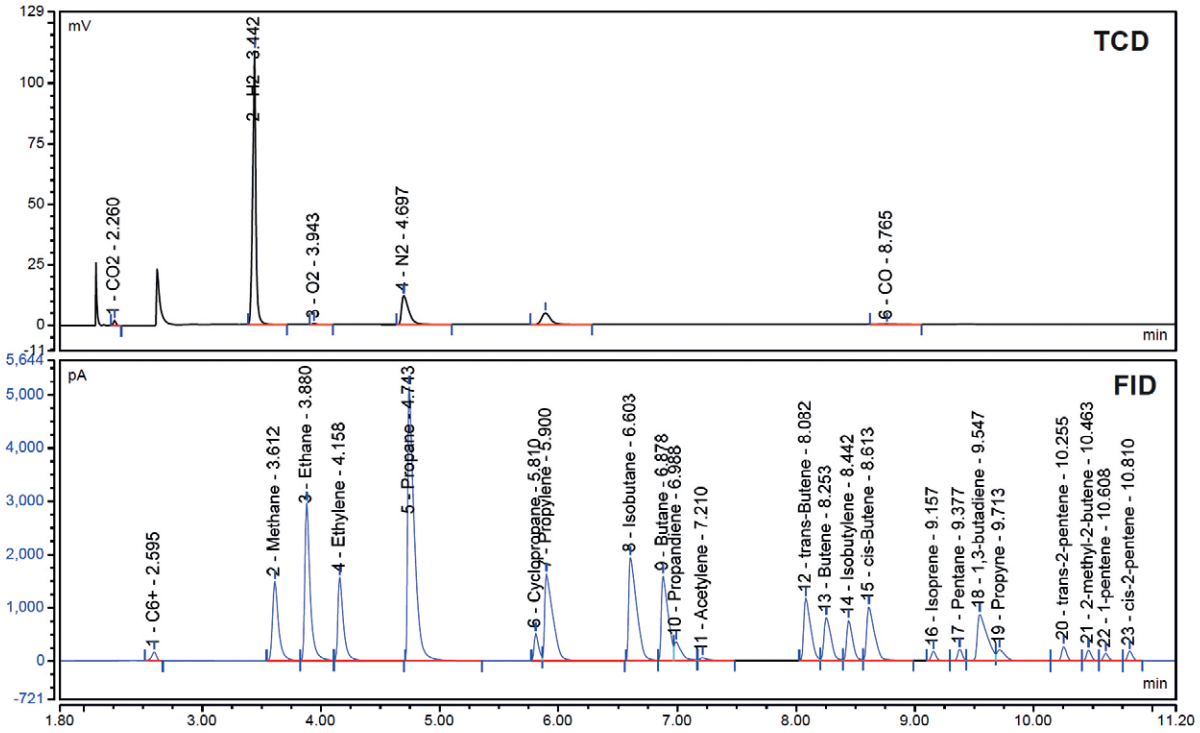

Figure 2. Chromatographic separation of the gas standard mixture. See Table 1 for composition.

First batch – Sample 1:

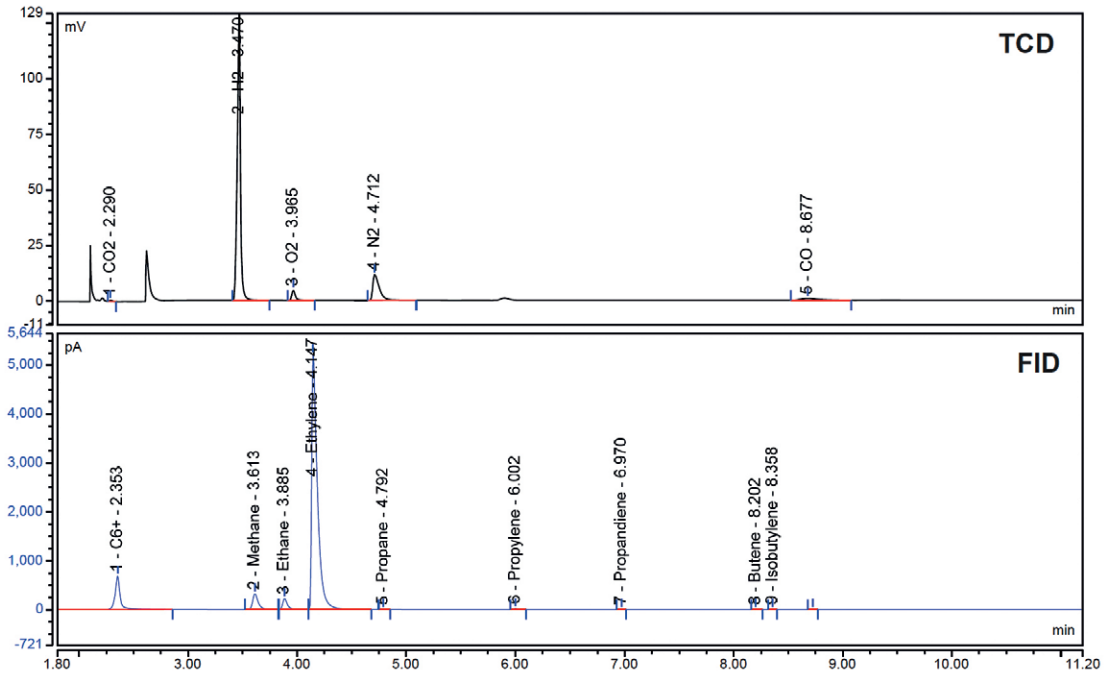

Figure 3. Chromatographic separation of Batch 1 – Sample 1

Table 3. Quantitative results for Batch 1 – Sample 1

Peak	Compound	Detector	Retention time (min)	Area (mV*min)	Height (mV)	Amount (%, V/V)	Corrected amount (%)
1	CO_2	TCD (Aux-Left)	2.290	0.014	0.59	0.80	0.94
2	H_2	TCD (Aux-Left)	3.470	4.40	138.1	18.66	22.13
3	O_2	TCD (Aux-Left)	3.965	0.17	4.66	5.42	6.43
4	N_2	TCD (Aux-Left)	4.712	0.80	11.44	38.90	46.13
5	CO	TCD (Aux-Left)	8.677	0.13	0.81	7.40	8.77
1	C6+	FID (Back)	2.353	35.69	679.3	0.40	0.47
2	Methane	FID (Back)	3.613	19.33	322.1	1.33	1.58
3	Ethane	FID (Back)	3.885	11.57	225.7	0.41	0.49
4	Ethylene	FID (Back)	4.147	310.9	5211.3	10.96	13.00
5	Propane	FID (Back)	4.792	0.13	3.13	0.003	0.00
6	Propylene	FID (Back)	6.002	0.97	24.32	0.023	0.03
7	Propandiene	FID (Back)	6.970	0.073	1.98	0.013	0.02
8	Butene	FID (Back)	8.202	0.09	2.40	0.002	0.00
9	Isobutylene	FID (Back)	8.358	0.041	1.17	0.0007	0.00

First batch – Sample 2:

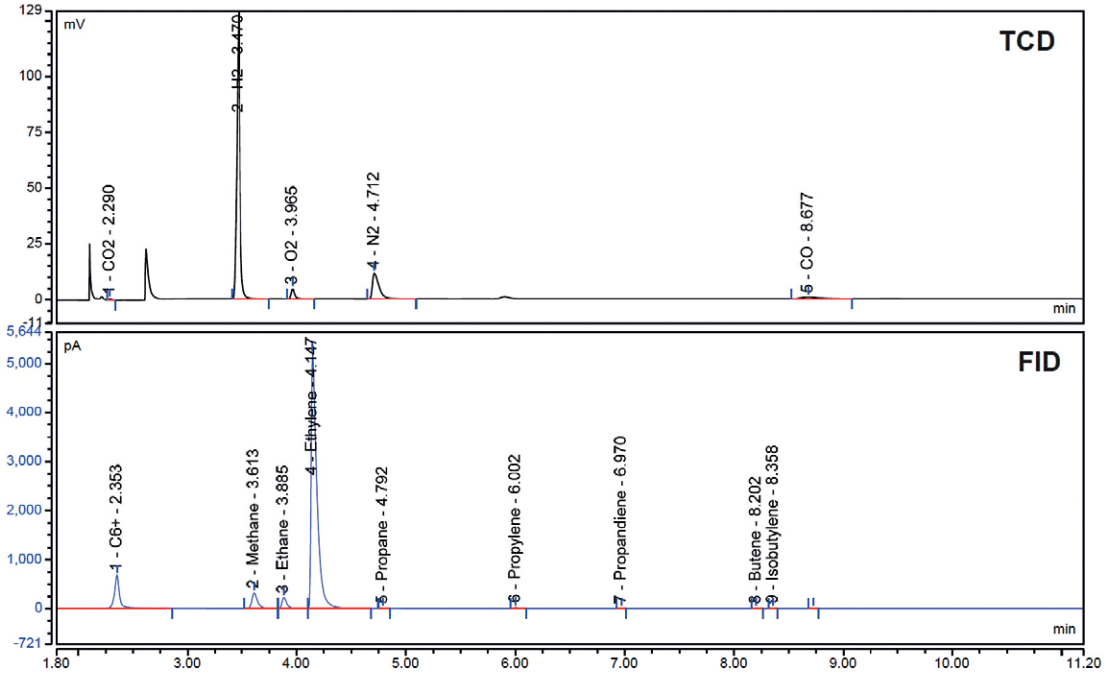

Figure 4. Chromatographic separation of Batch 1 – Sample 2

Table 4. Quantitative results for Batch 1 – Sample 2

Peak	Compound	Detector	Retention time (min)	Area (mV*min)	Height (mV)	Amount (%, V/V)	Corrected amount (%)
1	CO_2	TCD (Aux-Left)	2.272	0.01	0.56	0.77	0.88
2	H_2	TCD (Aux-Left)	3.452	3.97	128.0	16.84	19.25
3	O_2	TCD (Aux-Left)	3.948	0.17	4.60	5.44	6.22
4	N_2	TCD (Aux-Left)	4.698	0.89	12.46	43.87	50.16
5	CO	TCD (Aux-Left)	8.702	0.13	0.78	7.17	8.20
1	C6+	FID (Back)	2.355	33.48	634.3	0.37	0.42
2	Methane	FID (Back)	3.613	20.34	341.1	1.40	1.60
3	Ethane	FID (Back)	3.887	11.95	234.97	0.43	0.49
4	Ethylene	FID (Back)	4.148	315.8	5287	11.14	12.73
5	Propane	FID (Back)	4.795	0.11	2.78	0.003	0.00
6	Propylene	FID (Back)	6.007	1.01	24.89	0.024	0.03
7	Propadiene	FID (Back)	6.975	0.05	1.48	0.01	0.01
8	Butene	FID (Back)	8.207	0.06	1.79	0.001	0.00
9	Isobutylene	FID (Back)	8.365	0.03	0.87	0.0005	0.00

First batch – Sample 3:

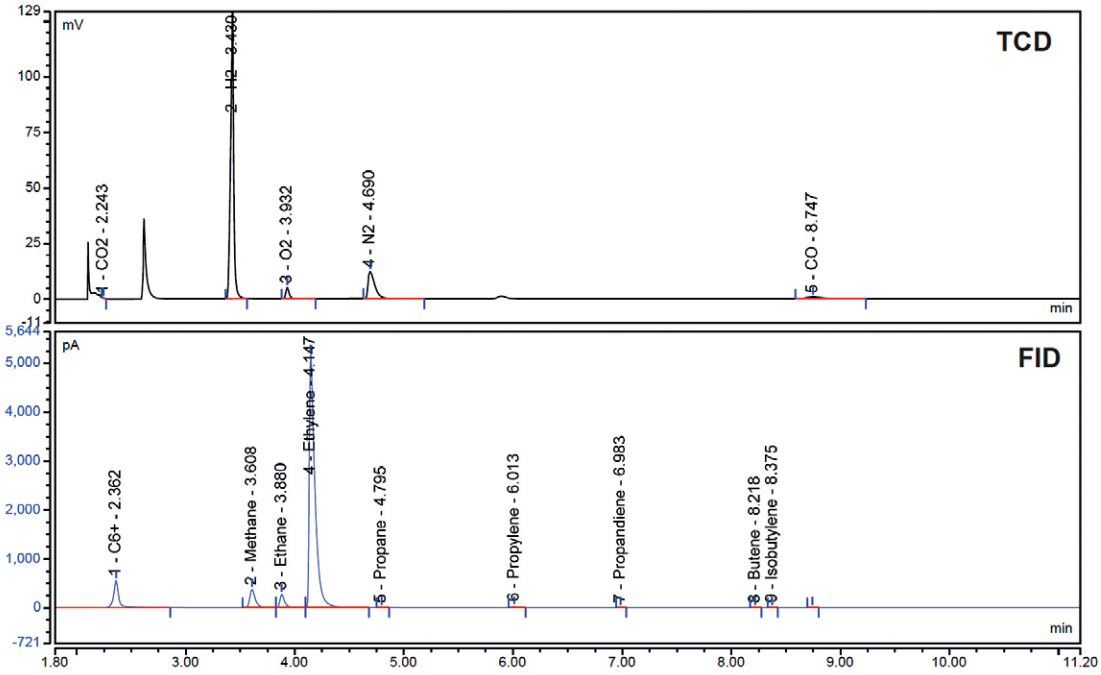

Figure 5. Chromatographic separation of Batch 1 – Sample 3

Table 5. Quantitative results for Batch 1 – Sample 3

Peak	Compound	Detector	Retention time (min)	Area (mV*min)	Height (mV)	Amount (%, V/V)	Corrected amount (%)
1	CO_2	TCD (Aux-Left)	2.243	0.006	0.31	0.31	0.36
2	H_2	TCD (Aux-Left)	3.43	4.21	133.58	17.85	20.22
3	O_2	TCD (Aux-Left)	3.932	0.19	5.15	6.06	6.87
4	N_2	TCD (Aux-Left)	4.690	0.88	12.28	43.36	49.11
5	CO	TCD (Aux-Left)	8.747	0.13	0.78	7.40	8.38
1	C6+	FID (Back)	2.362	29.63	560.10	0.33	0.37
2	Methane	FID (Back)	3.608	22.48	375.73	1.55	1.75
3	Ethane	FID (Back)	3.880	13.90	269.77	0.50	0.56
4	Ethylene	FID (Back)	4.147	308.43	5162.0	10.88	12.32
5	Propane	FID (Back)	4.795	0.16	3.86	0.004	0.00
6	Propylene	FID (Back)	6.013	1.07	26.50	0.025	0.03
7	Propadiene	FID (Back)	6.983	0.09	2.28	0.015	0.02
8	Butene	FID (Back)	8.218	0.10	2.60	0.002	0.00
9	Isobutylene	FID (Back)	8.375	0.04	1.11	0.0007	0.00

Second batch – Sample W:

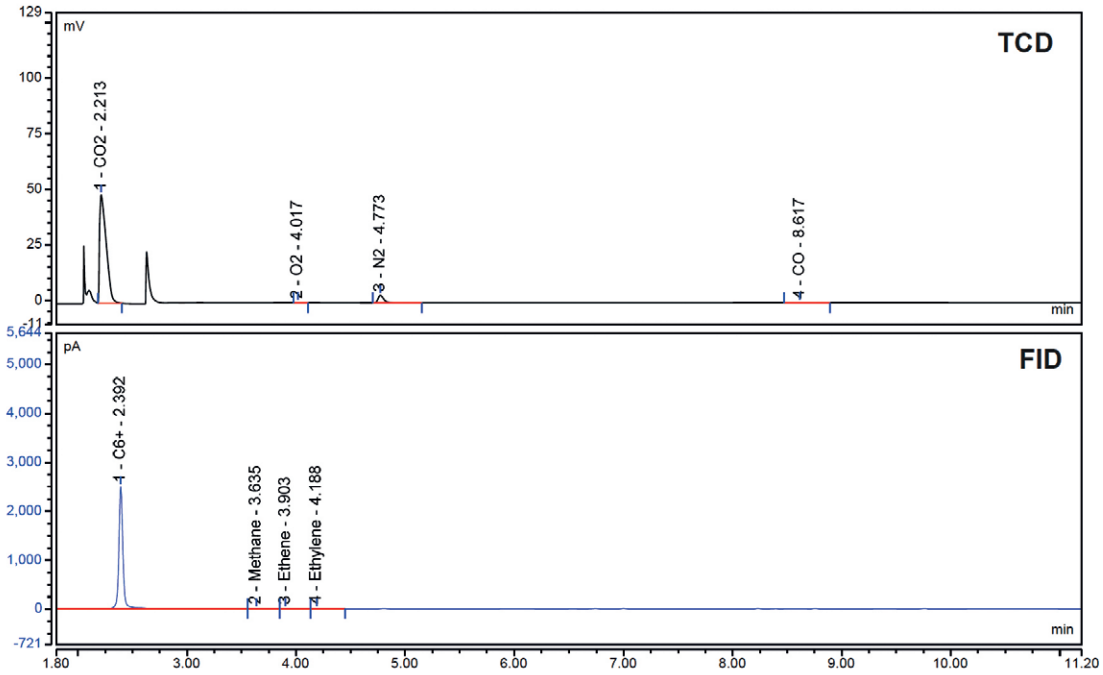

Figure 6. Chromatographic separation of Batch 2 – Sample W

Table 6. Quantitative results for Batch 2 – Sample W

Peak	Compound	Detector	Retention time (min)	Area (mV*min)	Height (mV)	Amount (%, V/V)	Corrected amount (%)
1	CO_2	TCD (Aux-Left)	2.213	3.41	48.67	79.65	92.93
2	O_2	TCD (Aux-Left)	4.017	0.006	0.15	0.10	0.12
3	N_2	TCD (Aux-Left)	4.773	0.20	3.31	4.81	5.61
4	CO	TCD (Aux-Left)	8.617	0.02	0.13	0.52	0.60
1	C6+	FID (Back)	2.392	113.32	2495.9	0.59	0.70
2	Methane	FID (Back)	3.635	0.49	3.94	0.017	0.02
3	Ethane	FID (Back)	3.903	0.37	5.25	0.007	0.01
4	Ethylene	FID (Back)	4.188	0.34	7.20	0.006	0.01

Second batch – Sample E:

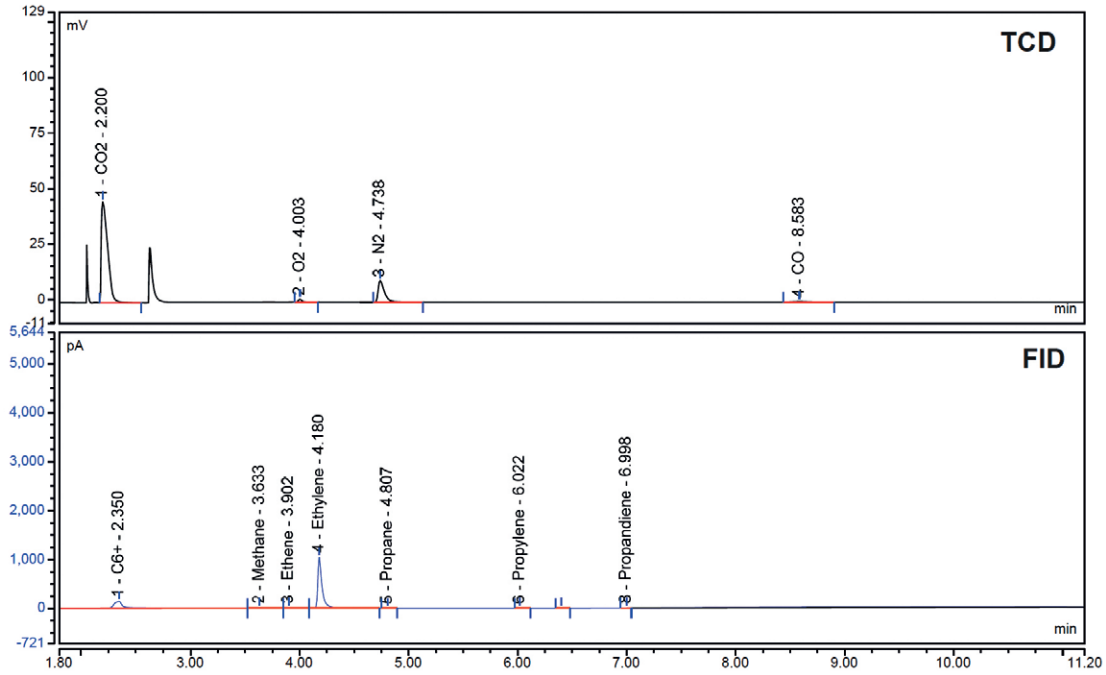

Figure 7. Chromatographic separation of Batch 2 – Sample E

Table 7. Quantitative results for Batch 2 – Sample E

Peak	Compound	Detector	Retention time (min)	Area (mV*min)	Height (mV)	Amount (%, V/V)	Corrected amount (%)
1	CO_2	TCD (Aux-Left)	2.200	3.09	45.53	72.10	80.04
2	O_2	TCD (Aux-Left)	4.003	0.05	1.24	0.87	0.97
3	N_2	TCD (Aux-Left)	4.738	0.63	9.60	15.25	16.93
4	CO	TCD (Aux-Left)	8.583	0.04	0.24	0.97	1.08
1	C6+	FID (Back)	2.350	13.57	142.90	0.07	0.08
2	Methane	FID (Back)	3.633	0.37	3.70	0.01	0.01
3	Ethane	FID (Back)	3.902	0.22	4.29	0.004	0.00
4	Ethylene	FID (Back)	4.180	46.36	1040.1	0.80	0.89
5	Propane	FID (Back)	4.807	0.02	0.43	0.0003	0.00
6	Propylene	FID (Back)	6.022	0.03	0.66	0.0003	0.00
7	Propandiene	FID (Back)	6.998	0.02	0.32	0.0003	0.00

Conclusion

The configured multi-valve, multi-column TRACE 1300 series GC system is a robust solution to detect the complex gas mixture from batteries swelling in less than 10 minutes, characterizing the aging and performance.

- The backflush configuration not only shortens the analysis time but avoids heavier compounds to damage the separation columns.
- A single injection allows qualitative and quantitative analysis of drum pack gas components, with the detection of both permanent gases and light hydrocarbons up to C6+.

Find out more at **thermofisher.com**

ThermoFisher SCIENTIFIC

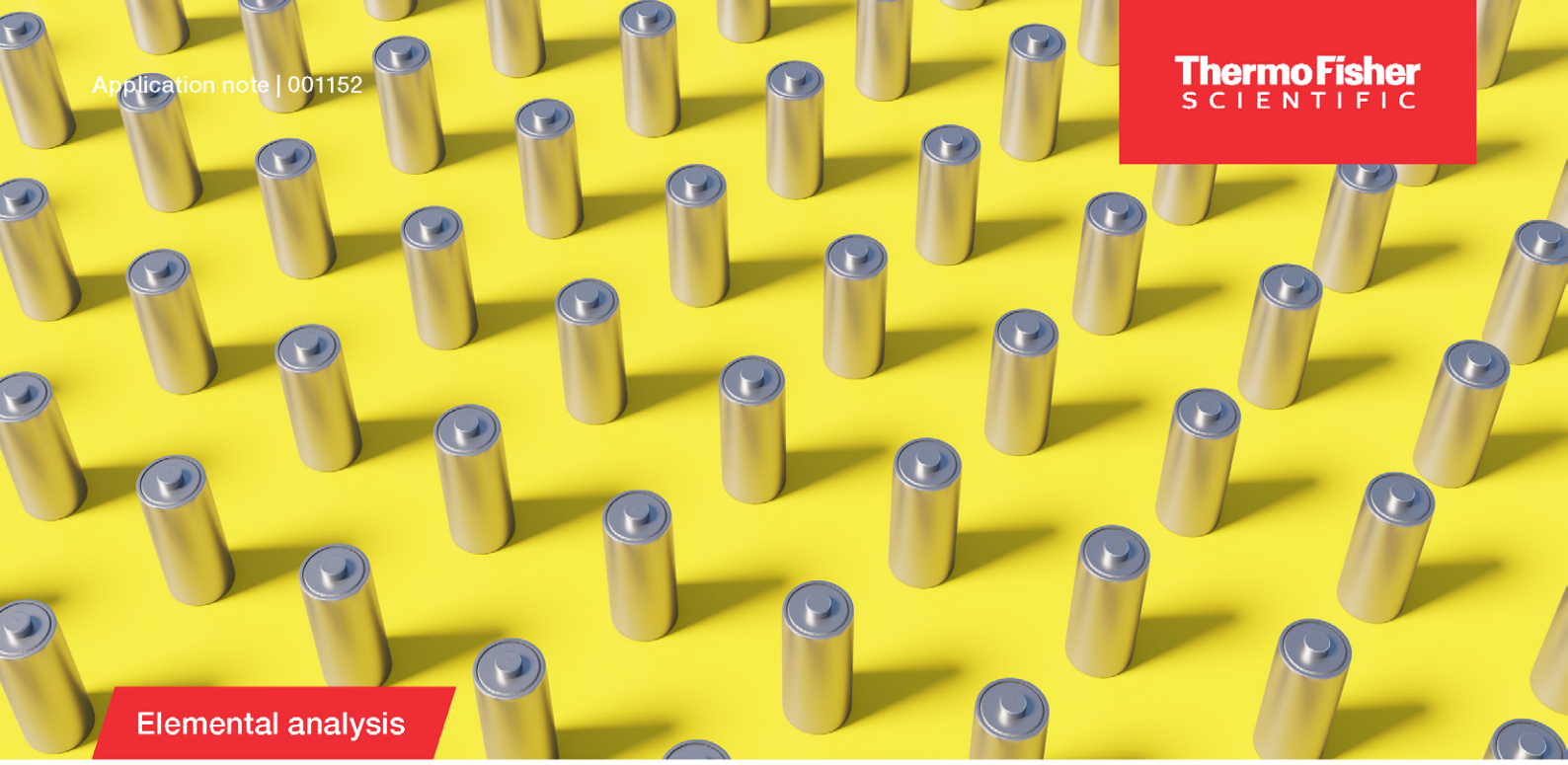

Application note | 001152

Elemental analysis

Characterization of battery samples by the Flash*Smart* Elemental Analyzer

Authors

Liliana Krotz[1], Mario Tuthorn[2]

[1]Thermo Fisher Scientific, Milan, Italy
[2]Thermo Fisher Scientific, Bremen, Germany

Keywords

Batteries, carbon, combustion, graphite, sulfur, quality control

Goal

Demonstrate accurate and precise CHNS determination in battery samples using the Thermo Scientific™ *FlashSmart*™ Elemental Analyzer

Introduction

During the development and production of batteries, quality control (QC) of raw, intermediate and finished products is required to assure high quality and performance, and also safety. A simple and fast way to monitor elemental composition of these products for QC is by using the Flash*Smart* Elemental Analyzer (EA). Elemental characterization by Flash*Smart* EA mainly focuses on two elements: **carbon and sulfur**. Carbon and sulfur elemental determination allows accessing information on the purity of material which is critical as changes in production can cause the introduction of impurities and ultimately impact the lifetime and energy storage capacity of the battery.

The electrochemical properties of $LiFePO_4$ cathodes with different carbon contents are analyzed to determine the role of carbon as conductive additive, whereas as lead paste exhausted batteries are analyzed for sulfur content. Carbon and sulfur determination are also performed on graphite material used in negative electrode production.

Method

The Flash*Smart* Elemental Analyzer (Fig. 1) uses dynamic flash combustion to perform quantitative elemental analysis, offering the flexibility to perform CHNS analysis in a single run.

Figure 1. Thermo Scientific Flash*Smart* Elemental Analyzer

For simultaneous CHNS determination, samples are weighed in tin containers and introduced into the combustion reactor via the Thermo Scientific™ MAS Plus Autosampler. After combustion, the produced gases are separated in a GC column, and detected by a Thermal Conductivity Detector (TCD) (Figure 2). For weight percent determination of CHNS a complete report is automatically generated by the Thermo Scientific™ Eager*Smart*™ Data Handling Software and displayed at the end of the analysis.

Single Sulfur determination by Flame Photometric Detector or simultaneous NCS determination configurations are available.

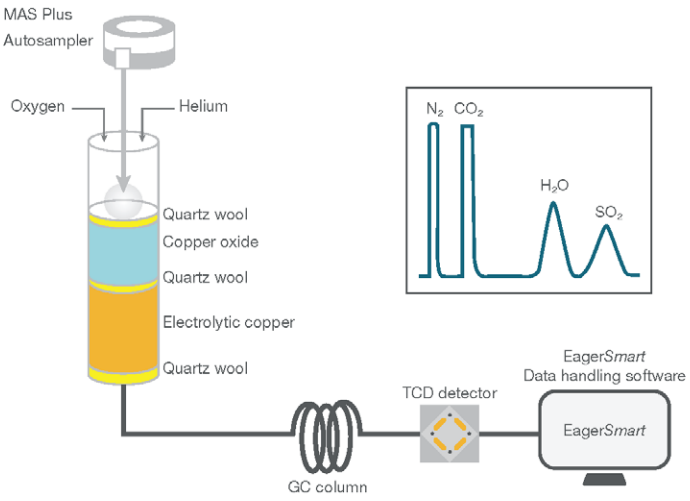

Figure 2. CHNS configuration

Results

The analysis of different batteries and graphite samples were performed to demonstrate the performance of the Flash*Smart* EA for CHNS wt% determination.

Carbon data of $LiFePO_4$ batteries

The capacity of the $LiFePO_4$ cathode increases as conductive additive content (carbon black or mixture of carbon black and graphite) is increased. Therefore, accurate and precise carbon content determination, as demonstrated in Table 1, is critical for QC. The calibration was performed with aspartic acid standard using K factor as calibration method. The sample weight was approx. 8-9 mg.

Table 1. Carbon data of $LiFePO_4$ batteries

Sample $LiFePO_4$ battery	C%	RSD%
1	4.54	0.77
	4.59	
2	7.57	0.47
	7.52	
3	4.82	0.15
	4.81	
4	5.16	0.69
	5.11	

Sulfur data of lead paste ($PbSO_4$, PbO_2, Pb) exhausted batteries

Sulfur content determination is important because sulfur affects the lifetime of the battery and the reduction of battery capacity. Table 2 demonstrates accuracy and precision of sulfur weight% determination in lead paste exhausted batteries. The calibration was performed with 2,5-Bis-(5-tert-butylbenzoxazol-2-yl)-thiophen (BBOT) standard using K factor as calibration method. The sample weight was 2-6 mg depending on the sample.

Table 2. Sulfur data of lead paste ($PbSO_4$, PbO_2, Pb) exhausted batteries

Sample $PbSO_4$, PbO_2, Pb exhausted battery	S%	RSD%
1	6.23	0.43
	6.22	
	6.18	
2	1.67	0.92
	1.66	
	1.64	
3	7.18	0.29
	7.19	
	7.22	
4	0.778	0.97
	0.772	
	0.762	
5	1.74	0.67
	1.72	
	1.72	

CHNS determination by TCD detector and trace Sulfur by FPD detector for QC of graphite

For lithium-ion batteries, the negative electrode (anode) material is generally made from graphite powder. Elemental analysis is used for C and S determination of graphite material in batteries for assessing material purity. Table 3 demonstrates how in a single run, 4 elements (CHNS) can be determined with high precision, and Table 4 demonstrates that trace sulfur determinations are also possible by using Flash*Smart* EA with an FPD detector.

Graphite samples were homogenized by a ball mill. For CHNS determination, the calibration was performed with 2 – 3 mg BBOT standard using K factor as calibration method; the sample weight was 1.8 – 2.2 mg; to obtain complete combustion the oxygen flow was 300 ml/min and the oxygen injection time 13 seconds.

For trace sulfur determination by FPD detector, the calibration was performed with a Soil reference material (0.0033 S%) using Quadratic Fit as calibration method; sample weight was 1 – 2 mg. Standard and samples were weighed with the addition of vanadium pentoxide.

Conclusions

The Flash*Smart* Elemental Analyzer, based on the combustion (modified Dumas method), determines CHNS of battery material in a wide range from low to high content and without the use of sample digestion or toxic chemicals, which is normally required by traditional methods. Simultaneous CHNS or NCS determination can be easily done in a single run, with support of dedicated Eager*Smart* Data Handling Software that provides you with customized reports of your data. Trace sulfur by the FPD detector can be analyzed also with only minor modifications of the analytical conditions. The Flash*Smart* Elemental Analyzer demonstrates excellent repeatability, reproducibility, accuracy, and precision in the analysis of different battery material in a cost-efficient and simple way.

Table 3. CHNS determination of graphite samples

Sample Graphite	N%	RSD%	C%	RSD%	H%	RSD%	S%	RSD%
1	0.0700	3.05	97.52	0.05	0.0200	8.98	0.0600	4.91
	0.0722		97.51		0.0199		0.0658	
	0.0744		97.60		0.0170		0.0612	
2	0.0600	3.25	91.59	0.30	0.0900	4.55	-	-
	0.0563		91.27		0.0823			
	0.0589		91.82		0.0850			

Table 4. Trace sulfur determination by FPD detector of graphite samples

Sample Graphite	ppm S	RSD%	Sample Graphite	ppm S	RSD%
A	42	1.29	B	21	2.56
	42			21	
	43			21	
	42			21	
	43			21	

Learn more at **thermofisher.com/OEA**

Application note

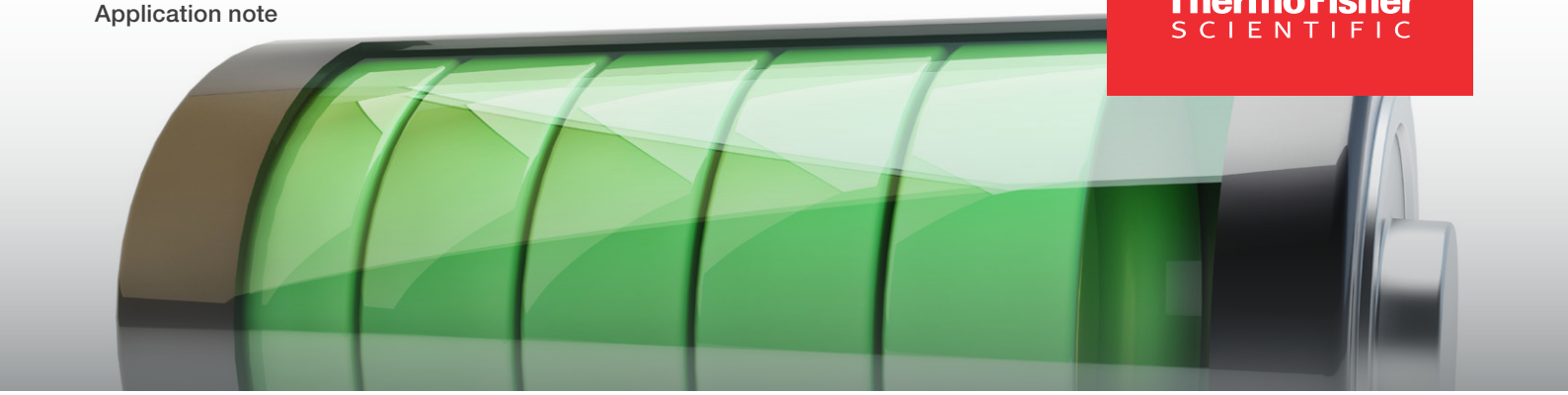

Continuous twin-screw compounding of battery slurries in a confined space

Author

Annika R. Völp

Keywords

Cathode slurry mixing, twin-screw extruders, battery rheology, Process 11 Compounder, HAAKE MARS Rheometer

Battery slurry production is commonly realized by batchwise compounding of active materials, carbon black, solvents, binders, and additives in stirred vessels. This bears the risk of batch-to-batch variations, is labor-intensive, and requires production downtimes. Also, the transfer from lab scale pre- paration of novel formulations to production scale is difficult.

Twin-screw compounding offers a continuous production process with precisely controlled material shear, heat transfer, material throughput, and residence time. It provides high reproducibility, less cleaning time, and high material efficiency. Two parallel, co-rotating and intermeshing screws, embedded in a cylindrical barrel with dosing ports, mix, knead, and shear materials and eventually convey the compound through an outlet at the barrel end. Attaching a die to the outlet extends the system to a twin-screw extruder. Scalability of twin-screw extruders' geometry enables easy transfer from lab processes to high-throughput production of slurries.

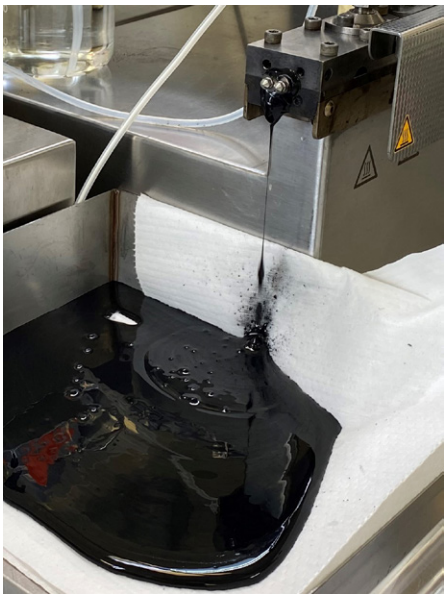

Figure 1. Cathode slurry compounded using Process 11 Twin-Screw Compounder.

Lab scale compounder

The Thermo Scientific™ Process 11 Parallel Twin-Screw Compounder represents all functionalities of a production extruder scaled down to lab size with throughputs ranging from 0.1 to 4.5 kg/hr. Its small footprint allows it to be placed entirely into glove boxes or other containment systems, together with liquid and solid feeders placed on its housing, as demonstrated in Figure 2. This is required for cathode materials that need to be handled in a dry environment and for protection of the operators from hazardous chemicals. Liquid barrel cooling and controlled degassing ensures safe operation. With a flexible screw design and five dosing positions along the barrel, the instrument enables quick changing of the composition of the slurries and the processing route.

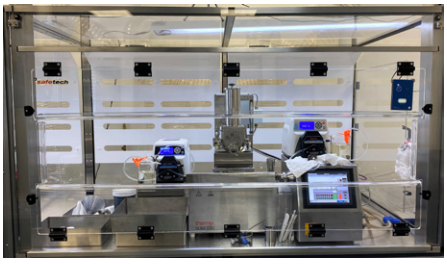

Figure X. Figure 2. Process 11 Twin-Screw Compounder, two liquid feeding systems, and one solid feeding system in a safety work bench. The setup captures a space of 770 x 830 x 730 mm.

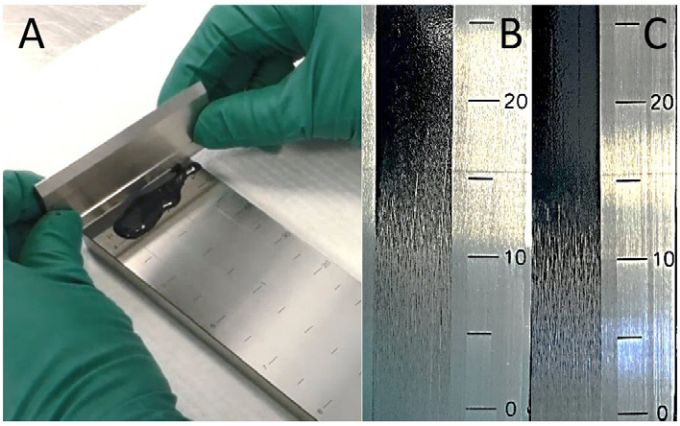

Figure 3. Examination of (A) cathode slurry on a grindometer. Average particle size of cathode slurry is bigger when produced at (B) high throughput than (C) low throughput.

Slurry characterization

A broad variety of slurry properties can be achieved within minutes, and producibility of novel formulations can be tested. Examination of the freshly compounded slurries on a grindometer shows differences in the grain size depending on the throughput, for instance, as shown in Figure 3. Rheological characterization of the slurries using the Thermo Scientific™ HAAKE™ MARS™ Rheometer reveals variations in the strain rate of dependent viscosity (see Figure 4). The characteristic flow curve determines the stability of the slurry suspension and its further processability in coating systems. For slurries stored in buffer tanks prior to coating, high viscosity at low shear rates (10^{-3} s^{-1}) is advantageous as it reduces sedimentation. During coating, however, high shear rates (10^{3} s^{-1}) occur and a high shear thinning behavior is advantageous. After coating, the slurries ideally quickly regain a high viscosity, which prevents the coating from spreading.

Conclusion

Downsides of batchwise battery slurry production are conquered by continuous twin-screw compounding. Thermo Fisher Scientific provides lab scale twin-screw extruders for battery slurry development that fit into spaces as small as glove boxes. The twin-screw compounding process is scalable, easing the transfer of process parameters established in the lab to application of production scale extruders. Precise characterization of the slurries' rheology using HAAKE MARS Rheometers allows one to predict the storage stability, coatability, and spreading behavior of the slurries.

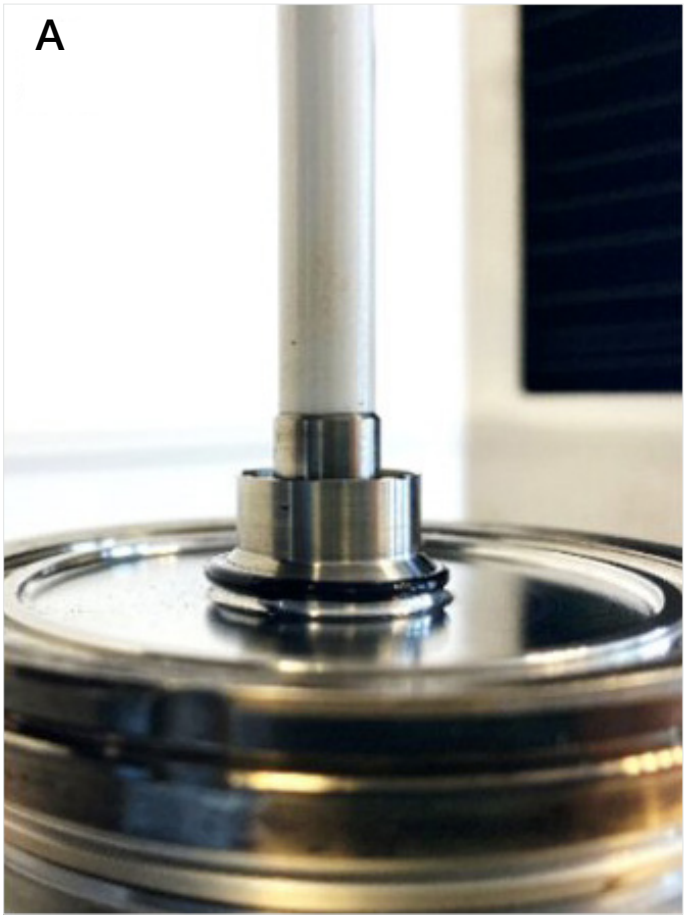

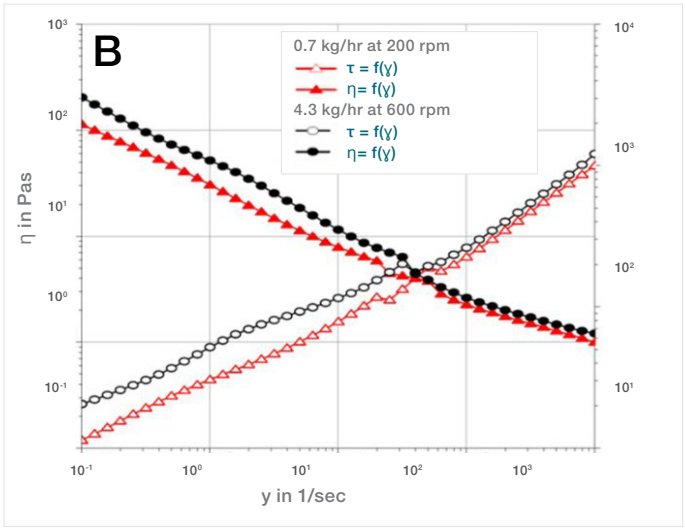

Figure 4. (A) Rheological characterization of cathode slurry in the HAAKE MARS Rheometer with plate–plate geometry. (B) Strain rate dependent viscosity function of cathode slurries produced at low and high throughput and screw speed, respectively.

Learn more at **thermofisher.com/battery-extrusion**

Application note

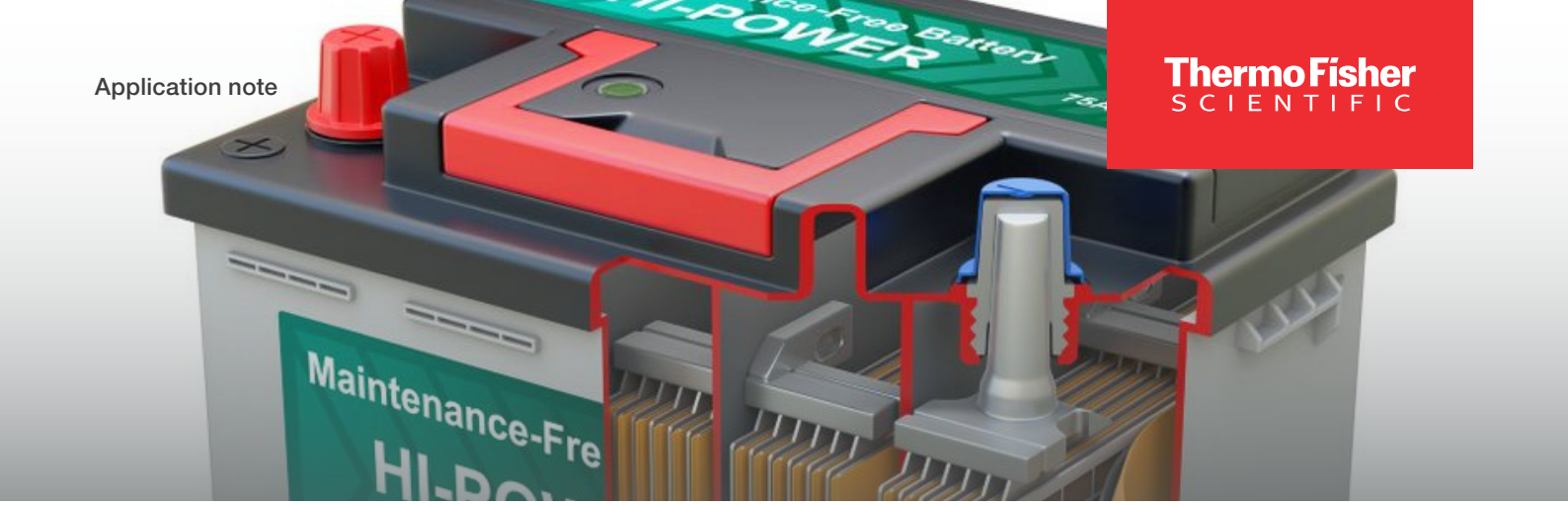

Cost-efficient and ecological twin-screw compounding of dry lithium-ion battery pastes

Author

Annika Völp Thermo Fisher Scientific, Karlsruhe, Germany

Keywords

Solvent-free electrode pastes, battery extrusion, 16 mm twin-screw extruder

Figure 1. Pharma 16 Twin-Screw Extruder with gravimetric powder and liquid dosing systems and Pharma FaceCut Pelletizer.

Challenges for efficient battery production

The global production of lithium-ion batteries will increase enormously with the rising demand for electromobility. In this respect, ecologically and economically efficient production of electrodes is crucial. Additionally, the process-related structures of the electrodes must be optimized in order to ultimately improve the range, safety, and performance of electric vehicles, while at the same time lowering the price for the consumer.

One approach to achieve such goals, is to develop innovative processes for dry or low-solvent electrode manufacturing. Conventional coating of the electrode collector foil requires low-viscous slurries with a solvent content of 45%.[1] Subsequent solvent evaporation and recycling consumes a majority of energy, using 20% of the total energy required for cathode manufacturing.[2] Solvent reduction in slurries could significantly improve the ecological and economic efficiency of electrode production. But it also requires novel processing solutions for compounding and coating of the anode and cathode pastes.

Low-solvent battery paste extrusion

Twin-screw extruders achieve fine dispersion in high-viscous pastes through strong shear forces acting on the material. This alone reduces the solvent content by 50% in cathode pastes.[3] Polytetrafluoroethylene (PTFE) forms fibrils under shear and has been determined to be a suitable binder, fixing the electrode structure and at the same time creating a pore network that ensures the diffusion of lithium ions. Compounding extrusion of active material with PTFE yields high-viscous electrode pastes with solvent contents below 5%.

Thermo Scientific™ extruders are successfully used in research projects for innovative electrode manufacturing.[4] The twin-screw extruder compounds anode material with minimized solvent added. The highly viscous pastes are processed into pellets with the Thermo Scientific Pharma FaceCut Pelletizer (Figure 2). In this shape, they are easily transported and stored without aging. To form electrodes, the pellets can later be coated on collector foil and calendared in one step.

This electrode manufacturing route is scalable to mass production and prospectively demands 60% less energy than conventional manufacturing.[4] The technology is expected to be applicable to polymer electrolyte electrodes and, after minor adjustments, to solid-state electrodes.

Extruder design

The split barrel design and the segmented screws allow for fast cleaning and process customization (Figure 3). This makes the twin-screw extruders ideal for the development of novel formulations and evaluation of extrusion in lab and pilot scale as a production compounding solution.

Depending on the availability of material, electrode pastes can be compounded with throughputs between 200 g/ hr and 30 kg/ hr with 11 mm, 16 mm, or 24 mm screw diameters. Identical geometry ratios enable easy scalability of the compounding process between the extruder sizes. All extruders are available in pharma grade stainless steel that is chemically resistant against corrosion, in CPM hardened steel that can withstand abrasion, or in nitriding steel 1.7361 (EN40B) that exhibits a well-balanced mix of both qualities.

References

1. Schunemann JH, Dreger H, Bockholt H, Kwade A. Smart electrode processing for battery cost reduction. *ECS Transactions*. 2016;73(1):153-159. doi:10.1149/07301.0153ecst
2. Bryntesen SN, Strømman AH, Tolstorebrov I, Shearing PR, Lamb JJ, Stokke Burheim O. Opportunities for the state-of-the-art production of lib electrodes - a review. *Energies*. 2021;14(5). doi:10.3390/en14051406
3. Dreger H, Bockholt H, Haselrieder W, Kwade A. Discontinuous and continuous processing of low-solvent battery slurries for lithium nickel cobalt manganese oxide electrodes. *Journal of Electronic Materials*. 2015;44(11):4434-4443. doi:10.1007/s11664-015-3981-4
4. "HEMkoop-Hochenergiematerialien - kosteneffizient und ökologisch prozessiert", BMBF project 03XP0117B, TU Braunschweig, Germany.

Figure 2. Pharma FaceCut Pelletizer cuts extruded paste into pellets with rotating blades directly at the die exit.

Figure 3. Twin-screw extruder split barrel design.

Learn more at **thermofisher.com/battery-extrusion**

ThermoFisher SCIENTIFIC

Battery Analysis Solutions from Thermo Fisher Scientific.

The preferred supplier for all your chemical, elemental and structural analysis needs in battery research, development and failure analysis.

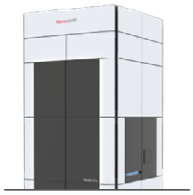
TEM


FTIR


ICP-MS


Desktop SEM


XPS


GC


GC-MS


FESEM


XRD


NMR


Ion Chromatography

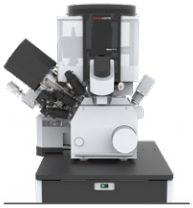
FIB-SEM


Raman


HPLC


LC-MS


Rheology


Twin-Screw Extrusion


Torque Rheometer


XRF

Find out more about Thermo Fisher Scientific capabilities for batteries at **thermofisher.com/battery-solutions**

thermo scientific